

Durham E-Theses

magnetization processes in permalloy overlays on magnetic bubble devices.

Garnett, Geoffrey William

How to cite:

Garnett, Geoffrey William (1981) *magnetization processes in permalloy overlays on magnetic bubble devices.*, Durham theses, Durham University. Available at Durham E-Theses Online:
<http://etheses.dur.ac.uk/7648/>

Use policy

The full-text may be used and/or reproduced, and given to third parties in any format or medium, without prior permission or charge, for personal research or study, educational, or not-for-profit purposes provided that:

- a full bibliographic reference is made to the original source
- a [link](#) is made to the metadata record in Durham E-Theses
- the full-text is not changed in any way

The full-text must not be sold in any format or medium without the formal permission of the copyright holders.

Please consult the [full Durham E-Theses policy](#) for further details.

MAGNETIZATION PROCESSES IN PERMALLOY OVERLAYS
ON MAGNETIC BUBBLE DEVICES.

BY

GEOFFREY WILLIAM GARNETT.

Thesis submitted to the University of Durham in
candidature for the degree of Doctor of Philosophy.

The copyright of this thesis rests with the author.
No quotation from it should be published without
his prior written consent and information derived
from it should be acknowledged.

Department of Physics,
University of Durham,
May, 1981.



To my wife, Audrey.

ACKNOWLEDGEMENTS

I would like to thank Professor B.H. Bransden and Professor A.W. Wolfendale for the use of research facilities and the Science Research Council for providing a grant.

I am most grateful to Dr. W.D. Corner for his advice and encouragement in pursuing this investigation. I would also like to thank Dr. B.K.Tanner and other members of the Solid State Research Group for useful discussions and Mr K. Moulson for technical assistance.

I would like to express my gratitude to the members of the Magnetic Bubble Research Group of the Plessey Co. Ltd. for providing research materials and collaborating in this project. In particular I would like to thank Dr. D.R.Brambley for acting as my industrial supervisor.

Finally I would like to thank my wife for typing and assisting with the preparation of this thesis.

Magnetization Processes in Permalloy Overlays on Magnetic

Bubble Devices

G. W. Garnett.

Using colloid techniques domain structure has been studied in several overlay components used in contemporary bubble devices. In isolated elements the demagnetized state is generally simple, containing a small number of domains. The influence of anisotropy on domain structure is demonstrated. Elements initially respond to applied fields by reversible domain boundary movement but in each case it has been found that partial saturation and hysteresis occur once the applied field exceeds a critical value, H_g . This causes the formation of remanent states with 'magnetization buckling' similar to that found in larger samples of thin-film permalloy. The relationship between H_g and element geometry and thickness and the formation of buckled states by a rotating field were investigated. Such states may adversely affect the operation of a bubble device. The approach to partial saturation in a simple bar has been modelled on the basis of a curved domain wall and approximate values for the saturation field calculated. The external field profile of the bar has also been obtained. Domain structure in various connected chevron columns (bubble detectors) was also studied. In contrast to isolated elements the initial 'zero-field' state in these components is generally one of saturation. This state can be broken by components of applied field parallel or perpendicular to the column and again magnetization buckling is involved. Magnetoresistance changes related to the buckled state were measured and found to be consistent with the colloid observations. These observations can be used to explain the characteristic magnetoresistance signal of a chevron column in a rotating field.

Foreword.

The majority of papers on magnetic bubble devices employ C.G.S. rather than S.I. units, and magnetic fields are usually measured in Oersted (Oe.) :

$$1 \text{ Oersted} \equiv \frac{1}{4\pi} \times 10^3 \text{ Ampere/meter}$$

(C.G.S.) (S.I.)

For ease of comparison with previous work the results of this thesis are presented in Oe.

CONTENTS

1						
	1.1	Introduction	1
	1.2	Magnetism	3
2	MAGNETIC DOMAINS					
	2.1	Introduction	10
	2.2	Exchange energy	10
	2.3	Anisotropy energy	11
	2.4	Magnetoelastic energy	13
	2.5	Magnetostatic energy	14
	2.6	Domain wall energy	17
	2.7	Domain structures	26
	2.8	Colloid techniques	32
	2.9	Magneto-optical techniques	35
	2.10	Electron microscopy	36
3	MAGNETIC BUBBLES					
	3.1	Introduction	40
	3.2	Stability of a bubble domain at rest	40
	3.3	Bubble wall structure	43
	3.4	Hard bubbles and bubble dynamics	44
	3.5	Materials	52
	3.6	Conventional bubble devices	58
	3.7	Bubble detectors	65
	3.8	Chip organization	68
	3.9	Device fabrication	69
	3.10	Ion-implanted bubble devices	73
	3.11	Bubble lattice devices	76
	3.12	Current-access bubble devices	78
	3.13	Applications	79

4	EXPERIMENTAL AND THEORETICAL WORK ON PERMALLOY OVERLAYS	
4.1	Introduction	82
4.2	Experimental measurements	82
4.3	Calculations	84
5	DESCRIPTION OF EXPERIMENT	
5.1	Samples	88
5.2	Microscope	88
5.3	Applied fields	89
5.4	Ferrofluid experiments	90
6	ISOLATED ELEMENTS - RESULTS AND DISCUSSION	
6.1	Energy and width of Bloch walls in permalloy ..	94
6.2	Bloch wall subdivision	98
6.3	Anisotropy in permalloy overlays	101
6.4	Domain structures in 16- μ m period overlays ..	110
6.5	Magnetization by reversible wall movement ..	116
6.6	Magnetization processes involving saturation and hysteresis	122
6.6.1	Magnetization processes in large rectangular permalloy bars	122
6.6.2	Saturation and hysteresis in overlay bars	129
6.6.3	Changes in Bloch wall structure ..	134
6.6.4	Partial saturation in pick-axe elements ..	136
6.6.5	Partial saturation in gap-tolerant patterns	139
6.7	Dependence of saturation field on element geometry and thickness	142
6.8	The formation of remanent states in a rotating field	145
6.9	Partial saturation in overlay bars on magnetic garnet	150
6.10	Significance of hysteresis for device operation	152
7	DETECTOR COLUMNS - RESULTS AND DISCUSSION	

7.1	Basic remanent domain structures	154
7.2	Magnetization reversal in a closed loop of permalloy	157
7.3	Magnetization reversal in chevron detector columns			161
7.4	Magnetoresistance variations related to buckling			171
7.5	Calculated magnetoresistance of a detector column during buckling	175
7.6	Significance of buckling in a detector column subjected to a rotating field	180
8	FIELD CALCULATIONS			
8.1	Introduction	186
8.2	'Free pole' density	190
8.3	Demagnetizing field	194
8.4	External field	204
8.5	Permanent stray field of the Bloch wall.		..	209
9	CONCLUSIONS AND SUGGESTIONS FOR FURTHER WORK			216

CHAPTER 1.

1.1 Introduction.

A magnetic bubble is a cylindrical domain which can exist in certain thin films of magnetic material. Bubbles only occur if the material has strong uniaxial anisotropy with the easy axis of magnetization perpendicular to the film surface. The bubble domain is, in effect, a small region of reverse magnetization in an almost saturated layer and its stability depends upon the application of a magnetic bias field perpendicular to the film (see figure 1.1). Such domains were observed in thin layers of the hexaferrite $Ba Fe_{12} O_{19}$ by Kooy and Enz (1960), but Bobeck (1967), was the first person to recognize their technical significance. Bubbles remain stable or 'non-volatile' providing a permanent bias field is supplied and they are small (diameters less than $1\mu m$ can now be achieved). They can also be made to move quite easily by the application of extra magnetic fields. This combination of properties led Bobeck to suggest that bubbles might be used to represent binary data in a new type of memory device.

Since this idea emerged much work has been done to understand the basic properties and behaviour of bubble domains and to develop suitable materials for devices. In most memories designed so far the method of controlling bubbles is to deposit a periodic pattern of thin film elements of soft magnetic material on top of the bubble medium. This pattern or 'overlay' is usually made of permalloy and can easily be magnetized by the application of a uniform field in the plane of the device. Bubbles are attracted by the magnetic poles which develop on individual overlay elements and reside in stable positions of



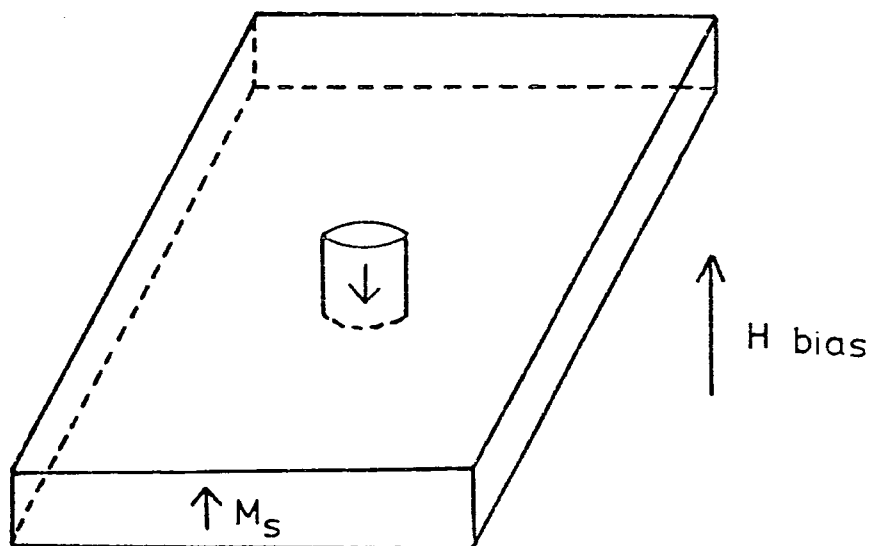


Fig. 1.1 Magnetic bubble configuration.

minimum energy. When the in-plane field is rotated, the pattern of magnetic poles on the permalloy changes and bubbles are forced to move along a particular track. Other functions required in a memory such as feeding in data by generating strings of bubbles and gaps (representing binary '1' and '0') or reading out data by detecting bubbles can also be incorporated in the overlay design.

The aim of this project was to study magnetic domains in the overlays used for magnetic bubble devices. The behaviour of these domains determines the magnetization processes which occur in an overlay and hence the magnetic fields which a bubble domain experiences.

1.2 Magnetism.

Magnetism has been described fundamentally as "a particular form of the material interactions originating between moving electrically charged particles" (Vonsovskii, 1974). This interaction is transmitted by the magnetic field. Thus, currents formed by the movement of electrical charge are always the source of magnetic field and in fact the magnetic properties of matter are mainly caused by the spin and orbital angular momenta of electrons. Different types of magnetic material can be distinguished according to the way they behave in applied magnetic fields. If \vec{H} is the applied magnetic field measured in ampere meter⁻¹, then the magnetic induction in free space is given by:

$$\vec{B}_0 = \mu_0 \vec{H}$$

where μ_0 is the absolute permeability of free space ($4\pi \times 10^{-7}$ Henry metre⁻¹) and \vec{B}_0 is measured in Tesla. Within a medium

the magnetic induction is given by:

$$\begin{aligned}\vec{B} &= \mu_0(\vec{H} + \vec{M}) \quad (\text{SI, Sommerfeld convention}) \\ &= \vec{B}_0 + \mu_0 \vec{M}\end{aligned}$$

where \vec{M} is the magnetization defined by the vector sum of magnetic dipole moments per unit volume (measured in ampere metre⁻¹). If the component of magnetization in the direction of applied field (M_H) is divided by the value of applied field (H) then we obtain the magnetic susceptibility per unit volume of material.

$$K = \frac{M_H}{H} \quad (\text{Dimensionless})$$

K gives a measure of the ease with which a material is magnetized by an applied field. Magnetic behaviour may also be described in terms of permeability, μ , which is the ratio of magnetic induction to applied field.

$$\mu = \frac{B}{H} \quad (\text{measured in Henry metre}^{-1})$$

Relative permeability is obtained by dividing μ by the absolute permeability of free space:

$$\begin{aligned}\mu_r &= \frac{\mu}{\mu_0} \quad (\text{Dimensionless}) \\ \mu &= 1 + K\end{aligned}$$

Paramagnetic materials have small positive values of susceptibility, usually less than 10^{-3} at room temperature. Paramagnets contain permanent magnetic dipoles but in the absence of applied fields there is a random distribution of dipole orientations due to thermal agitation. The magnetization is therefore zero. When a field is applied, the moments tend to align parallel to the field producing a weak magnetization

proportional to H . Much more important in technology however are those materials which exhibit ferromagnetism. The transition elements iron, cobalt and nickel and certain rare earths are ferromagnetic. So too are many alloys such as permalloy which combines two ferromagnetic metals; iron and nickel. Ferromagnetic solids contain atoms with permanent magnetic dipoles and are characterized by a critical temperature known as the Curie point. Above this temperature the magnetic dipoles are essentially independent and the material behaves as a paramagnet. Below the Curie point ordering of magnetic dipoles occurs on an atomic scale producing a spontaneous magnetization, M_s . The value of M_s rises as the temperature is reduced reaching a maximum at absolute zero.

Weiss (1907) attempted to explain ferromagnetism by postulating the existence of a fundamental molecular field. Below the Curie point the magnetic atoms are aligned parallel to the molecular field whose strength is proportional to the magnetization. On this basis it can be shown that there is paramagnetic behaviour above the Curie temperature, T_c , with a susceptibility given by:

$$\chi = \frac{C}{T - T_c} \quad C = \text{Curie Constant.}$$

This generally agrees well with experimental measurements. At $T = T_c$, χ becomes infinite so a finite value of M may exist with $H = 0$. A physical explanation of the ordering of magnetic dipoles is provided by Quantum mechanics in terms of inter-atomic exchange forces. There is a certain degree of overlap between the electron charge distributions on adjacent atoms. For a simple system of

two atoms with electron spin vectors \vec{S}_i and \vec{S}_j , the energy of exchange interaction takes the form:

$$E_{\text{ex.}} = -2J\vec{S}_i \cdot \vec{S}_j$$

where J is the exchange integral. This equation represents the Heisenberg exchange interaction and is a consequence of the Pauli Exclusion Principle. If we change the spin orientation on either atom then we must compensate by altering the spatial charge distribution in the overlap region.

For the ferromagnetic elements Fe, Co and Ni, J has a positive value. This means that the state of parallel spins has minimum energy. The spin-spin interaction is opposed by thermal agitation and at high enough temperatures, i.e. above T_c , the order is destroyed.

Other types of magnetic ordering are possible based upon the exchange interaction. If J is negative the state of minimum energy occurs with anti-parallel spins on adjacent atoms. This type of ordering is termed antiferromagnetic, with zero spontaneous magnetization existing below the critical temperature.

In other materials there is antiparallel ordering with a resultant magnetization due to imbalance between opposing magnetic moments. Such behaviour is termed ferrimagnetic and may arise because the antiparallel magnetic dipoles differ in magnitude or in number. The magnetic garnets used in bubble devices are ferrimagnetic. Ferrimagnetic materials have Curie temperatures above which the Curie-Weiss law holds but in the ordered state the dependence of M on temperature may be more complex than for a ferromagnet. The existence of compensation points will be

discussed later in relation to bubble materials.

Although the elementary moments of a ferromagnet become aligned on an atomic scale producing a spontaneous magnetization it is an experimental fact that the overall magnetization of a ferromagnetic body is usually zero in the absence of applied fields. To explain this apparent contradiction, Weiss suggested that real specimens are actually split up into a number of small regions. Within each region or 'domain' there is uniform magnetization but the domains are magnetized in different directions. It is therefore possible for the sample as a whole to be 'demagnetized'. When a magnetic field is applied magnetization can occur in two ways. In weak fields the boundaries between domains can move so that domains magnetized in a similar direction to the applied field grow whilst other domains contract. In certain pure samples of permalloy this process involves such a small amount of energy that saturation can very nearly be achieved in fields approximately 10^{-5} times the value of M_s . In stronger fields the magnetization in an entire domain may rotate towards the field direction. Bitter (1931) proved that domains actually exist by covering the surface of a ferromagnetic specimen with a liquid containing fine particles of magnetite. The magnetite particles are attracted to stray fields above domain boundaries thus mapping the intersection of domain structure with the specimen surface.

The existence of domains explains why the magnetization process of a ferromagnet exhibits hysteresis. If the component of magnetization in the direction of applied field (M_H) is plotted against the value of applied field H , then a curve of the type shown in figure 1.2 usually results. (Morrish, 1965)

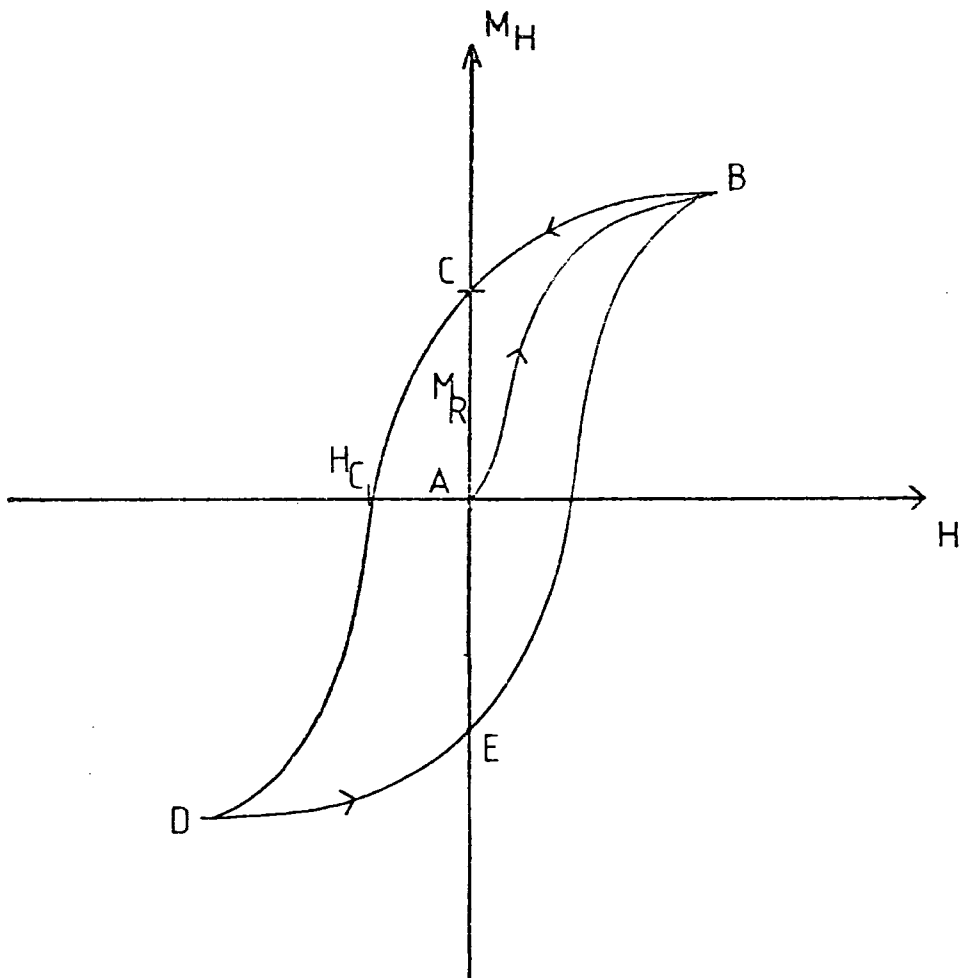


Fig. 1.2 Schematic magnetization versus applied field for a ferromagnetic body (Morrish, 1965).

From an initial state of demagnetization (A), the value of M_H increases to saturation at B. The section of curve AB is referred to as the 'magnetization curve'. The full cycle of magnetization depicted by the path BCDEE is known as the 'hysteresis loop'. The term hysteresis refers to the way magnetization 'lags behind' the applied field during this cycle. When the field is brought to zero (at point C) there is still a remanent magnetization M_R present, and a reverse field H_C (the coercivity) is required to completely demagnetize the specimen.

Hysteresis results from the way domain structures respond to an applied field. Since the magnetic behaviour of different materials depends on changes in domain structure, the factors which govern domain formation and the different techniques available for observing domains will be discussed in the next chapter.

CHAPTER TWO MAGNETIC DOMAINS.

2.1 Introduction.

The behaviour of a ferromagnetic material is largely governed by the effects of applied fields on the domain structure. Domains exist as a result of energy minimisation, so to understand the theory of magnetic domain structures it is necessary to consider the total magnetic free energy of a ferromagnetic solid. This can be expressed as a combination of the following components.

- 1/ Exchange energy
- 2/ Anisotropy energy
- 3/ Magnetoelastic energy
- 4/ Magnetostatic energy
- 5/ Domain wall energy.

2.2 Exchange Energy

A ferromagnet possesses permanent dipole moments and an interaction between electron spins results in parallel alignment of dipoles. For two electron spins the energy of interaction was represented in chapter one by the Heisenberg exchange energy:

$$E_{\text{ex.}} = -2J \vec{s}_i \cdot \vec{s}_j \quad (2.1)$$

Where J is the exchange integral. For a lattice of spins, the total exchange energy involves a summation over all pairs of spins \vec{s}_i, \vec{s}_j :

$$E_{\text{ex.}}^{\text{(Total)}} = -2 \sum_{ij} J_{ij} \vec{s}_i \cdot \vec{s}_j$$

This expression can be simplified by considering only nearest-neighbour interactions and by assuming J_{ij} to have the same value (J) for all pairs of adjacent spins. The energy between two adjacent spins then takes the form:

$$E_{\text{ex.}} = JS^2\phi^2 \quad (2.2)$$

for small values of the angle ϕ between spins. On this basis, the macroscopic exchange energy density in a solid will be determined by the distribution of magnetization vectors in the following way:

$$E_{\text{ex.}} = A \left[(\nabla\alpha_1)^2 + (\nabla\alpha_2)^2 + (\nabla\alpha_3)^2 \right] \text{ (Landau and Lifshitz, 1935) } \quad (2.3)$$

where $\alpha_1, \alpha_2, \alpha_3$ are the direction cosines of magnetization.

A is known as the 'exchange constant'.

The value of A depends on J, S , and the lattice spacing between spins. Exchange energy density so defined is only zero in regions where the magnetization is uniform in direction. The value of A can be determined experimentally. For 80/20 Ni Fe, Methfessel et al. (1962) obtained $A = 0.55 \times 10^{-11} \text{ Jm}^{-1}$ ($0.55 \times 10^{-6} \text{ erg cm}^{-1}$). Exchange energy is usually assumed to be isotropic in magnetization direction.

2.3 Anisotropy Energy

It is an experimental fact that there are 'preferred' or 'easy' directions for magnetization within a ferromagnetic crystal. This may be formally expressed using anisotropy energy functions. These functions depend upon the direction of magnetization relative to the crystal lattice and for particular 'easy' direct-

ions the energy is a minimum. Whereas exchange energy results from atomic scale spin-spin interactions, magnetocrystalline anisotropy is due to interaction between spin moments and the crystal lattice.

In a uniaxial material with only one easy axis for magnetization, anisotropy energy density is given by:

$$E_k = K_1 \sin^2 \Theta + K_2 \sin^4 \Theta + \dots \text{etc.} \quad (2.4)$$

where Θ is the angle between magnetization and the preferred axis, and K_1, K_2 etc. are the anisotropy constants of the material (measured in Jm^{-3}). K_1 is usually much bigger than the other anisotropy constants and therefore it is often a good approximation to consider only the first term in the series. The corresponding anisotropy function in a crystal with cubic symmetry is:

$$E_k = K_1 (\alpha_1^2 \alpha_2^2 + \alpha_3^2 \alpha_1^2 + \alpha_2^2 \alpha_3^2) + K_2 \alpha_1^2 \alpha_2^2 \alpha_3^2 + \dots \text{etc.} \quad (2.5)$$

where α_i represent the direction cosines of magnetization. Anisotropy may also be measured by the value of externally applied field, B_k , which would be required to rotate the magnetization away from the easy direction into a so-called 'hard' direction. This corresponds to a rotation of 90° in a uniaxial system. By equating magnetostatic field energy with the uniaxial anisotropy expression it can be shown that:

$$B_k = \frac{2K_1}{M_s} \quad (2.6)$$

A bubble film is an example of a uniaxial system with the easy

axis lying perpendicular to the film plane. A bubble film capable of supporting 12 μm bubbles for example would have a magnetization of about $\mu_0 M_s = 0.01$ Tesla and a value of B_k around 0.03 Tesla.

It is an established fact that thin films of permalloy produced in the presence of an applied field often possess in-plane uniaxial anisotropy. A great deal of research on such films was performed during the 1950's and 60's (eg. see M.S. Blois Jr., 1955). Although the magnetocrystalline anisotropy constants of bulk Ni-Fe crystals with the same composition are near zero, polycrystalline films may be produced with anisotropies equivalent to several Oe. The effect of anisotropy on domain structures in overlays will be discussed later.

2.4 Magnetoelastic Energy.

In general if the magnetization of a ferromagnetic specimen is varied, changes occur in the dimensions of the specimen. This effect is known as magnetostriction. The coupling which occurs between elastic strain and the magnetization direction is described by the magnetoelastic energy density, E . In the simplest case of a specimen with isotropic magnetostriction:

$$E_{\sigma} = -\frac{3}{2} \lambda_s \cos^2 \Theta \quad (\text{Morrish (1965) P.325}) \quad (2.7)$$

for small values of the angle Θ between the stress $\vec{\sigma}$ and the magnetization. In this equation λ_s is a mean saturation magnetostriction coefficient. The value of λ_s for thin films of Permalloy with approximately 80% Ni and 20% Fe is negligible. Therefore the magnetic properties of these films are effectively independent of stress.

2.5 Magnetostatic Energy.

The magnetostatic potential energy density within a ferromagnetic body due to an externally applied magnetic induction \vec{B}_0 is given by:

$$E_{B_0} = - \vec{M} \cdot \vec{B}_0 \quad (2.8)$$

This potential energy arises from the torque exerted on each elementary magnetic dipole by the applied field. In general, a magnetized body of finite dimensions produces both an external field and a field within itself. The internal or 'demagnetizing field' gives rise to magnetostatic energy by interacting with the magnetization. This self-energy density can occur whether or not there is an externally applied field and is given by:

$$E_S = - \frac{1}{2} \vec{M} \cdot \vec{B}_S \quad (2.9)$$

where B_S represents the local demagnetizing field and the factor $\frac{1}{2}$ arises in order to avoid counting dipole-dipole interactions twice. If the distribution of magnetization within a ferromagnetic body is given, the associated demagnetizing field can be obtained from the following general equation:

$$\vec{B}_S = \mu_0 \vec{\nabla} \left[\int_S \frac{\vec{M} \cdot \hat{n}}{r} dS + \int_V \frac{\vec{\nabla} \cdot \vec{M}}{r} dV \right] \quad (2.10)$$

(O'Dell (1974) P.120)

r represents the distance between the point where B_S is to be evaluated and the point of integration, and n is a unit vector at the surface of the body, directed perpendicularly into the body. If we use the concept of 'magnetic free poles' to describe the

source of field then the first integral, taken over the entire surface of the body, represents the component of \vec{B}_s produced by free poles at the surface. The term $\vec{M} \cdot \hat{n}$ represents the density of free poles per unit area. The second integral is associated with free poles within the body of the solid which occur whenever there is non-zero divergence of magnetization.

The demagnetizing field is only uniform in the special case of an isotropic ellipsoid magnetized uniformly along a major axis. In that case \vec{B}_s is antiparallel to \vec{M} and proportional in magnitude to the intensity of magnetization. Therefore we may write:

$$\vec{B}_s = - D(\mu_0 \vec{M}_s) \quad (2.11)$$

where D is the 'demagnetizing factor', a dimensionless constant determined by geometry. The self energy is then given by:

$$E_s = \frac{\mu_0}{2} D M_s^2 \quad (2.12)$$

Demagnetizing factors for a range of ellipsoids have been calculated (Stoner, 1945), (Osborn 1945). If the semi-major axes of an ellipsoid are a, b and c then the corresponding demagnetizing factors D_a, D_b and D_c obey the relation:

$$D_a + D_b + D_c = 1. \quad (2.13)$$

So from symmetry, the demagnetizing factor for a sphere ($a=b=c$) is:

$$D = \frac{1}{3}.$$

If the dimension of an ellipsoid along a , b , or c is allowed to become very large, the corresponding demagnetizing factor tends towards zero because of the $\frac{1}{r}$ factor in equation (2.10). For example if $a = b$ and c tends to infinity, equation (2.13) gives:

$$D_c = 0, \quad D_a = D_b = \frac{1}{2} \quad (2.14)$$

This corresponds, approximately, to the case of a long thin rod. The demagnetizing factor perpendicular to an infinite plane sheet can also be obtained as a limiting case. In the plane of the sheet $D_a = D_b = 0$ whilst perpendicular to the sheet $D_c = 1$. The demagnetizing field within a thin film magnetized to saturation perpendicular to the film plane is therefore $-\mu_0 \vec{M}_s$. The corresponding magnetostatic energy density will be $\frac{1}{2} \mu_0 M_s^2$. The magnetization would therefore be expected to lie in the plane of a thin film in order to avoid such a large magnetostatic energy. For materials with low anisotropy such as permalloy this is essentially true. The demagnetizing field can only be overcome by strong anisotropy such as that which occurs in bubble films, forcing the magnetization vector to point out of the plane.

The demagnetizing field within a body of arbitrary shape and magnetization distribution will in general be non-uniform. However it is possible to calculate 'average' or 'effective' demagnetizing factors based upon the assumption that a body is uniformly magnetized. In that case the divergence of magnetization is zero so the second integral in equation (2.10) disappears and there are only surface free-poles to consider. The problem is therefore reduced to calculating the energy of a system of charged sheets each with a free pole density determined by $\vec{M} \cdot \hat{n}$. This

approach is valid for materials with high anisotropy. In this way Rhodes and Rowlands (1954) calculated demagnetizing factors for uniformly magnetized rods with square cross-section .

2.6 Domain Wall Energy.

Since domains are magnetized in different directions, the boundaries or 'walls' between adjacent domains represent regions in which there is a change in magnetic dipole orientation. Consequently there must be exchange energy associated with a domain wall. There may also be anisotropy energy involved if magnetic dipoles are rotated away from easy directions and magnetostatic energy if magnetic 'free-poles' are produced. These contributions together result in a certain amount of energy per unit area of domain wall which must be taken into account when considering the total magnetic free energy of a specimen containing domains. Domain wall energy and thickness may be estimated using simple models for the spin transition region.

The simplest model consists of a plane wall separating two domains magnetized in opposite directions along the easy axis of a uniaxial system. Magnetic dipoles rotate gradually about an axis perpendicular to the wall (assumed to be infinite in extent) and there is no magnetostatic energy involved. According to this model, known as a Bloch wall, dipole orientation varies only with displacement x perpendicular to the wall, as illustrated in figure (2.1). For a unit area of wall the anisotropy energy, F_k is given by:

$$F_k = \int_{-\infty}^{\infty} (K_1 \sin^2 \theta) dx \quad (2.15)$$

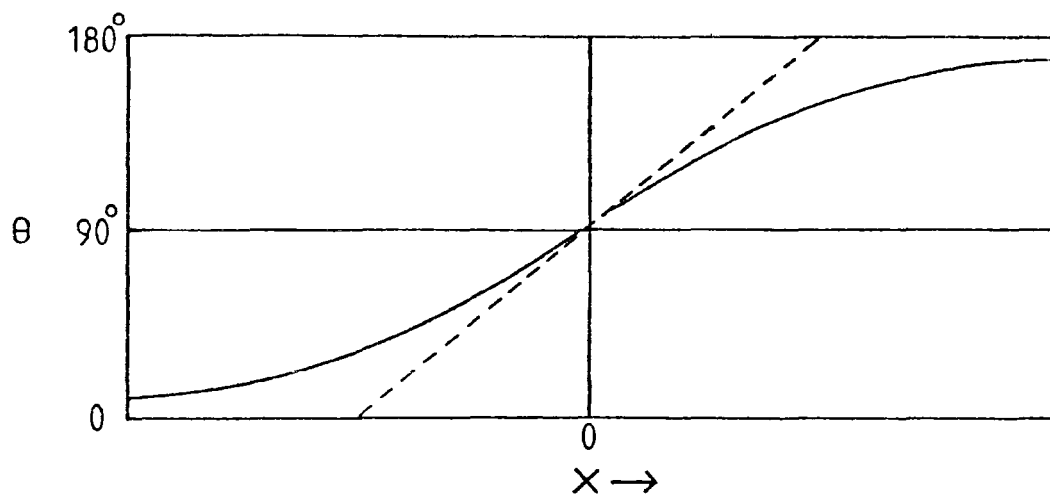


Fig 2.1 Direction of magnetization θ as a function of distance x measured from the centre of a 180° Bloch wall (solid line). Dashed line indicates asymptotic wall width. (After Craik and Tebble (1965) p.25)

For simplicity we assume that spin moments are arranged on a simple cubic lattice with spacing a , then from equation (2.2) the exchange energy between a pair of adjacent spins on the x axis will be:

$$\begin{aligned} E_{\text{ex}} &= JS^2(\partial\Theta)^2 \\ &= JS^2a^2\left(\frac{d\Theta}{dx}\right)^2 \end{aligned}$$

So the total free energy per unit area of wall due to exchange is:

$$F_{\text{ex}} = \frac{JS^2}{a} \int_{-\infty}^{\infty} \left(\frac{d\Theta}{dx}\right)^2 dx$$

For a simple cubic lattice, $\frac{JS^2}{a}$ is in fact equal to the exchange constant, A :

$$F_{\text{ex}} = A \int_{-\infty}^{\infty} \left(\frac{d\Theta}{dx}\right)^2 dx \quad (2.16)$$

This expression is generally true for all types of lattice symmetry. The total energy per unit area of wall, F_w , is the sum of exchange and anisotropy contributions:

$$F_w = \int_{-\infty}^{\infty} (K_1 \sin^2\Theta + A\left(\frac{d\Theta}{dx}\right)^2) dx \quad (2.17)$$

In equilibrium, the exchange energy is reduced if the wall becomes infinitely thick whilst anisotropy energy is minimized if wall thickness tends to zero. The finite wall thickness found in practice represents a compromise between these two opposing effects. Minimizing equation (2.17) leads to the condition:

$$K_1 \sin^2\Theta = A\left(\frac{\partial\Theta}{\partial x}\right)^2 \quad (2.18)$$

This indicates that there is 'detailed balancing' between the local anisotropy energy density and the local exchange energy density at each point inside the wall. The solution of equation (2.16) for the equilibrium wall profile is :

$$x = \left(\frac{A}{K_1}\right)^{\frac{1}{2}} \log \tan \frac{\Theta}{2} \quad (2.19)$$

The wall does not have strictly defined limits on the x-axis, but an estimate of wall thickness, δ , can be obtained from the tangent to the curve at the centre (indicated by the broken line in figure (2.1))

$$\begin{aligned} \delta &= \pi \left(\frac{\partial x}{\partial \Theta}\right)_{[x=0]} \\ &= \pi \left(\frac{A}{K_1}\right)^{\frac{1}{2}} \end{aligned} \quad (2.20)$$

The equilibrium wall energy per unit area is given by:

$$\delta_w = 4(AK)^{\frac{1}{2}} \quad (2.21)$$

The element cobalt is an example of a uniaxial system. Substituting values for the exchange constant of cobalt, $A \simeq 1.03 \times 10^{-11} \text{ Jm}^{-1}$ and the uniaxial anisotropy constant $K_1 \simeq 4.1 \times 10^5 \text{ JM}^{-3}$ (taken from Craik and Tebble (1965)) gives the following estimates for the energy and width of a 180° domain wall in cobalt:

$$\begin{aligned} \delta_w &\simeq 8 \times 10^{-3} \text{ Jm}^{-2} \\ \delta &\simeq 1.6 \times 10^{-8} \text{ m.} \end{aligned}$$

This gives an idea of the orders of magnitude involved in

domain wall parameters. The anisotropy of cobalt is relatively high, however, and it is clear from the expression for δ that much thicker walls are to be expected in low anisotropy materials. In materials with different types of anisotropy, Bloch wall transitions through angles other than 180° may occur. The important characteristic of all Bloch walls, however, is that magnetic dipoles rotate only about an axis perpendicular to the plane of the wall with zero divergence of \vec{M} . This implies that there are no 'free poles' within the body of the wall to produce magnetostatic energy. Eventually where a Bloch wall intersects the external surface of a specimen strips of 'free-pole' will occur because of the component of magnetization which emerges normal to the surface. In bulk materials these strips of magnetic pole are wide apart so the magnetostatic energy caused by their interaction is negligible. In this situation the Bloch wall provides a minimum energy configuration for the boundary between domains. In thin magnetic films however the magnetostatic energy of a Bloch wall is important since the strips of free pole may be separated by distances comparable with wall thickness. Néel (1955) considered the effect of magnetostatic energy on domain walls and predicted a new type of spin transition in thin films. In a so-called 'Néel wall' magnetic dipoles rotate about an axis contained in the plane of the wall so that magnetization may remain parallel to the film surface. The difference between Bloch and Néel walls is illustrated diagrammatically in figure 2.2. There are no surface free poles associated with a Néel wall but there is internal magnetostatic energy because the divergence of \vec{M} is no longer zero. To compare the total energy of these alternative configurations it is necessary to calculate the magnetostatic contribution in each case. In

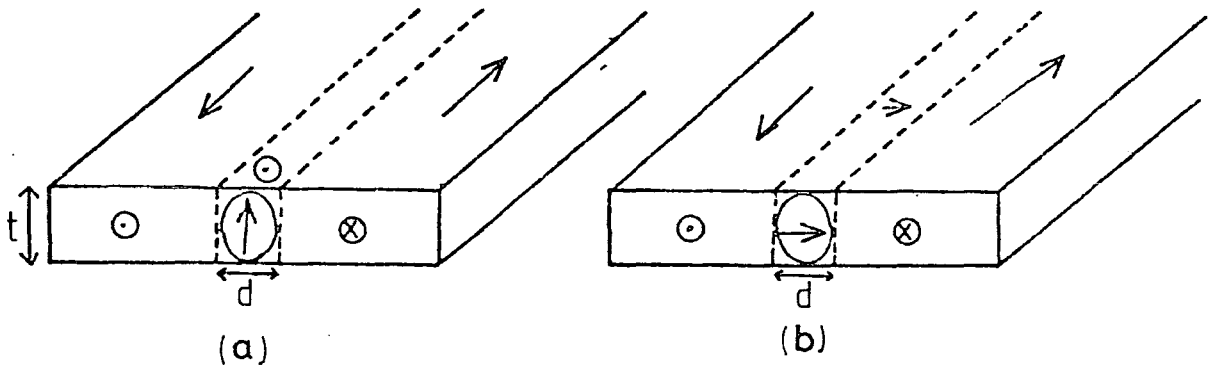


Fig. 2.2 Average magnetization within (a) a Bloch wall and (b) a Néel wall.

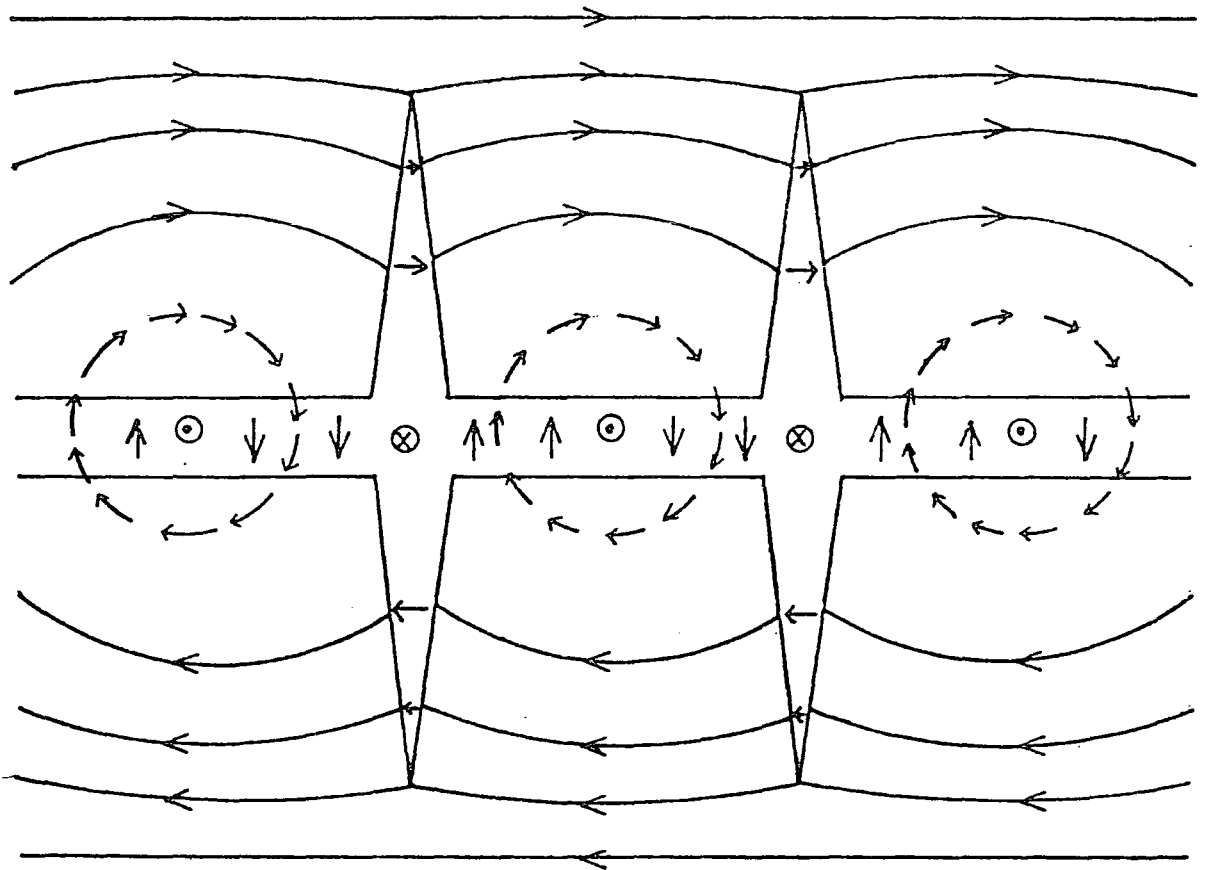


Fig. 2.3 Structure of a Cross-tie wall as interpreted by Huber et al. (1958).

reality the demagnetizing fields involved are non-uniform and difficult to analyse exactly. In Néel's calculation the magnetic energy of a cylinder with elliptical cross section is considered. The cylinder has dimensions comparable with those of the domain wall and a uniform magnetization based upon the average magnetization illustrated in figure 2.2 . Néel's results can be summarized as follows . The demagnetizing factor for a cylinder uniformly magnetized as in figure 2.2 (a) is given by :-

$$D = \frac{d}{d+t}$$

So from equation (2.12) the magnetostatic energy density within the cylinder is:

$$E_s = \frac{\mu_0}{2} \left(\frac{d}{d+t} \right) M_e^2 \quad (2.22)$$

M_e is the average magnetization of the cylinder and Néel assumed $M_e = M_s$. Similarly the demagnetizing factor for a cylinder magnetized as in figure 2.2 (b) is given by:

$$D = \frac{t}{d+t}$$

Therefore a Bloch wall of width d in a film of thickness t has a magnetostatic energy per unit area approximately equal to:

$$F_s = \frac{\mu_0}{2} \left(\frac{d^2}{d+t} \right) M_s^2 \quad (2.23)$$

whilst the corresponding energy of a Néel wall in the same situation is approximately given by:

$$F_s = \frac{\mu_0}{2} \left(\frac{dt}{d+t} \right) M_s^2 \quad (2.24)$$

As expected the Bloch wall has lower magnetostatic energy in bulk specimens where $t \gg d$. However as t is reduced there must come a point where the sum of exchange, anisotropy and magnetostatic energy is lower for a Néel wall than for a Bloch wall. According to Néel and to Middlehoek (1961) the transition should occur at a film thickness of about 400 Å. Permalloy films used in bubble device preparation are usually about 4000 Å thick. Therefore, on the basis of Néel's estimates, domains in overlay elements should be separated by Bloch walls. The actual energy and width of Bloch walls in overlays will be estimated later.

In the two types of spin transition considered so far the direction of magnetization varies only along an axis perpendicular to the boundary layer. Any plane of atoms parallel to the boundary plane contains magnetic dipoles with the same orientation. This may be true for the two limiting cases of very thin or very thick specimens but more complex types of spin structure may occur in-between. For example 'Cross-tie' walls were first reported by Huber, Smith and Goodenough (1958) in thin film specimens of permalloy. The structure of a Cross-tie wall as interpreted by Huber et al. is illustrated in figure 2.3. The Cross-tie wall is essentially made up of closely spaced Néel- and Bloch-type spin transitions. Along the centre plane of the wall, magnetization is directed alternately parallel and perpendicular to the surface of the film. Because the anisotropy of permalloy is very low, the complex demagnetizing fields associated with this structure distort the magnetization on either side of the wall as shown in figure 2.3. It has been found experimentally (Methfessel, Middlehoek and

Thomas, 1960) that cross ties occur in films between about 900 \AA and 200 \AA thickness, separating the two regions of thickness where there are distinct Bloch-type or Néel-type boundaries.

In films thicker than 900 \AA there may still be modifications to the standard Bloch wall. In particular, it is possible for the sense of rotation of magnetic dipoles to change along the length of a Bloch wall. The magnetic stray field emerging from the intersection of the domain wall with the specimen surface then alternates in sign because the associated strip of 'free-pole' alternates in polarity. This phenomenon has often been revealed using the colloid technique, for example in films of permivar (Williams and Goertz, 1952) and in whiskers of iron (DeBlois and Graham, 1958). Examples of alternating Bloch wall segments in permalloy elements will be discussed later.

2.7 Domain Structures.

With the various contributions to magnetic free energy in a ferromagnetic solid defined, the origin of domains can be considered qualitatively. From equation (2.3), exchange energy is clearly minimized if magnetic dipoles are perfectly aligned giving uniform magnetization, and by definition the anisotropy energy is a minimum when the magnetization lies along a particular direction. The atomic scale forces of exchange and anisotropy on their own would therefore seem to predict uniform magnetization rather than domain structure. However, it was demonstrated by Landau and Lifshitz (1935) that the explanation of domain subdivision lies in the possibility of reducing magnetostatic energy. In contrast to exchange and anisotropy contributions, magnetostatic energy arises from dipole-dipole interactions on a macro-

scopic scale. Several possible domain configurations for a simple cube are illustrated in figure 2.4.

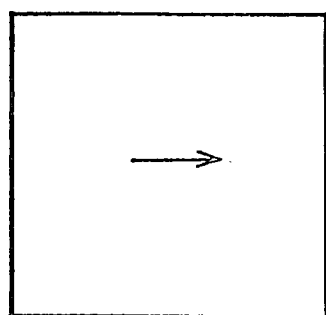
Figure 2.4(a) represents a saturated state consisting of a single domain. The total magnetostatic energy in this case is $\frac{1}{6} \mu_0 M_s^2 V$ (Rhodes and Rowlands, 1954) where V is the volume of the cube. This result can be obtained by considering a system of two sheets of magnetic free pole and for iron represents an average energy density of roughly $3 \times 10^5 \text{ Jm}^{-3}$. This energy density can be reduced if the sample is divided into two domains magnetized in opposite directions as illustrated in figure 2.4(b). Subdividing the surface free pole in this way produces both the stray field outside and the demagnetizing field within the cube. Further subdivision, figure 2.4(c) produces an even lower magnetostatic energy component but increases the amount of energy associated with the formation of domain boundaries. Kittel (1949) calculated that the magnetostatic energy of a series of parallel strips of pole with alternating sign is given by:

$$E_s = 0.8525 \mu_0 M_s^2 D,$$

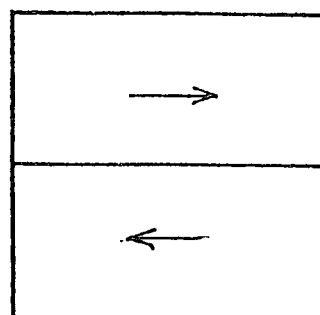
where D is the strip width. A cube with edge x m. divided into parallel slab domains with width D therefore has a total magnetostatic energy per unit volume given by:

$$F = 1.705 \mu_0 M_s^2 D/x.$$

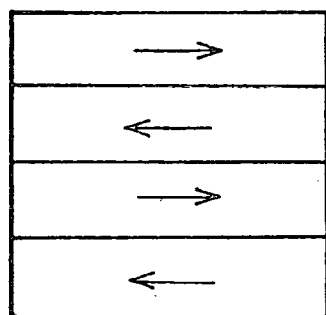
The energy stored in domain walls per unit volume is $F_w = \gamma/D$ where γ is the energy per unit area of wall. The equilibrium domain width can be estimated by minimizing the total energy



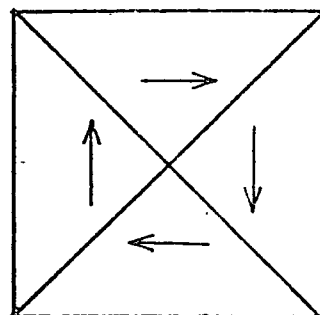
a



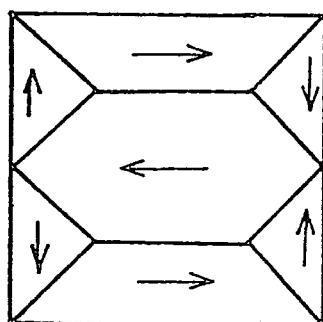
b



c



d



e

Fig. 2.4 Simple domain configurations in a cube (cross-section).

density. For example parallel slab domains in a cube of iron with an edge of 1 cm would be approximately 10^{-5} M. wide (substituting values for γ and $\mu_0 M_s$) and the total energy density would be approximately $6.0 \times 10^3 \text{ Jm}^{-3}$.

Figures 2.4(d) and(e) illustrate closure domain systems which eliminate magnetostatic energy completely. The normal component of magnetic flux is conserved across each domain boundary and the magnetization is everywhere parallel to the external surface (except for a small leakage of flux where Bloch walls meet the surface). Simple flux closure patterns of this sort have been observed in single crystal whiskers of iron (De Blois and Graham, 1958) grown so that outer surfaces correspond to equivalent (100) crystal planes. Iron has cubic anisotropy ($K_1 > 0$) so all the domains in a closure system can be magnetized along easy directions. Iron also has a positive magnetostriction coefficient so there is a certain amount of magnetoelastic energy associated with the 'mismatch' of strain directions between orthogonal domains. The optimum state will therefore depend on the minimization of domain wall and magnetoelastic energy contributions combined.

Domains exist in order to minimize magnetostatic energy but the type of domain structure which occurs in a given specimen depends on a number of factors. The most important are the shape and size of the specimen and the exchange, anisotropy and magnetostriction constants of the material. These material parameters determine which of the magnetic energy components dominates.

Size plays an important role in very small particles which may in certain circumstances exist as single domains. This is because the reduction in magnetostatic energy which could be

obtained by the formation of domain structure is outweighed by the positive energy associated with boundary walls. Kittel (1946) obtained an estimate for the critical particle size below which single domains should occur by comparing the magnetostatic energy of a saturated sphere with the energies of alternative configurations. The critical size for a typical ferromagnet according to this calculation is of the order of 10^{-8} m.

Bulk specimens with strong uniaxial anisotropy usually exhibit 'open-flux' domain structures similar in principle to figure 2.4(c). A typical uniaxial system consists of 180° domains magnetized in opposite directions along the preferred axis. In this case the anisotropy component of magnetic energy is dominant and outweighs the magnetostatic energy associated with surface free poles. In uniaxial bubble film the ratio of anisotropy field $2K_1/M_s$ (equation 2.6) to the demagnetizing field $\mu_0 M_s$ defines the 'Quality factor', Q :

$$Q = \frac{2K_1}{\mu_0 M_s^2} \quad (2.25)$$

In practical bubble materials Q must exceed unity.

In thin films of permalloy magnetostatic energy is usually the dominant factor. As a result magnetization is constrained to lie in the plane of the film and 'flux-closure' domain arrangements are prevalent. Exchange coupling causes magnetic dipoles at the top and bottom surfaces of the film to be parallel and domain structures are essentially 'two-dimensional'. A review of the ferromagnetic properties of thin films can be found in the text by Prutton (1964).

The classical domain concept is based upon regions of uniform

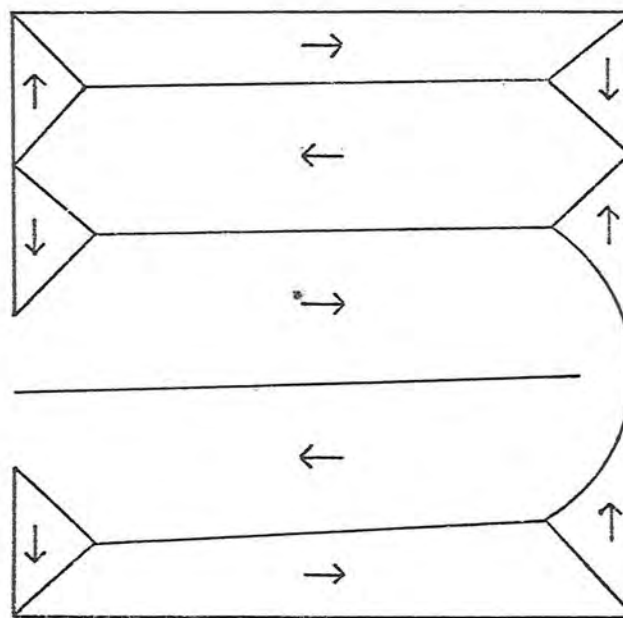
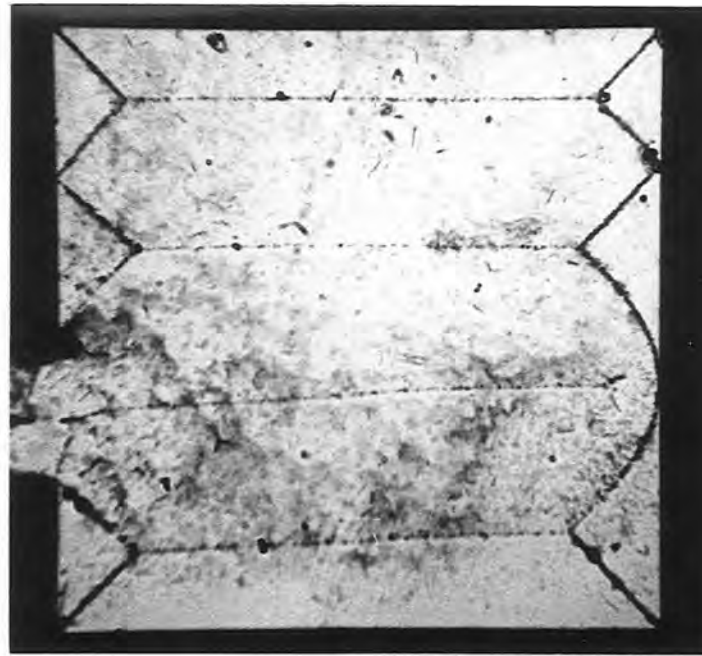


Fig. 2.5 (a) Domain wall pattern in a thin film sheet of permalloy (approx. $100 \times 100 \times 0.4 \mu\text{m}$) revealed in a dry colloid deposit. (b) Possible interpretation in terms of magnetization directions.

magnetization separated by thin boundaries. This corresponds closely to the real situation in materials with strong anisotropy. In materials with low anisotropy such as permalloy, the variation in magnetization may take place gradually and smoothly over dimensions much larger than a typical domain wall width. Such a transition can be inferred from the domain wall pattern shown in figure 2.5. The micromagnetics approach to ferromagnetism developed by Brown (1962) does not assume the existence of domains. Instead the theory begins with a magnetization vector of constant magnitude and an orientation which simply varies as some function of position. The forces representing exchange, anisotropy, magnetostriction and magnetostatic energies are introduced to find the equilibrium state of lowest energy. This method can be applied to simple systems (for example fine particles) but the behaviour of larger 'multi-domain' systems cannot be predicted in this way. In these systems the conventional approach to domain theory must be adopted. A domain model is postulated (perhaps based upon observation) and expressions for each type of magnetic energy are calculated. The equilibrium domain dimensions can then be found by minimizing the total energy of the system. It may also be possible to show that the energy of a given domain structure is less than any alternative configuration. Fortunately there are now several methods available for observing domains and domain walls. A review of these methods will now be given.

2.8 Colloid Techniques.

The basic colloid technique developed from the early experiments of Bitter (1931) who provided the first direct observation of domain structure. A suspension of magnetic particles

(usually Fe_3O_4) is formed in a suitable carrier liquid such as water. If the particles are sufficiently small, the suspension is stable against precipitation and forms a true colloid. A layer of colloid is formed between the sample and a glass coverslip. Domain structure at the specimen surface gives rise to non-uniform stray fields and colloid particles tend to congregate where these fields are most intense. The resulting 'colloid pattern' can be studied under the microscope. A colloid particle with a permanent dipole moment μ in a local field represented by \vec{B} will have a magnetostatic potential energy given by:

$$\begin{aligned} E &= -\vec{\mu} \cdot \vec{B} \\ &= -\mu B \cos \Theta \end{aligned} \quad (2.26)$$

The force experienced by colloid particles due to variations in the field is given by:

$$\begin{aligned} F &= -\vec{\nabla} (E) \\ &= \mu \vec{\nabla} (B \cos \Theta) \end{aligned} \quad (2.27)$$

Colloid particles therefore tend to migrate towards equilibrium positions associated with field maxima. The distribution of field maxima is determined both by the surface domain structure and by externally applied fields. When domains are magnetized parallel to the surface (for example in a permalloy film) the stray field is strongest above domain boundaries and the resulting pattern usually consists of thin lines of heavy colloid density as in fig. 2.5. When domains have a component of magnetization normal to the surface, on the other hand, a different type of contrast may be

obtained. Areas of surface free-pole with alternate polarity can give rise to stray fields directed into or out of the plane. An external field applied perpendicular to the surface therefore favours colloid collection above domains magnetized in a particular direction, producing so-called domain contrast. The profile of magnetic fields emanating from a surface divided into sheets of free-pole with alternate polarity has been treated by Craik (1966)

Colloid patterns can nowadays be conveniently obtained using a commercial 'ferrofluid'. A ferrofluid is essentially an ultra-stable colloidal suspension of single domain ferromagnetic particles (e.g. Fe_3C_4) dispersed in a carrier liquid. The properties and applications of ferrofluids have been reviewed in a recent paper by Popplewell and Charles (1979). Apart from water, several carrier liquids are available including ester, hydrocarbon or silicone oil. The particles are usually coated with a dispersant to prevent aggregation by Van der Waal's forces.

The colloid technique has several limitations. Only surface structure may be studied and domain wall movements can only be observed if they are sufficiently slow to allow for colloid migration. Resolution is limited by the optical microscope.

Resolution can be improved if the dried colloid technique developed by Craik and Griffiths (1958) is used. A film of colloid containing cellacol is allowed to dry onto a prepared specimen surface. The film can then be removed for study either in an electron microscope or an optical microscope. Apart from an improvement in resolution there is also better contrast because the dried film achieves a thickness much less than that of a liquid colloid layer. The colloid particles therefore experience higher intensity stray fields in the immediate neighbourhood of the sample. This

technique records a static domain pattern and this is obviously a drawback if changes in domain structure are to be observed.

A more recent improvement in technique is described by Khaiyer and O'Dell (1976). They report the observation of domain walls in permalloy bars using ferrofluid and 'Interference Contrast'. This technique was first described by Nomarski and Weil (1955) and since then several microscope manufacturers (e.g. Vickers) have made interference contrast modules commercially available to be fitted onto optical microscopes. The basic principle is that the incident light beam is sheared into two orthogonal and coherent plane polarised components by a birefringent element in the illuminating path. A matched birefringent wedge in the viewing path exactly recombines the two wave forms. A perfectly flat specimen simply produces a constant background colour but slight variations in height result in a change of interference colour. In metallurgical use, variations in depth of the order of $10^{-3}\mu\text{m}$ arising from boundaries or inclusions may be detected. Lines of heavy colloid deposit on domain walls may be imaged with enhanced contrast.

2.9 Magneto-optical Techniques.

If a magnetic body is transparent, plane polarized light transmitted through the body experiences a rotation of the plane of polarization if there are components of magnetization along the propagation direction. This phenomenon is known as the Faraday effect and the amount of rotation is proportional to the specimen thickness and to the strength of magnetization. The sense of rotation depends on the direction of \vec{M} , so a microscope fitted with polarizer and analyzer can image domains magnetized in different

directions. The Faraday effect has been used extensively to study bubble domains in transparent films.

Rotation may also occur in the plane of polarization when light is reflected from the surface of a magnetized body. This is the Kerr effect which is usually employed in one of three different modes:

- 1/ Polar effect, where there is a component of magnetization normal to the specimen surface.
- 2/ Longitudinal effect, where there is a component of magnetization parallel to the specimen surface and to the plane of incidence.
- 3/ Transverse effect, where the component of magnetization lies parallel to the specimen surface but perpendicular to the plane of incidence.

In all cases the effect can be represented by a rotation of the plane of polarization, the sense of rotation depending on the direction of magnetization. The different modes are discussed by Carey and Isaac (1966). The Kerr effect has been used in the study of overlay bars, this will be discussed later.

2.10 Electron Microscopy.

An electron travelling with velocity \vec{v} through a medium where there is induction \vec{B} , experiences the classical Lorentz force:

$$\vec{F} = -e(\vec{v} \wedge \vec{B}) \quad (2.28)$$

Where e is the charge on the electron. If a sample containing magnetic domains is sufficiently thin to allow the transmission of an electron beam, different domains may scatter the beam in different directions according to the Lorentz force. This explains in a simple way how transmission electron microscopy (Lorentz microscopy) may be utilized for domain observation. The technique was first reported by Hale, Fuller and Rubinstein (1959) and has been reviewed by Grundy (1977). Grundy describes how bubble domains may be observed using the electron microscope. Apart from the advantage of high resolution the technique can also provide information on the spin structure within bubble walls. Various experiments on bubble materials sufficiently thin for examination in the electron microscope are reported by Grundy et al. (1974). The main problem with this technique is the limitation on specimen thickness. With a 100 kV accelerating voltage the maximum thickness is about 2000 Å and in the most powerful machines available at present the limit would seem to be about 5000 Å. Bubble domains have been observed in thin samples of uniaxial materials such as cobalt (bubble diameter typically 0.1 to 0.3 μm) and $\text{Pb Fe}_{12} \text{O}_{19}$ (0.3-3.0 μm bubbles). These materials may be important in future device work if the trend towards smaller bubbles continues.

Jones, Grundy and Brambley (1978) have reported the observation of domains in permalloy propagation circuits using Lorentz microscopy. The permalloy films (approximately 0.2 μm thick) were mounted on thin (300 Å) carbon substrates and an electron microscope with a maximum accelerating voltage of 1 MV was used. The mechanism of contrast in bubble layers or permalloy films is illustrated in figure 2.6. In the defocused image each bubble

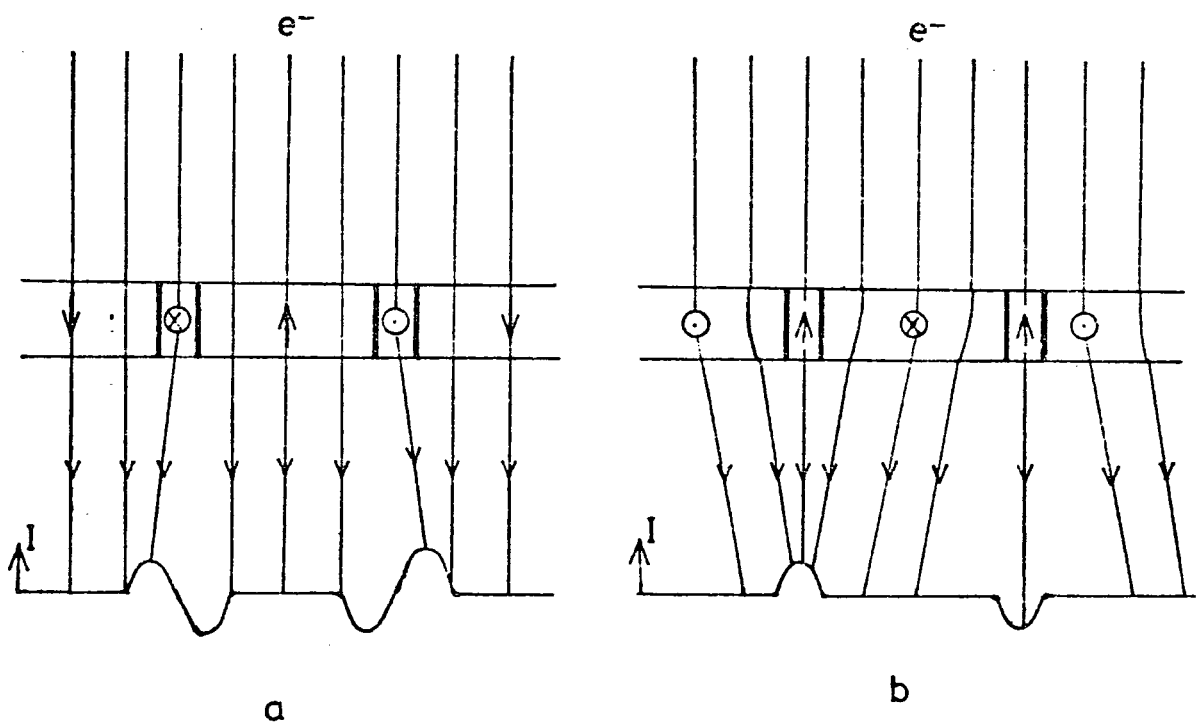


Fig. 2.6 Schematic illustration of contrast for (a) bubble domains and (b) permalloy domains in the electron microscope. I represents the intensity in the defocussed image.

domain wall appears as a combined black-white band whilst each domain wall in permalloy is imaged as either a bright or dark band. The high resolution available may be important in studying smaller circuit elements as bubble diameter is reduced.

Magnetic contrast in specimens too thick for Lorentz microscopy has been obtained using the scanning electron microscope (S.E.M.). Examples may be found in papers by Banbury and Nixon (1967) and P.J. Fathers et al.(1974). The contrast is referred to as type I or type II depending on whether the deflection of secondary electrons in stray fields above the specimen or the deflection of incident electrons by magnetic induction within the specimen is involved. Because of the difference in mechanism the contrast is generally lower than that which can be obtained in Lorentz microscopy. To date no domain studies in overlays using S.E.M. have been reported.

The preceding discussion has centered upon methods of observation which are capable of revealing domains in bubble layers or permalloy overlays. A more complete description of techniques available can be found in the texts by Carey and Isaac (1966) and Craik and Tebble (1965). The experimental details of the colloid technique used in this project will be described in chapter 5.

CHAPTER 3 "MAGNETIC BUBBLES"

3.1 Introduction

The idea of using magnetic bubbles to store information was first presented by Bobeck (1967). Since then the magnetic bubbles technology has developed rapidly and several companies are now producing commercial memory devices. At the same time there has been considerable research into the fundamental properties of bubble domains, especially their dynamic behaviour in applied fields. In this chapter a short review of basic magnetic bubble properties will be given, leading on to a discussion of materials, devices and the function of permalloy overlays. Finally, some of the areas where bubble devices might find application will be mentioned.

3.2 Stability of a Bubble Domain at Rest.

Isolated bubble domains can exist in stable equilibrium provided the applied bias field, H_B , is maintained within a certain range defined by $H_R < H_B < H_C$. If the bias field falls below H_R (the 'run-out' field) bubbles distort into strip domains. If the bias field exceeds H_C the bubbles collapse. Inbetween these limits the bubble diameter varies (almost linearly) with the strength of H_B . A complete theory for the static stability of bubble domains was presented by Thiele (1970). The equilibrium bubble size is determined by a minimum energy condition. The total bubble energy, E_T , has three components: E_W the domain wall energy, E_B the magnetostatic energy due to the externally applied bias field and E_S the magnetostatic self-energy associated with the bubble domain configuration

$$E_T = E_W + E_B + E_S \quad (3.1)$$

To simplify matters, an infinite film of thickness h can be

considered, containing a single bubble with circular cross section, radius r and a domain wall of negligible width. This last assumption is reasonable considering the characteristically high anisotropy of most bubble materials. If the wall is assumed to have a constant surface energy per unit area, δ_w , which is independent of bubble radius then the total energy is simply given by:

$$E_w = 2\pi r h \delta_w \quad (3.2)$$

and from equation (2.8) the bias field term is given by:

$$E_B = \pi r^2 h M (\mu_0 H_B) \quad (3.3)$$

where M is the film magnetization. E_w and E_B and the radial derivatives $\frac{dE_w}{dr}$ and $\frac{dE_B}{dr}$ are all positive. Each of these energy components therefore gives rise to an inward force on the bubble wall. The magnetostatic self-energy associated with a bubble domain is more difficult to obtain. In a rigorous analysis, Thiele (1969) obtained the following expression:

$$E_S = -\pi \mu_0 M^2 h^3 I(x) \quad (3.4)$$

where $x = \frac{2r}{h}$,

$$I(x) = \frac{x^2}{2} - \frac{2x^3}{3\pi} + \frac{x^3}{3} \int_0^\infty J_1^2(y) \cdot y^{-2} \cdot \exp\left(\frac{-2y}{x}\right) dy \quad (3.5)$$

and $J_1(y)$ is the first Bessel function. The shape of the resulting total energy function is shown in figure 3.1(a) for a typical garnet film used in device work. The minimum in total energy corresponds to the stable bubble radius and from the graph the

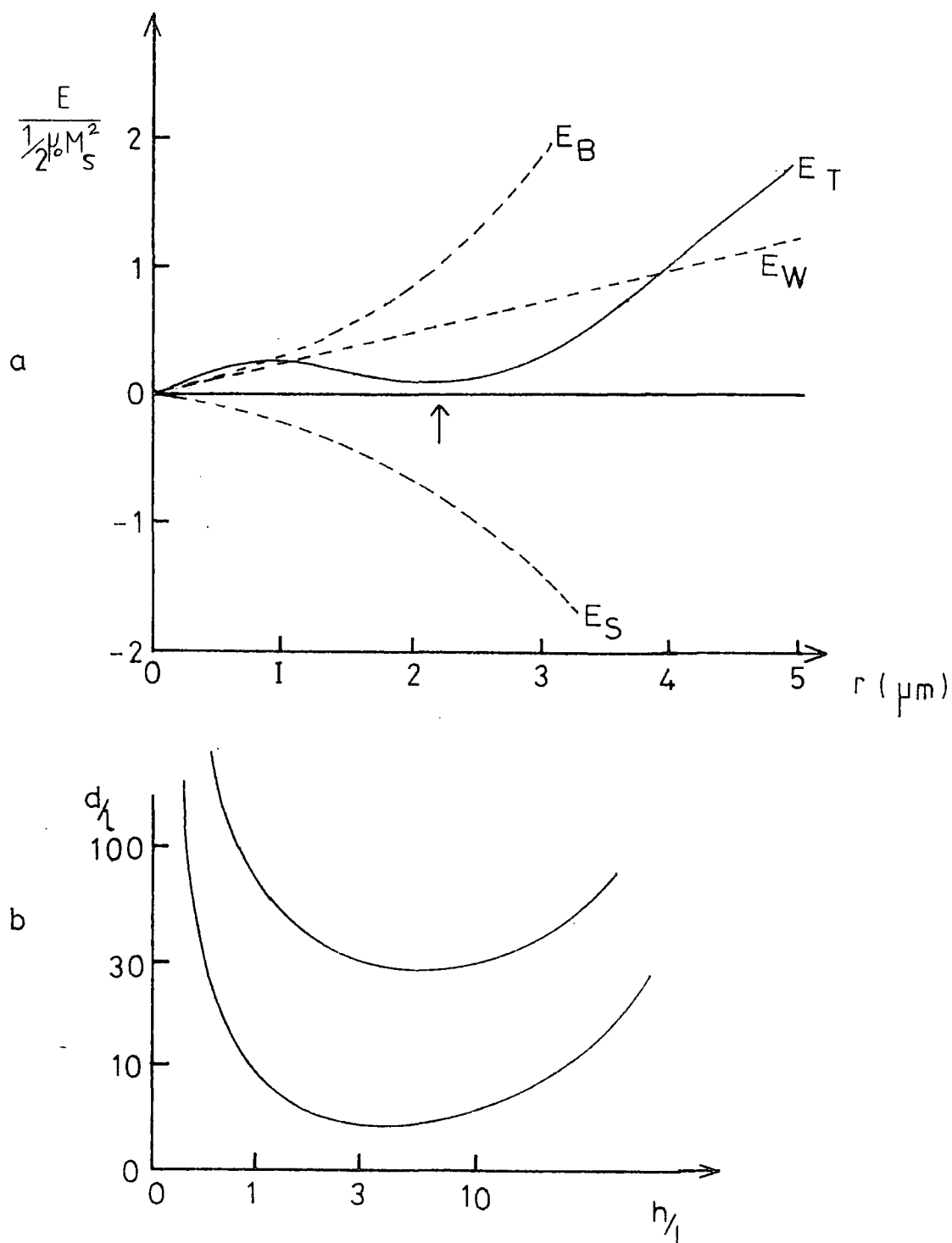


Fig. 3.1 (a) Energy of an isolated bubble domain as a function of radius in a typical garnet film (after P.J.Grundy (1977)). Arrow indicates stable bubble radius. (b) Dependence of collapse and run-out diameters on the ratio $\frac{h}{l}$

variation of bubble radius with bias field can be understood qualitatively. Increasing the bias field alters only the E_B curve which rises and causes the energy minimum to move towards smaller radius. The minimum also becomes shallower and eventually disappears at bubble collapse. Similarly, reducing the bias field increases the stable bubble radius up to the point where the bubble domain is no longer stable against elliptical deformations and 'runs-out' into a strip domain.

Thiele showed that the range of stability between run-out and collapse depends on the ratio of film thickness to the parameter l , the 'material length' of the particular bubble material. Material length is defined by the wall energy density divided by the magnetostatic energy per unit volume of the saturated film:

$$l = \frac{\gamma_w}{\mu_0 M_s^2} \quad (3.6)$$

The collapse and run-out diameters are plotted in figure 3.1 (b) as functions of the ratio h/l . Clearly l is important in determining bubble size. In most practical devices the film thickness, h , has been chosen so that bubble diameter $d \approx 8 \times l$ and $d \approx h$.

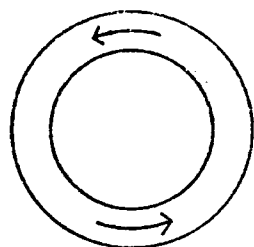
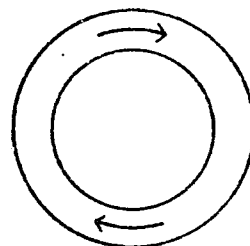
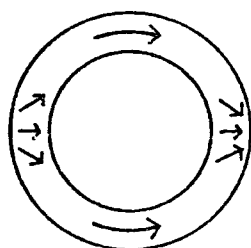
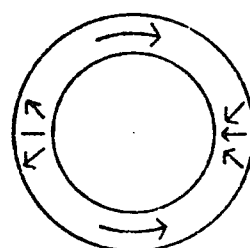
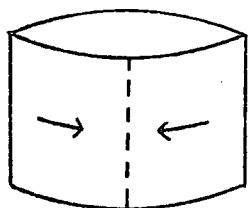
3.3 Bubble Wall Structure

In the preceding discussion of bubble stability the bubble wall was assumed to have negligible width and was simply represented by a surface energy density, γ_w . In fact the bubble wall may have complex internal structure and this can have a marked effect on the dynamic behaviour of bubbles in applied fields. In a recent review of this subject Humphrey (1980) remarks that bubble materials are characterized by high anisotropy and low magnetization ($\mu_0 M_s \approx .02$ T). As a result, magnetostatic energy

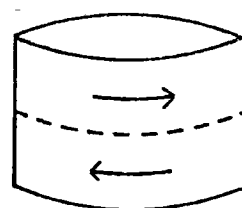
within bubble walls is negligible compared with the exchange and anisotropy components. In chapter two the importance of magneto-static energy in materials such as permalloy was seen in the distinction between essentially Bloch-type walls in bulk specimens and Néel walls in thin films. The wall surrounding a bubble domain can be a complex combination of both Bloch- and Néel- type transitions. figure 3.2 is a schematic representation of several possible bubble wall states. The pure Bloch wall can occur with two types of 'chirality' (figure 3.2(a,b,)) ie. there are two possibilities for the sense of spin rotation within the wall. The sense of spin rotation may also change around the domain boundary giving different Bloch segments separated by sections of Néel wall. The Néel sections, termed vertical Bloch lines, (VBL) occur in pairs and can themselves have two types of chirality as shown in (figure 3.2(c,d)). The wall can also be subdivided vertically and the transition region is then termed a horizontal Bloch line (figure 3.2(f)). The wall index, S , is defined by the number of complete 2π spin rotations around the wall perimeter. Thus, for example, pure Bloch wall states have $S=1$. Discontinuities consistent with Bloch line structure have been observed by Lorentz microscopy in thin samples of materials such as cobalt capable of supporting sub-micron bubble domains. (e.g. Grundy et al.,1971).

3.4 Hard Bubbles and Bubble Dynamics.

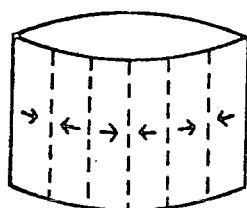
Peculiarities in the behaviour of bubble domains and the idea of complex wall structure were first described by Tabor et al. (1972) and by Malozemoff (1972). In particular they reported the existence of 'hard' bubbles which behave differently in applied fields from 'normal' bubbles. Hard bubbles collapse at

(a) $S=1$ (b) $S=1$ (c) $S=0$ (d) $S=2$ 

(e)



(f)



(g)

Fig 3.2 Illustration of possible bubble wall states.

a higher value of bias field than normal bubbles and the diameter range from run-out to collapse may be 10:1 compared with only 3:1 for a normal bubble. Bubble transport experiments frequently use a simple one-dimensional gradient in bias-field to drive bubbles. If the bias field gradient is $\frac{dB}{dx}$, the bubble magnetostatic energy, E_B , varies with x and so the bubble experiences a driving force equal to $-\frac{dE_B}{dx}$. The gradient may be produced by pulsing two parallel current-carrying conductors spaced about 100 μ m apart on the film surface. In such experiments it was found that some bubbles move parallel to the gradient as might be expected whilst others move at an angle. The deflection (through angles as large as 80°) can be either to the right or left. Finally, 'hard' bubbles were found to have a much lower mobility during transport and this is probably their most undesirable property in a device situation.

To explain all this behaviour the idea of vertical Bloch lines in bubble walls was introduced and in particular it was proposed that the hard bubble contains a large number of closely packed VBL's as suggested diagrammatically in figure 3.2(g). This model has been quite successful in explaining the experimental facts. For example in the discussion of isolated bubble stability it was assumed that the Bloch wall energy density was independent of bubble radius. However in the case of a hard bubble it can be shown (Malozemoff, 1972) that wall energy density actually rises as the bubble diameter shrinks in an increasing bias field. This results from the interaction (in the form of exchange coupling) between closely-packed VBL's. The contracting force associated with the radial derivative of total wall energy, $\frac{dE_w}{dr}$, is therefore reduced in comparison with a normal bubble for which γ_w is approximately constant. Thus the collapse of a hard

bubble requires a stronger bias field.

The deflection of bubbles relative to a field gradient can also be explained in terms of wall structure. Bubbles containing no VBL's as in figure 3.2 (a) and (b) will be asymmetrical with respect to any direction of motion through the bubble centre. Slonczewski et al. (1973) showed that this asymmetry causes a deflection to the left or right depending on the particular chirality of the bubble. On the other hand a 'symmetrical' bubble containing two VBL's with $S=0$ as in figure 3.2(c) may travel parallel to the field gradient. Slonczewski et al. obtained the following expression for the deflection angle Θ in terms of wall index S :

$$\sin\Theta = 4vs \div \gamma D^2(\Delta H)^2 \quad (3.7)$$

where v is the bubble velocity, γ is the gyromagnetic ratio and ΔH is the difference in bias field across the bubble diameter D . Another phenomenon associated with bubble translation is the so-called 'dynamic conversion' effect whereby the number of VBL's may change during bubble motion. The resulting change in deflection angle causes erratic bubble movement. (Vella Coleiro et al., 1973)

Since the existence of hard bubbles and processes such as dynamic conversion are undesirable in a bubble device several methods have been developed for controlling bubble wall states and suppressing hard bubbles. These methods include coating the bubble layer with a thin film of permalloy (Rosencwaig, 1972), adding a second garnet layer with slightly different composition (Bobeck et al., 1972) and subjecting the garnet layer to ion-implantation (Wolfe and North, 1972). In each case the aim is to

form a surface layer where the magnetization is parallel rather than perpendicular to the film. For bubble domains 'capped' in this way the two Bloch line state is preferable and hard bubbles are unlikely to occur (Rosencwaig, 1972). During ion-implantation, which is the most commonly used technique, a damaged surface layer (typically 0.1 μ m thick) is formed with considerable local strain. Magnetostriction converts this into an in-plane anisotropy which may overcome the uniaxial anisotropy. A typical dosage might be 100 keV Ne ions at approximately 10^{14} ions cm^{-2} .

As mentioned earlier, simple bias field gradients have been widely used to study bubble dynamics in different materials. A bubble domain actually moves by rotation of the magnetic moments within its wall and this process dissipates energy so the motion is damped. The level of damping determines the speed at which bubbles may be propagated and therefore has some bearing on the data rate which can be achieved in a device. There is quite a spread in velocities between different bubble materials so it is important to be able to quantify dynamic bubble properties. There are four important parameters usually used to characterize bubble dynamics. These are the coercivity H_c , mobility μ , breakdown velocity V_p and saturation velocity V_s . In most good quality bubble garnets the coercivity, representing pinning effects on the domain wall, is very small. (usually less than 10_e .) Once coercivity has been overcome, bubble velocity increases linearly with ΔH (bias field increment across a bubble diameter). The constant of proportionality is mobility, μ (often quoted in $\text{cm sec}^{-1} O_e^{-1}$). A linear relationship between plane domain wall velocity and applied field had been known to exist long before the development of bubble domains. (e.g. Galt, 1954) The damping effects can be represented by a drag force perpendicular to the

domain wall with magnitude βv ; v is the wall velocity and β is a constant. A local field B applied parallel to the magnetization on one side of a plane 180° Bloch wall exerts a pressure of $2M_S B$ on that wall therefore the equilibrium wall velocity will satisfy the following equation:

$$2M_S B = \beta v. \quad (3.8)$$

The viscous parameter β , first introduced by Landau and Lifshitz (1935), thus leads to a linear relationship between wall velocity and applied field. The motion of a cylindrical bubble wall with circular cross-section can be treated in the same way (for example see O'Dell, 1974), to obtain the dependence of bubble velocity v on bias field 'gradient' ΔH :

$$v = \frac{\mu}{2} w (\Delta H - \frac{8}{\pi} H_C) \quad (3.9)$$

In this equation the coercivity H_C has been introduced to represent pinning of the bubble wall by imperfections. It should be noted that μ_w represents the plane wall mobility and that quoted values of bubble mobility usually refer to $\mu = \frac{\mu_w}{2}$.

The link between bubble mobility and damping processes was studied by Hagedorn (1971) who gave the following expression for mobility in terms of uniaxial anisotropy K_u , exchange constant A , gyromagnetic ratio γ , and the Gilbert damping factor α :

$$\mu = \frac{\gamma}{\alpha} \left(\frac{A}{K_u} \right)^{\frac{1}{2}} \quad (3.10)$$

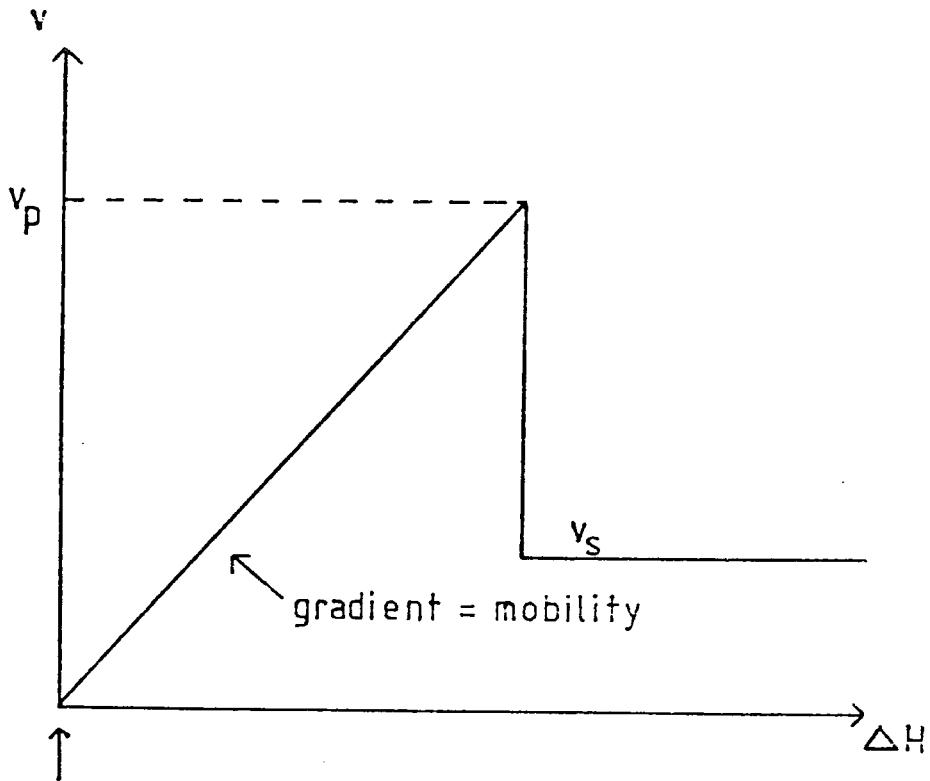
This equation is important when deciding on suitable bubble materials as will be discussed later. The linear dependence of

velocity on drive field eventually breaks down at a critical velocity V_p and beyond this point velocity drops to a roughly constant saturation level V_s as shown schematically in figure (3.3). Slonczewski (1973) devised a model involving the dynamics of Bloch lines to explain 'velocity breakdown' effects. This model is based on the idea that horizontal Bloch lines may be created in a moving bubble wall, with the ability to travel vertically through the bubble medium. Dynamic HBL's in turn generate vertical Bloch lines on intersecting the film surface, thus hardening the bubble and eventually leading to wall instability. According to Slonczewski's calculations the maximum velocity is given by

$$V_p = \frac{24\gamma A}{h\sqrt{K_u}} \quad (3.11)$$

where h is the film thickness and γ is the gyromagnetic ratio. Druyvesteyn et al. (1975) quote a value of 4 ms^{-1} for V_p by substituting into eq.ⁿ (3.11) the relevant quantities for a typical bubble garnet capable of supporting $6\mu\text{m}$ diameter bubbles. Since the period of a $6\mu\text{m}$ bubble device would be around $24\mu\text{m}$ this would limit the maximum bit rate and operating frequency to 166 KH_z .

Unfortunately on this point there seems to be rather poor agreement between theory and experiment. As Humphrey (1980) puts it, "It is necessary to measure the 'saturation' velocity to know of its existence" and the experimental 'saturation' effects are usually found to occur above the theoretically predicted value. In experiments involving propagation tracks in particular, high velocities can be obtained without any signs of saturation. O'Dell (1974) attributes this to the stabilizing influence of the gradients at the bubble wall when a bubble domain is propagated in a moving 'parabolic' field well beneath an overlay track. For



(N.B. Coercivity usually very small)

Fig. 3.3 Schematic relationship between bubble velocity v and bias field gradient ΔH for a bubble translated by a simple bias field gradient. (ΔH = difference in bias field across bubble diameter)

example Vella-Coleiro et al. (1973) obtained velocities as high as 28ms^{-1} without any signs of saturation during domain transport in an epitaxial $(\text{YFe}_u)_3 (\text{GaFe}_e)_5 \text{O}_{12}$ film with approximately $5\mu\text{m}$ diameter bubbles. The corresponding device data rate at this speed would be approximately 1.4MHz . Most commercial devices being built at present operate at 100kHz (mainly because of the problems associated with drive field coils at higher frequency) so the limiting velocity effects do not yet pose a serious problem in devices.

3.5 Materials.

Having described the essential static and dynamic properties of bubble domains the factors involved in choosing a suitable bubble material can be considered. To be competitive with existing memory technologies bubble devices must provide large capacity storage with high data rate at low cost. So two important requirements will be to have small bubbles and high mobility. An extensive review of bubble materials has been written by Nielsen (1976) .

The static and dynamic properties of bubble domains are essentially determined by a number of material parameters. These are the characteristic material length l , the quality factor Q , the uniaxial anisotropy constant K_u the magnetization M_s and the exchange constant A . These parameters are related by two equations.

$$Q = \frac{2K_u}{\mu_0 M_s^2} \quad (3.12)$$

$$L = \frac{\delta_w}{\mu_0 M_s^2} = 4 \frac{\sqrt{AK_u}}{\mu_0 M_s^2} \quad (3.13)$$

The material length depends on the energy per unit area of the

bubble wall, δ_w . In the equation above this has been expressed in terms of A and K_u using equation 2.21 derived in chapter two. The first basic property required of a bubble material is uniaxial anisotropy and this must be strong enough to give $Q > 1$ for static bubble stability. In addition, the bubble must be capable of withstanding in-plane drive fields in conventional devices, and for a device to operate with acceptably low error rates it turns out that Q must be greater than about 3.

To optimize stability bubble diameter, d should be approximately equal to film thickness, h , and d should be roughly equal to 8 to 9 times the material length. Thus bubble size and packing density are essentially decided by the value of l . As can be appreciated from equation 3.13 the trend towards smaller bubbles has demanded materials with larger M_s . At the same time, films deposited on substrates have taken the place of crystal platelets because of the condition $h \approx d$.

Of the four parameters introduced in the discussion of bubble dynamics mobility is probably the most important. According to equation 3.10, μ is proportional to $(K_u)^{-\frac{1}{2}}$ so high mobility is likely to be found in materials with low K_u . Although $Q > 3$ is necessary for stability, materials with very high Q (and K_u) are probably going to have inadequate mobility. On top of all these requirements it is also important that bubble properties should not vary strongly with temperature.

These factors have to be borne in mind when surveying the list of uniaxial materials which are capable of supporting bubble domains. A great deal of the early research was based on orthoferrites, in fact these materials were used in the pioneering work of Bobeck (1967). Orthoferrite platelets with orthor-

hombic anisotropy and the chemical formula $R Fe O_3$ ($R = \text{rare earth}$). can be prepared from bulk crystals. However due to low magnetization the material length for a typical orthoferrite, $YbFeO_3$, is $20\mu\text{m}$ and the bubble diameters (of the order of $100\mu\text{m}$) are therefore rather large for devices. At the other extreme, thin films of cobalt can be produced with the necessary uniaxial anisotropy (along a $[0001]$ axis) and the material length corresponds to bubble diameters of the order of $0.1\mu\text{m}$. The problem with cobalt is its strong anisotropy which leads to rather poor dynamic bubble behaviour. Another well known uniaxial material system, the hexagonal ferrites is capable of supporting bubble domains. A typical example, $Ba Fe_{12}O_{19}$, can support $0.05\mu\text{m}$ bubbles (Van Uitert et al., 1970). However this material also suffers from poor dynamic bubble mobility caused by a high value of K_u .

The materials most commonly used in present-day bubble devices in fact belong to the rare earth garnet system with basic formula $R_3Fe_5O_{12}$. R can be a rare earth or Yttrium. The oxygen atoms form three types of 'pocket' or site which may be occupied by the other ions of the system. These sites labelled a, d and c have octahedral, tetrahedral and dodecahedral symmetry. The basic magnetic cell of $Y_3Fe_5O_{12}$ can be expressed as $Y_{24}Fe_{40}O_{96}$, where 24 iron atoms occupy 'd' sites whilst the remaining 16 iron atoms occupy 'a'-sites. The 'c'-sites contain Yttrium atoms. Both a-a and d-d couplings are ferromagnetic. However the exchange constant for a-d coupling is negative, resulting in antiferromagnetic ordering between the 'a' and 'd' sublattices. Yttrium iron garnet (YIG) therefore exhibits ferrimagnetism below the Curie Point with a net magnetic moment per unit magnetic cell arising from the $24-16=8$ uncompensated iron atoms. Yttrium is non-magnetic but

if a rare earth with magnetic moment replaces Yttrium the magnetic behaviour becomes more complex. There are now three magnetic sublattices which contribute to the magnetic behaviour and it is common for rare earth iron garnets to exhibit a compensation point. This is a temperature between zero and T_c (curie point) where magnetization falls to zero because the moments of the opposing sublattices exactly cancel. The variation of magnetization with temperature for a typical rare earth iron garnet is illustrated in figure 3.4.

The magnetic anisotropy of garnets is fundamentally cubic, however it was found by Bobeck et al. (1970) that certain platelets cut from flux-grown crystals have sufficient uniaxial anisotropy to support bubble domains. The next important step was the development of the liquid phase epitaxy (LPE) process for depositing garnet films with the same uniaxial anisotropy on to non-magnetic substrates of gadolinium gallium garnet ($Gd_3 Ga_5 O_{12}$ or 'GGG'). In this process the constituent oxides are dissolved in a suitable flux of lead oxide-boric oxide held in supersaturation at a temperature around $1000^{\circ}C$ (Giess et al., 1972, Levinstein et al., 1974). The substrate has to be oriented parallel to a particular crystal plane (usually (111)) and be highly perfect since the epitaxial film 'copies' the structure of its substrate. Substrate wafers 7 to 8 cms. in diameter cut from chzochralski-grown boules are available commercially. A clean and polished GGG wafer is immersed in the melt until a film of the required thickness has grown. It is believed that there are two mechanisms by which uniaxial anisotropy may be produced in L.P.E. films. A small lattice mismatch between the epitaxial layer and substrate will give rise to stress-induced anisotropy. However there is also a

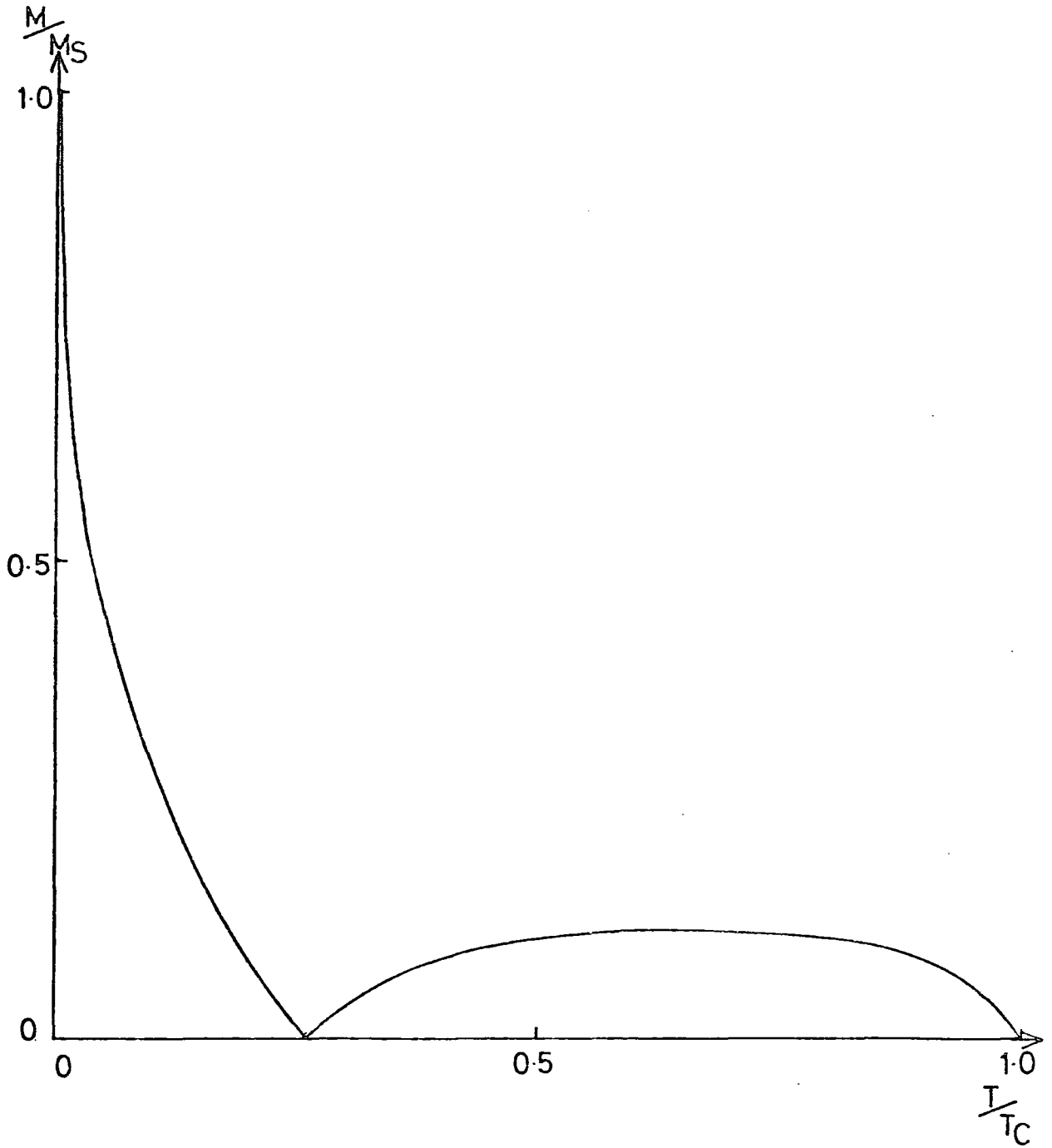


Fig. 3.4 Variation of magnetization with temperature for a typical rare earth-iron garnet exhibiting a compensation point.

growth-induced component of anisotropy which is more difficult to explain. One proposed mechanism is short range ordering of Fe-rare earth ion pairs (Rosencwaig et al. 1971).

The garnet system is particularly useful because of its versatility. Parameters such as anisotropy, K_u , can be changed by mixing the rare earth components and the value of M_s can be controlled directly by diluting the iron component with non-magnetic elements such as Al or Ga. As a result bubble diameter may be varied from about $15\mu\text{m}$ down to $0.5\mu\text{m}$. Devices being marketed at the present time use 3 to $4\mu\text{m}$ diameter bubbles.

Two current areas of research into garnets are of particular interest. Schultz et al. (1979) report that the properties of garnet epi-layers may be adapted by laser annealing. Localized heating by the laser causes a redistribution of the sites occupied by Fe and Ga atoms in Ga-substituted YIG. This results in an increased value of M_s and a localized reduction in bubble diameter. Upon cooling, the new structure and properties are 'frozen-in'. Voermans et al. (1979) describe methods for increasing bubble mobility. By depositing L.P.E. films onto (110) rather than (111) surfaces an in-plane anisotropy component is produced which does not prevent the film from supporting bubble domains but does increase bubble velocities by about one order of magnitude.

Progress towards smaller diameter bubble garnets poses several problems, because of the need to increase M_s (Kestigian et al., 1979). In the garnet system A is roughly constant so it is evident from equations (3.9) and (3.10) that reducing bubble diameter whilst keeping Q constant causes M_s to rise in proportion to d^{-1} and K_u to rise in proportion to d^{-2} . Raising the value of M_s in a conventional field access device requires the drive field

amplitude to increase so the power consumption must rise (Kryder et al., 1974) It is also evident from equation 3.7 that larger values of anisotropy will have an adverse effect on the mobility.

For bubble diameters less than $0.5\mu\text{m}$, rare earth garnets do not have sufficient magnetization and alternative materials are needed. Amorphous alloys containing transition metal-rare earth combinations may be the solution. Chaudhari et al. (1974) reported that the properties of Gd-Co-X alloys where X is a non-magnetic element (eg. Au, Cu, Mo) could be 'fine-tuned' for bubble domain applications. The advantage of this system is that for a given bubble diameter M_s may be made much lower than the corresponding garnet value by suitable adjustment of the Gd/Co ratio. Bubble diameters in the 0.2 to $2\mu\text{m}$ range have been achieved and working devices based on such alloys have been constructed in the laboratory.

3.6 Conventional Bubble Devices

In this section a brief description will be given of how bubble domains are used in devices and of the part played by permalloy overlays.

To control bubble position, movable potential energy wells must be created and this is most readily achieved using inhomogeneous applied fields. In particular, bubbles will reside in regions where the bias field is lowest so it is desirable to produce a closely-packed pattern of bias field minima. In early devices this was achieved by 'current-access'. A pattern of current-carrying conductors was laid on top of the bubble medium and these conductors activated in sequence produced the necessary field gradients. (Bobeck et al., 1969)

For small bubbles the fabrication of suitably fine conductors is difficult and this method has been succeeded by a 'field-access' approach. In the field-access device bubbles are controlled by stray fields emanating from thin film permalloy elements. The permalloy pattern is deposited onto a spacer layer (approximately $1\mu\text{m}$ thick) of silica and is subjected to a uniform rotating in-plane 'drive' field. The early permalloy designs were essentially different combinations of the basic rectangular 'I-bar'. Of these the 'T-bar' track (Perneski, 1969) illustrated in figure 3.5(a) has been the most widely used. The operation of a T-bar track can be most easily understood in terms of the travelling pattern of 'magnetic-poles' which develop on the bars as the drive field rotates. The bubble, acting as a magnetic dipole, is propagated through one period of the circuit for each rotation of the field. The shape anisotropy of a rectangular bar clearly plays an important part. The drive field easily magnetizes the bar lengthways because of the low 'demagnetizing factor' but the same field applied across the width of the bar produces a minimal effect because of the large demagnetizing fields in this direction. Figure 3.5(a) also illustrates the Perneski-type bubble generator, which consists of a large square of permalloy with a permanent 'seed' bubble domain located beneath. The seed is forced to stretch out onto the T-bar track and then to break in two so that a new bubble is launched onto the track during each period of the rotating field. The T-bar track is bi-directional; if the sense of rotation of the drive field is reversed bubbles propagate in the opposite direction and would be annihilated on arrival at the generator. Figure 3.5 shows two more propagation structures based on rectangular bars: the 'Y-bar' (Danylchuck, 1971) and the

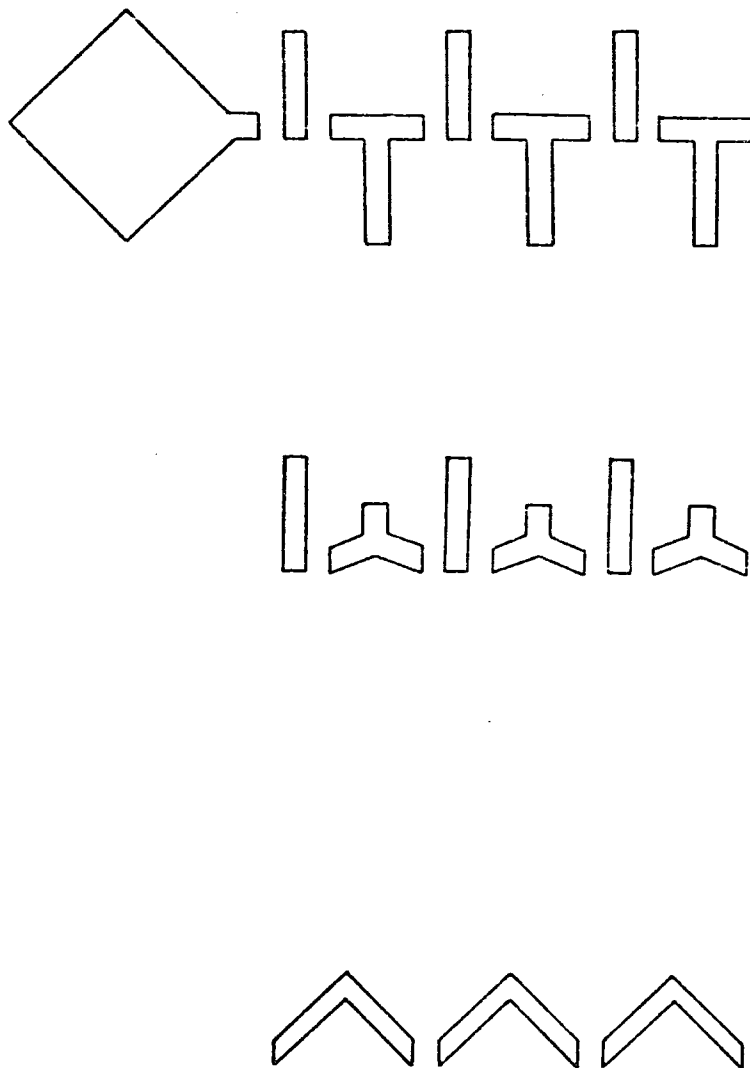


Fig. 3.5 Bubble domain propagation tracks:

- (a) T-bar
- (b) Y-bar
- (c) Chevron

'chevron' (Bobeck et al.,1971). Of these the chevron is still used in many devices for stretching bubble domains into strip domains (to be discussed later).

Different circuit elements can be characterized by their operating margins. The range of bias field, H_z , over which the circuit functions properly is plotted as a function of the drive field (H_{xy}) amplitude. Typical operating margins for T-bar propagation are shown in figure 3.6(a)(Almasi,1973) together with an indication of the probable failure mechanisms which occur outside the useful operating area. For the example given an operating point of 30 Oe drive field and 110 Oe bias field would seem sensible. It has to be borne in mind, however, that all other functional elements such as generators and detectors have their own bias margins and since the whole chip operates in a single magnetic field combination, overlap of margins is essential.

The period of a propagation pattern, P , defines the packing density of stored information which can be achieved. To keep bubble interactions to a minimum, the period is usually about four times the bubble diameter. From the point of view of fabrication the most critical feature in a T-bar circuit is the gap between elements. The period to gap ratio for this pattern is approximately 16:1. To increase bit density there has been a continual trend towards smaller bubble diameters. With the scaling down of T-bar patterns problems were encountered since optical lithography cannot be used when the minimum feature (the gap between elements) approaches the wavelength of light. For bubble diameters of $4\mu\text{m}$ and less an overlay design with relatively large minimum feature was needed.

Partly for this reason T-bars have been largely superseded

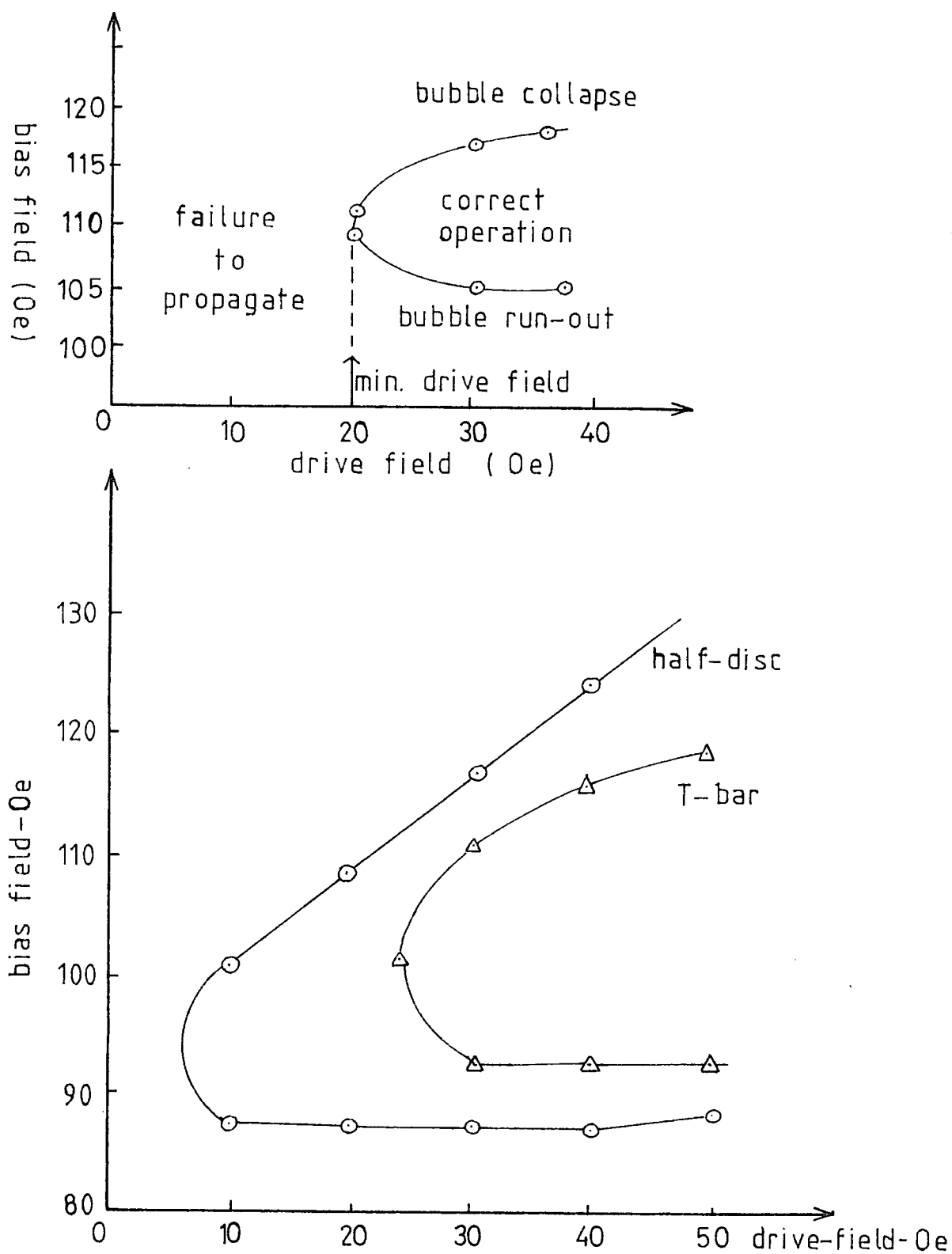


Fig. 3.6 Operating margins for (a) T-bars at 500 Hz (Almasi 1973) and (b) T-bars and half-discs in a quasi-static mode (Gergis et al., 1976)

in modern devices by the so-called 'gap-tolerant' designs. Three different gap-tolerant propagation tracks are illustrated in figure 3.7. These are (a) symmetric half-discs (Gergis et al., 1976), (b) asymmetric half-discs (Bonyhard and Smith, 1976) and (c) asymmetric chevrons (Bobeck, 1977). These designs have a period to gap ratio of approximately 8:1 so for 4 μ m bubbles the gap is 2 μ m compared with only 1 μ m for a corresponding T-bar track. For the same lithography process and line-width control the bit density can effectively be increased by a factor of four. The gap-tolerant patterns have several other advantages. There is only one permalloy feature per propagation period and there are no permalloy links between adjacent tracks. (Such a link existing between parallel T-bar tracks can mediate bubble interactions under certain circumstances.) Also the gap occurs between what are essentially parallel bars in a gap tolerant track so when the bubble crosses the gap between elements it experiences two strong parallel poles. (Adjacent bars in a T-bar track are orthogonal.) As a result the operating margins are improved, the minimum drive field for propagation can be as low as 10 Oe compared with the limit of approximately 20 Oe for a T-bar track. In figure 3.6 (b) a comparison is made between the propagation margins of half-disc and T-bar patterns with circuit period 18 μ m (Gergis et al., 1976)

In modern devices there has also been a shift away from the use of Perneski type generators based on 'seed domains' in favour of 'nucleate generators'. A typical nucleate generator consists of a long 'pick-axe' shaped permalloy element with an associated 'hairpin' conductor loop. The strong pole created on the end of the 'pick-axe' by the drive field can be supplemented by a suitably timed current pulse to create a field strong enough to

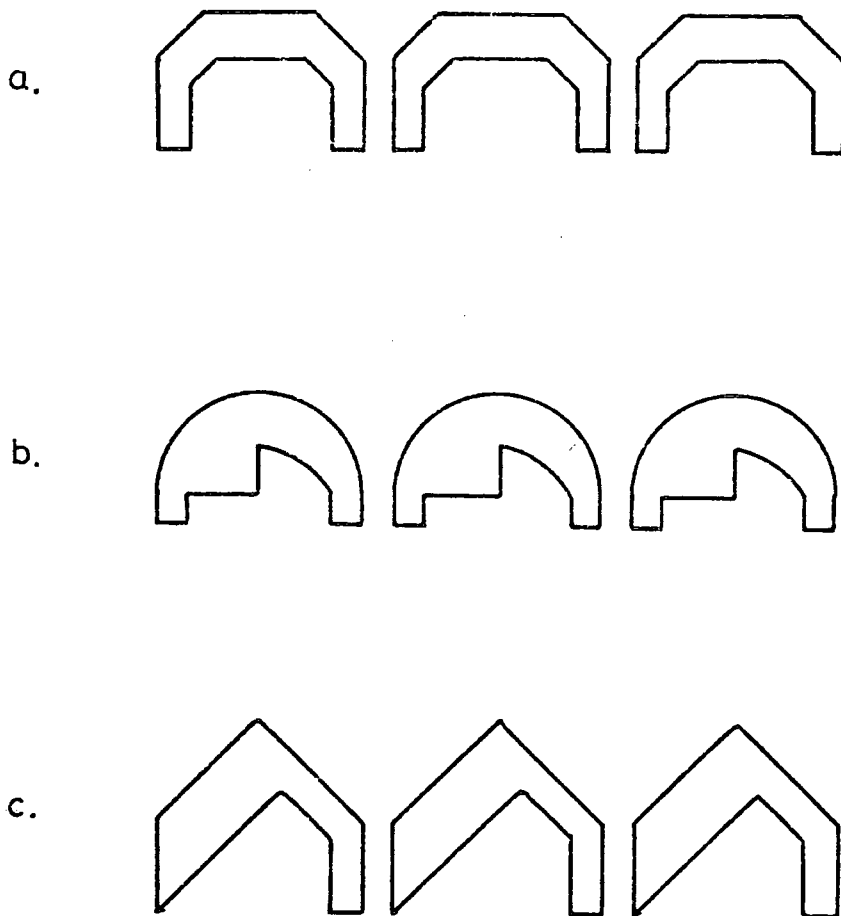


Fig. 3.7. Three gap tolerant circuit patterns:

(a) Half-disc

(b) Asymmetric half-disc and

(c) Asymmetric chevron.

nucleate a new bubble domain. Hairpin conductors can also be used to collapse bubbles by reversing the current flow thus providing erasure.

3.7 Bubble Detectors

To read data out of a conventional bubble memory a system for detecting the presence of bubbles is required. Several methods have been used for detecting bubble domains including the Faraday effect (Strauss, 1971), but in practice it is most convenient to detect the stray field of the bubble. This can be achieved by straightforward induction (Bobeck et al., 1969), by the Hall effect (Strauss and Smith, 1970) or by using magnetoresistance (Almasi et al., 1971). Only magnetoresistive detectors will be considered here since these are employed in virtually all the devices being produced at present.

The electrical resistance of a magnetic conductor depends upon the distribution of magnetization relative to the direction of current flow. This is the phenomenon of magnetoresistance. In thin film permalloy the resistivity is greatest when the magnetization lies parallel to the current flow (or antiparallel since magnetoresistance is an even effect.). If the magnetization rotates through 90° a drop in resistivity of about 3% occurs. Thus if a steady current, I , is passed through a permalloy element, the stray field of a passing bubble domain causes changes in the permalloy magnetization and the corresponding resistance change, ΔR , produces a voltage signal $V = I\Delta R$. In practice only a fraction of the maximum 3% change can be achieved since the stray field of the bubble may only cause slight changes in the permalloy domain structure. Fortunately the signal can be increased if the

bubble is stretched out to form a strip domain.

In the early 'Chinese Character' detector of Strauss et al., (1972) suitable permalloy elements were used to cause stretching parallel to the direction of bubble motion. After detection the strip was allowed to revert to a bubble domain thus providing non-destructive read out. However, stretching along the direction of motion increases wall velocity on the leading edge of the bubble and may incur the limiting velocity effects described in section 3.4. In the 'chevron expander' detector introduced by Archer et al., (1972) this problem is overcome by stretching the bubble perpendicular to the direction of motion. This is achieved by a series of chevron columns or stacks of increasing length. An important distinction between various magnetoresistive detectors is the thickness of permalloy used for the actual conducting 'sense' element. The so-called 'thick-thin' detectors use 200-400 Å permalloy for the sense element and this has to be deposited separately from the propagation circuit which is typically 4000 Å thick. The point is that in-plane demagnetizing fields are reduced by using a thinner layer so the magnetizing effect of a bubble stray field is increased. Unfortunately this type of detector demands an extra step in the fabrication process.

The 'thick' expander detector developed by Bobeck et al., (1973) cuts out this extra step by employing the same 4000 Å permalloy for both propagation circuit and detector element. This means that the resistivity change is smaller so the bubble has to be stretched further to give a satisfactory signal. This type of detector is now the most popular in conventional bubble devices and an example is shown in figure 3.8. The current path is provided by a column of chevrons with interconnections. Several geometries

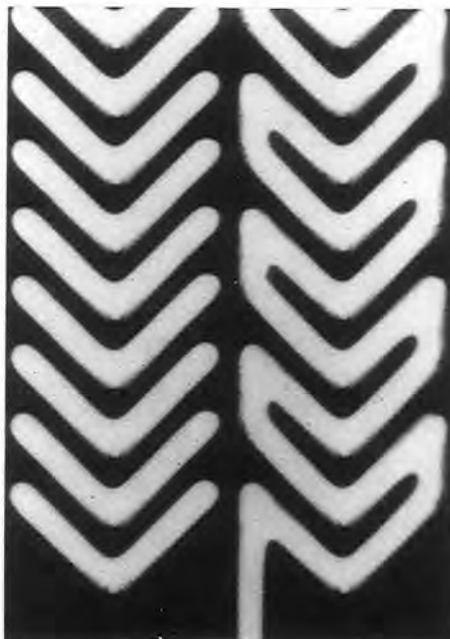


Fig. 3.8 Typical geometry for a chevron column bubble detector. Bubbles are stretched into strip domains by stacks of chevrons as on left of picture. The strips, travelling from left to right, pass beneath a connected column carrying the detector current.

of detector column have been used in the past. A study of the domain structures which occur both in isolated and connected elements of detector systems will be presented later.

In operation the detector is continuously subjected to the rotating in-plane drive field so in fact the resistance varies continuously. The effect of a passing bubble domain is to superimpose an additional field on top of the drive field. To extract a useful signal, chevron columns are usually arranged in pairs. Bubbles are presented to an 'active' column whilst a second 'dummy' column, isolated from bubbles, sees only the rotating drive field. The two detectors are connected to a differential amplifier whose output should record only the bubble signal. Finally, as an example of the sort of signal which can be achieved, Bobeck et al., (1973) obtained a 3mV output using a 5mA current in a 314 chevron column for 6 μ m bubbles.

3.8 Chip Organization

Using the functions of generation, propagation and detection described so far, the basic building block of a conventional bubble memory- the shift register- can be constructed. The single shift register is basically a continuous loop of track served by a generator and detector. Bubble patterns may be circulated indefinitely in the loop and the stored information may be accessed using the detector.

If a large capacity chip is constructed in the form of a single serial loop, the access time for an arbitrary bit is rather long. (The average access time for a 64 k bit loop operating at 100 kHz is 0.32 seconds) For certain applications this is acceptable. For a memory where the speed of access is important the chip can

be organized on a 'major-minor loop' basis. The minor loops are essentially small shift registers and these serve to store the data. A data pattern is assembled in the major loop in serial form and then transferred in parallel to the minor loops for storage. To access the memory, bubbles are transferred in parallel back into a major loop connected to a detector system. The major-minor loop concept was first reported by Bobeck and Scovil in their early review of magnetic bubbles (1971). The layout of a simple multiloop chip is illustrated schematically in figure 3.9. Several laboratories have successfully built major-minor loop chips. For example, Bonyhard and Smith (1976) describe a 68 k bit, 16 μ m period multiloop bubble memory chip design with a layout of 131 minor loops containing 523 bits each.

A multiloop design obviously requires elements or 'gates' which will cause transfer of bubbles between major and minor tracks. Furthermore, if non-destructive read-out from the minor loops is desired, replicate gates must be provided. Transfer and replicate gates have been designed as combinations of special permalloy elements with controlling conductor loops. The gates are activated by the field gradients which occur when the conductor is energized. In the absence of current, bubbles circulate indefinitely around the minor loops. Fortunately it has been found that gap-tolerant propagate elements such as the asymmetric chevron are readily adaptable to the formation of 90^o/180^o turns and replicate/transfer gates.

3.9 Device Fabrication.

The typical steps involved in the fabrication of conventional field-access bubble chips are outlined below.

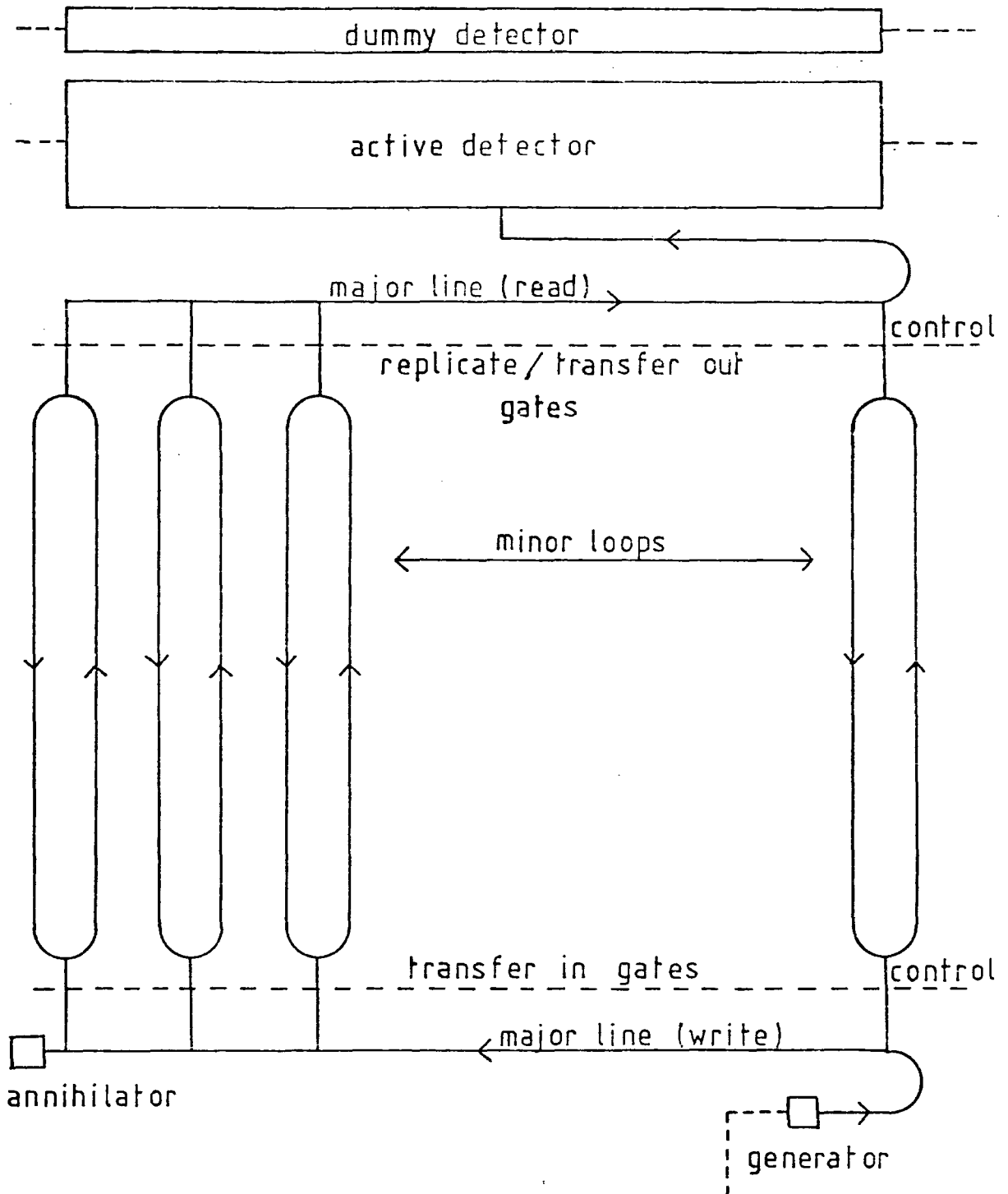


Fig. 3.9 Schematic layout of a major-minor loop chip.
(Dashed lines represent conductors)

1. Preparation of GGG substrates (A Chzochralski-grown crystal is sliced into wafers which are then polished).
2. L.P.E. growth of bubble garnet film.
3. Ion implantation to suppress hard bubbles.
4. Deposit a $0.25\mu\text{m}$ SiO_2 layer (This reduces any stress on the L.P.E. garnet which might arise from the conductor layer).
5. Deposit a conducting film (eg. gold or Al/Cu alloy) approximately $0.5\mu\text{m}$ thick. Define and ion-mill the conductor pattern.
6. Deposit a $0.8\mu\text{m}$ SiO_2 layer (This insulates the conductor layer from the permalloy and produces the optimum spacing between the permalloy propagation tracks and the bubble garnet).
7. Deposit a $0.4\mu\text{m}$ permalloy layer, define and ion-mill the propagation tracks and detectors.
8. Deposit a final SiO_2 layer, approximately $1\mu\text{m}$ thick to 'passivate' the device and etch windows in this layer to the gold bonding pads. Wires may then be bonded to the chip.

A cross-section of the resulting structure is shown schematically in figure 3.10(R.J.Fairholme, 1974)

In the devices produced by Plessey the films of permalloy, gold and silica were sputter deposited, although evaporation and electroplating can also be used. Patterns were defined in photo-resist using a standard photolithography system. The wafer is ion-milled by bombarding with a neutralized argon ion beam so that the conductor or permalloy patterns are created by using the resist as a 'sacrificial image'. Wafer diameters are usually around 5cm whilst a typical chip size is $0.5 \times 0.5\text{cm}^2$.

The next stage is to test the operating characteristics of every complete device contained on the wafer. At Plessey this was performed by a microprocessor-controlled probe tester capable of

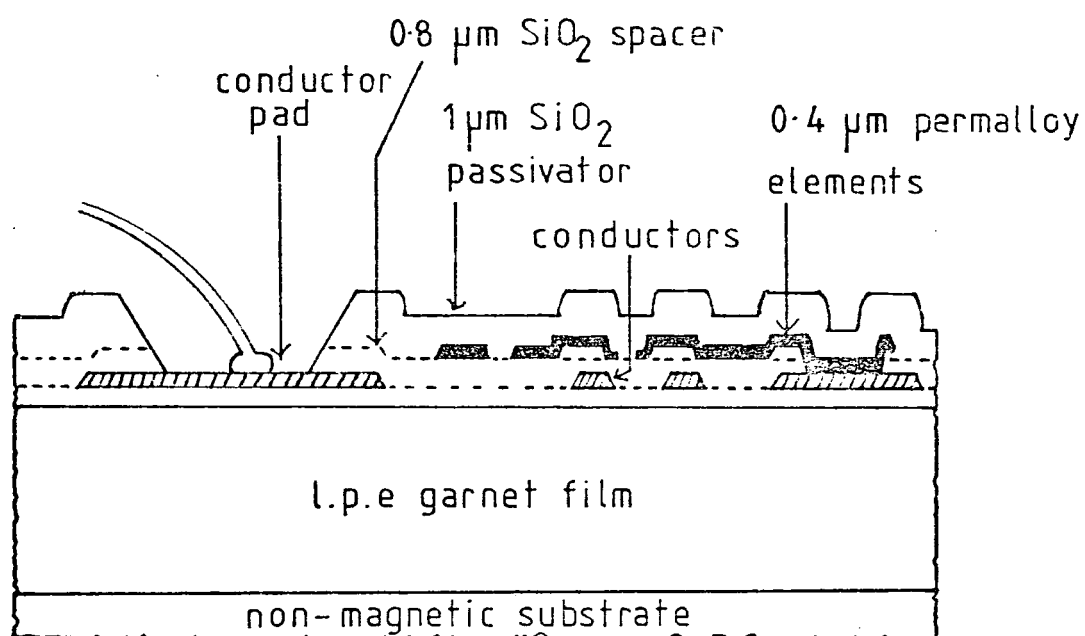


Fig. 3.10 Structure of a typical bubble device with conventional permalloy propagation pattern. (R.J. Fairholme, 1974)

driving a variable bias field and rotating field. With such a system the operating margins are tested by feeding data through each chip. Those chips which do not meet the specified bias margin, which is usually around 10 Oe, are inked so that the wafer can then be sawn and the good chips retained. Finally the successful chips are packaged. The rotating field is generally provided by two orthogonal coils fed with sine and cosine current waveforms and the bias field can be supplied by small permanent magnets combined with suitable mu-metal 'pole-pieces'. The complete package is then tested using a second microprocessor controlled test station.

An interesting problem associated with fabrication is the effect of step coverage. It is evident from figure 3.10 that because of the underlying conductor pattern, steps occur in the permalloy elements. Such steps often pose problems because the bias field can magnetize the step area. Thus an extra force is exerted on bubble domains passing near to the step and this can have an adverse effect on operating margins. This problem and some of the possible solutions (methods for producing a planar permalloy layer) are discussed in a recent paper by Roman et al., (1980).

3.10 Ion Implanted-Bubble Devices.

In section 3.4 it was pointed out that ion-implantation can be used to create a surface layer in bubble garnets where magnetization lies parallel to the film plane. Wolfe and North (1974) reported that planar domain structures exist in implanted layers and that these structures could be revealed using ferrofluid. It was also discovered by Wolfe et al., (1972) that the implanted layer could be used to manipulate bubble domains in a new type of

field access device.

To create a propagation pattern, a layer of gold or photoresist is deposited on top of an L.P.E. garnet and then patterned using conventional lithography. This pattern protects certain areas of garnet during subsequent ion-implantation and the non-implanted regions (with unaltered uniaxial anisotropy) form the 'propagation track'. The track often consists of a connected string of discs ('contiguous discs') as illustrated in figure 3.11(a). Bubbles prefer to lie near the edge of a disc and as the in-plane field rotates bubbles are propagated along the perimeter of the disc pattern.

Ferrofluid experiments have indicated (eg. Jouve and Puchalska, 1979) that propagation occurs because of 'charged walls' in the implanted layer (figure 3.11(b)). Bubbles are linked magnetostatically with these charged walls and the latter are rotated 'propeller-fashion' around contiguous discs by the drive field. The implanted patterns are much coarser than a conventional permalloy overlay, in fact it has been claimed that the 'minimum feature' may be as large as four times the bubble diameter (Lin et al., 1977). By contrast, the minimum feature in a gap-tolerant permalloy pattern is about half the diameter of a bubble domain. Using the same lithography techniques an order of magnitude increase in bit density would therefore seem feasible.

Ion-implanted bubble devices have not yet reached the production stage but all the functions required in a major-minor loop circuit such as bubble generation, transfer and detection have been demonstrated recently on a laboratory scale (Nelson et al., 1980).

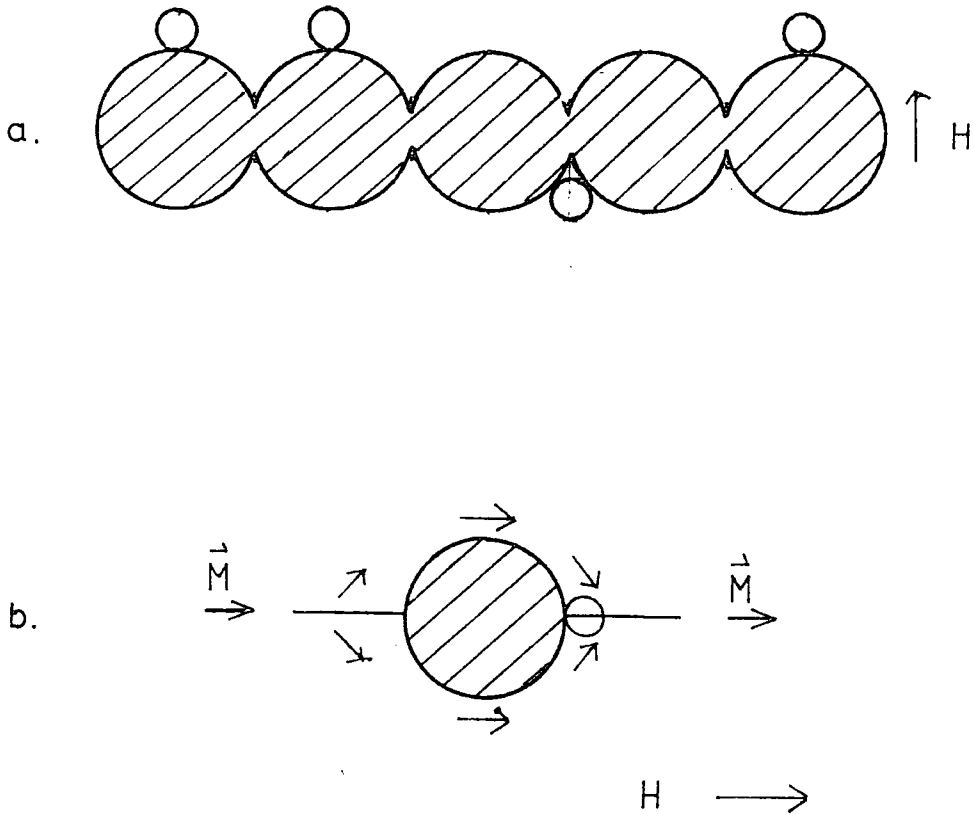


Fig. 3.11 (a) Illustration of ion-implanted 'contiguous-disc' propagation. Bubbles, represented by small circles, propagate around the non-implanted areas (shaded). H represents in-plane drive field.

(b) The mechanism of propagation is based upon charged walls in the ion-implanted layer.

3.11 Bubble Lattice Devices.

In conventional bubble memory devices binary information is coded by the presence or absence of bubbles in a shift register. To maintain the integrity of the stored information, bubbles have to be kept a certain distance apart (usually 4 bubble diameters, centre to centre) so that bubble interactions are kept to a minimum. The number of bits which can be stored per unit area in such a device is therefore equal to $(4d)^{-2}$ where d is bubble diameter. If the number of bubbles per unit area is increased, mutual repulsion will eventually lead to the formation of a close-packed hexagonal bubble array or 'lattice'. Figure 3.12 shows such a lattice in a high contrast garnet epilayer revealed by the Faraday effect. Unlike the 'isolated' bubble, a lattice can be stable without an applied bias field. This is essentially because the overlapping stray fields of adjacent bubbles produce a self-biasing effect. The stability of a lattice can be treated in the same way as an isolated bubble by considering total magnetic energy. (eg. Druyvesteyn and Dorleijn, 1971). The use of a bubble lattice to store information was first described by Voegeli et al. (1975) as a means of increasing bit density.

Instead of 'presence -absence' coding of binary data, a lattice memory has to exploit 'wall state coding'. Thus, for example, binary 1 and 0 can be represented in a lattice by the $S=1$ and $S=0$ bubbles which were illustrated in figure 3.2 (a) and (c). Most of the devices built so far have used current-carrying conductors to create the necessary field gradients for bubble manipulation. (eg. Hu et al., 1978) To maintain the structure of information stored in a lattice it is not possible to manipulate individual bubbles. Instead a whole column has to be added or

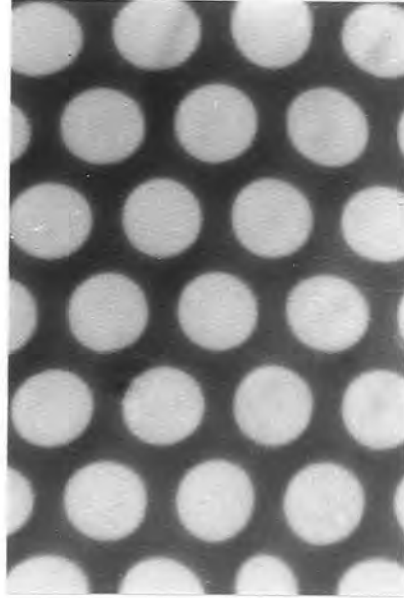


Fig. 3.12 Bubble lattice in a substituted rare earth-iron garnet in zero applied field. (Bubble diameter approximately $8\mu\text{m}$.)

subtracted during the writing and reading processes. Bubble coding can be achieved in practice because the $S=0$ state is stable in the presence of a strong in-plane field whilst the $S=1$ state is only stable in weak in-plane fields. To access data, bubbles can be sorted according to their deflection in a field gradient. One of the problems with this type of device is that writing and reading take place in 'isolated-bubble' regions which have different bias field requirements to the lattice. Although lattice memories have not yet been developed as far as conventional devices, work is still in progress notably at the research laboratories of IBM Ltd.

3.12 Current-Access Bubble Devices.

As mentioned in section 3.6, early devices used current-carrying conductors to manipulate bubble domains but this method was overtaken by the development of permalloy overlays. It now appears that this situation may eventually be reversed by a new generation of current-access devices being developed by Bobeck and co-workers at Bell Labs. (Bobeck et al., 1979).

In the new device the coil drive system and permalloy overlay are replaced by one or more thin film conducting layers deposited on top of the bubble medium. Each layer is etched with a pattern of oval-shaped holes. When these layers are fed with suitable A.C. currents, current 'vortices' around the holes move magnetic bubbles. This type of drive was in fact first described by Walsh and Charap (1974). The absence of drive coils reduces the bubble package size by about one-third and simplifies the electronics required to drive the devices. The operating frequency can be increased by an order of magnitude and the resulting drop in access time should enhance the potential for bubble memories in computing systems.

3.13 Applications.

The development of various types of memory device has largely been stimulated by the rapid growth of the information processing industry. A digital computer needs memories for storing both data and programs and an important factor determining the speed of a computing system is the time taken up by storage and retrieval of information. 'Access time' is therefore the most significant parameter for any storage system. Unfortunately the cost per bit rises with reductions in access time so a computing system usually exploits a variety of storage systems from expensive 'fast' memories (usually random access) to much cheaper and slower 'mass' memories (usually serial access). figure 3.13, based on a review of magnetic materials and applications by I.S.Jacobs (1979) illustrates the range of devices available.

ACCESS TIME			
10^{-9} s. (FAST)	10^{-6} s. (MID_RANGE)	5×10^{-3} s. (SLOW)	1s.
Bipolar*	CCD*	Fixed head disc/drum	
MOS*	Magnetic bubble	Moving head disc	
Ferrite core	Beam-addressable	Tape	
Flat thin film	Magneto-optic	Thin film heads	
Plated wire	(future)	(entering)	
INCREASING COST PER BIT			

Figure 3.13 A survey of memory/storage technologies (after I.S. Jacobs, 1979). Non-magnetic technologies are marked thus *.

As can be seen from figure 3.13, magnetic phenomena have already been used extensively in the memory/storage field. In each case the signal or information is stored in terms of the direction of magnetization. This diagram also indicates the so-

called 'access-gap' which exists (or rather existed until quite recently) between 'mass' memories based on discs, drums or tape and 'fast' memories based mainly on semiconductors. Multiloop bubble devices with access times below 5×10^{-8} s. could fill this gap but there is already a strong competitor in the form of charge-coupled devices (CCD's). In the CCD information is represented by 'packets' of electrical charge (Amelio, 1974). W.F. Druyvesteyn et al. (1975) have compared the essential features of these two rival technologies. One of the important advantages of bubble memories is that they are truly non-volatile: if the power supply is switched off the stored information is not lost. If loss of information from a CCD is to be avoided the power supply cannot be shut down completely, only reduced. Unlike bubbles, the packets of electrical charge in a CCD have to be 'refreshed'. The typical fabrication process for a bubble memory is much simpler than the established processes for manufacturing semiconductor devices such as the CCD. In particular, less masks are needed. One mask to define conductors and a second to define the propagation circuit are sufficient. As a result the production yield and cost per bit can be very competitive for bubble devices. The main advantage of CCD's is probably their compatibility with other semiconductor microelectronics which can be incorporated on the same chip. Furthermore, CCD's can handle both analogue and digital signals whilst bubble storage is limited to the handling of digital material. Because of the interaction between bubble domains there is the potential that logic could be built into a bubble device. However this has not yet been realized in commercial devices. For CCD'S a maximum operating frequency of 100 MHz has been predicted but the operating frequency of most commercial bubble devices being produced

at present is 100 KHz. If the new generation of current access devices under development at Bell Labs. is successful this frequency could be significantly increased. The high frequency operation of drive coils in a conventional device is more limiting than the intrinsic speed of bubble materials.

Apart from filling the 'access-gap' in computer technology other areas of application exist for bubbles. For example low volume, low power memories would be attractive in military and avionics systems. Non-volatility is also important. The first reported commercial application of bubble devices has occurred in the telecommunications field. At Bell laboratories a digitized voice system has been established in which a 16 k bit capacity single shift register stores a 12 second message. Bell Labs have also used bubble memories in a switching system for directing one telephone call to another subscriber's number. Another interesting area of application arises from the display potential of bubble domains. Special bismuth-substituted garnets can be prepared with exceptionally good Faraday rotation (Scott and Lacklison, 1976).

In conclusion, it can be said that the prospects for bubble devices seem good. The 'state of the art' at present is that several companies are manufacturing 250 k bit, 16 μ m period chips whilst Rockwell has produced the first megabit capacity chip. The scale down from 16 μ m period is already underway in the laboratory and it has been demonstrated that conventional permalloy devices, with gap tolerant features, will be adequate at least down to 8 μ m period, 2 μ m bubble diameter (eg. Orihara et al., 1979). Below this, ion-implanted 'contiguous discs' with coarse features will become more important. For sub-micron bubbles a shift from garnets towards amorphous alloys seems inevitable. Drive systems based on conducting sheets should also feature in the bubble devices of the future.

CHAPTER 4 EXPERIMENTAL AND THEORETICAL WORK ON PERMALLOY OVERLAYS.

4.1 Introduction

Since the development of conventional bubble devices there has been a considerable amount of research into the distribution of magnetization in permalloy elements and the resulting magnetic fields. A brief review of this work will now be given.

4.2 Experimental measurements.

Several of the techniques described in chapter two have been used to study the magnetization in overlay bars. Some involve direct interaction with \vec{M} (e.g. using polarized light or electrons) whilst others depend on the stray fields caused by magnetization (e.g. using colloid particles).

A Kerr effect probe with a light spot of $3\mu\text{m}$ diameter was used by Krinchik et al. (1975) to measure the average magnetization in T- and I-bars and later chevron column bubble detectors (Krinchik et al., 1978). They used the transverse mode but the polar effect can also be used for the purpose of domain wall mapping as described by Huijer et al. (1978). In this case the vertical component of magnetization associated with a Bloch wall is detected. Ma (1976) used the transverse Kerr effect on a larger scale to measure the response of arrays of I-bars to uniform applied fields. The application of Lorentz microscopy to permalloy overlays was reported by Jones et al. (1978). Domain walls were imaged with high resolution in T- and I-bars and simple chevrons, however there are limitations on the thickness of sample and support which can be used. In this case the permalloy was approximately $0.2\mu\text{m}$ thick.

Several workers have used the colloid technique (with Bitter colloid and subsequently ferrofluid) to reveal domain walls in permalloy bars. Y.S. Lin (1972) and Khaiyer and O'Dell (1976) studied T- and I-bars with this technique. Khaiyer and O'Dell also introduced Nomarski Interference Contrast as a useful accessory for studying colloid patterns. Ferrofluid has been used more recently by Huijer et al. (1979) to study the hysteretic behaviour of large ($100 \times 12 \times 0.3 \mu\text{m}$) rectangular bars of permalloy. The results of these investigations will be discussed in the next chapter in context with the present study of $16 \mu\text{m}$ -period circuits. Another technique which has been applied to permalloy bars is the Vibrating Sample Magnetometer. Doyle and Casey (1973) measured the response of two-dimensional arrays of I-bars to uniform applied fields with a VSM.

A few experiments have been directed towards probing the external field of overlay bars. Hsin et al. (1971) used large, scaled-up T- and I-bars several cm in size for their field measurements. However the domain structure would clearly be quite different from that existing in μm -sized bars. George and Chen (1972) used bubble domain observations in their study of realistic sized elements. First the diameter of bubbles in permalloy-free regions was plotted against bias field. This was compared with the diameter versus bias field curve for a bubble beneath an overlay and the difference gave a measure of the effective 'bias field' created by the permalloy. Their results suggested that an I-bar magnetized by an in plane field and/or the stray field of the bubble domain produces a 'field well' some way in from the end of the bar. From the bubble domain shape it was deduced that this well was reasonably symmetrical about a

vertical axis.

4.3 Calculations

Magnetization and field calculations fall into two groups: Those based on domain models and those based on continuum models for the magnetization. In a continuum model the presence of domains and domain boundaries is ignored. Those calculations which have attempted to consider the domain structure known to exist in permalloy bars will be discussed in chapter 8. In this section a brief review of continuum models will be given. The two approaches have been compared recently by Huijjer et al. (1980)

Most continuum models attempt to find a minimum energy configuration for \vec{M} and in most cases magnetostatic energy is assumed to dominate. The total energy is then approximately given by the sum of applied field and demagnetizing field components:

$$E = -\mu_0 \int_V \vec{M}(\vec{r}) \cdot \vec{H}_a(\vec{r}) dV - \frac{\mu_0}{2} \int_V \vec{M}(\vec{r}) \cdot \vec{H}_d(\vec{r}) dV \quad (4.1)$$

Here \vec{H}_a represents the total applied field, being the sum of a uniform drive field and the non-uniform stray field of bubble domains if present. As defined in chapter 2 (eqⁿ.2.10), the demagnetizing field $\vec{H}_d(\vec{r})$ depends on the magnetization \vec{M} not only at \vec{r} but at all other points in the volume of permalloy, V . For a minimum energy state small variations in \vec{M} should produce no changes in E and it can be shown (Copeland, 1972) that

$$\vec{H}_d(\vec{r}) = -\vec{H}_a(\vec{r}) \quad (4.2)$$

For a given applied field the magnetization should be so arranged that the demagnetizing field is everywhere equal and opposite to the local applied field. It is generally assumed that \vec{M} is everywhere parallel to the permalloy plane.

Many calculations have been based on the simplest case of a rectangular bar and one of the earliest was described by Copeland (1972). This one-dimensional model ($M_x(x)$) established that the centre of a bar would become saturated at a certain applied field termed 'H'₇₅ since the net magnetization at this point was approximately $0.75M_s$. For a bar of length L, width W and thickness T the following approximation was obtained:

$$H_{75} = M_s \frac{T}{L} F\left(\frac{W}{L}\right) \quad (\text{S.I.})$$

$$\text{where } F\left(\frac{W}{L}\right) \simeq \frac{W}{L} \left[1 + \frac{W}{L}\right]^{-1} \quad (4.3)$$

Partial saturation measurements will be presented in chapter 6 and compared with this model in chapter 8.

Lin (1972) applied a Fourier series approach to the case of a periodic array of rectangular bars. The bar shape, magnetization and demagnetizing fields were all represented with Fourier series allowing a one-dimensional \vec{M} distribution to be determined. George and Archer (1973) developed Copeland's model further to consider the motion of a bubble domain along a rectangular bar. The magnetostatic barriers which this involved were interpreted in terms of drive field requirements. This work was basically one-dimensional but an extension to two dimensions was later provided by George and Hughes (1976).

Whereas the majority of continuum models have been based

on the energy of a permalloy bar, Almasi and Lin (1976) estimated the flux emanating from a bubble domain and trapped by the permalloy. This allowed approximate analytical expressions for the operating margin to be obtained.

The Fourier series approach of Lin was subsequently developed by Dove et al. (1975) so that the influence of bubble domains could be included. The same group also studied the effects of finite permalloy permeability (Dove et al., 1976) and interaction effects between neighbouring bars (Watson et al., 1976). They have recently presented a review of the Fourier series approach (Huijjer et al., 1981).

In the past few years continuum models have been applied to the study of non-rectangular elements. Ishak and Della Torre (1978) developed an iterative method for determining the magnetization distribution in an arbitrary two-dimensional permalloy shape. Beginning with an assumed distribution for \vec{M} , the demagnetizing field is calculated for an array of points. This is used to predict a new magnetization distribution and the process is repeated until convergence is obtained. Potential well profiles for symmetric and asymmetric chevrons and half-discs were subsequently obtained (Ishak and Della Torre 1979). Similar elements were treated by Matsutera and Hidaka (1979) by dividing each element into a finite number of square blocks. The field wells generated by these elements are not so regular as that found beneath a simple I-bar. A comparison of symmetrical and asymmetrical elements has suggested that the latter have improved field gradients.

Finally the application of continuum modelling as an aid to device design has been described recently by Collins and Cole

(1980). Using a large host computer and an on-line display terminal a system involving bubbles, permalloy shapes and conductors can be modelled interactively.

CHAPTER 5 DESCRIPTION OF EXPERIMENT.

5.1 Samples.

All the samples studied in this project were prepared at the Allen Clark Research Centre of the Plessey Company Ltd.. Standard techniques of bubble device fabrication were used. Films of NiFe were first sputter-deposited onto silica-coated bubble garnet epilayers or non-magnetic substrates (GGG). These complete films were then tested with a B-H loop plotter to determine coercivity and anisotropy (most often uniaxial). Finally the pattern was defined using normal photolithography and ion-milling.

The range of samples available included early T-and I-bar circuits with period $32\mu\text{m}$. However the majority of samples had propagation tracks based on $16\mu\text{m}$ -period asymmetric chevrons. These samples also contained a variety of experimental detector column geometries together with pick-axe nucleate elements. Some larger areas of permalloy were also present in all samples. In each detector the column period was $20\mu\text{m}$ though the width of individual chevron bars varied from approximately $6\mu\text{m}$ down to a nominal $1\mu\text{m}$. The successful fabrication of $1\mu\text{m}$ bars with conventional photolithography is difficult and in the majority of columns a nominal bar width of $2.1\mu\text{m}$ was employed. The overlays also contained a number of T- and I- bars with bar widths of 2.1 and $1\mu\text{m}$.

Samples with this overall design were manufactured using 4 different thicknesses of permalloy: 0.3 , 0.35 , 0.4 and $0.45\mu\text{m}$. A few samples containing $16\mu\text{m}$ -period asymmetric half-discs $0.4\mu\text{m}$ thick on bubble garnet were also provided.

5.2 Microscope.

Ferrofluid patterns were studied with a Vickers M17 (type E) microscope. This microscope was suitable for observation in transmitted and reflected light simultaneously. However most of the work was done using reflected light and a Vickers Differential Interference Contrast unit (Nomarski). This can be supplied as a standard accessory with the M17 microscope. The range of objectives used included 63xDRY (N.A. 0.90), 45xCIL (N.A. 0.95) and 80xCIL (N.A. 1.32). Photographs were obtained on 35mm film using an SLR camera with exposure times around 1 second. In some cases, depending on the setting of the interference contrast unit, exposure times of 4 or 5 seconds were required.

5.3 Applied Fields.

Coils for providing in-plane fields (H_{xy}) and bias fields (H_z) were mounted directly on the microscope stage with the sample supported in the centre. In-plane fields were produced by a ferrite toroid wound with four coils. Opposite coils were fed in series opposition. The wound toroid had overall dimensions as follows: i.d. 65mm, o.d. 110mm and depth 16mm. The X-and Y-windings can be activated independently if D.C. in-plane fields are required. Lacklison et al. (1977) show a plot of the field produced by ferrite core drive coils. They conclude that the field varies by less than 10% over 80% of the volume enclosed by the toroid. (The field varies most near the toroid itself). The field variation over a bubble chip (typical size: 5mmx5mm) at the centre of the toroid should therefore be very small. Bias fields were provided by a small solenoid mounted within the toroid. The bias coil produced 160 Oe per Amp whilst the individual windings of the toroid provided 17.9 Oe per Amp.

A rotating in-plane field can be produced by feeding the toroid with sine and cosine current waveforms. For simple ferrofluid experiments in which a field is rotated slowly and brought to rest at an arbitrary orientation a rotating turntable was manufactured as an alternative to the toroid. Small permanent magnets were mounted on the turntable and the in-plane field calibrated in terms of the pole separation.

For magnetoresistance measurements gold wires were bonded to the detector pads on a few samples. This was performed at the Plessey Laboratories.

5.4 Ferrofluid Experiments.

For good results with ferrofluid the sample should be as clean as possible. For the experiments described here, specimens were washed in 'Decon-90' solution (diluted 1:19 with water) at 55-60°C for 15-20 mins. This included at least 5 mins. immersion in an ultrasonic tank. The sample was then rinsed for a similar period in a succession of distilled water tanks. Aqueous-base ferrofluid (type 'A01', Ferrofluidics Corporation) was then applied to the sample whilst still wet.

It is desirable to obtain ferrofluid patterns with optimum resolution and contrast, especially when studying permalloy bars 1 or 2µm wide. A number of experimental methods were examined. The simplest method is to place a conventional glass coverslip on top of the ferrofluid and then observe with a dry objective. However the picture quality obtained in this way can be limited. Contrast arises from the 'piles' of enhanced particle density associated with the stray fields of domain walls. These stray fields are highly localized (they fall off rapidly with distance

because there are equal but opposite magnetic 'free-poles' on either surface of the permalloy). Ideally the depth of ferrofluid should correspond to the 'height' of the particle deposits above domain walls. Any additional ferrofluid can only serve to reduce the observed contrast. Using a conventional coverslip the pattern often appears to be obscured in this way.

To some extent the effect can be alleviated by suitable dilution of the ferrofluid, however much better contrast was obtained by replacing the flat coverslip with a thin curved flake of glass. (Flakes are produced by blowing and then breaking large bubbles of glass). As suggested schematically in figure 5.1(a) the flake is held, convex side down, by the surface tension of the surrounding liquid to form a very thin layer of ferrofluid at the centre. (Undiluted ferrofluid can be used). The flakes were estimated to be between 12 and 20 μm in thickness compared with approximately 90 μm for commercially available coverslips. (As an extra bonus this means that high resolution objectives with short working distance are easier to use). The disadvantage of this technique is that drying of the ferrofluid limits observation time to half an hour or less.

To approach the limit of optical resolution it is necessary to use oil immersion objectives. Ferrofluid itself can be used as the immersion medium but there is then a drastic reduction in contrast as the total ferrofluid layer is now many times thicker. It was found that this problem could be solved by floating a layer of immersion oil directly on top of a thin film of ferrofluid. In this way very high resolution can be achieved (some details of wall structure within 1 μm bars become visible). However it was found difficult to achieve reasonable viewing times as there is a

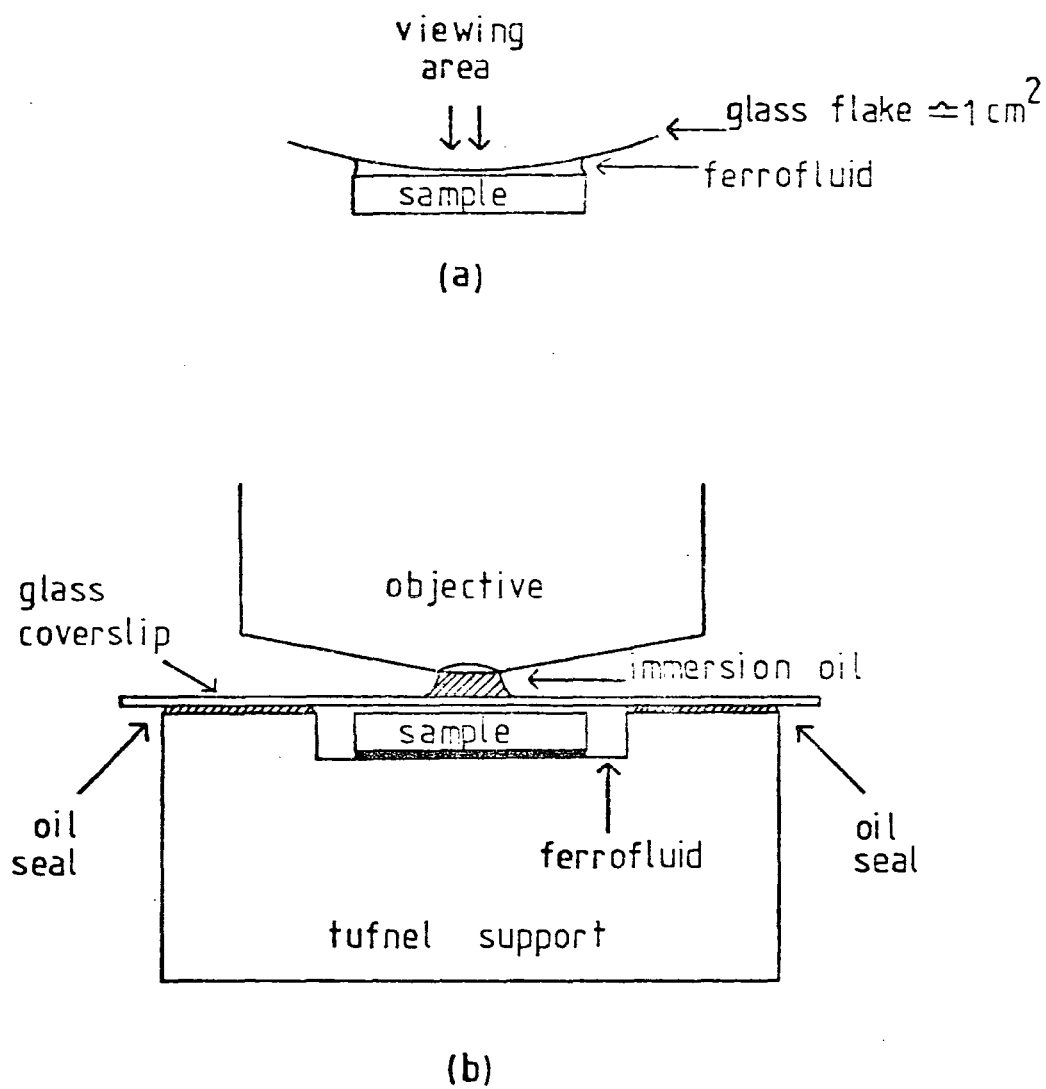


Fig. 5.1 Arrangements used in ferrofluid experiments.

tendency for the oil/water interface to be unstable.

The arrangement finally chosen for the majority of experiments is shown in figure 5.1(b). The sample is placed in a small circular well (the sample is fractionally thicker than the depth of the well) and covered with ferrofluid. A conventional coverslip is then placed on top of the specimen with a thin film of oil forming a seal around the periphery. The oil holds the coverslip down in close contact with the sample and the oil immersion objective is then brought into position. Again the resolution and contrast are generally good but because of this 'sealed module' approach the viewing time can be extended over many hours. This is particularly useful when a long series of observations are required in order to establish, for example, the mean field required to partially saturate a permalloy bar.

CHAPTER 6 ISOLATED ELEMENTS - RESULTS AND DISCUSSION

6.1 Energy and width of Bloch walls in permalloy elements.

In chapter 2 the magnetostatic energy of domain walls in thin films was discussed. According to calculations of Néel based on a simple wall model, a transition from Bloch to Néel walls occurs when a film is of the order of a few 1000 Å thick. The overlays studied here range in thickness from 3000 Å to 4500 Å so it is to be expected that domains in these samples are separated by Bloch walls. However the magnetostatic contribution to wall energy is still important especially since anisotropy is low. In the limit of zero anisotropy, wall width would be infinite were it not for the magnetostatic energy term. Using Néel's model approximate values for the wall parameters can be obtained. The same calculation has been performed by Middlehoek (1963) for permalloy films in the thickness range 0 to 2000 Å.

Consider a plane Bloch wall of width d and energy per unit area F representing a spin transition through angle 2θ . It is assumed that $\vec{\nabla} \cdot \vec{M} = 0$ so the component of magnetization normal to the wall plane is constant. If the wall lies parallel to the xy -plane in cartesian coordinates, the spins rotate about the z -axis as illustrated in figure 6.1. The angle θ between the spins and the z axis is constant. A simple linear transition is assumed so that :

$$\phi = -\frac{\pi}{2} \quad \text{for } z < -\frac{d}{2}$$

$$\phi = \frac{\pi}{d}z \quad \text{for } -\frac{d}{2} \leq z \leq \frac{d}{2}$$

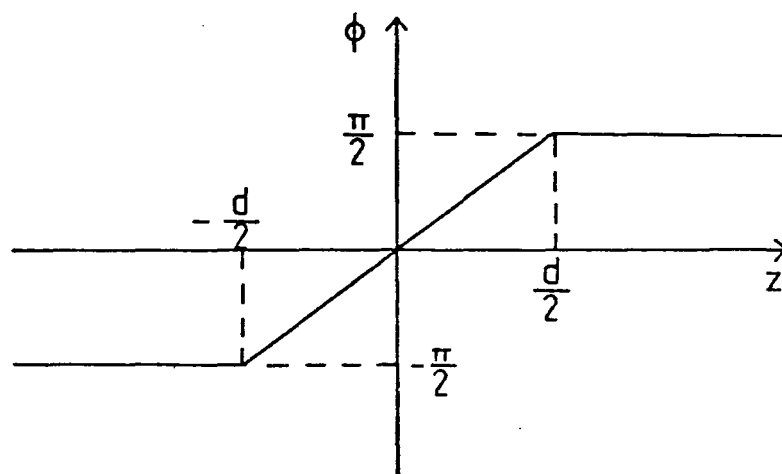
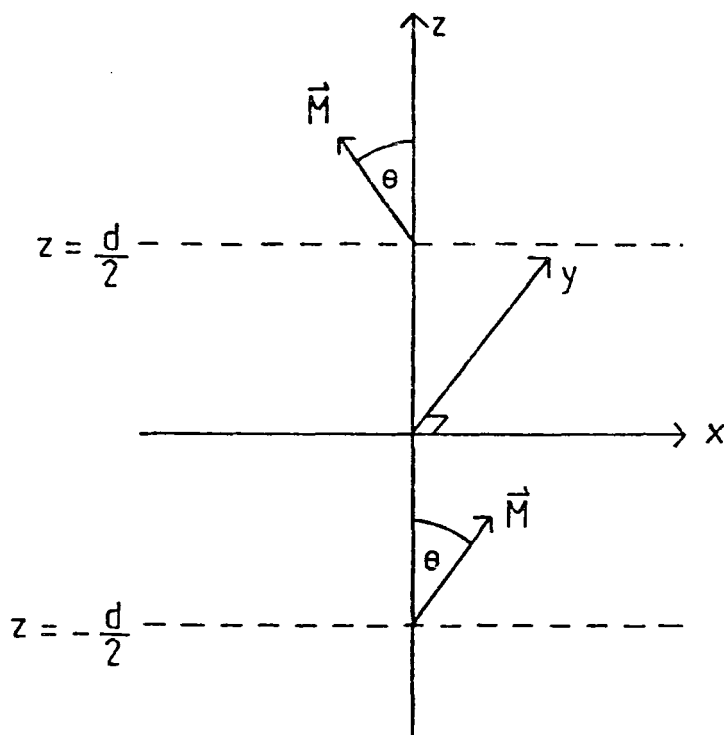


Fig. 6.1 Simple model for a 2θ Bloch wall of width d lying parallel to the xy -plane. ϕ is the angle between the yz plane and a plane containing the magnetization vector and the z -axis

$$\phi = \frac{\pi}{2} \quad \text{for } z > \frac{d}{2}$$

where ϕ is the angle between the yz-plane and the plane containing the spin vector and the z-axis. If for simplicity the spins are assumed to occupy a simple cubic lattice then the angle between two adjacent spins along the z axis is:

$$\begin{aligned} d\Omega &= \sin\theta \left(\frac{d\phi}{dz}\right) a \\ &= \sin\theta \frac{\pi}{d} a \end{aligned}$$

where a is the lattice spacing. From equation 2.2 the corresponding exchange energy is:

$$dE = JS^2 \sin^2\theta \cdot \frac{\pi^2}{d} \cdot a^2$$

where J and S are the exchange integral and spin as defined in section 2.2. The exchange energy per unit area of wall will therefore be:

$$\begin{aligned} F_{\text{ex.}} &= \frac{JS^2}{a} \sin^2\theta \cdot \frac{\pi^2}{d} \\ &= A \sin^2\theta \cdot \frac{\pi^2}{d} \end{aligned} \tag{6.1}$$

where A is the exchange constant.

Using Néel's model the wall is represented by a cylinder with elliptical cross-section (fig. 2.2). From equation 2.23 the resulting magnetostatic energy per unit area of wall is given by:

$$F_s = \frac{\mu_0}{2} \frac{d^2}{d+t} M_{\text{av}}^2$$

where t is the film thickness and M_{av} is an average magnetization within the cylinder normal to the film plane. The component of magnetization normal to the film plane, M_n , varies across the wall:

$$M_n = M_s \sin\theta \cos\left(\frac{\pi z}{d}\right), \quad -\frac{d}{2} \leq z \leq \frac{d}{2}$$

$$M_n = 0, \text{ elsewhere.}$$

The average value of M_n within the wall is:

$$\begin{aligned} \bar{M}_n &= \frac{1}{d} \int_{-\frac{d}{2}}^{\frac{d}{2}} M_s \sin\theta \cos\left(\frac{\pi z}{d}\right) dz \\ &= \frac{2}{\pi} M_s \sin\theta \end{aligned}$$

The r.m.s. value of M_n is:

$$\begin{aligned} M_n &= \left[\frac{1}{d} \int_{-\frac{d}{2}}^{\frac{d}{2}} M_s^2 \sin^2\theta \cos^2\left(\frac{\pi z}{d}\right) dz \right]^{\frac{1}{2}} \\ &= \frac{M_s}{\sqrt{2}} \sin\theta \end{aligned}$$

Since the model is only an approximation it is not important which of these two values is used for M_{av} since both will give the same order of magnitude of results. Taking the r.m.s. value gives the total magnetostatic energy per unit area of wall to be:

$$F_s = \frac{\mu_0}{4} \frac{d^2}{(d+t)} M_s^2 \sin^2\theta \quad (6.2)$$

The total energy per unit area of wall is then:

$$E_T = \left[\frac{A\pi^2}{d} + \frac{\mu_0}{4} \left(\frac{d^2}{d+t} \right) M_s^2 \right] \sin^2 \theta \quad (6.3)$$

Minimizing w.r.t. d gives the following equation for the equilibrium wall width:

$$\frac{4A\pi^2}{\mu_0 M_s^2} = \frac{d^3(d+2t)}{(d+t)^2} \quad (6.4)$$

Therefore, according to this model, the wall width is independent of wall angle (2θ). The solution of equation 6.4 can be substituted into equation 6.3 to obtain the equilibrium energy per unit area of wall. The wall energy is evidently proportional to $\sin^2\theta$ for a given permalloy thickness, t , so the energy density of a 90° wall will be half that of a 180° wall. Taking the values $A \approx 10^{-11} \text{ Jm}^{-1}$, $\mu_0 = 4\pi \times 10^{-7} \text{ Hm}^{-1}$ and $M_s \approx 8 \times 10^5 \text{ Am}^{-1}$ for permalloy, estimates for the energy and width of a 180° Bloch wall were obtained for the range of thickness relevant to the present study. The results are shown in figure 6.2. The wall becomes broader and the energy density falls as film thickness increases. This is because the magnetostatic energy term is reduced as t increases.

6.2 Bloch Wall Subdivision.

In the preceding calculation it was assumed that the Bloch wall consisted entirely of left-handed or right-handed spin rotation. However it was noted in chapter two that the magnetostatic energy arising from magnetic poles at the film surface is reduced if the Bloch wall subdivides into alternate left- and right-handed segments. These segments are separated by Bloch-lines, regions of wall with Néel character. Segmentation certainly occurs in thin film permalloy. As an example fig. 6.3(a,b) shows the ferro-

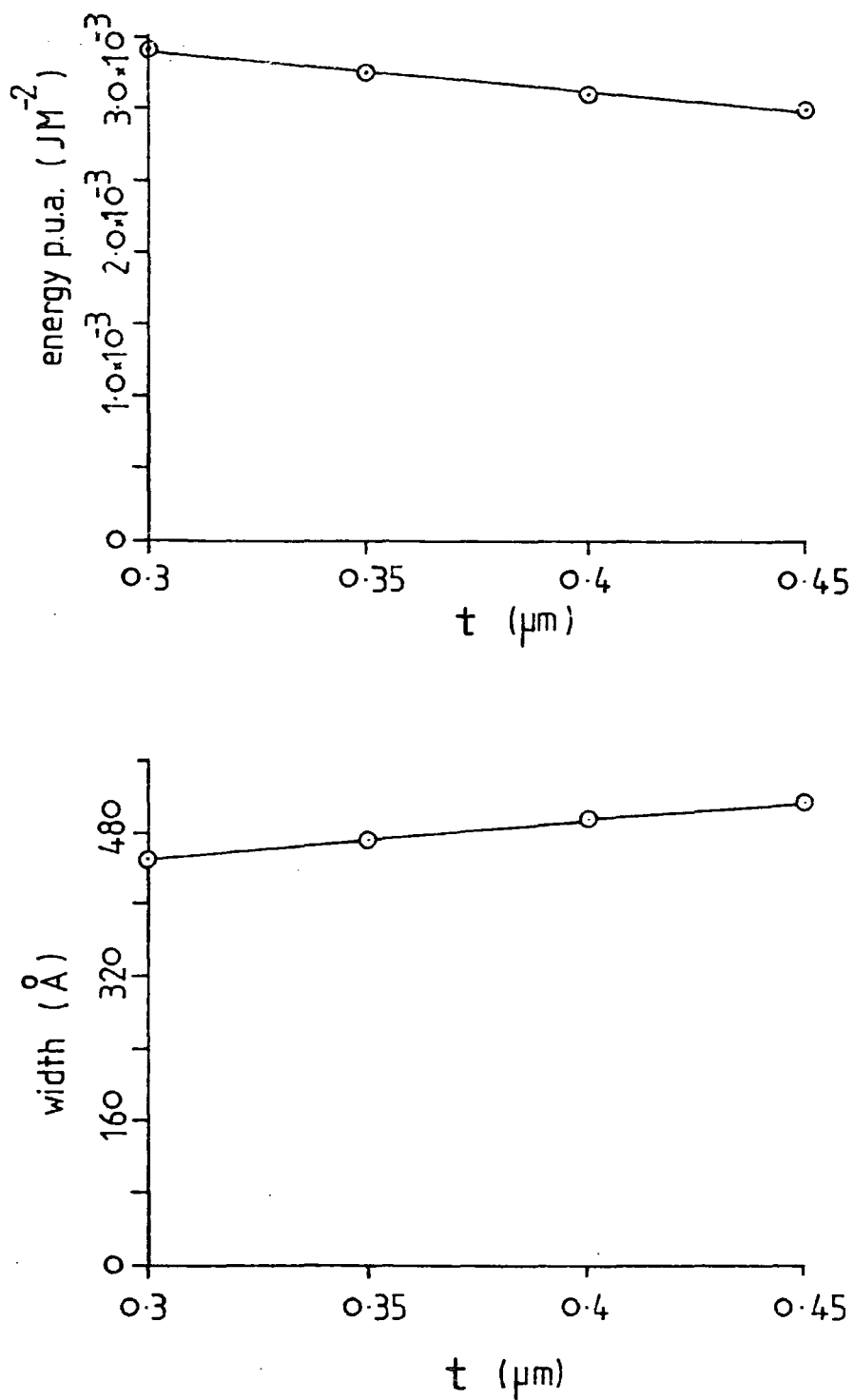


Fig. 6.2 Energy(per unit area)and width of a 180° Bloch wall as functions of permalloy film thickness (t).

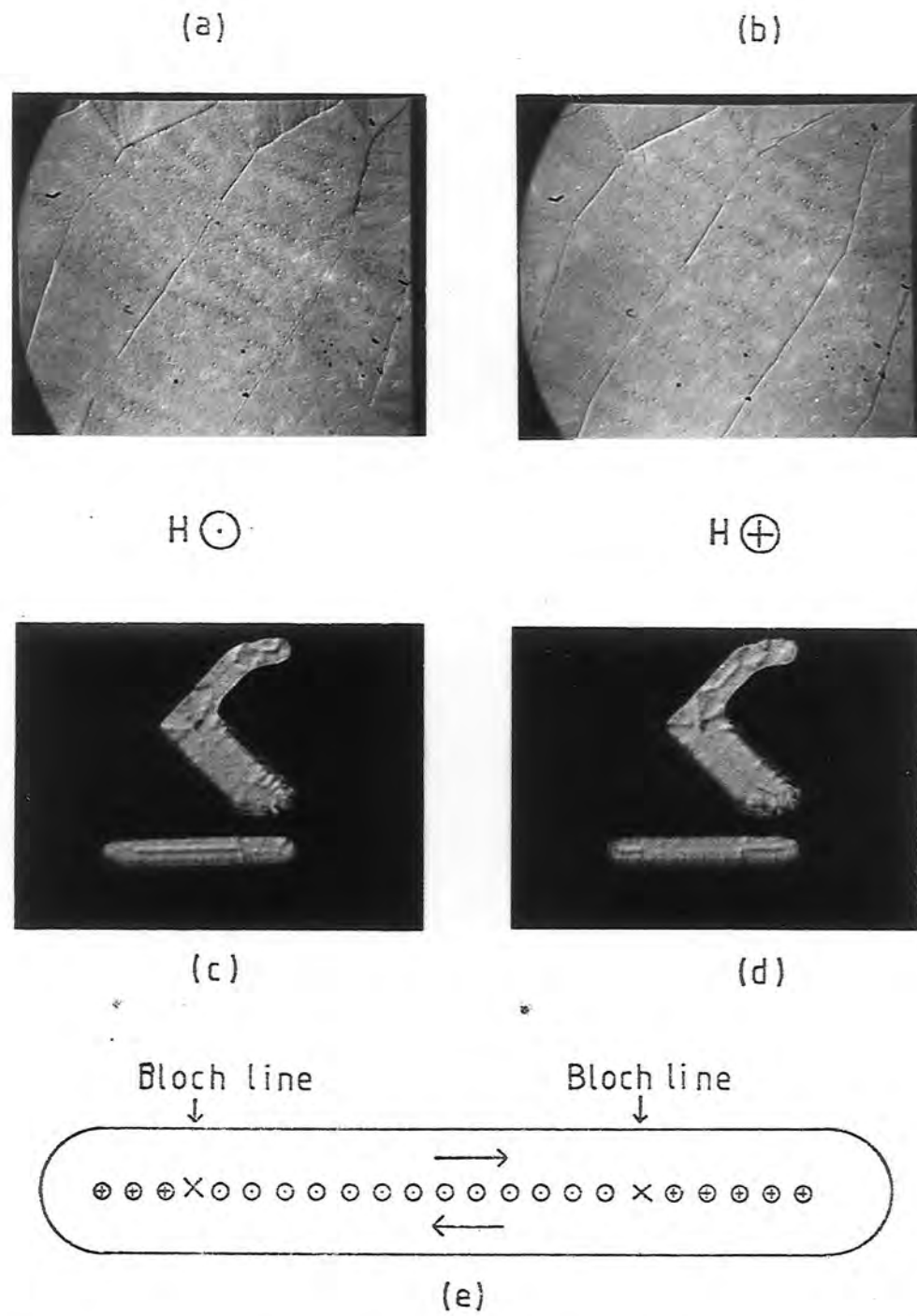


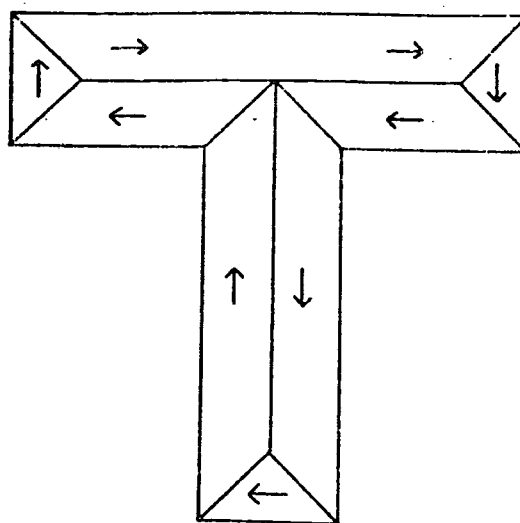
Fig. 6.3 Ferrofluid reveals the Bloch wall structure in a large area of permalloy, $0.45\mu\text{m}$ thick (a and b) and in an I-bar $15 \times 2.1 \times 0.35 \mu\text{m}$. (c and d). The bias field, H , is 5 Oe in (a) and (b) and 18 Oe in (c) and (d). The deduced spin structure of the wall is illustrated in (e).

fluid patterns on a square sheet of permalloy $94 \times 94 \times 0.45 \mu\text{m}^3$ with alternate bias fields applied perpendicular to the film plane. Fig. 6.3(c,d) shows similar broken ferrofluid deposits on an overlay bar. The deduced spin structure of the 180° Bloch wall is shown in fig 6.3(e). Clearly a rigorous calculation of wall width and energy should include the reduction of magnetostatic energy caused by subdivision. Shtrikman and Treves (1960) performed such a calculation on the basis of a periodic 'domain structure' within the wall. However in permalloy elements the subdivision is far from periodic. The length of individual segments may vary from less than $1 \mu\text{m}$ to greater than $10 \mu\text{m}$. Also it will be shown in section 6.6 that dynamic changes may occur in the distribution of Bloch wall segments and the number of Bloch lines under the influence of an in-plane field. For these reasons a correction to the calculated energy and width of the Bloch wall will not be attempted here. The estimates based on Néel's model are in any case approximate.

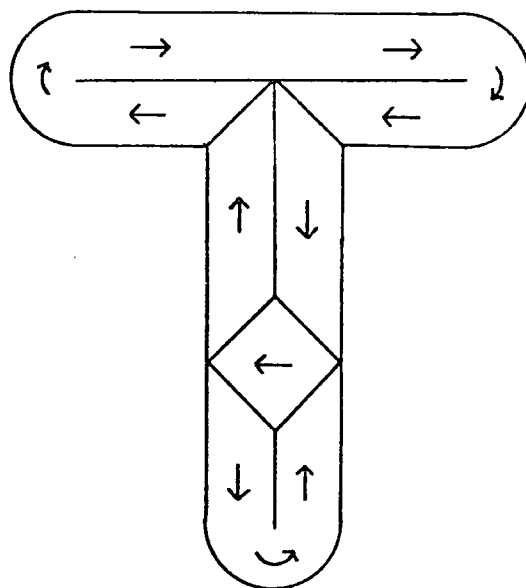
6.3 Anisotropy in Permalloy Overlays.

As a first step in studying domain structure in overlays some early T- and I-bar samples with period $32 \mu\text{m}$ were investigated. Domains in T- and I-bars have been observed by several workers. Y.S.Lin (1972) obtained Bitter patterns in a T-bar (bar width approximately $7.6 \mu\text{m}$) on non-magnetic substrate. The structure consisted of 180° walls and simple triangular closure domains as illustrated in fig. 6.4(a). Lin found that magnetization proceeded by domain growth with fields applied along the bar and by measuring wall displacement a linear relationship between net magnetization and field was observed up to saturation.





(a)



(b)

Fig. 6.4 Typical domain structures in T-bar elements :
(a) Lin (1972), (b) Khaiyer (1976).

Khaiyer and O'Dell (1976) and Khaiyer (1976) found similar structures in overlay bars on glass substrate and on LPE magnetic garnets. They found that the central domain wall bowed slightly when a field was applied and that closure domains did not form on rounded bar ends as shown in fig. 6.4(b). This diagram also illustrates an 'internal closure domain' (ICD) consisting of four 90° walls. Similar domains have been found in iron whiskers, for example by deBlois and Graham (1958). Khaiyer reported that bars deposited on magnetic garnet frequently contained ICD's whilst those on glass substrate did not, and that the position of domain walls could be deformed locally by the garnet stray field. Some of these features have also been observed in 'thin' ($0.2\mu\text{m}$) permalloy circuits by Lorentz microscope (G.A. Jones et al., 1978) together with additional fine structure such as coarse ripple. In these samples, however, there was frequent non-appearance of domain walls in some bars, the authors suggested that this could be due to the thickness. It will be demonstrated later that thickness plays an important part in determining saturation fields.

Fig. 6.5 shows remanent domain patterns in a $32\mu\text{m}$ -period T-bar circuit on magnetic garnet revealed in a dry colloid deposit. Several bars have a remanent structure based on a central 180° wall as described above. Further examination of the colloid deposit indicates small wall displacements due to the garnet stray fields. However the most striking feature of these patterns is the complexity of structure found in certain elements. All the bars lying in a particular direction are filled with ICD's. Khaiyer (1976) suggested that ICD's occur because they are nucleated by the garnet stray fields when the overlay is formed. However the pattern of stripe domains in the sample studied here

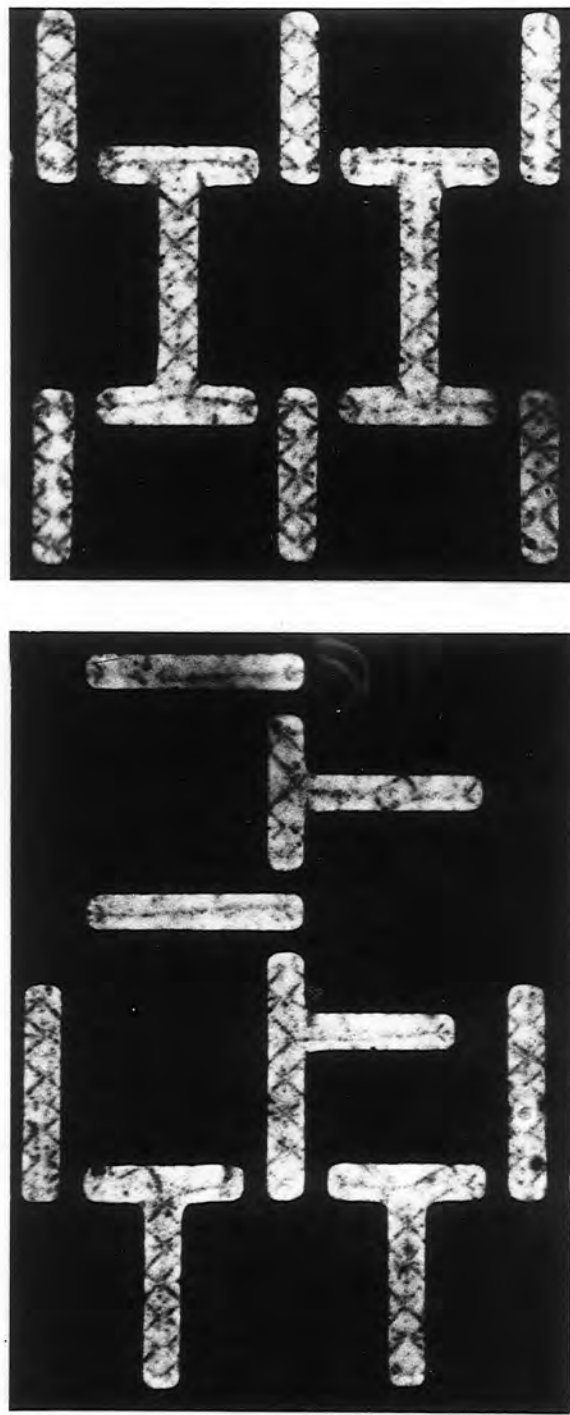


Fig. 6.5 Remanent domain wall structures in a 32 μm period overlay on magnetic bubble garnet. (Dried ferrofluid deposit.)

was random and it will be shown later that similar multiple domain states form even after saturation of the bars. It therefore seems more likely that in-plane anisotropy is responsible for the complex structure. Unfortunately no hysteresis measurements exist for the unpatterned films in this case but the degree of anisotropy can be estimated.

Consider the magnetic energy of a long rectangular bar containing a periodic string of ICD's as in fig 6.6(b) and for comparison the energy of a bar containing a single 180° wall as in fig 6.6(a). Each bar has width W , thickness t and an assumed uniaxial anisotropy with the easy direction running perpendicular to the long bar axis. The anisotropy energy density is given by:

$$E_k = K_1 \sin^2 \theta$$

where θ is the angle between the magnetization and the easy axis and K_1 is an anisotropy constant. Magnetostriction is ignored so the total magnetic energy of each bar in zero field consists of anisotropy energy and wall energy. Considering a length W in each case the respective energies will be:

$$E_T(a) = WtF_{180^\circ} + W^2tK_1$$

$$\begin{aligned} E_T(b) &= \frac{4W}{\sqrt{2}}F_{90^\circ} + \frac{1}{2}W^2tK_1 \\ &= \sqrt{2} WtF_{180^\circ} + \frac{1}{2}W^2tK_1 \end{aligned}$$

where F_{90° and F_{180° represent the energies per unit area of 90°

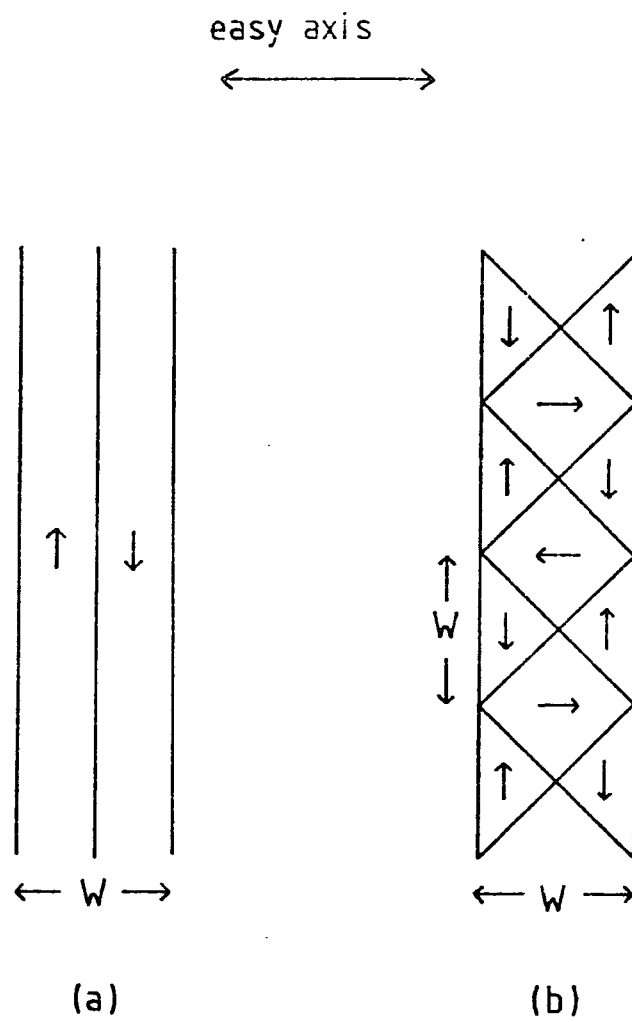


Fig. 6.6 Alternative domain structures in a long thin bar of permalloy of width W and thickness t .

and 180° walls respectively and on the basis of the earlier calculation it is assumed that $F_{90^\circ} = 0.5F_{180^\circ}$. If there is no anisotropy domain structure 'a' is favourable, structure 'b' has the lower energy of the two when

$$WtF_{180^\circ} + W^2tK_1 > \sqrt{2}WtF_{180^\circ} + \frac{1}{2}W^2tK_1$$

$$K_1 > \frac{2}{W}(\sqrt{2}-1)F_{180^\circ}$$

or in terms of the anisotropy field, $B_K = \frac{2K_1}{M_s}$,

$$B_K > \frac{4}{WM_s}(\sqrt{2}-1)F_{180^\circ} \quad (6.5)$$

For the sample in question, W and t were approximately $4\mu\text{m}$ and $0.4\mu\text{m}$ respectively. From fig. 6.2 the value of F_{180° in these bars would be approximately $3.1 \times 10^{-3} \text{Jm}^{-2}$ and the corresponding domain wall width would be roughly 490 \AA . Substituting these values into 6.5 together with $M_s \approx 8 \times 10^5 \text{ Am}^{-1}$ for permalloy gives $B_K > 16 \times 10^{-4} \text{ T}$ as the condition for multiple closure domain structures. The effect of anisotropy on wall energy has been ignored in this calculation. In fact if the walls are of the order of 490 \AA wide they occupy only a small volume of the bar (roughly 1.2% for bar 'a' and 3.5% for bar 'b') so this approximation seems reasonable. Permalloy films deposited for bubble devices generally contain in-plane anisotropies equivalent to a few Oe. In equation 6.5, B_K is inversely proportional to bar width, W , so domain structure is less likely to be modified by anisotropy in more recent overlay circuits with higher packing density and reduced bar widths. In $16\mu\text{m}$ permalloy tracks containing bars

approximately $2\mu\text{m}$ wide no examples of elements filled with closure domains were found.

The effects of anisotropy are evident in some of the larger areas of permalloy which surround the active circuit. For example the domain wall pattern of fig. 6.7(a) resembles the structure proposed by Landau and Lifshitz (1935) for uniaxial materials (Illustrated in fig. 6.7(b)). Fig. 6.7(c) shows a typical domain pattern in a long thin strip of permalloy oriented perpendicular to the easy axis. The interpreted domain structure for a bar perpendicular to the preferred axis is given in fig. 6.7 (d). In these ferrofluid patterns the stripe domains of the garnet substrate are also clearly visible. In the absence of applied fields the total magnetic energy per unit length of this structure is given by the sum of wall and anisotropy components:

$$E_T = E_W + E_K$$

$$= \frac{4}{D} \frac{Dt}{\sqrt{2}} F_{90^\circ} + \frac{1}{D} (y-D)t F_{180^\circ} + \frac{1}{D} \frac{D^2}{2} t K_1$$

where t is the film thickness, D is the domain spacing and y is the bar width.

$$\therefore E_T = t \left[\sqrt{2} + \frac{y-D}{D} \right] F_{180^\circ} + \frac{tDK_1}{2}$$

$$\text{assuming } F_{90^\circ} = 0.5F_{180^\circ}$$

The energy is a minimum with respect to D for the equilibrium wall spacing:

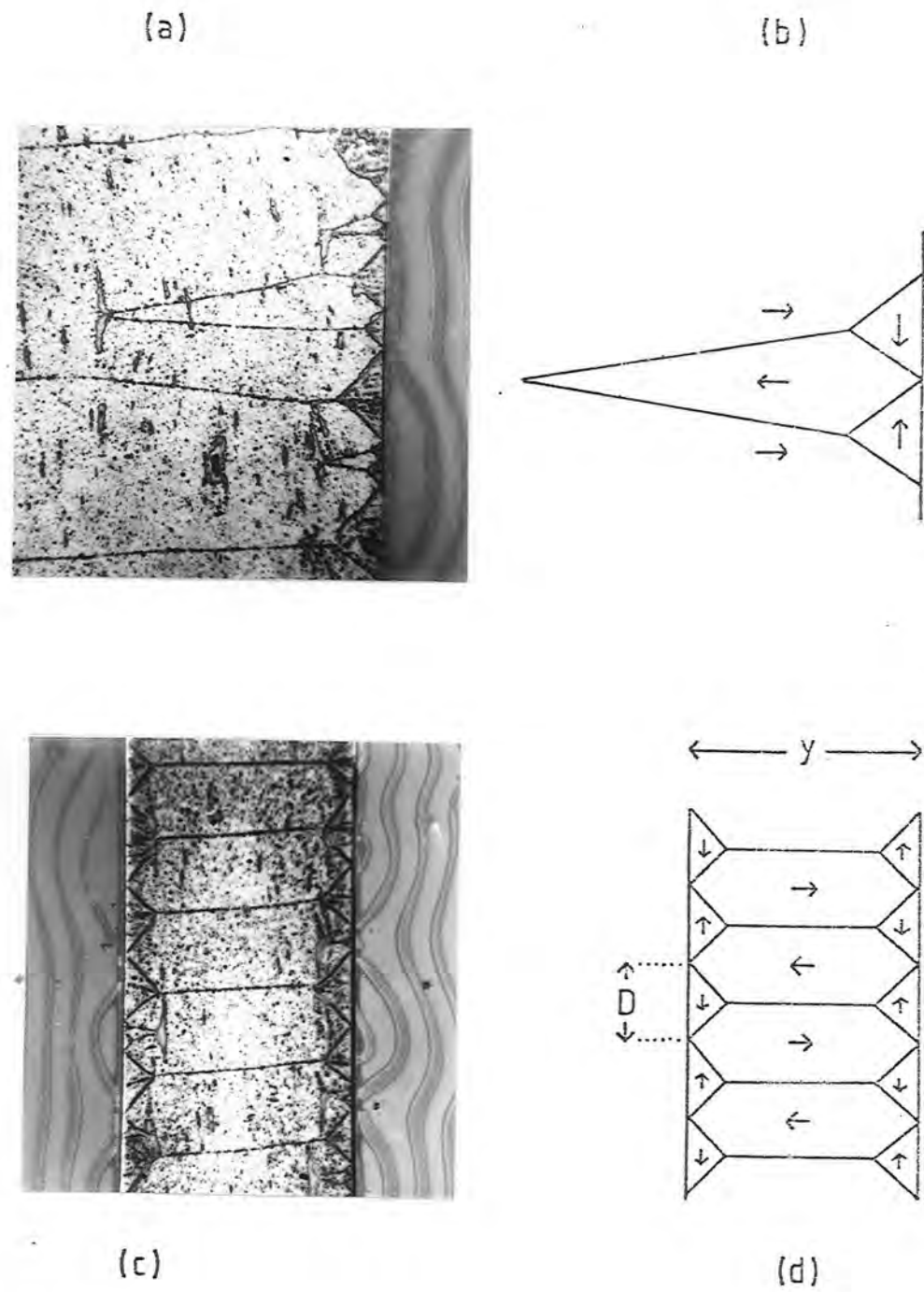


Fig. 6.7 (a) Closure domain structures in thin film permalloy
 (b) Theoretical structure predicted by Landau and Lifshitz (1955) for a uniaxial material. (c) Closure domains in a bar perpendicular to the easy axis. (d) Idealized domain pattern.

$$D_0 = \left[\frac{2 F_{180^\circ} y}{K_1} \right]^{\frac{1}{2}} \quad (6.6)$$

In fact the sample contains several bars with this type of domain structure and a range of widths from 6.2 to 19.3 μm . The wall spacing D_0 was estimated for each bar from colloid patterns. In fig. 6.8 the value of D_0 is plotted against $y^{\frac{1}{2}}$. The graph confirms a linear relationship between D_0 and $y^{\frac{1}{2}}$ even though the bars are subjected to the stray fields from the garnet layer, a factor which was ignored in the preceding calculation. The best fit to the data points gives a gradient of $2.41 \times 10^{-3} \text{ m}^{\frac{1}{2}}$.

$$\therefore \frac{2F_{180^\circ}}{K_1} y^{\frac{1}{2}} \simeq 2.41 \times 10^{-3}$$

substituting $F_{180^\circ} = 3.1 \times 10^{-3} \text{ Jm}^{-2}$ and $M_S = 8 \times 10^5 \text{ Am}^{-1}$ gives:

$$B_K = \frac{2K_1}{M_S} \simeq 2.7 \times 10^{-3} \text{ Tesla}$$

So the domain structures in larger areas of permalloy are consistent with an overall degree of anisotropy which would be sufficient to modify T- and I- bar elements according to equation 6.5.

6.4 Domain Structures in 16- μm period overlays.

Some features of the domain structures which occur in overlays of the type used in more recent devices will now be discussed together with their behaviour in applied fields.

Fig. 6.9 shows typical colloid deposits on 16- μm period asymmetric chevron elements and I-bars in zero applied field. The bars generally contain 180° walls and occasional closure

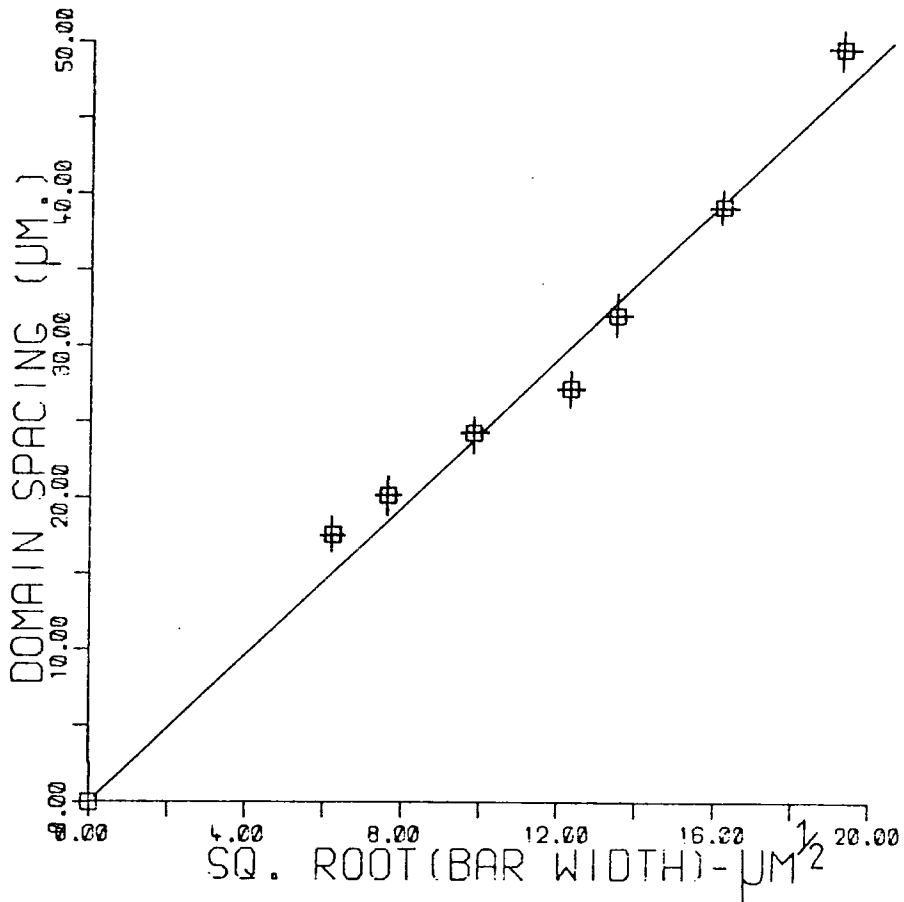


fig. 6.8 Domain spacing (D_0) versus square root of bar width ($y^{1/2}$) for rectangular strips of permalloy.

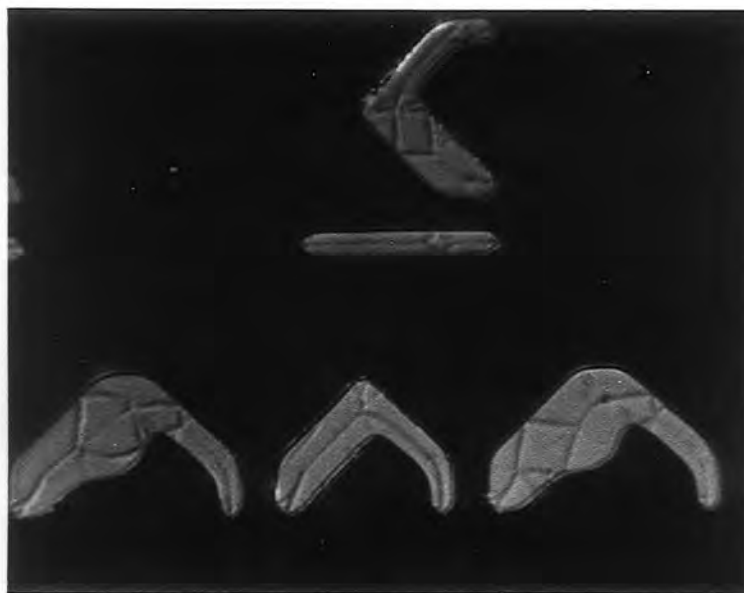


Fig. 6.9 Ferrofluid patterns showing typical remanent domain structures in asymmetric chevrons on non-magnetic garnet. Elements on bubble garnet show similar structures.

domains as observed in larger rectangular bars by previous workers. However on this scale of fabrication (bar width approximately $2.1\mu\text{m}$) the corners of elements are generally rounded off because of the limitations of optical lithography. The result is that triangular closure domains like those observed in iron whiskers do not always form at the ends of an element. Khaiyer and O'Dell (1975) reported the same effect in bars $8\mu\text{m}$ wide. Instead of a closure domain there can be a smooth transition with magnetization rotating parallel to the edge of the permalloy. It is easy to show that this configuration is energetically favourable by comparing the total energy of the two structures illustrated in fig. 6.10. If the bar edge is taken to be a perfect semicircle then it seems reasonable to assume the following distribution of \vec{M} for fig. 6.10(b)

$$\vec{M}(x,y) = (M_S \cos\theta, -M_S \sin\theta)$$

using the coordinates defined in the diagram. Since this satisfies $\vec{\nabla} \cdot \vec{M} = 0$ and there is no component of magnetization normal to the external surface there is no magnetostatic energy involved. According to equation 2.3 the exchange energy density of the structure is given by:

$$E_{\text{ex}}(x,y) = A \left[(\vec{\nabla}\alpha_1)^2 + (\vec{\nabla}\alpha_2)^2 + (\vec{\nabla}\alpha_3)^2 \right]$$

where A is the exchange constant and $\alpha_1, \alpha_2, \alpha_3$ are the direction cosines of magnetization. In this case:

$$\alpha_1 = y(x^2+y^2)^{-\frac{1}{2}}$$

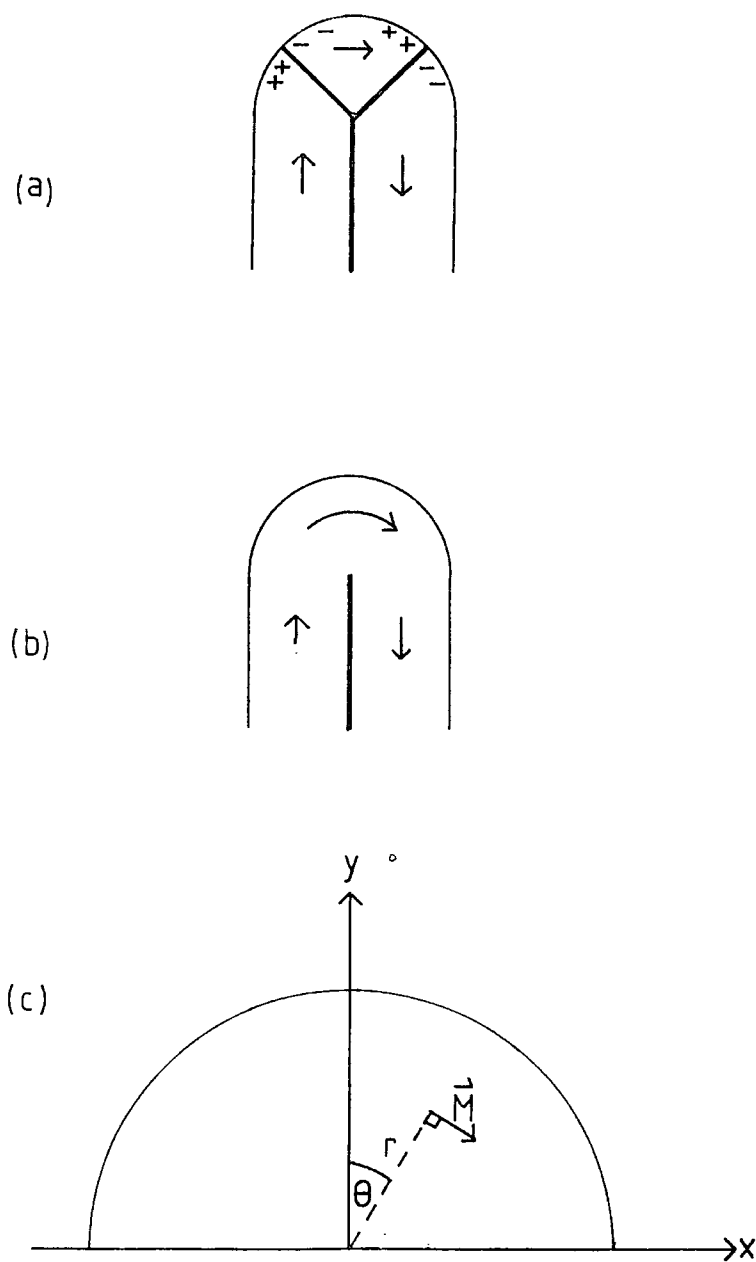


Fig. 6.10 Two alternative configurations for the reversal of magnetization in a permalloy bar. The coordinates used for estimating the exchange energy of configuration (b) are shown in (c).

$$\alpha_2 = x(x^2+y^2)^{-\frac{1}{2}}$$

$$\alpha_3 = 0$$

Substituting these values gives:

$$E_{\text{ex}}(x,y) = A(x^2+y^2)^{-1}$$

$$\text{or } E_{\text{ex.}}(r,\theta) = \frac{A}{r^2}$$

If the permalloy is assumed to have thickness t the total exchange energy is:

$$F_{\text{ex.}} = \int_{r_0}^R \int_{-\frac{\pi}{2}}^{\frac{\pi}{2}} \frac{A}{r^2} t \, dr \, d\theta$$

$$= At\pi \log_e \left(\frac{R}{r_0} \right) \quad (6.7)$$

The finite lower limit, r_0 , is taken in order to exclude a singularity at the origin. The value of r_0 is not immediately apparent but in the limiting case it can be no smaller than the spacing between two adjacent atomic moments so let $r_0 \hat{=} 3\overset{0}{\text{A}}$. Taking $R \hat{=} 1\mu\text{m}$, $t = 0.4\mu\text{m}$ and $A \hat{=} 10^{-11}\text{Jm}^{-1}$ gives $3.2 \times 10^{-17}\text{J}$ for the total energy. The alternative closure domain possesses both wall energy and magnetostatic energy since there are non-zero components of magnetization normal to the edge of the bar. The wall energy is simply:

$$E_w = 2RtF_{90^\circ}$$

$$\hat{=} 1.2 \times 10^{-15}\text{J}$$

The magnetostatic contribution is difficult to estimate since the demagnetizing field is non-uniform. However even without this positive contribution it is evident that the energy of structure 'b' is at least an order of magnitude less than the energy of the closure domain.

Rotation of magnetization is also evident in asymmetric chevron elements. Fig. 6.11 is an interpretation of the most commonly occurring domain structures in these elements. In 32 μ m-period overlays it was found that anisotropy played an important part in determining the demagnetized state. In 16 μ m-period patterns no examples of bars filled with closure domains were found however there is some correlation between the easy axis direction (obtained from hysteresis measurements on permalloy films before processing) and the distribution of elements of types 'a', 'b' and 'c' in fig. 6.11. This effect is illustrated in fig. 6.12. Similar domain configurations were observed in permalloy elements on magnetic garnet substrate suggesting that the stray fields associated with the bubble medium play a very minor role in determining domain structure.

6.5 Magnetization by reversible wall movement.

In low fields asymmetric chevron elements respond by reversible wall movements. Fig. 6.13 shows how the colloid pattern is modified by an applied field of 8.5 Oe. The central domain wall is displaced to one side. If the directions of magnetization within domains are assumed to remain constant during this process then the net component of magnetization can be estimated from wall displacement. Wall displacement was measured from a series of colloid patterns in which the applied field

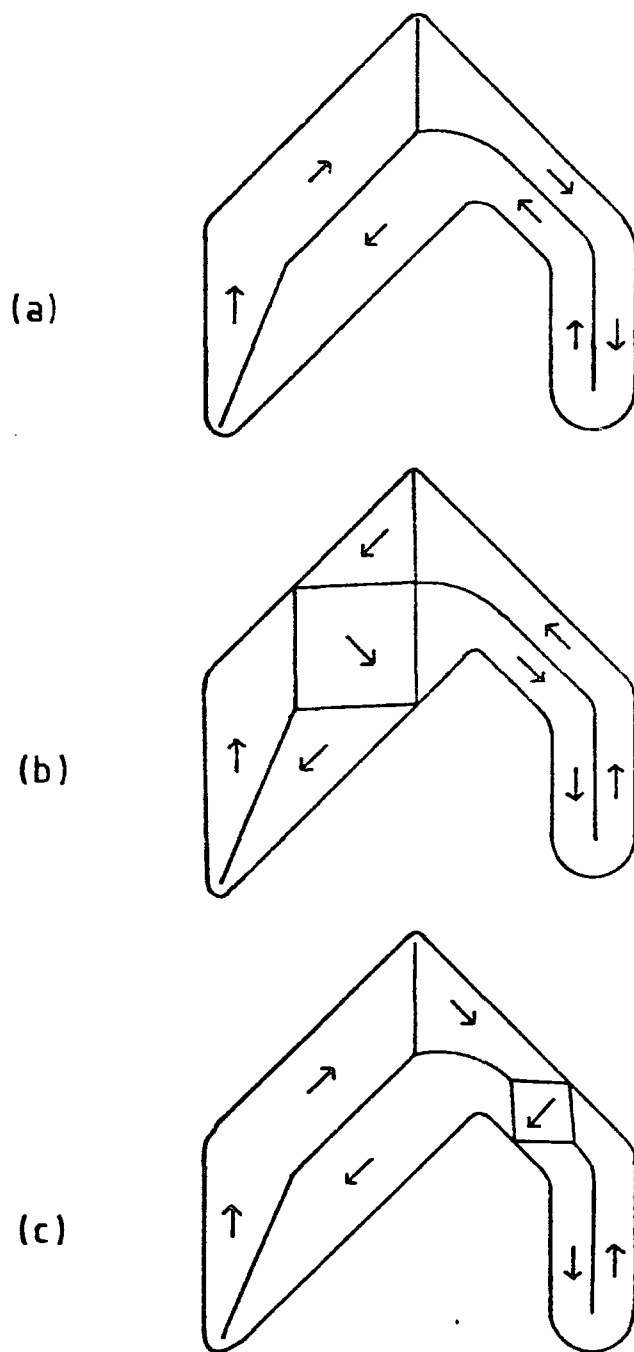


Fig. 6.11 Commonly occurring domain configurations in asymmetric chevron elements.



↙ Preferred axis for magnetization (B-H loop)

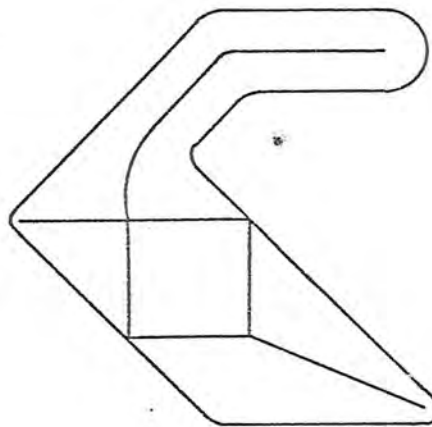


Fig. 6.12 In some samples there is correlation between the anisotropy measured from B-H loops and the distribution of closure domains.



→
8.5 Oe.

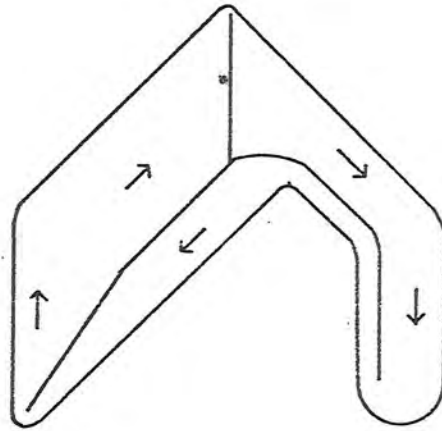


Fig. 6.13 Asymmetric chevrons respond to 'weak' in-plane fields by reversible domain wall movement.

varied between ± 20 Oe. Beyond these limits the position of the wall is difficult to determine since there is considerable loss of contrast. Maximum wall contrast is observed in zero applied field when the only sources of field which can modify the ferrofluid density are the strips of free pole formed above domain walls. Measured magnetization curves for samples 0.3 and 0.45 μm thick are plotted in fig. 6.14. The elements exhibit a linear response as observed in I-bars by Lin (1972) and by Khaiyer and O'Dell (1975). When the applied field is removed the wall returns to its central position and no displacement can then be measured within the limits of resolution. The conclusion is that in the 'low field' region the coercivity and remanence are comparable with the values measured in the permalloy films before processing. (Hysteresis measurements gave $H_c = 1.05$ Oe for the complete 0.3 μm thick film and 0.9 Oe for the 0.45 μm film.)

For each set of data points in fig. 6.14 a straight line passing through the origin provides a good fit. Because of the errors involved in measuring wall displacements below 1 μm it is difficult to establish whether there is a significant difference in gradient between the two magnetization curves. However on the basis of a least squares fit, the thinner sample would appear to approach saturation more rapidly. The dependence of demagnetizing fields on thickness in thin film elements will be discussed later. If the linear behaviour is assumed to continue beyond the region of observation then extrapolation suggests that the 0.3 μm and 0.45 μm elements will saturate at 37.1 Oe and 46 Oe respectively. The actual behaviour of gap-tolerant propagation elements in fields up to and beyond saturation will be described later.

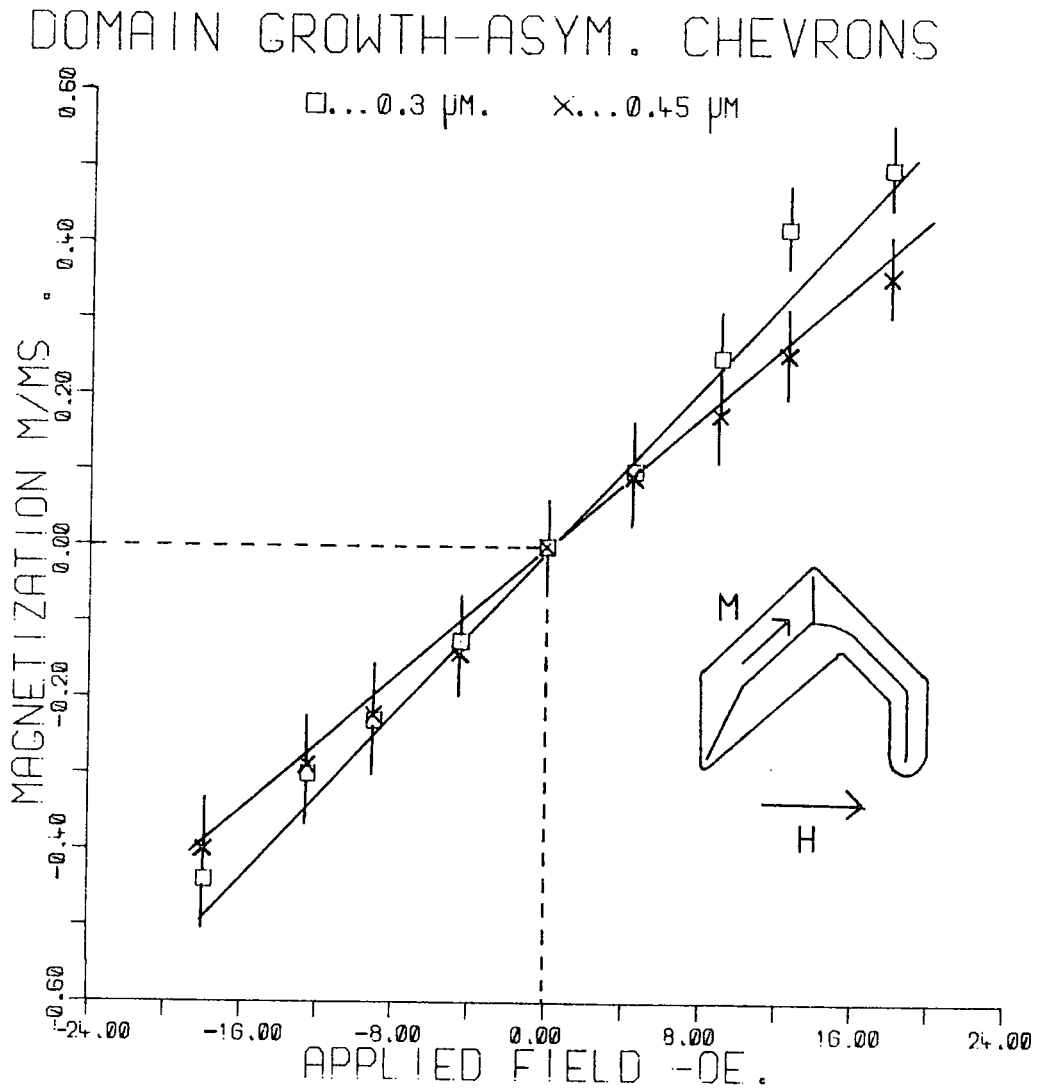


Fig. 6.14 Magnetization versus applied field (from ferrofluid observations) in asymmetric chevrons 0.3 μm thick and 0.45 μm thick.

6.6 Magnetization processes involving saturation and hysteresis.

Demagnetized overlay elements usually have simple domain wall structures which respond to weak applied fields by reversible wall motion. Most theoretical models for permalloy bars assume a well behaved linear response to applied fields. This assumption is supported by the observations of the previous section however it has been found that partial saturation may occur if the applied field is sufficiently strong. In general this seems to lead to the formation of remanent states and hysteresis, phenomena which may have a considerable effect on the operation of an element. Even when the remanence is removed, irreversible changes in domain structure may be discovered.

Although similar effects have been seen in large rectangular samples of permalloy they have not been reported before for $16\mu\text{m}$ -period overlay elements. A variety of elements was studied here, including I-bars, T-bars, 'Pick-axe' elements, asymmetric chevrons and half-discs. A primary objective was to establish which elements would saturate and in what level of applied field. The dependence of saturation field on permalloy thickness and element geometry will be discussed. Some of the previous work on rectangular samples will be described first as several features of the domain behaviour in these specimens are also found in $16\mu\text{m}$ -period overlays.

6.6.1 Magnetization process in large rectangular permalloy bars.

Huijer et al. (1978) studied domain structures in $100 \times 12 \times 0.3 \mu\text{m}^3$ bars using Bitter technique observations and small spot Kerr effect measurements. They found that two types of domain configuration predominated in the demagnetized bars, (illustrated in

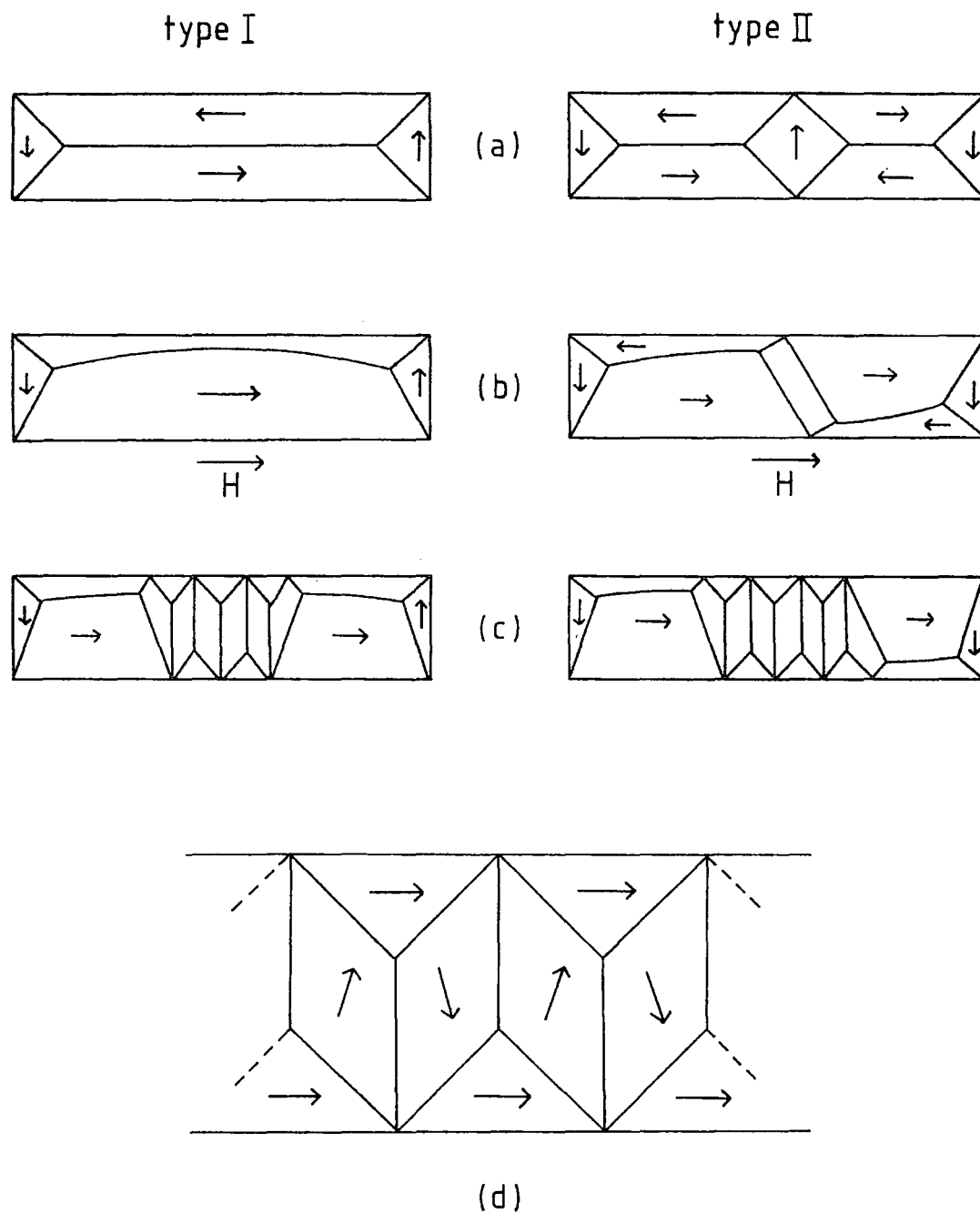


Fig. 6.15 (a) Type I and type II remanent domain structures in rectangular bars $100 \times 12 \times 0.3 \mu\text{m}$ (Huijjer et al., 1979) and (b) their response to in-plane fields. (c) shows the remanent states following partial saturation. An interpretation of the 'buckled' section is given in (d).

fig. 6.15(a)). Fig. 6.15(b) shows how the bars respond to a field applied along the bar axis. It turns out that the distributions of average magnetization along the bar (as measured by the Kerr effect) are very similar for type I and type II bars. This suggests that the actual domain structure has no significant influence on the overall magnetic response (Huijer et al. (1980)).

In a different study, Huijer et al. (1979) reported that when the field was raised to a critical value, H_g (approximately 7.5 Oe.) the Bloch wall reached the edge of the bar and the internal closure domain collapsed. On reducing the field a remanent state was found containing many transverse walls, as illustrated in fig. 6.15(c). The original domain structures were restored only by reducing the applied field to zero or in some cases applying a small reverse field. It was found in type II elements that the internal closure domain could return at a different location but that the 'type' of structure was preserved. This is because an extremely large field would be required to change the orientation of magnetization in the end closure domains. A type I bar has antiparallel orientation in these domains and a type II bar has a parallel orientation.

The remanent state results from edge annihilation of the domain walls and consequently the proportion of the bar occupied by transverse walls increases as the amount by which H exceeds H_g . A simple model was established for the remanent structure based on the assumption $\vec{\nabla} \cdot \vec{M} = 0$ in the middle of the bar (see fig. 6.15 (d)).

Kryder et al. (1980) observed similar structures whilst studying the reversal of magnetization in narrow permalloy strips. However in these specimens the initial state was one of longitud-

inal saturation (the permalloy thickness ranged from 1800A down to 300A). On the basis of ferrofluid observations, high coercivity was explained in terms of a 'buckling' of magnetization perpendicular to the length of the stripe. The structure of transverse walls in this state is essentially the same as in fig. 6.15(d).

Kryder et al. developed a model for buckling which is best explained in terms of the sequence of idealized magnetization configurations shown in fig.6.16. In a weak reverse field (10e. for a sample $100\mu\text{m} \times 6.4\mu\text{m} \times 300\text{A}$) magnetization ripple occurs causing a pattern of alternating magnetic poles to form along the edges of the stripe (fig.6.16(b)). The stray fields arising from this pole distribution act in alternate half-wavelengths of the ripple to oppose or support the direction of average magnetization. Increasing H strengthens the ripple to the point where stray fields are large enough to 'pin' triangular closure domains parallel to the original direction of saturation. (fig6.16(c)). In the alternate half wavelengths only narrow domain walls form because the stray fields oppose the average magnetization.

Kryder et al. obtained estimates for the total magnetic energy of the buckled state. This is a sum of applied field, anisotropy exchange and magnetostatic stray field components. The total energy was found to have a minimum with respect to the ripple wavelength, λ , when λ is approximately equal to the stripe width, W. This agreed with the experimental observations. Although these calculations were performed numerically for the particular samples they used, Kryder et al. predicted that the condition $\lambda \approx W$ in the buckled state should hold for thicker samples also.

Fig 6.17(a) and(b) shows two ferrofluid patterns on permalloy strips $25\mu\text{m}$ wide and $0.4\mu\text{m}$ thick deposited on bubble

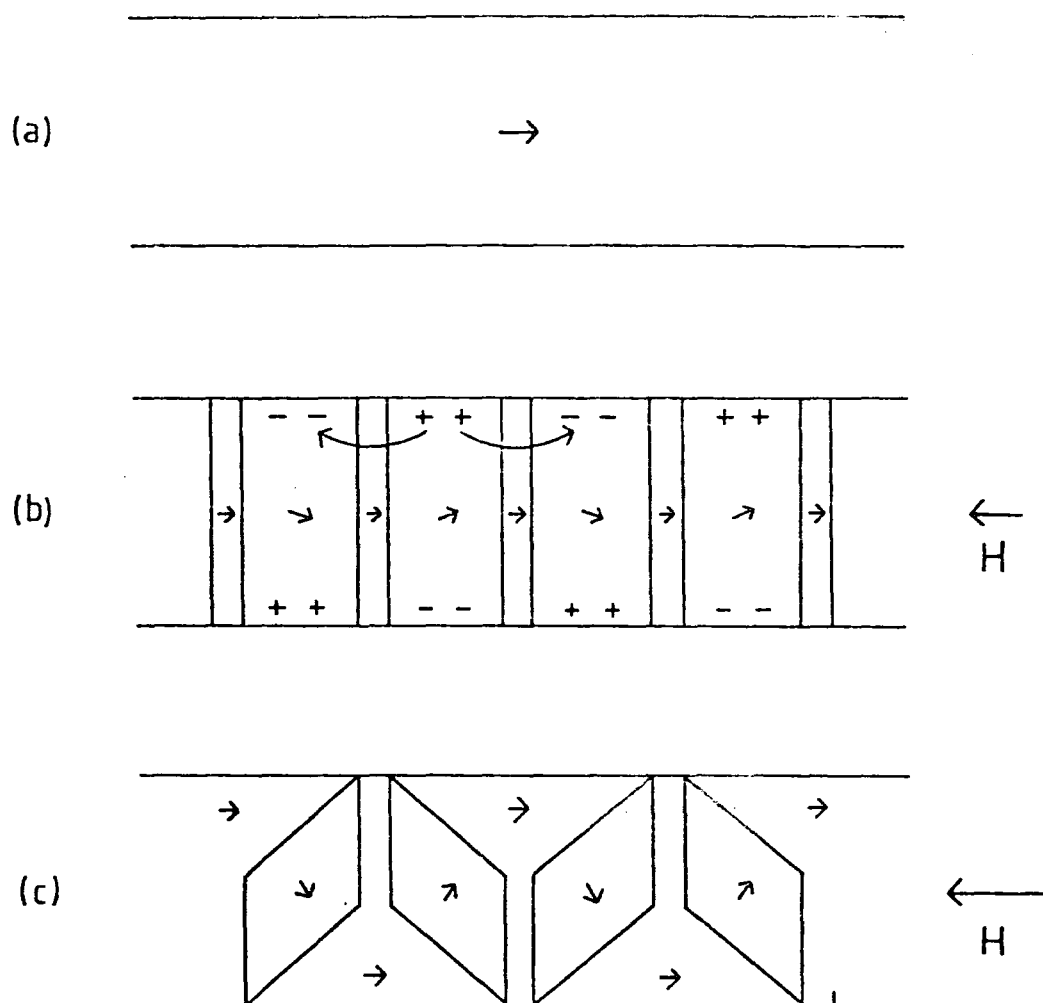


Fig. 6.16 Model explaining the formation of magnetization buckling (Kryder et al., 1980). (a) saturated bar. (b) ripple leads to stray fields which cause triangular closure domains to form (c).

garnet substrate. The strip shown in (a) illustrates a commonly occurring demagnetized state but strip(b) shows a buckled domain pattern resulting from the application of a longitudinal saturating field. (Both photographs were taken in zero field). Although the spacing of walls is far from regular (due probably to the stray fields of the garnet layer) the type of structure is identical to that illustrated in fig6.15(d).

Buckling occurs quite generally following saturation in these samples. However in a few cases the remanent state was found to differ from those reported by Huijer et al. and Kryder et al.. The domain patterns shown in fig6.17(c) and(d) are examples. Again the structure consists of transverse domains, the interpretations given (which assume that domains at the edge of the bar are magnetized parallel to the edge and $\nabla \cdot \vec{M} = 0$.) suggest a net component of magnetization along the strip, but comparison with fig6.16 reveals additional triangular closure domains along the edge of the strip.

On the basis of Kryder's model it would seem feasible that these alternative structures could occur in thicker permalloy films. Referring back to fig. 6.16 the stray fields caused by ripple act so as to form the large triangular domains in alternate half wavelengths but in the remaining half wavelengths the stray fields oppose the average direction of magnetization. In these positions walls alone formed in the samples studied by Kryder et al. (1980). In a thicker film the stray field could nucleate a small triangular closure domain instead. In the model of Kryder et al. the stray field energy component, E_m , is proportional to t^2 where t is the film thickness. All other components are proportional to t . Therefore in the samples studied here where

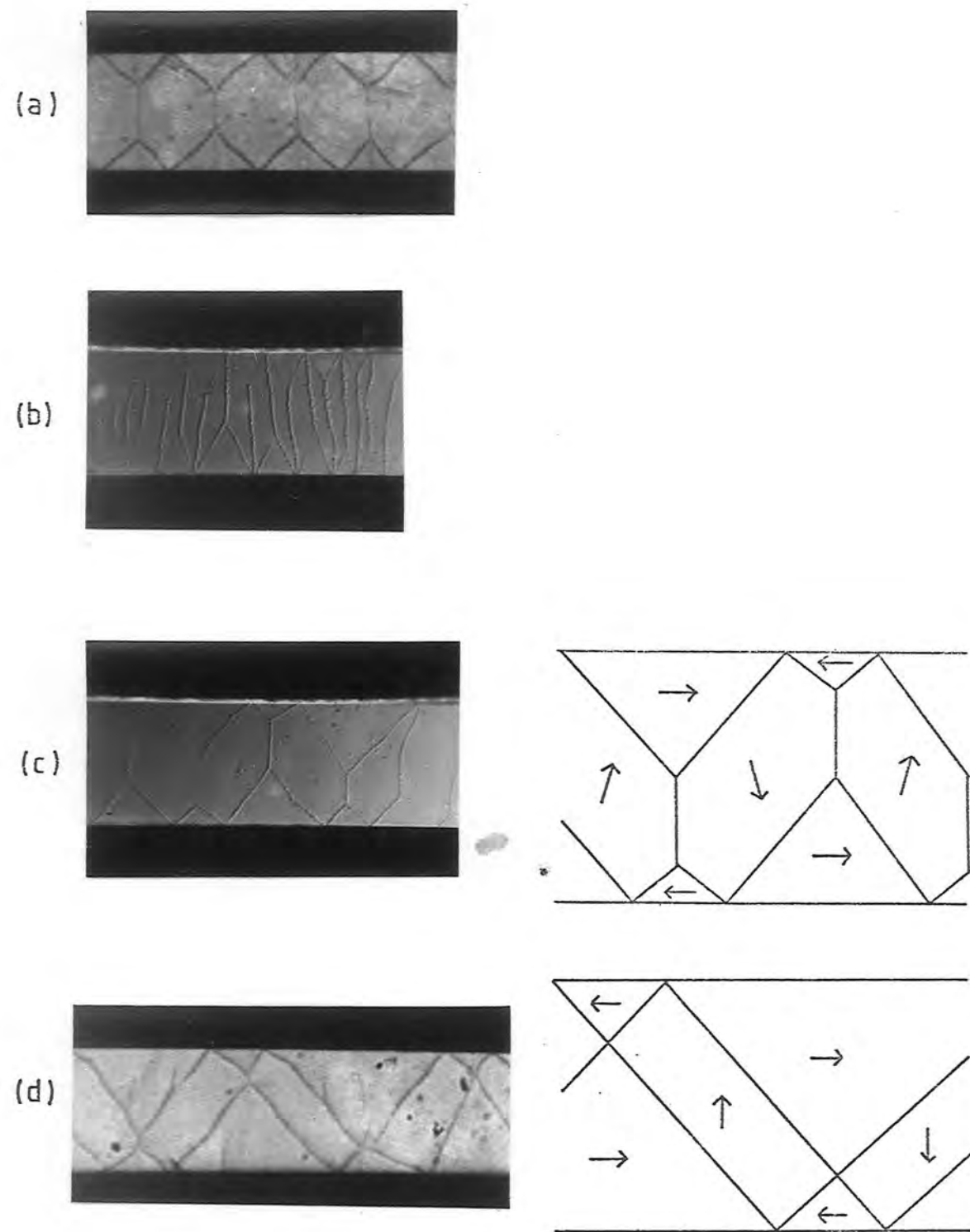


Fig. 6.17 Domain patterns in strips of permalloy 25 μm wide.
 (a) Demagnetized state. (b) Remanent buckled state. (c) and (d) Remanent structures with additional closure domains.

t is 4000\AA as opposed to 300\AA , E_m will certainly be dominant. For thin permalloy more detailed information on the processes of magnetization reversal in strips can be gained by using Lorentz microscopy rather than ferrofluid. In such a study Herd et.al. (1979) observed magnetization reversal in strips 2 to $30\mu\text{m}$ wide and with thicknesses: 300\AA , 450\AA and 600\AA . For the 600\AA film a series of micrographs demonstrates that a remanent buckled state similar to fig 6.17(b) makes a transition to a state similar to fig 6.17(c) when a reverse field of $1.50e$ is applied.

6.6.2 Saturation and hysteresis in overlay bars.

Examples of magnetization buckling in overlay elements will now be given. The simplest element to consider is the I-bar, still used to a limited extent in circuits. Plessey $16\mu\text{m}$ -period circuits contain I-bars with approximate dimensions $15 \times 2.1\mu\text{m}$ and $25 \times 2.1\mu\text{m}$.

Fig. 6.18(a) shows the demagnetized domain structure in a $25 \times 2.1\mu\text{m}$ bar. By reference to the work of Huijer et al. (1978) this would correspond to a type I bar consisting of a single magnetic circuit. In weak applied fields the element magnetizes by reversible flexing of the 180° wall. However, following the application of a longitudinal field of $17.90e$, a buckled configuration results (fig 6.18(b), zero field). The central portion of the bar contains transverse domain walls and the 180° walls remaining on either side are clearly displaced from centre. The bar has a remanent magnetization in zero field.

This state was found to persist in fields applied perpendicular to the bar axis up to and above the level of field used in a device ($400e$). When a reverse field of $2.10e$ is applied along the

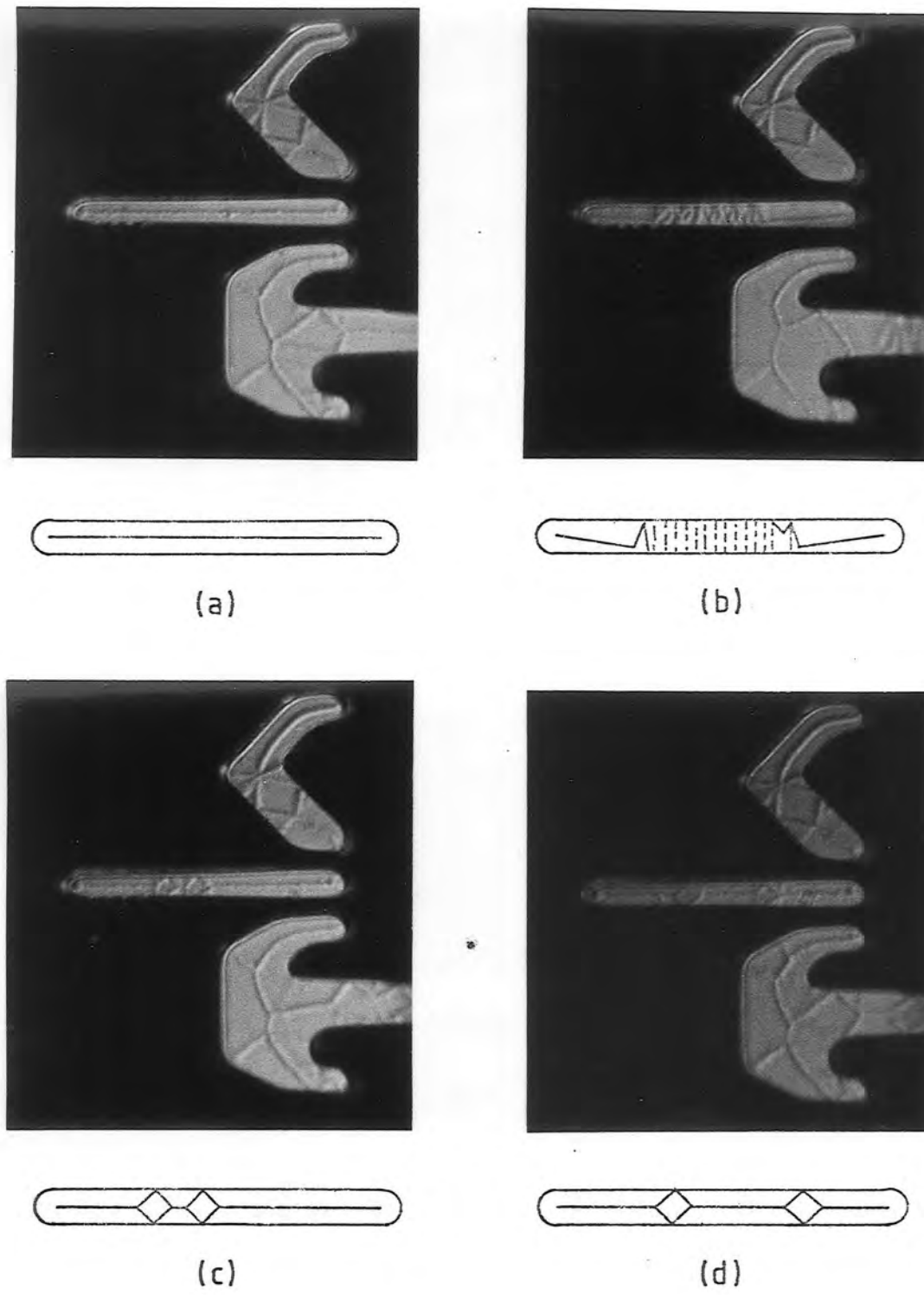


Fig. 6.18 Sequence of domain structures in a $25 \times 2.1 \times 0.35 \mu\text{m}$ bar. (a) Demagnetized state. (b) Buckled state following saturation. (c) and (d) Closure domain pairs formed following subsequent saturations.

bar axis the ferrofluid pattern suddenly breaks and the configuration of fig. 6.18(c) is formed. The bar is once more demagnetized but there are now two internal closure domains in the region previously occupied by buckle. From this state the bar may again be partially saturated by fields $H \gg H_g$ applied in either direction along the bar axis. H_g is approximately 15.5 Oe for the bar in question. The reverse field required to break the remanence is generally a few Oe. Following saturation the bar may return to a single wall state or to a state containing two internal closure domains. Fig 6.18(d) shows such a state following a subsequent saturation. Exceptionally a bar may contain four closure domains following remanence.

It was also found that bars which initially contained a single closure domain (corresponding to type II bars in Huijer's classification) could be partially saturated by essentially the same magnitude of field, H_g . This seems to confirm the conclusion of Huijer et al. (1980) that the magnetostatic response does not vary significantly between type I and type II bars. After each saturation and demagnetization it was observed that type II bars could contain one or three closure domains.

The conclusion to be drawn from these observations is that bars remain type I or type II (for the magnitude of field used in a device) even though the number of domains can change. In other words the directions of magnetization at each end of a bar are preserved (parallel or antiparallel) so closure domains are created or annihilated in pairs. This is illustrated in fig 6.19 for both types of bar.

That the buckled state represents a net magnetization is confirmed by the application of a uniform field. Fig. 6.20(a)

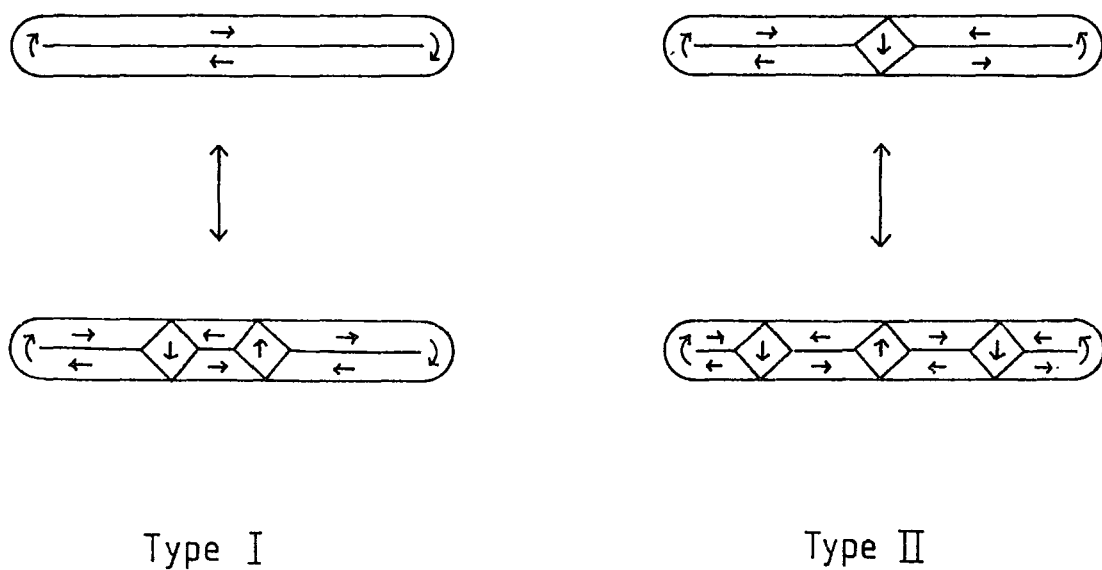


Fig. 6.19 Following partial saturation, irreversible changes can occur in the domain structure of permalloy bars. Closure domains can be created or annihilated in pairs.

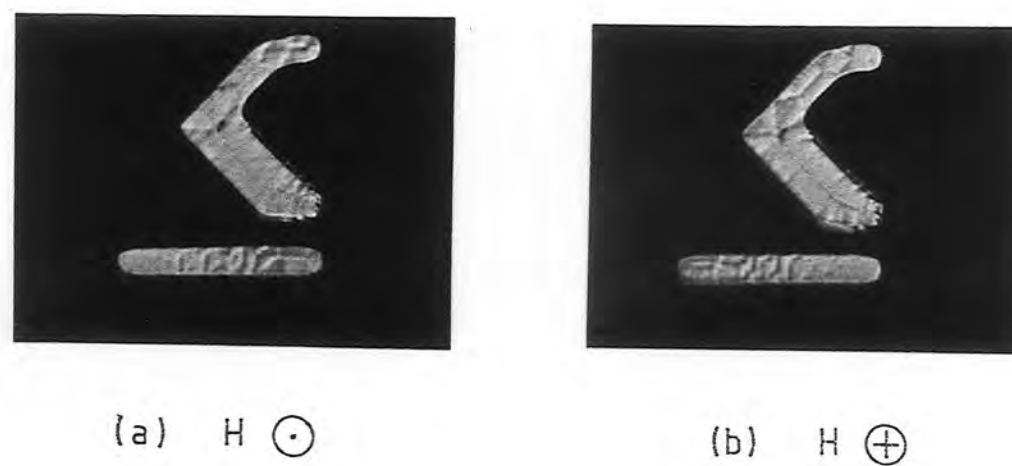


Fig. 6.20 Changes in the ferrofluid density above a bar subjected to alternate bias fields are consistent with remanent magnetization (following partial saturation). $H = 18 \text{ Oe}$.

shows the ferrofluid density above a $15 \times 2.1 \mu\text{m}$ bar which has been saturated by a field of 61 Oe. applied from left to right in the photograph. The bias field of 18 Oe is applied out of the plane resulting in an enhancement of particle density to the right of the bar. Fig 6.20(b) shows that the effect is reversed with the direction of bias field (now directed into the plane). Maxima in ferrofluid particle density correspond to maxima in the local field which is the vector sum of the uniform bias field and the non-uniform stray field of the bar. Thus the observed changes are consistent with a remanent magnetization.

6.6.3 Changes in Bloch Wall Structure.

Bloch walls within permalloy elements may be divided into sections with different spin structure as indicated in section 6.2. Lorentz microscopy has demonstrated that dynamic changes can occur in bubble wall structure in applied fields. Ferrofluid observations show that wall structure in permalloy bars may change under the influence of in-plane fields.

Fig. 6.21(a) and(b) shows the colloid pattern on a demagnetized bar with a bias field of 4.5 Oe directed alternately into and out of the plane. The domain wall consists of two Bloch segments separated by a Bloch line near the centre of the bar. For applied fields within the region of linear response it was found that no changes in structure could be detected. Fig. 6.21 (c) and(d) shows the same bar in alternate bias fields following partial saturation by a longitudinal field of 270 Oe. The intermediate buckled state was removed by a reverse field of 2.7 Oe. Although the domain structure is the same as in fig. 6.21(a) the 180° wall is a new wall formed after the collapse of the buckled

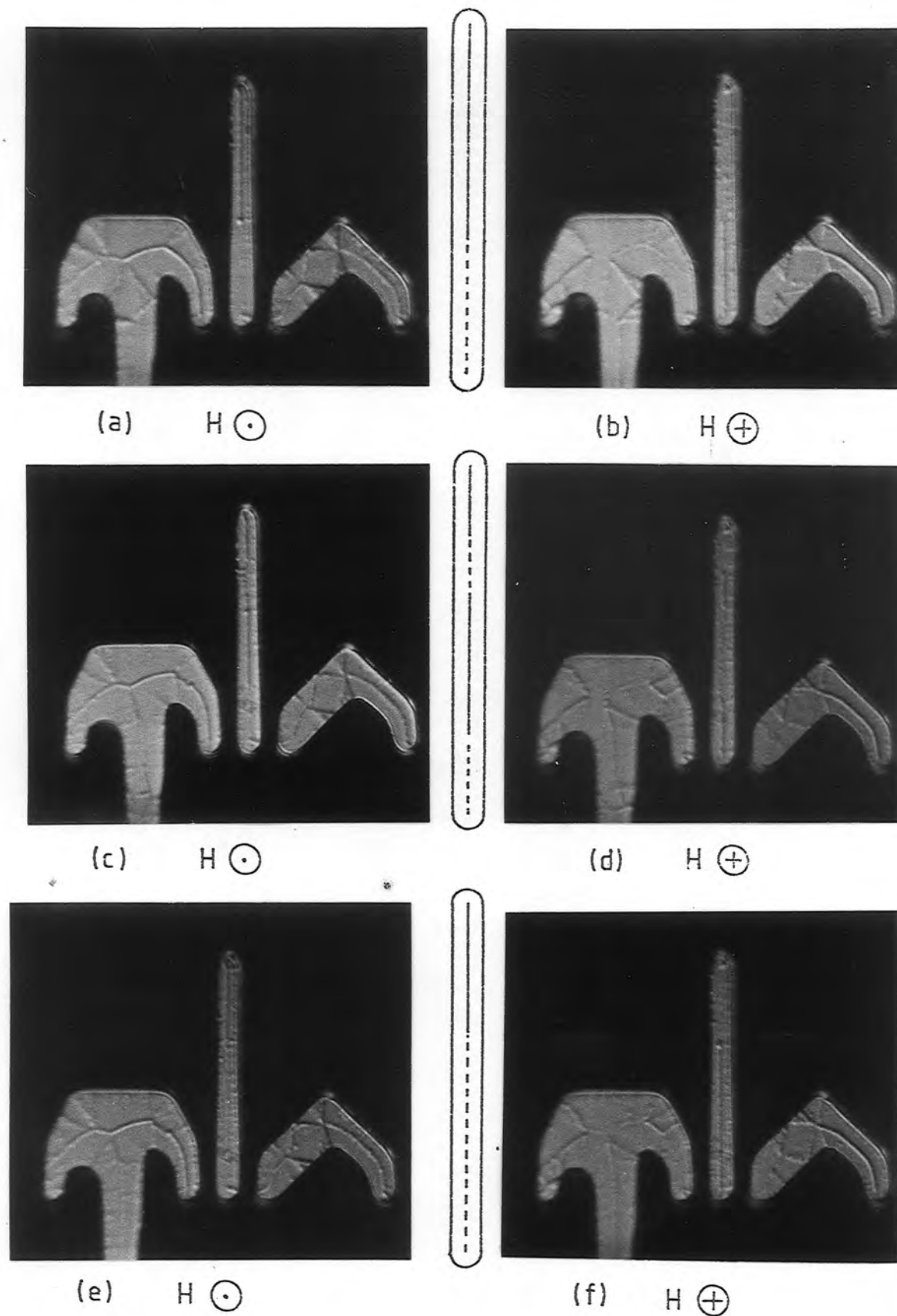


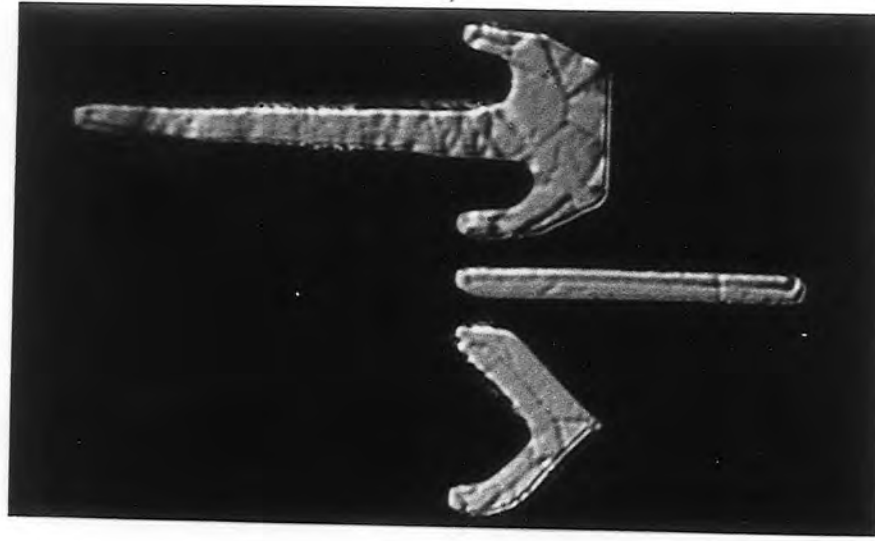
Fig. 6.21 Changes in the Bloch wall structure of a permalloy bar following partial saturation. Bias field $H = 4.5$ Oe.

state. This wall appears to contain four Bloch segments. After saturating the bar a second time the wall reverts to a state of two Bloch segments (fig. 6.21(e),(f).).

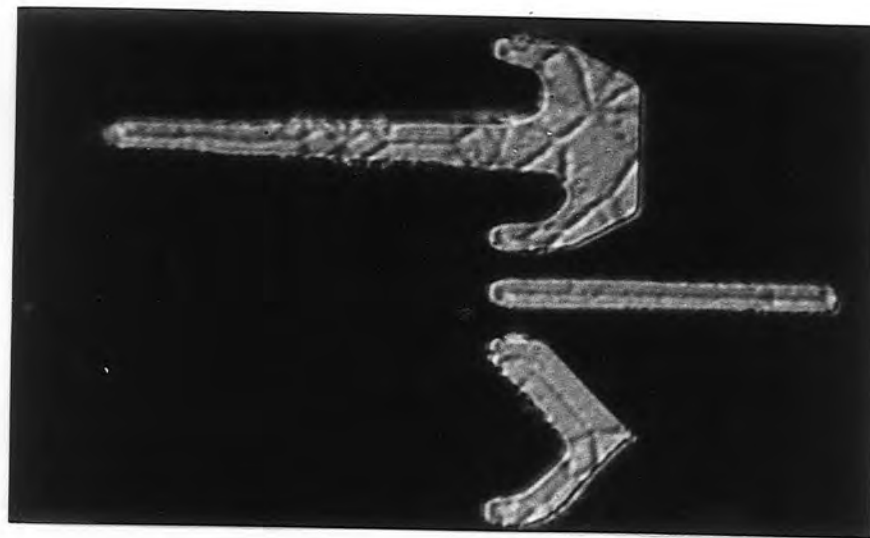
Figure 6.21 suggests that the wall structure near the ends of the bar remains the same. This might be expected since saturation only occurs over a central portion of the bar. If this is generally true then alterations of wall structure have to comply with a boundary condition similar to that which governs changes in the number of domains. In particular, Bloch lines will be created or annihilated in pairs.

6.6.4 Partial saturation in pick axe elements.

Having established that partial saturation occurs in simple bars more complex overlay elements were studied. Figure 6.22 shows a sequence of domain wall configurations in a 'Pick-axe' element and I-bar. Before applying fields to this sample it was found that both elements already possessed a remanent magnetization. Figure 6.22(a) shows magnetization buckle in the 'Pick-axe' and a Bloch wall in the I-bar which is displaced from the centre. However this type of remanence was only seen in one case as opposed to magnetization buckling. Both elements were demagnetized by applying a reverse field of 6 Oe as indicated in fig. 6.22 (b). The I-bar has type-I structure and a pair of closure domains is apparent in the middle of the pick-axe limb Fig. 6.22(c) demonstrates buckled states formed by an in-plane field of 48 Oe. By comparing this photograph with fig. 6.18(b) it is apparent that a much larger proportion of the bar is occupied by the buckled configuration after applying 48 Oe than after applying 17.9 Oe. This agrees with the observations of Huijser et al.

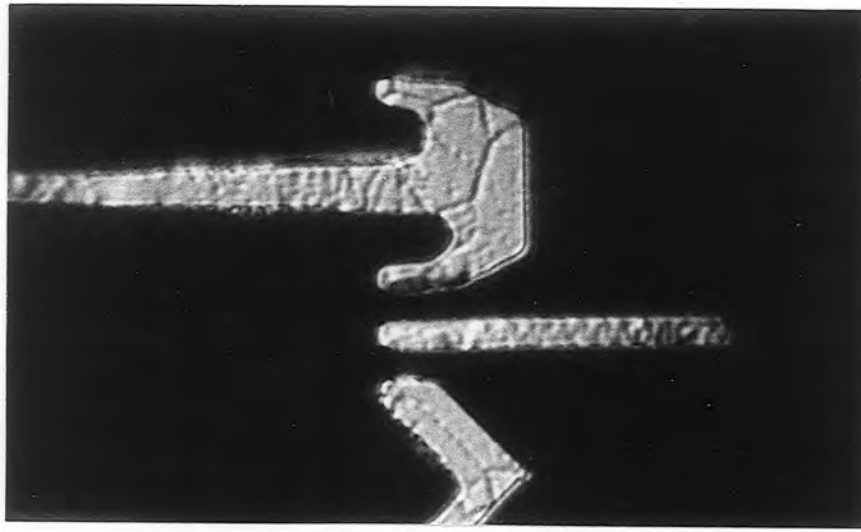


(a)

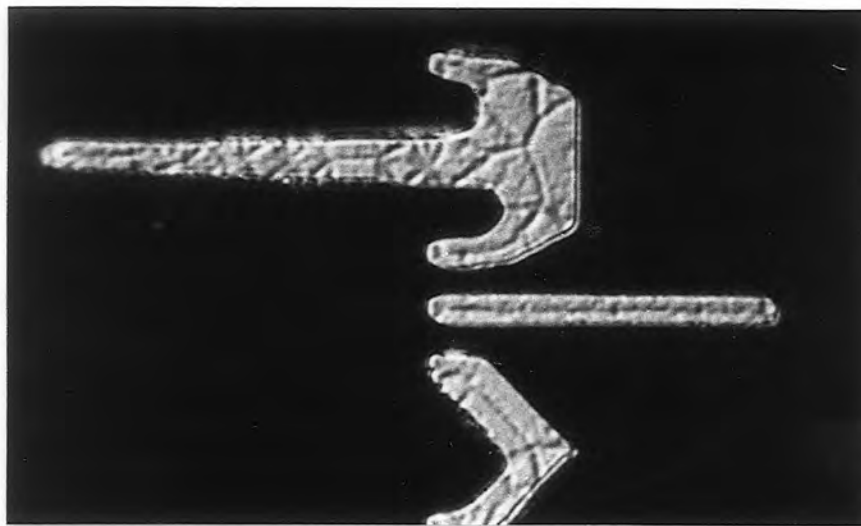


(b) ← Reverse field direction

Fig. 6.22 Sequence of domain configurations in pick-axe and I-bar elements. (a) Initial state (b) Demagnetized following the application of a small reverse field (6 Oe).



(c) \longleftrightarrow Field axis



(d)

Fig. 6.22 Continued. (c) Buckled states formed by saturation in a field of 48 Oe. (d) Elements demagnetized by a reverse field of 3 Oe.

(1979) in $100 \times 12 \times 0.3 \mu\text{m}$ rectangular bars. The length of Bloch wall which suffers edge annihilation increases with the magnitude of applied field. Finally, fig. 6.22(d) shows the same elements demagnetized by a reverse field of 3 Oe. The I-bar has returned to its initial state but the number of domains in the pick-axe has increased. This illustrates the fact that changes in domain structure similar to those found in type I and type II bars can also occur in more complex elements.

6.6.5 Partial saturation in gap tolerant patterns.

Figure 6.23(a) shows the ferrofluid pattern on a $16 \mu\text{m}$ period asymmetric chevron element in zero field following the application of a field of 48 Oe in the direction shown. A section of magnetization buckle has formed in the small chevron limb. When a reverse field of 0.5 Oe is applied the chevron returns to its demagnetized state consisting of a small number of domains (fig 6.23(b)). Irreversible changes in the large chevron limb require stronger fields. Fig. 6.23(c) shows a remanent state formed after the application of 77 Oe along the same direction. This has a region of buckle in the wide limb. This time the element demagnetizes when the reverse field reaches 2.5 Oe as shown in fig 6.23(d). Partial saturation can also be observed with fields applied parallel to the limbs of the chevron however saturation always occurs most readily in fields parallel to the propagation direction (creating magnetization buckle in the small limb). Again it was found that pairs of closure domains could be formed after partial saturation. With fields strong enough to saturate both limbs of the chevron it was observed that closure domain pairs could be formed with one

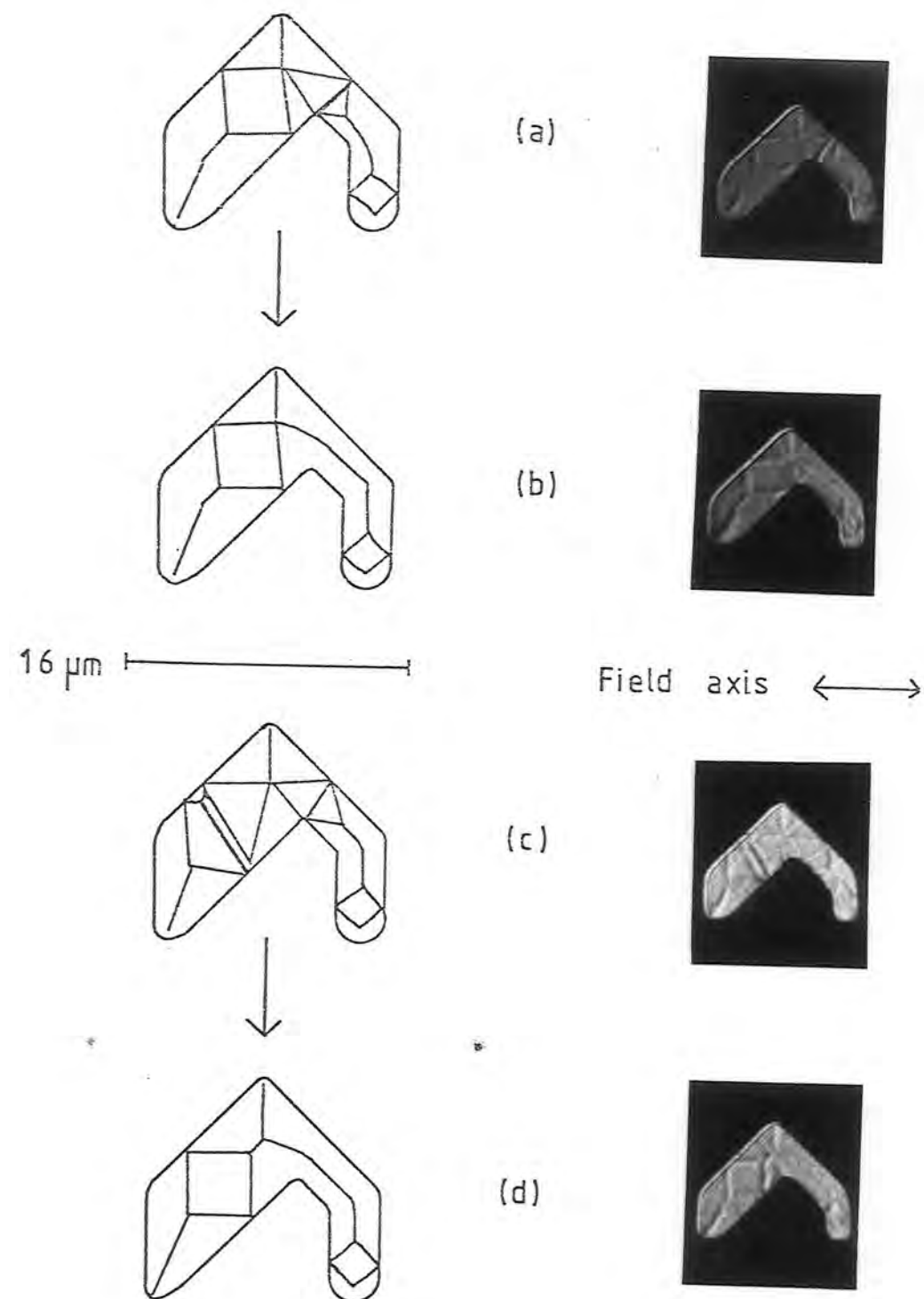


Fig. 6.23 Remanent states formed in asymmetric chevron elements (a) by a field of 48 Oe, (b) demagnetized by a reverse field of 0.5 Oe, (c) by a field of 77 Oe, (d) demagnetized by a reverse field of 2.5 Oe.

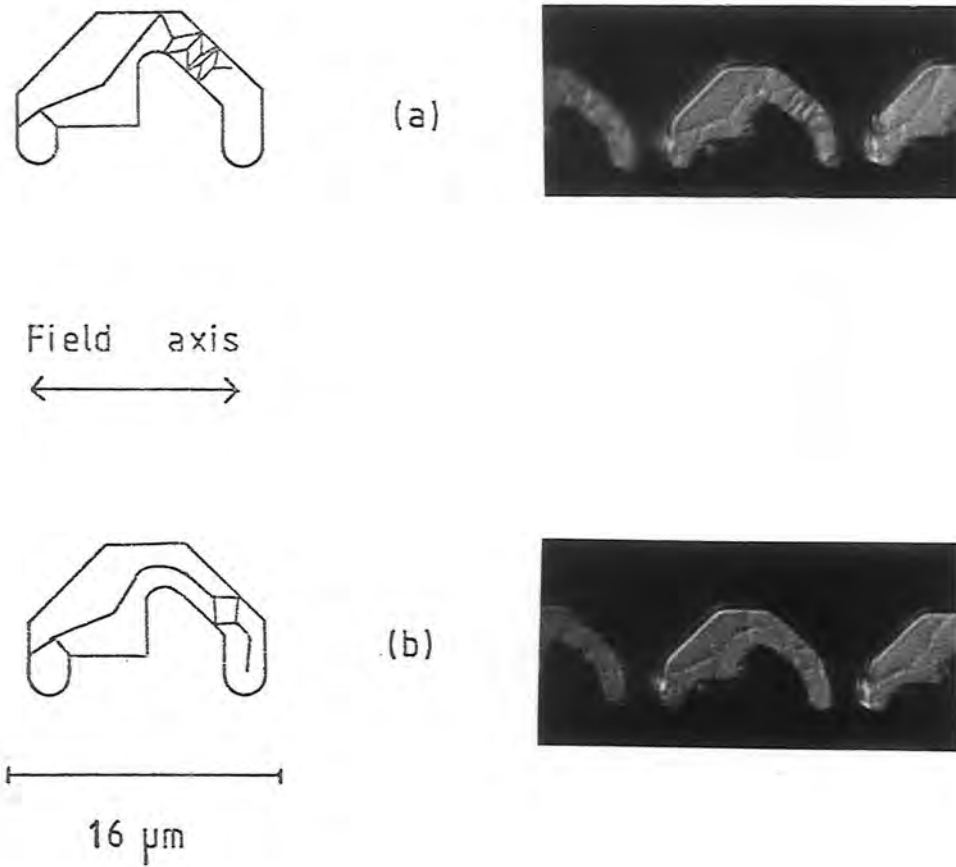


Fig. 6.24 (a) Typical magnetization buckling in an asymmetric 'half-disc' element. (b) Demagnetized by a reverse field of 5 Oe.

domain in each limb.

Partial saturation in asymmetric half-discs produces similar features. Again magnetization buckling occurs first in the smaller limb as illustrated by fig. 6.24(a). In this case the permalloy is deposited on magnetic garnet substrate and saturation occurs in fields of approximately 15 Oe. (It will be shown later that the presence of a bubble substrate reduces saturation fields)

6.7 Dependence of Saturation Field on Element Geometry and Thickness.

The minimum field required to partially saturate a given permalloy element can be estimated from a series of ferrofluid observations. For each element the applied field was gradually increased and then reduced to zero in order to observe whether remanent states had formed. This procedure was repeated several times, each time with a slightly higher maximum field until a remanent state was identified. This sequence was performed a number of times to obtain an average value of H_g . Wherever possible H_g was measured for two identical elements with orthogonal orientations on the same chip. The intention was to average out any effects due to in-plane anisotropy but in fact no correlation (within the accuracy of the measurements) could be found between H_g and the easy axis direction. Five types of element were studied on samples 0.3, 0.35, 0.4 and 0.45 μm thick. In fig 6.25 the saturation field for 25x2.1 μm and 15x2.1 μm bars is plotted against permalloy thickness. Although there are only four points for each element a straight line seems to provide a satisfactory fit to the data. As might be expected the lower

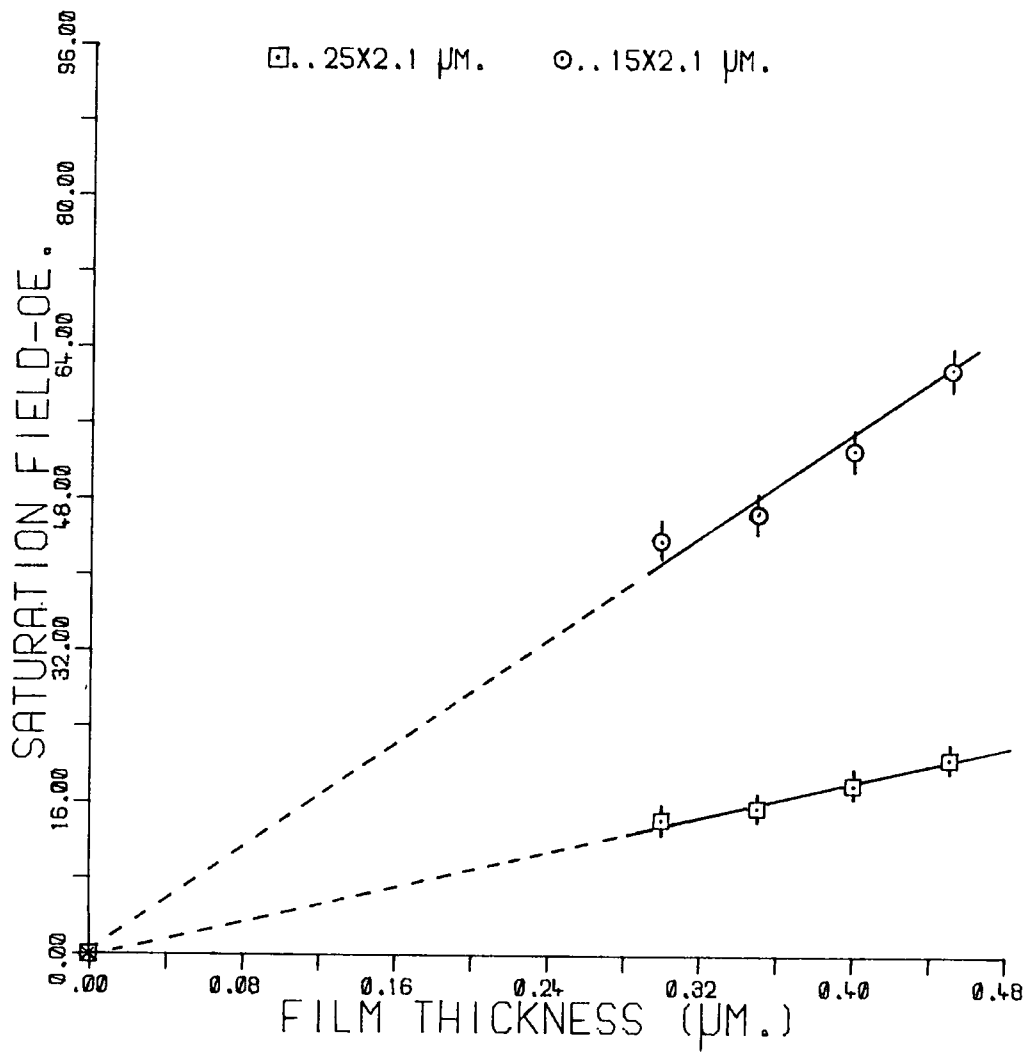


Fig 6.25 Field required for partial saturation (H_s)
 in I-bars 25X2.1 μm and 15X2.1 μm.

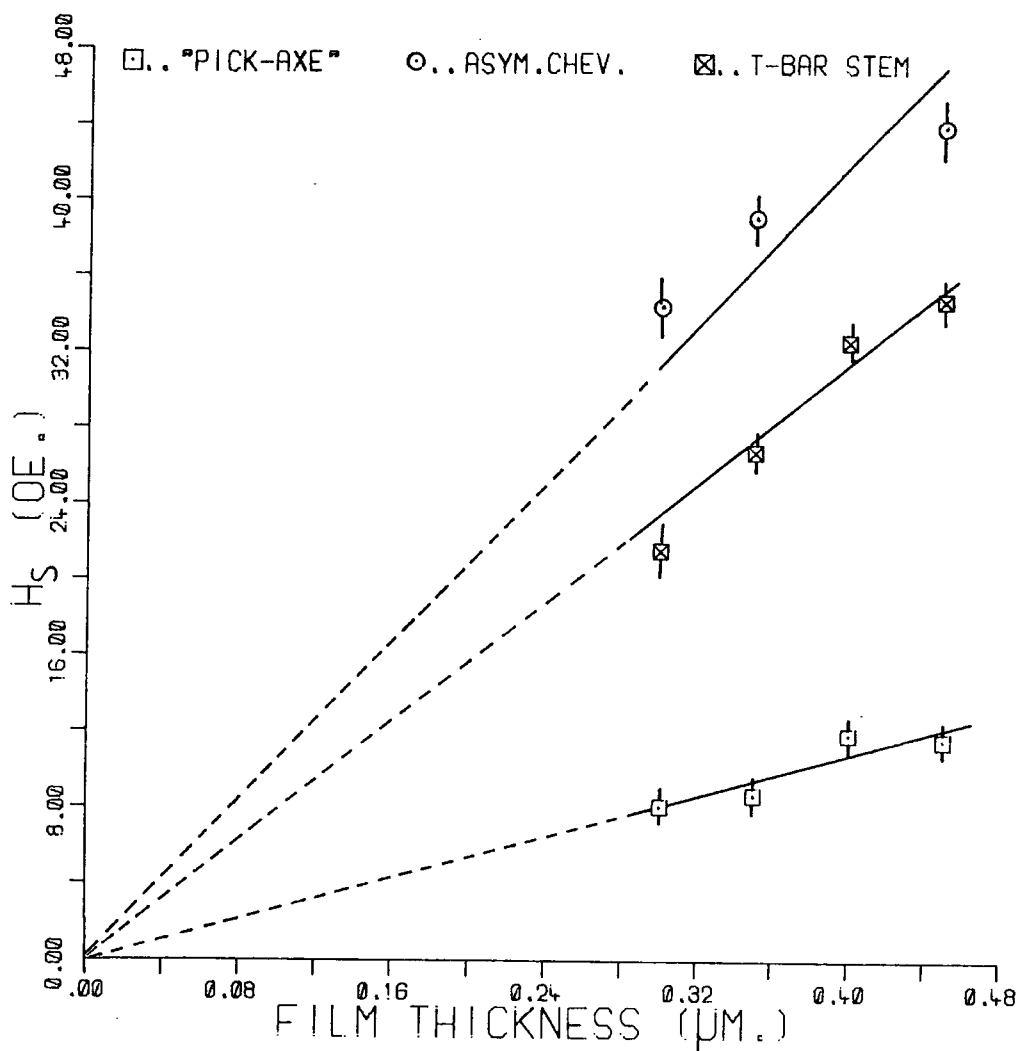


Fig. 6.26 Field required for partial saturation (H_s) in asymmetric chevron, T-bar and pick-axe elements.

saturation fields are found in the long bar. The ratio of gradients between the two least squares fits is 2.98. The saturation fields for asymmetric chevron, T-bar and pick-axe elements are given in figure 6.26. Again the dependence on permalloy thickness is approximately linear. As might be expected the long thin pick-axe has the lowest saturation fields. This element is designed to produce a strong pole for bubble nucleation consequently it saturates in fields of the order of 10 Oe. By contrast the more compact asymmetric chevron has a larger region of linear response. It is interesting to compare the values of H_S for these elements with those predicted by extrapolating the domain wall displacement curves of fig.6.14. The latter predicts $H_S = 37.1$ Oe and 46 Oe for chevrons 0.3 μ m and 0.45 μ m thick respectively. Saturation is actually observed at 34.5 Oe and 44 Oe in these elements. Saturation is manifested as buckling in the small chevron limb.

6.8 The formation of remanent states in a rotating field.

It has been shown that remanent states form in overlay components when D.C. fields of sufficient intensity are applied along particular directions. These states are generally stable in applied fields perpendicular to the direction of remanent magnetization and a small reverse field is usually required to produce demagnetization. From these observations in D.C. fields it is to be expected that a uniform rotating field of sufficient amplitude ($\geq H_S$) will also produce remanent states. Remanence should persist as the field rotates away from the axis along which a bar has been saturated until there is a small reverse field component along this axis. Observations in quasi-static rotating

fields confirm these predictions.

Figure 6.27(a) shows the initial domain wall structure in three demagnetized elements; pick-axe, I-bar and asymmetric chevron located at the beginning of a propagation track. The D.C. saturation fields determined for similar components of the same thickness were 8.7 Oe, 15.6 Oe and 38 Oe respectively. Following the application of a quasi-static rotating field of amplitude 8 Oe no remanence was observed. Magnetization appeared to proceed entirely by reversible wall motion. However fig. 6.27(b) shows that when the field amplitude was increased to 11 Oe a buckled wall configuration formed in the pick-axe. This photograph was taken in zero field the 'drive-field' having been switched off at $\theta = 90^\circ$. With the field switched on again it was found that the magnetization buckle persisted until the field rotated to approximately $\theta = 100^\circ$. At this point the buckle 'collapsed' so that in zero field the element was once more demagnetized. The field was rotated to $\theta = 0$ and then increased in amplitude to 25 Oe. Subsequently remanent configurations formed both in the pick-axe and the I-bar. The relevant domain pattern is shown in figure 6.27(c) in zero field. Again the field was switched off at $\theta = 90^\circ$. Figure 6.27(d) shows both elements demagnetized when the field had rotated to $\theta = 100^\circ$. With a rotating field of 40 Oe the domain structure in all three elements was observed to undergo irreversible changes. This is evident from fig 6.27(e) (zero field). In this case the field was switched off in the direction $\theta = 180^\circ$. The asymmetric chevron clearly possesses a new domain structure. Finally after the application of a rotating field with gradually decreasing amplitude all three elements were demagnetized producing the

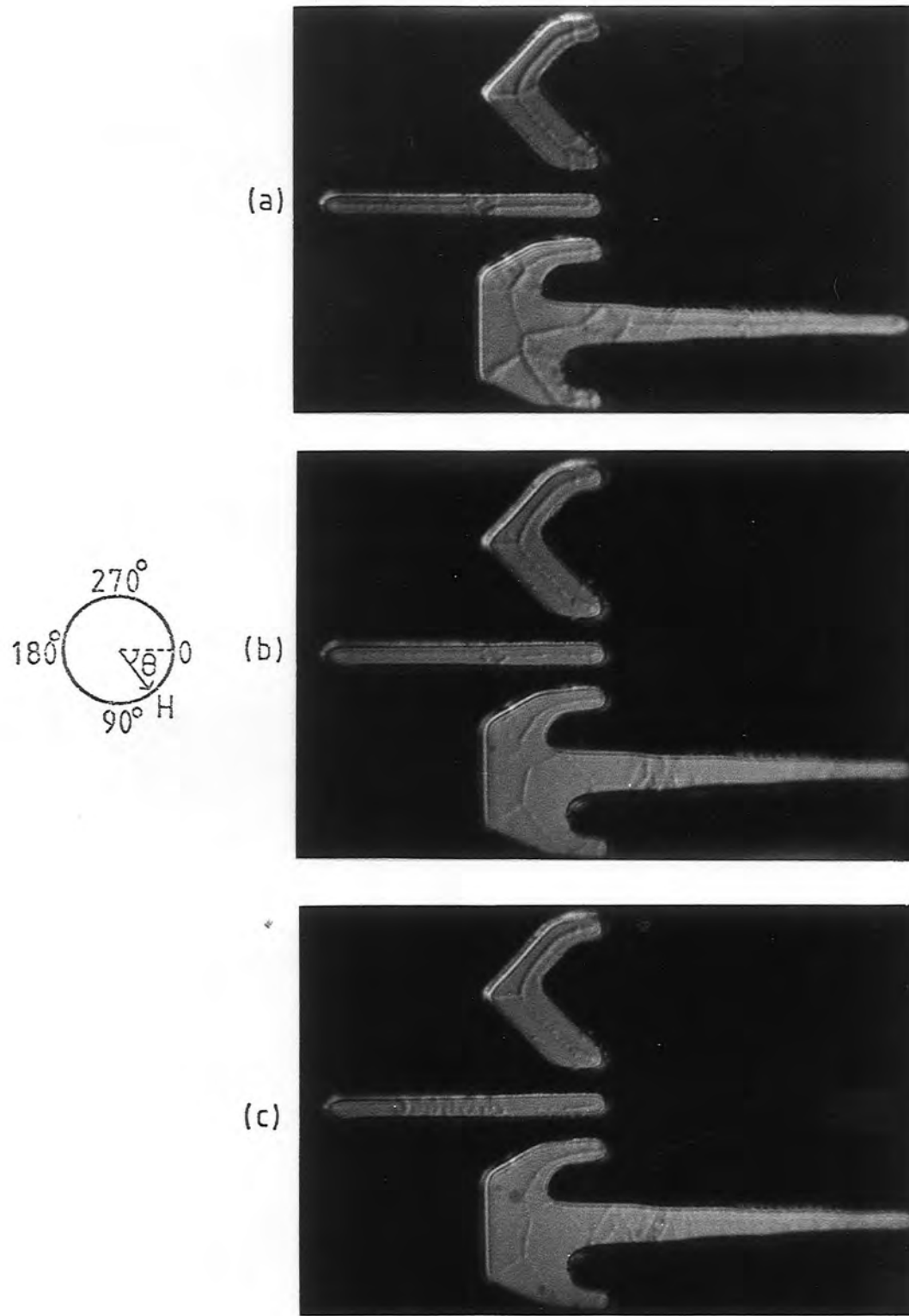


Fig. 6.27 Series of remanent states formed by a rotating field of increasing magnitude (see text).

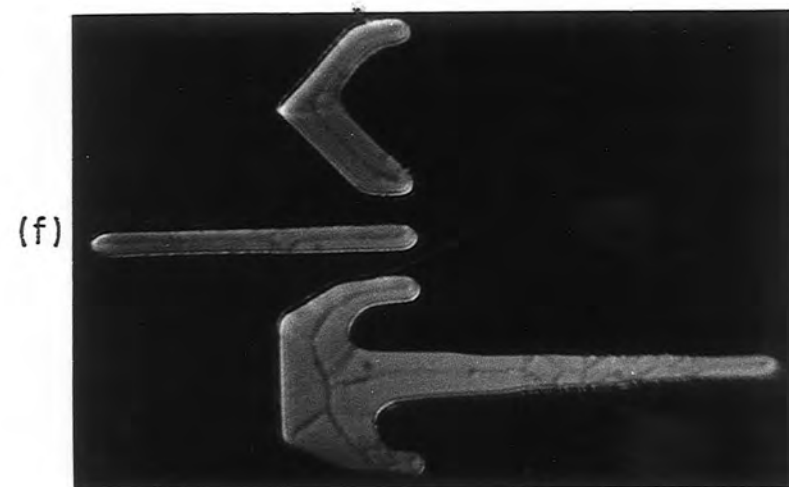
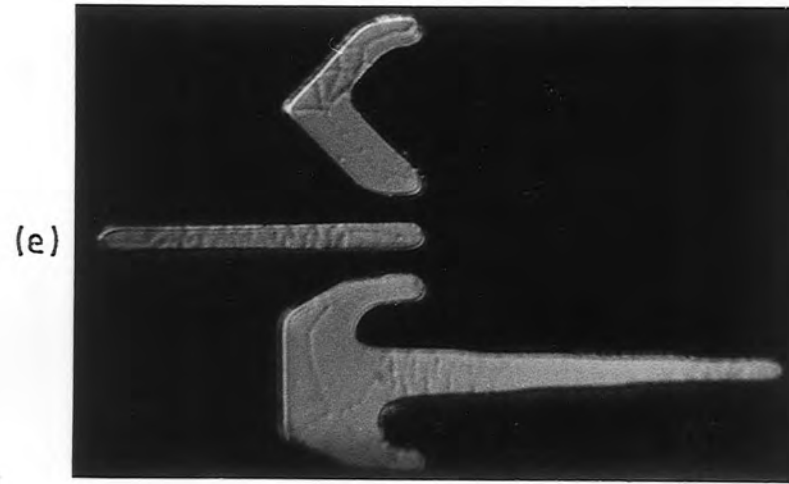
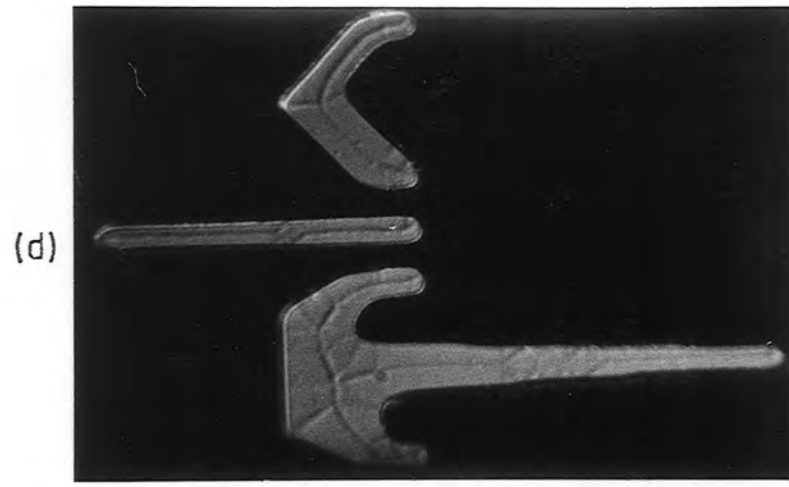


Fig. 6.27 Continued (see text)

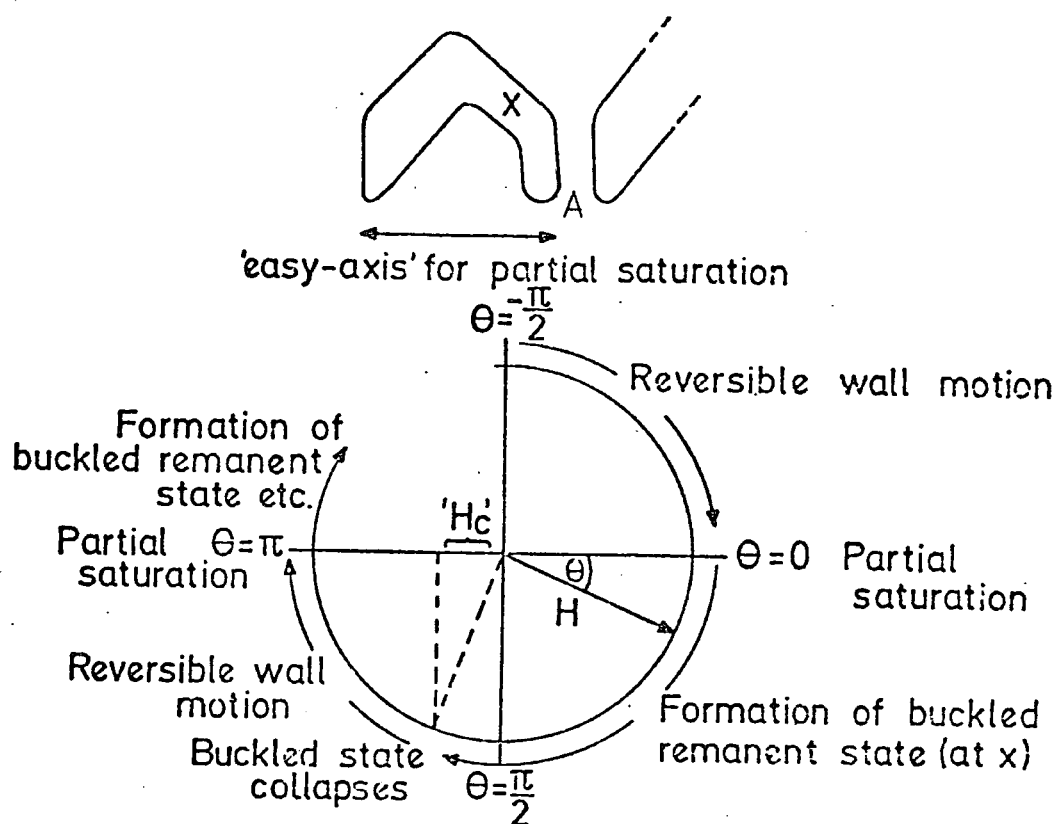


Fig. 6.28 Typical observed hysteresis in a quasi-static rotating field H .

ferrofluid pattern shown in fig. 6.27(f). The structure resembles the original shown in fig. 6.27 (a). The typical hysteretic behaviour for an element in rotating field is summarized in fig. 6.28 for the case of an asymmetric chevron.

6.9 Partial saturation in overlay bars on magnetic garnet.

In a bubble device the overlay experiences an in-plane drive field and the non-uniform bubble field. The bubble generally follows a magnetostatic potential well created by the overlay. As a result the in-plane component of bubble field within an overlay element supports the uniform drive field (on average). This suggests that the uniform applied field required to partially saturate an overlay bar should be reduced if a bubble domain occupies the magnetostatic potential well beneath the bar. As a first step in investigating the influence of the bubble medium, partial saturation fields were obtained for various elements on magnetic garnet. No bias field was applied so the garnet contained a random pattern of stripe domains. For each element H_g was obtained as an average over many ferrofluid observations (as described earlier). The values of H_g for each element are compared in fig 6.29 with the corresponding saturation fields in elements of the same thickness ($0.35\mu\text{m}$) on non-magnetic substrate (G.G.G.). As expected H_g is reduced in each case by the presence of the bubble medium but the amount of reduction increases from 1.5 Oe for a pick-axe element to 20 Oe. for a $15 \times 2.1\mu\text{m}$ I-bar. In fact the reduction appears to increase almost linearly with the original magnitude of H_g on non-magnetic substrate.

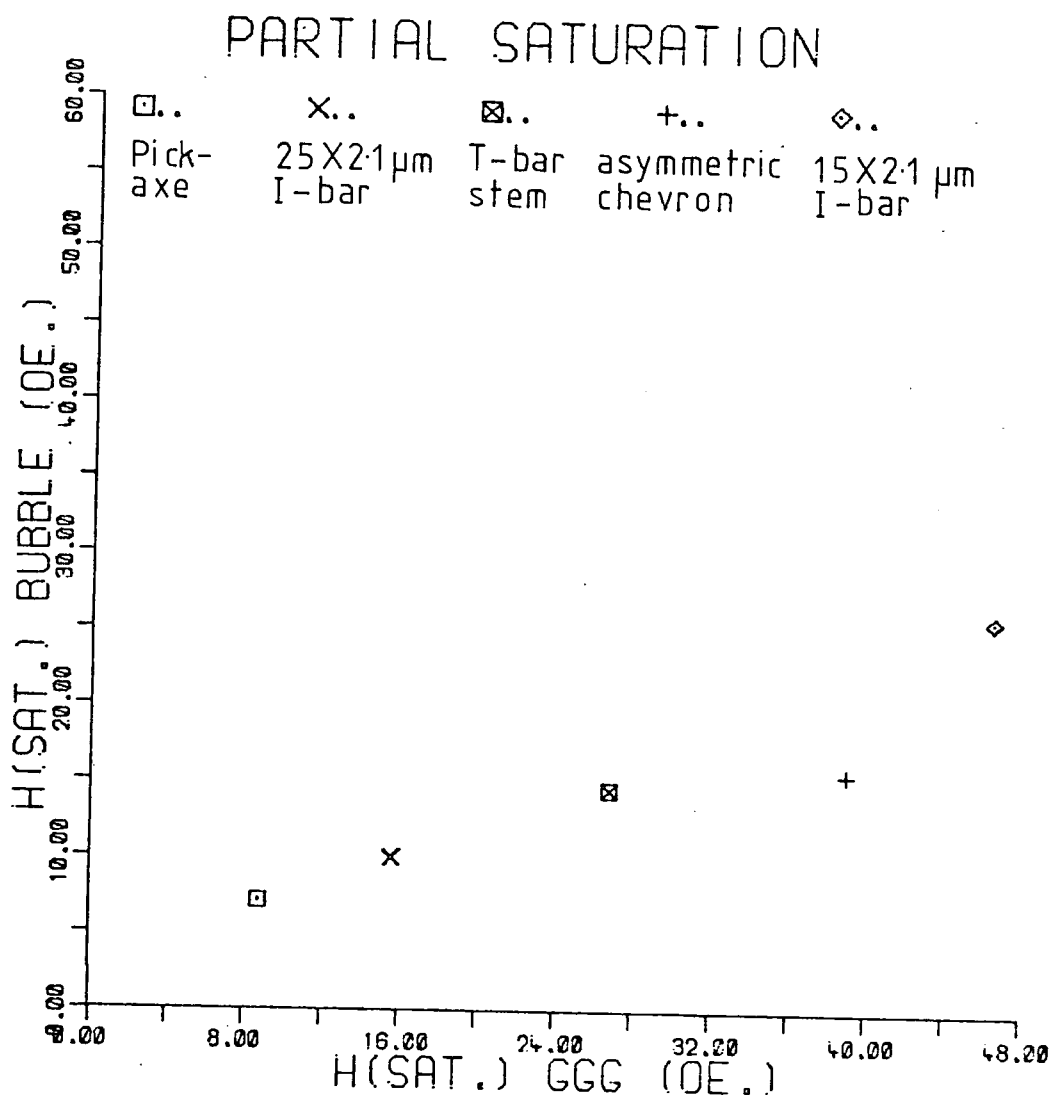


Fig. 6.29 A comparison of partial saturation fields in elements on bubble garnet substrate with those measured in similar elements on GGG.

6.10 Significance of hysteresis for device operation.

Hysteresis in an overlay should affect the operation of a bubble device because of the stray fields associated with remanent magnetization. Cohen et al. (1979) observed that high remanence and coercivity produce poor operation in both H-I bar and half-disc circuits manifested in large values of the minimum drive field ($H_{xy \text{ min}}$). The above authors studied H-I bar circuits in which the effect is worse. A measure of 'coercivity' was obtained by locating a bubble beneath one end of a permalloy bar and then recording the minimum field required to transfer the bubble to the opposite end of the bar: ' H_{bbl} '. In general samples with high H_{bbl} had large values of $H_{xy \text{ min}}$. This was attributed to the 'anomalous propagation' failure mechanism in which a bubble fails to pass from an I to an H particularly if there is already a bubble (in the adjacent track) located on the H. Remanence in the H-bar is supported by the stray field of the second bubble domain. Evidence for high remanence was also gained from ferrofluid observations. Domain walls were observed in demagnetized bars whilst in other bars (with remanence) no walls could be detected. For a given applied field (26 Oe) remanence was observed in 0.5 μm thick bars but not in 1 μm thick bars. This is consistent with the results given in fig. 6.25 and 6.26 which show an approximately linear increase of H_s with thickness.

The present study indicates that remanence also occurs in gap-tolerant propagation tracks. The behaviour of asymmetric half-discs and chevrons is similar; in both the buckled states form first in the small limb. In a gap-tolerant circuit however adjacent tracks are not connected and only one bubble at a

time is associated with a given permalloy feature. Anomalous propagation as found in H-I bar circuits cannot occur in a gap-tolerant design. However it is possible to predict a failure mechanism based on the observed magnetization buckling in asymmetric chevrons and half-discs which will raise the value of $H_{xy \text{ min}}$. Referring back to fig. 6.28, a bubble propagating from left to right during this rotating field sequence would be located approximately at 'A' at $\theta = \frac{\pi}{2}$ and would normally be drawn towards a strong pole forming on the next element to the right (assuming the bubble domain is magnetized into the plane of the diagram). However, remanence in the small chevron limb at X would produce a residual attractive pole thus reducing the effective field gradient across the gap.

CHAPTER 7 DETECTOR COLUMNS - RESULTS AND DISCUSSION.

7.1 Basic remanent domain structures.

A typical domain wall pattern in a chevron detector column as revealed by ferrofluid is shown in fig. 7.1(a). As with propagation elements the basic structures in elements on non-magnetic substrate or bubble garnet are the same. Whereas isolated elements contain 180° domain walls and closure domains typifying the demagnetized condition, the pattern of transverse walls in the detector column suggests a saturated state with a continuous flow of magnetization. George et al. (1976) observed similar ferrofluid patterns on this type of detector in the absence of applied fields. In fact this type of configuration seems to occur quite generally for this geometry of detector. Columns with nominal bar widths of $1\mu\text{m}$, $2.1\mu\text{m}$ and $6\mu\text{m}$ all had similar domain structures.

That each limb of a column should be saturated is consistent with the minimum energy principle. Magnetization runs parallel to the edge of the column so there is no stray field energy and the total area of domain walls is minimized. A basic distinction between different column designs lies in the position of the connecting bar between chevrons. If the connecting bar is drawn in from the ends of the chevrons the minimum energy state is such that the flow of magnetic saturation still follows the path taken by the detector current. However, additional closure domains may form as shown in the ferrofluid pattern of fig. 7.1(b).

Several geometries of column were studied. In all but one case similar features of domain structure were observed. All these columns showed some type of continuous magnetization flow

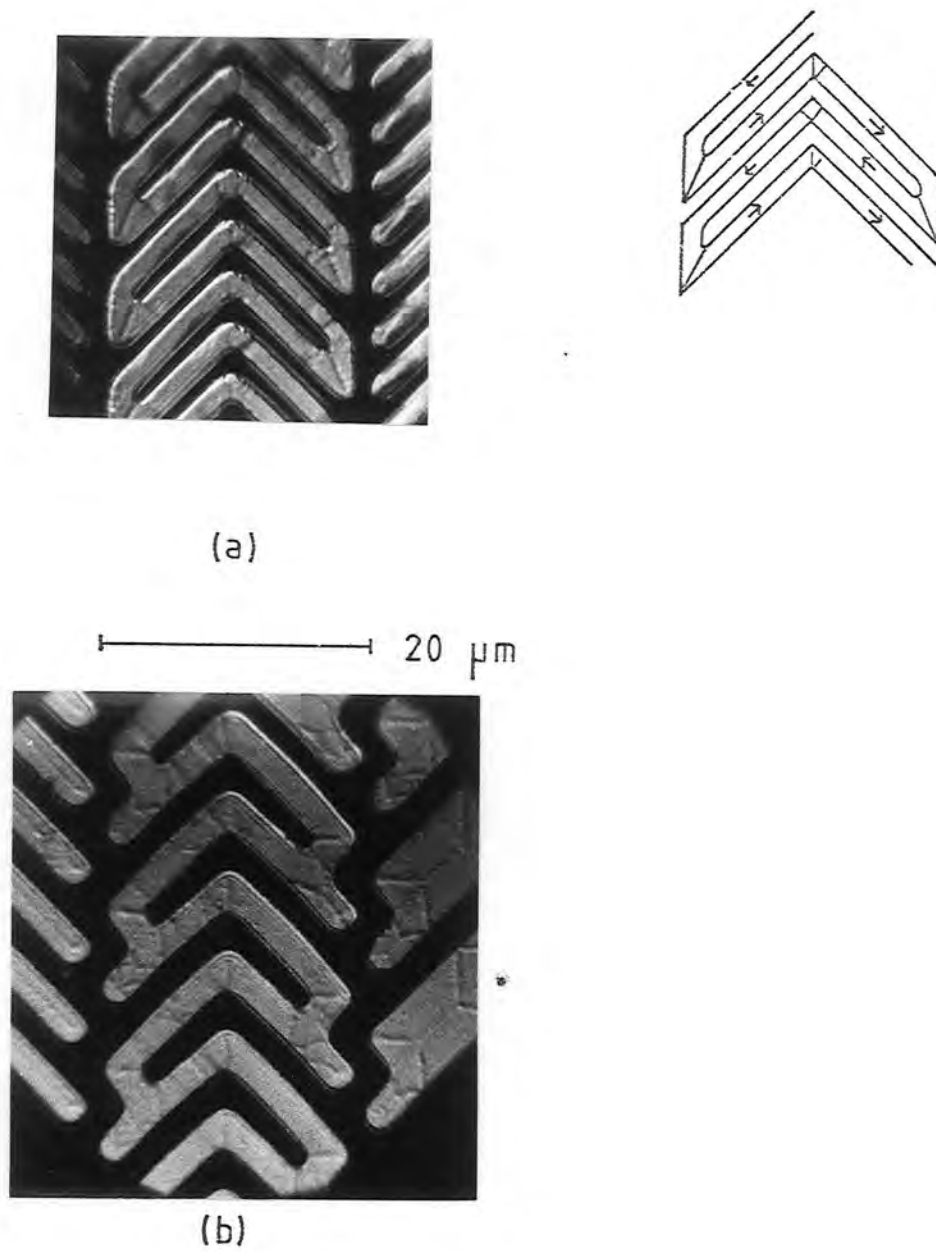
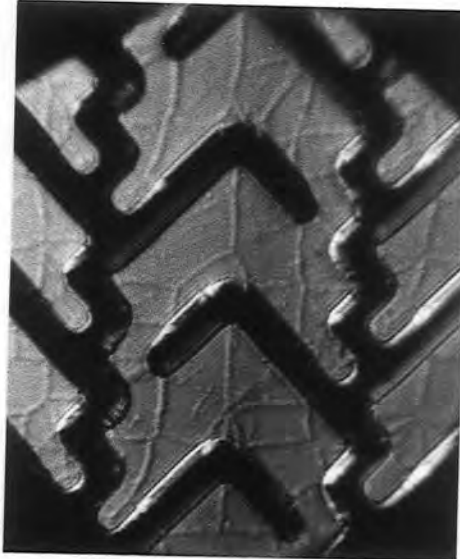


Fig. 7.1 (a) Typical ferrofluid deposit on a connected-chevron column in zero field suggesting a continuous flow of magnetization along the column.
(b) Details of domain structure may vary with column geometry.



—|————|—
20 μm

Fig. 7.2 An exceptional column design in which the elements are not saturated (zero field).

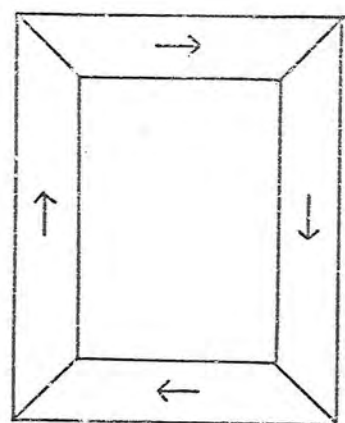
which was apparently not affected by varying conditions of in-plane anisotropy from sample to sample. The one exception was the column design shown in fig. 7.2. In this case the connecting bars between elements are much narrower than the elements themselves and the column is not magnetically saturated. However the wall displacements (in zero field) do suggest that there is a net component of magnetization in the column (probably limited by the amount of flux which the connecting bar can carry when saturated). The presence or absence of domains in a detector is important when the response to applied fields is considered.

7.2 Magnetization reversal in a closed loop of permalloy.

In zero field, detector columns are generally characterized by domain structures with continuous flux flow. If a uniform in-plane field is applied across a detector column the magnetization in chevron limbs is directed alternately parallel and antiparallel to the field. Before describing the response of such a configuration to applied fields the behaviour of a simpler but analagous system will be discussed.

The experiments of Williams and Shockley (1949) on 'picture frame' specimens are well known. Their sample consisted of a hollow rectangle of single crystal iron with overall dimensions $1.9 \times 1.3 \times 0.074$ cm. thick. The minimum energy state was found to consist of four domains running in the same direction forming a closed loop of flux (fig. 7.3(a)). In applied fields magnetization occurred by the formation and lateral displacement of Bloch walls.

Figure 7.3(b) shows the ferrofluid pattern on a permalloy 'picture frame' with overall dimensions $29 \times 23 \times 0.3 \mu\text{m}$. Bloch walls



(a)



(b) Zero field

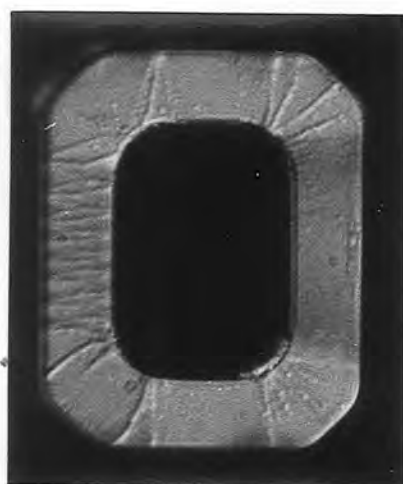
(c) $H = 13.5 \text{ Oe} \downarrow$ (d) $H = 9.5 \text{ Oe} \leftarrow$

Fig. 7.3 Minimum energy domain structure observed in a 'picture frame' specimen of Si-Fe by Williams and Shockley (1949). (b) Zero field domain structure in a closed loop of permalloy. (c) and (d) show magnetization reversal proceeding by buckling.

occur in the four corners but each limb is saturated as in a detector column. For small in-plane fields no changes are apparent in the structure but if the field intensity is increased to roughly 13.5 Oe a clear pattern of magnetization buckle forms in one of the limbs (fig 7.3(c)). If the direction of applied field is rotated through 90° buckle forms in the adjacent limb, this time at a lower field (approximately 9.5 Oe.) (fig. 7.3(d)). Buckling represents an intermediate stage in the process of magnetization reversal so the direction of magnetization flow in the loop is clockwise.

Fig 7.4 shows a sequence of ferrofluid patterns with an in-plane field of increasing magnitude. The buckling which is visible at 14.5 Oe (fig. 7.4 (a)) subsequently breaks at 20.4 Oe to form the intermediate state shown in fig. 7.4 (b). As the field is increased the intermediate state is reduced at 22 Oe to a simple Bloch wall (fig. 7.4 (c)). Beyond this point the limb can respond to applied fields by lateral displacement of the Bloch wall. However if the magnitude of the applied field falls below a certain value the Bloch wall is annihilated at the edge of the bar. If the field is then increased magnetization reversal proceeds by buckling once more. Similarly if the applied field is increased above a certain level the Bloch wall is annihilated at the opposite side of the bar. The limb is then saturated parallel to the applied field. Subsequently reducing the applied field again causes buckling.

In fig. 7.4 (c) the small regions of magnetization buckle essentially form the transition between a section of permalloy magnetically saturated in one sense and a section substantially magnetized in the opposite sense. It will be shown later that

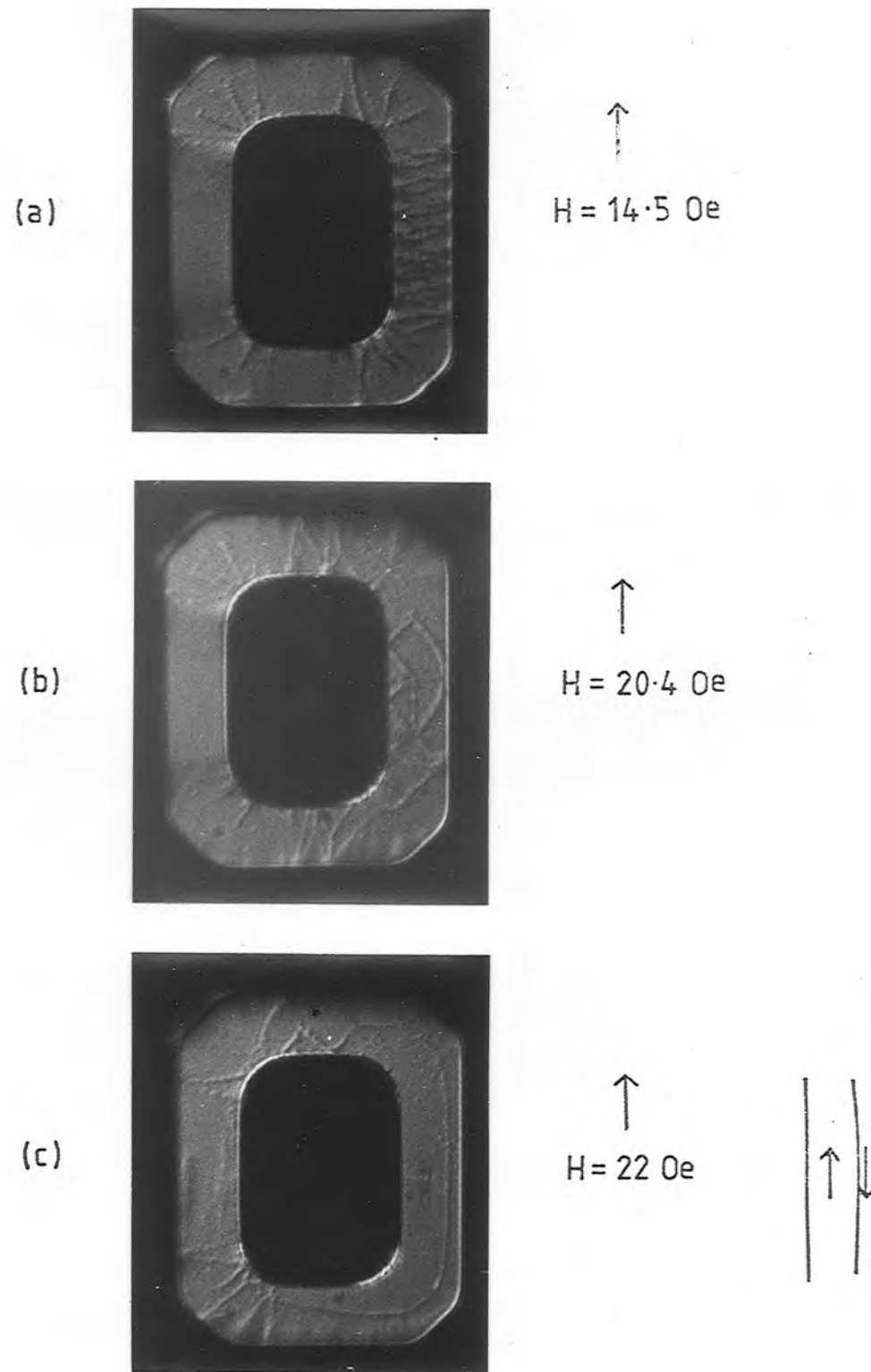


Fig. 7.4 In a closed loop of permalloy reversal proceeds beyond buckling to form 180° walls (initial state of magnetization clockwise).

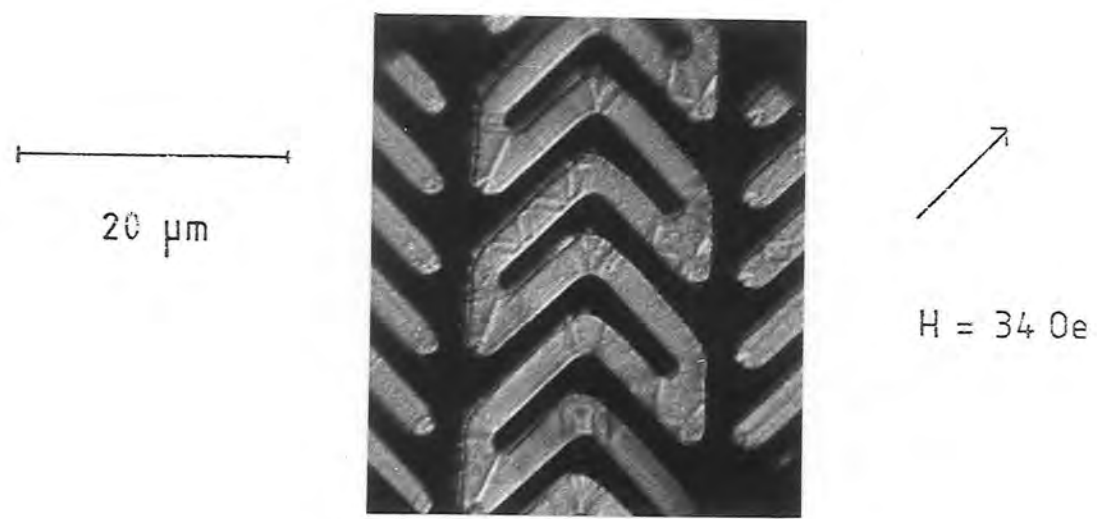
a similar configuration may occur in chevron columns.

7.3 Magnetization reversal in chevron detector columns.

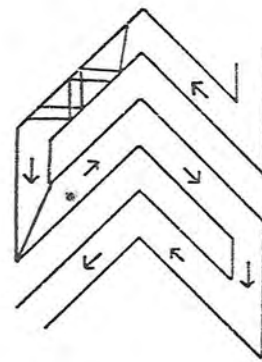
The response of a detector to transverse fields (H_x) is illustrated in fig. 7.5 (a) for the case of a chevron column on non-magnetic substrate. As in the case of a picture frame specimen the initial domain structure is stable in weak applied fields (ie. approximately 0-10 Oe) however when the field reaches a certain level transverse domain walls, characteristic of buckling, appear in one of the chevron limbs. It is not possible to state conclusively to which of the structures shown in fig. 6.17(b), (c) or (d) the buckling corresponds. From the location of buckling it can be deduced that the direction of magnetization flow in the column is as illustrated in fig. 7.5 (b).

Fig 7.6 (a) shows magnetization buckling in a detector column on magnetic garnet substrate subjected to a transverse field of 14.2 Oe. As expected, buckling occurs in alternate limbs, never in adjacent limbs, however it is interesting to note that reversal does not occur simultaneously in all chevrons where the direction of magnetization opposes the field. This was evident in fig 7.5. Also the buckling does not fill a whole chevron limb simultaneously.

As in the case of a picture frame specimen buckling breaks as the field increases to leave simpler structures based on 180° walls. A small number of internal closure domains may also appear. Fig 7.6(b) shows the configuration which results from increasing the field to 16 Oe. Beyond this point the column responds to variations in the applied field by lateral movement of the domain walls. However if the applied field is reduced sufficiently (to



(a)



(b)

Fig. 7.5 Magnetization buckling in a chevron limb when the direction of magnetization opposes the applied field.

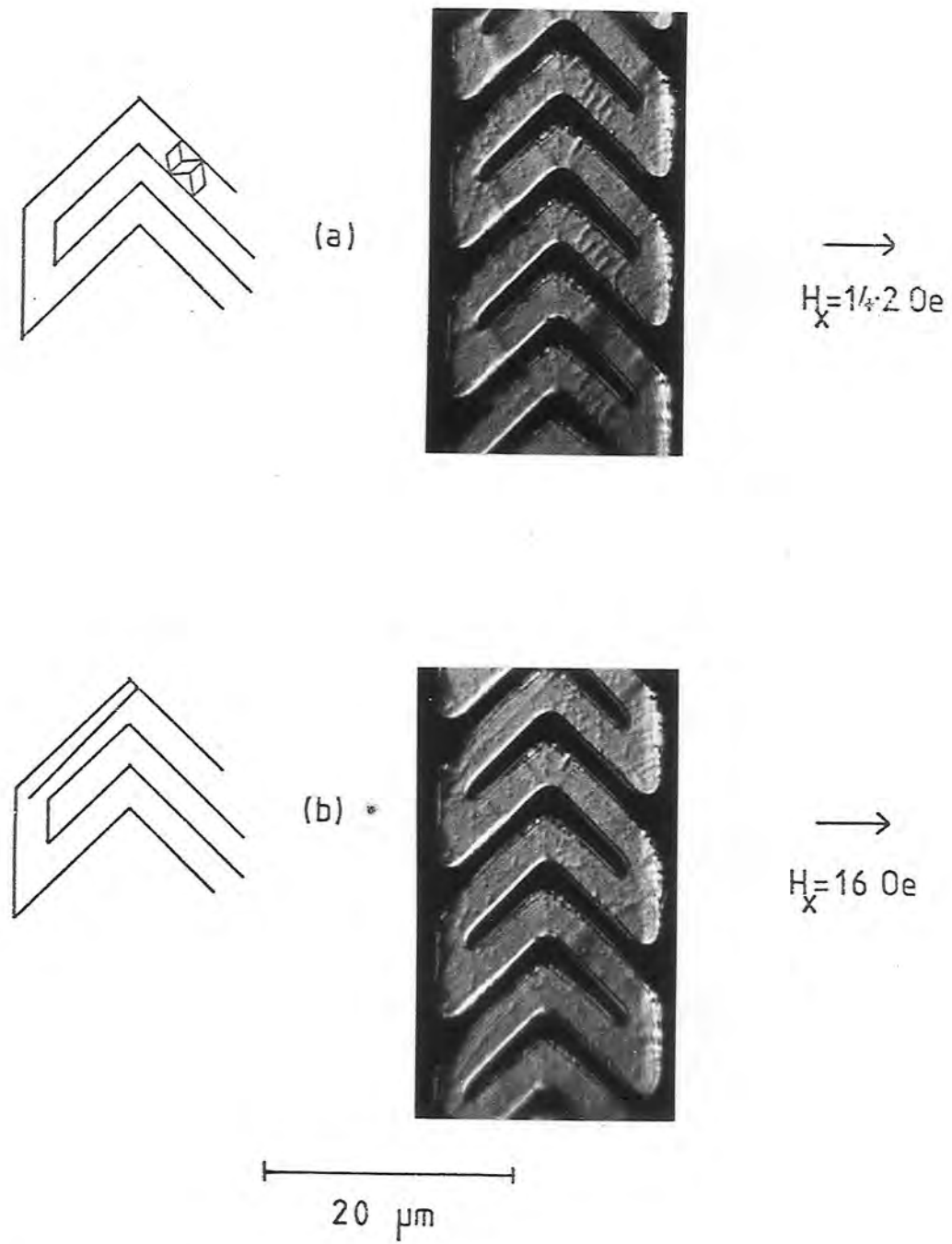


Fig. 7.6 (a) Magnetization buckling in a transverse field is followed by (b) the formation of 180° walls.

a few Oe) the walls collapse at the edge of the column and the original saturated state is restored. Applying the transverse field once more causes the whole process of buckling to be repeated before 180° walls and reverse domains can be reformed. The same type of behaviour was observed in all detector columns (on magnetic and non-magnetic substrates) in which the initial state was one of saturated magnetization. As an example fig 7.7 (a) shows buckling in alternate limbs of a detector with centre connecting bars in an applied field of 21.5 Oe.

The response of a column to applied fields clearly reveals the direction of magnetization flow. In some samples small sections of magnetization buckle were observed even in zero applied field. An example is given in fig. 7.7(b) for the case of a detector with nominal bar width $1\mu\text{m}$. There is also a 180° wall adjacent to the buckled section. Wherever this configuration occurred it was found, by applying suitable fields, that the direction of magnetization flow reversed at that point. Thus the situation in fig. 7.7(b) is analagous to that in the picture frame sample of fig. 7.4 (c) where the buckled sections represent similar transitions

To summarize, transverse fields above a certain level have the effect of temporarily reversing the direction of magnetization in alternate chevron limbs. When the field is removed the column returns to its initial state. By contrast fields applied parallel to the column (H_y) can irreversibly switch the direction of magnetization throughout the whole column. Reversal occurs by intermediate buckling as demonstrated in fig. 7.8. This state is unstable, a slight increase in the applied field leads to a domain structure which is virtually indistinguishable from

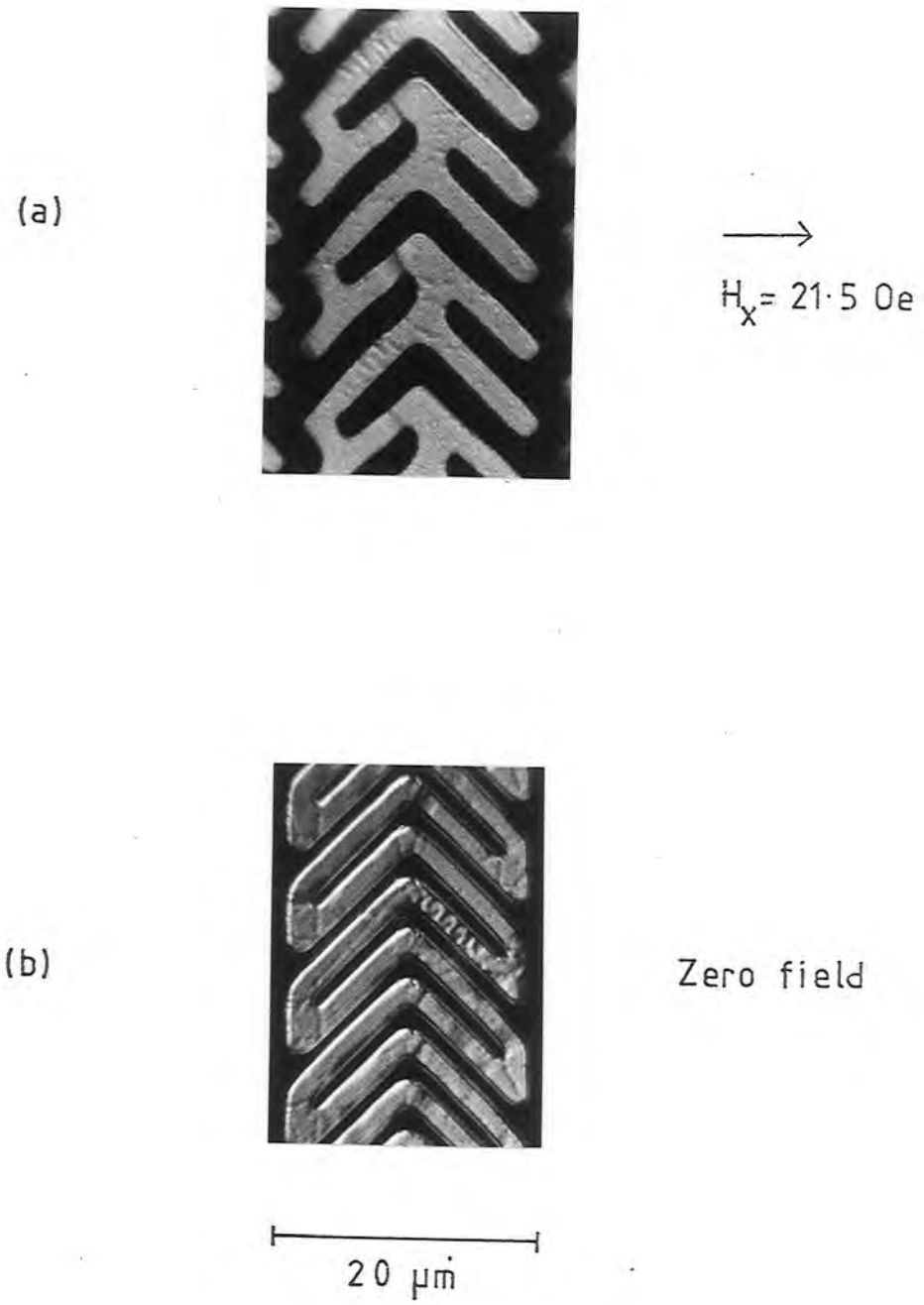


Fig. 7.7 Examples of buckling in chevron columns. The configuration in (b) occurs in zero field and represents a reversal of the direction of magnetization flow.

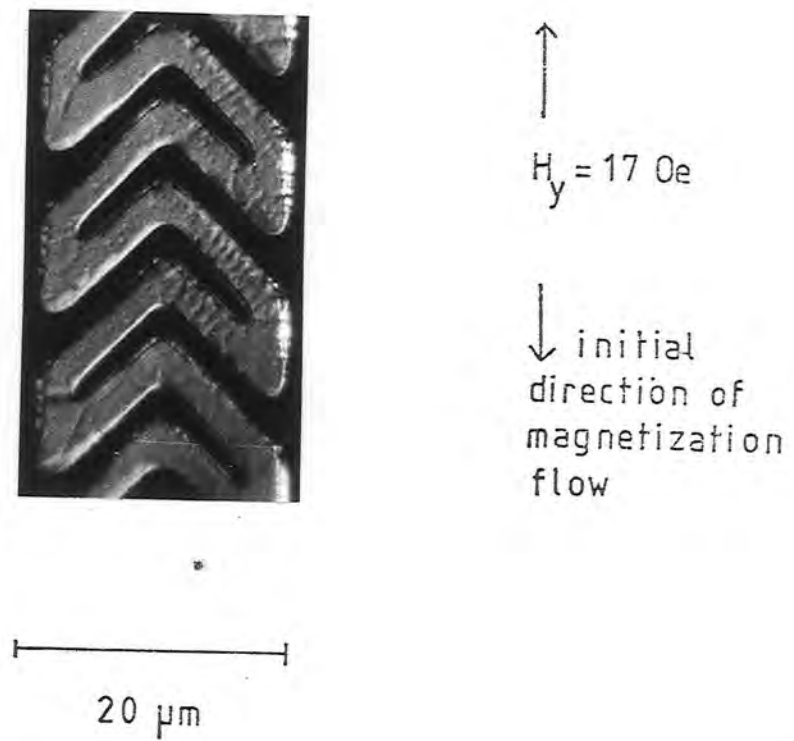
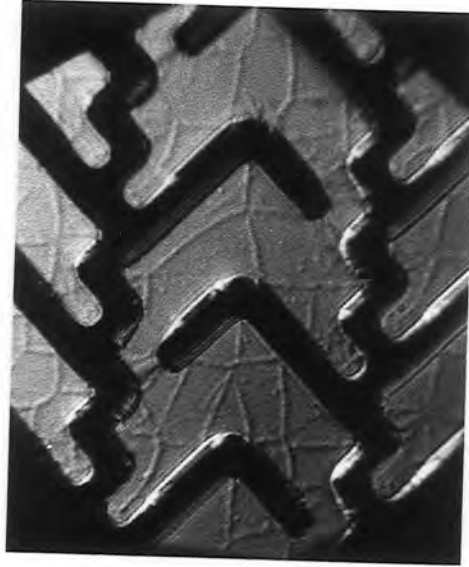


Fig. 7.8 Fields applied parallel to a chevron column may reverse the direction of flux flow. Reversal proceeds via an intermediate state which involves buckling.

the initial state. Applying transverse fields, however, confirms that the direction of flow has been reversed. Again it is noticeable that buckling does not appear throughout the whole column simultaneously. In the case of columns which contain reversal points as in fig. 7.7 (b) it was found that the application of a switching field parallel to the column established the whole column in a single state of magnetization flow.

The only type of column studied which responded to applied fields without the formation of magnetization buckle was that which had an initial unsaturated state (fig. 7.2). In this case both the isolated and connected elements respond to transverse fields (H_x) by reversible wall movements (at least up to 50 Oe). However fairly weak fields (typically 2-3 Oe) applied parallel to the column cause switching between two stable states as can be seen from the ferrofluid pattern of fig. 7.9 in zero field. This pattern results from applying a field of approximately 2.5 Oe parallel to the same column shown in fig. 7.2 (ie. from top to bottom in the photograph). The irreversible change in domain structure is evident from a comparison of fig. 7.9 with fig. 7.2.

For each type of column the switching field was estimated from a series of ferrofluid observations. The results, given in fig. 7.10 show that the switching field depends on the position of connecting bars between chevrons. These results are for samples 0.45 μ m thick. The dependence of switching field on film thickness was obtained by studying the reversal process in columns 0.3, 0.35, 0.4 and 0.45 μ m thick. The results are plotted in fig. 7.11. The coercivity in thin rectangular strips of permalloy (as defined by the field required to switch the direction of magnetization) increases as film thickness is reduced (Kryder et al.1980).



20 μm

Fig. 7.9 Chevron column in which switching occurs by domain wall movement rather than buckling.

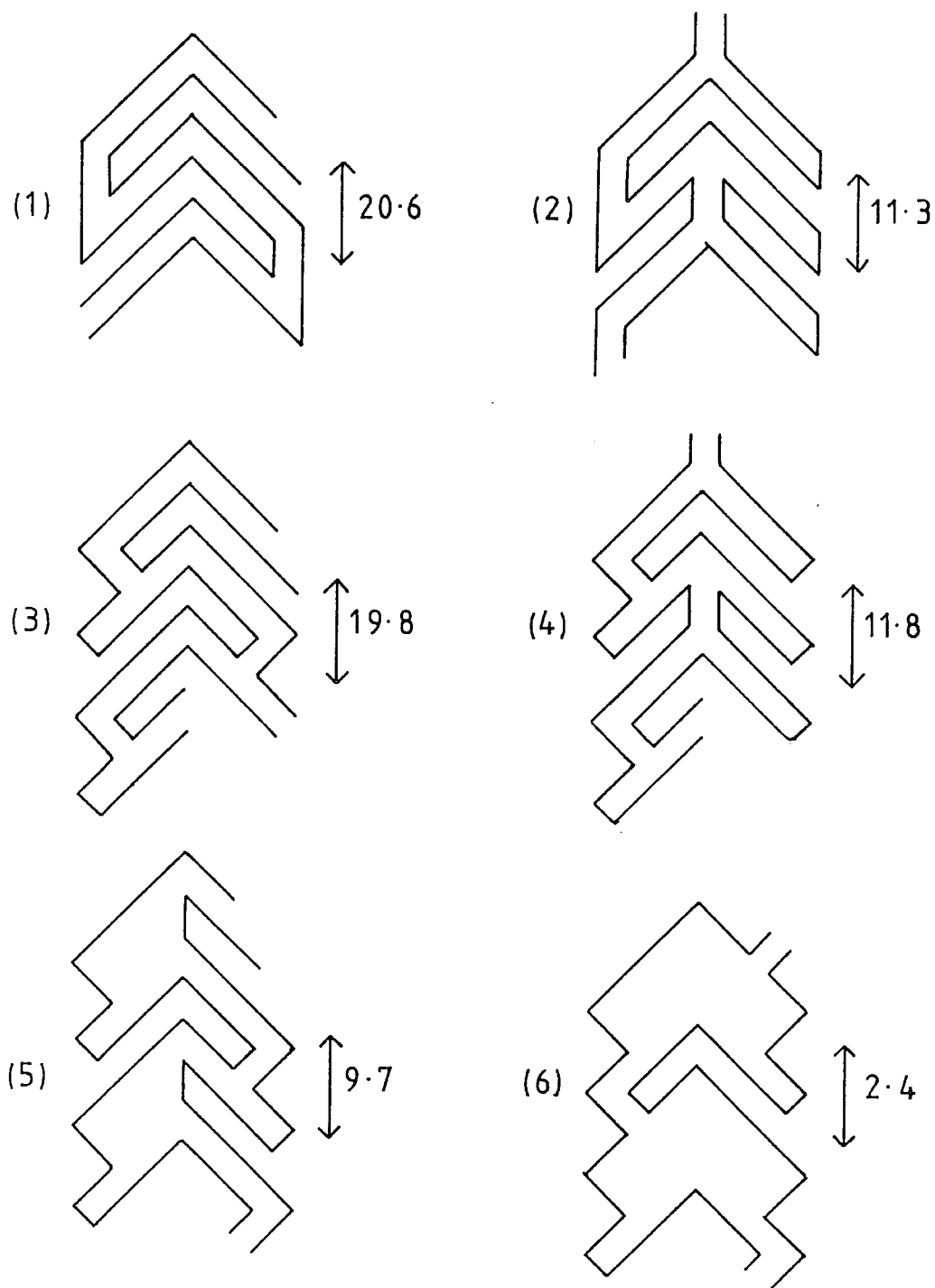


Fig. 7.10 Average field (in Oe) required to switch the direction of flux flow in various chevron columns. These values were measured in samples 0.45 μm thick.

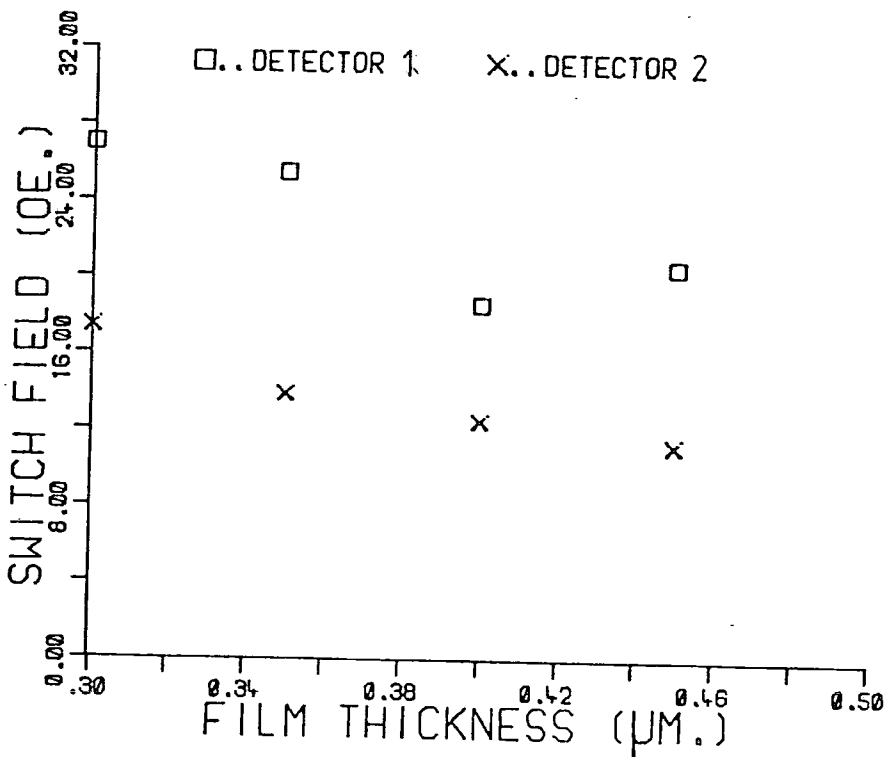
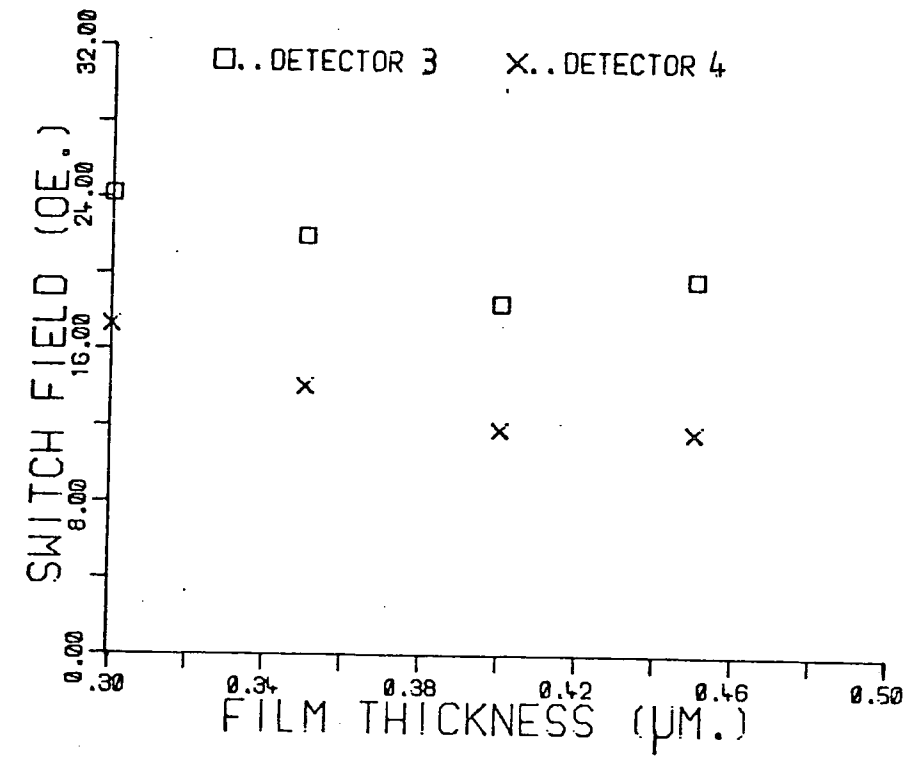


Fig. 7.11 Dependence of switching field on permalloy thickness in four types of detector column (as numbered in fig. 7.10).

From fig. 7.11 it would appear that a similar dependence on thickness occurs in these chevron columns.

7.4 Magnetoresistance variations related to buckling.

The magnetoresistive effect in permalloy is such that the electrical resistance is lower when the magnetization is perpendicular to the current than when the magnetization and current are parallel or anti-parallel. When no fields are applied to a detector column the domain patterns suggest that the magnetization and current follow the same path. This is a high resistance state as was reported by George et al. (1976). The ferrofluid patterns described in the previous section show that field components parallel to the column (H_y) may reverse the direction of flux flow via an intermediate buckled state (fig. 7.8). Since the buckled configuration introduces components of magnetization normal to the current path a drop in resistance should occur during the process of reversal. Buckling also occurs in alternate chevron limbs when fields are applied perpendicular to a column (H_x).

The resistance of a detector column was measured as a function of applied fields. The detector current was provided by a stable constant voltage supply. Small variations in current associated with the magnetoresistance effect were monitored by measuring the voltage across a 10Ω resistor in series with the detector. The voltage was measured with a digital voltmeter.

In fig. 7.12(a) the percentage change in resistance is plotted for fields applied parallel to the column (H_y). The column (previously subjected to a field along the negative Y-axis sufficient to establish flux flow in that direction) shows a drop

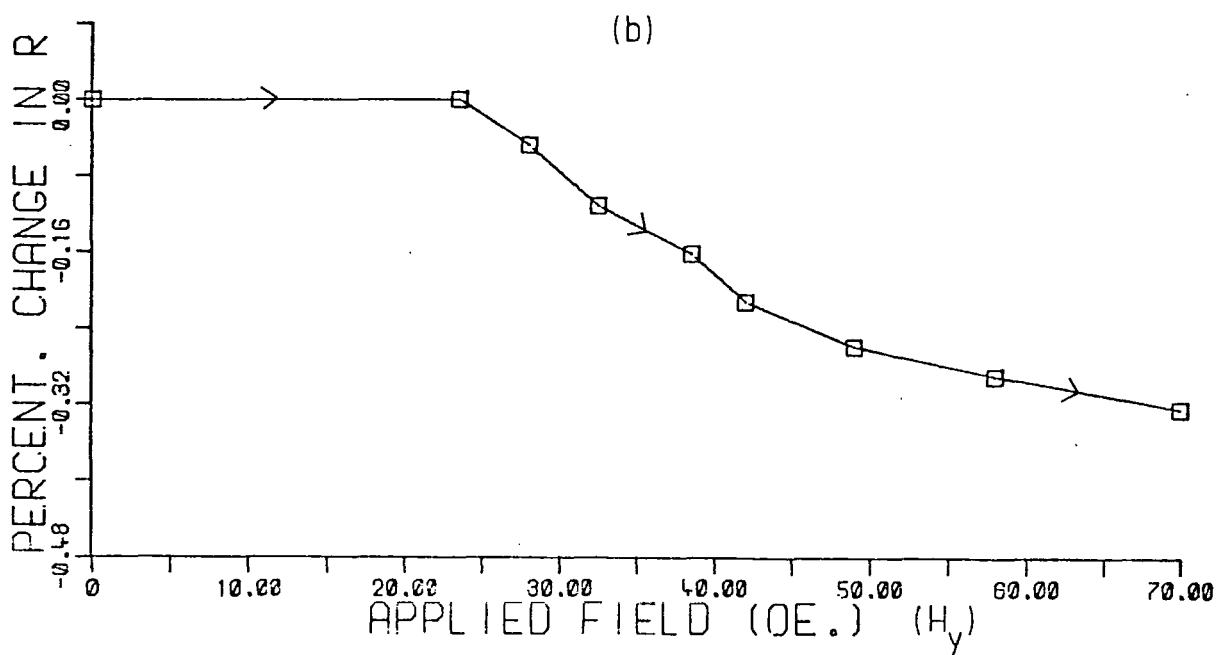
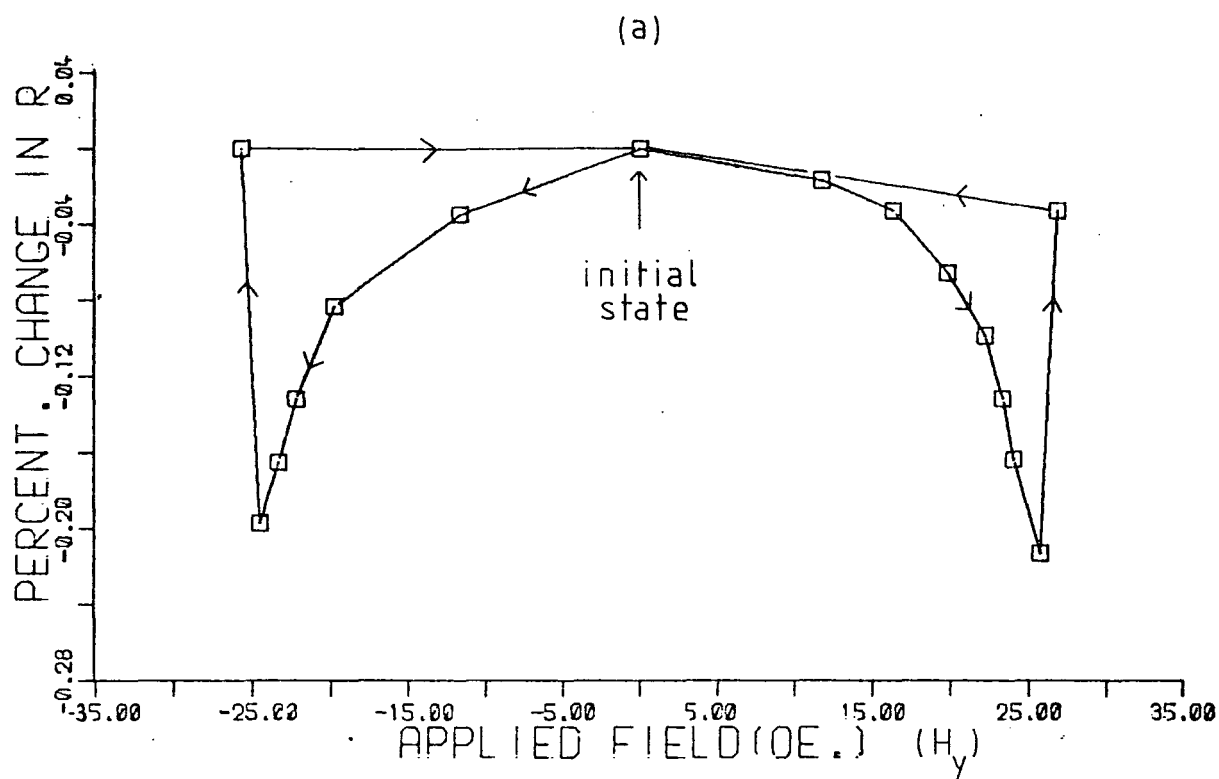


Fig. 7.12 Magnetoresistance variation in a chevron column when the field is (a) antiparallel or (b) parallel to the remanent flow of magnetization.

in resistance as expected when the field is applied along the positive Y-axis. The signal reaches a minimum and the column resistance then returns rapidly to near its initial value. If the field is reduced to zero and then applied along the negative Y-axis the process is repeated. The complete characteristic resembles the magnetoresistance of a thin rectangular strip subjected to longitudinal fields reported by Kryder et al. (1980). If the field is applied parallel to the flow of flux there is no significant change in resistance up to the level of field where switching occurs. Beyond this a gradual (and reversible) drop in resistance occurs as illustrated in fig. 7.12(b). Unfortunately ferrofluid observations cannot provide information on the processes which occur in strong fields. However it would seem reasonable that sufficiently strong fields cause the magnetization in chevron limbs to rotate away from the current direction and towards the field direction.

The change in resistance caused by a field applied perpendicular to the column (H_x) is plotted in fig. 7.13(a). As the field increases there is a drop in resistance associated with magnetization buckle. Beyond the minimum the resistance rises again as the buckle collapses to form 180° walls and closure domains. A bar divided perfectly into anti-parallel domains would have virtually the same high resistance as a saturated bar. However the simple domain structure and the continuous flow of magnetization have now been broken so even as the chevron limbs approach saturation the resistance does not rise as high as its initial value. Fig. 7.13(b) shows that if the field is reduced to zero having reached a maximum value of 41 Oe the resistance returns smoothly to its original value. It can be deduced that

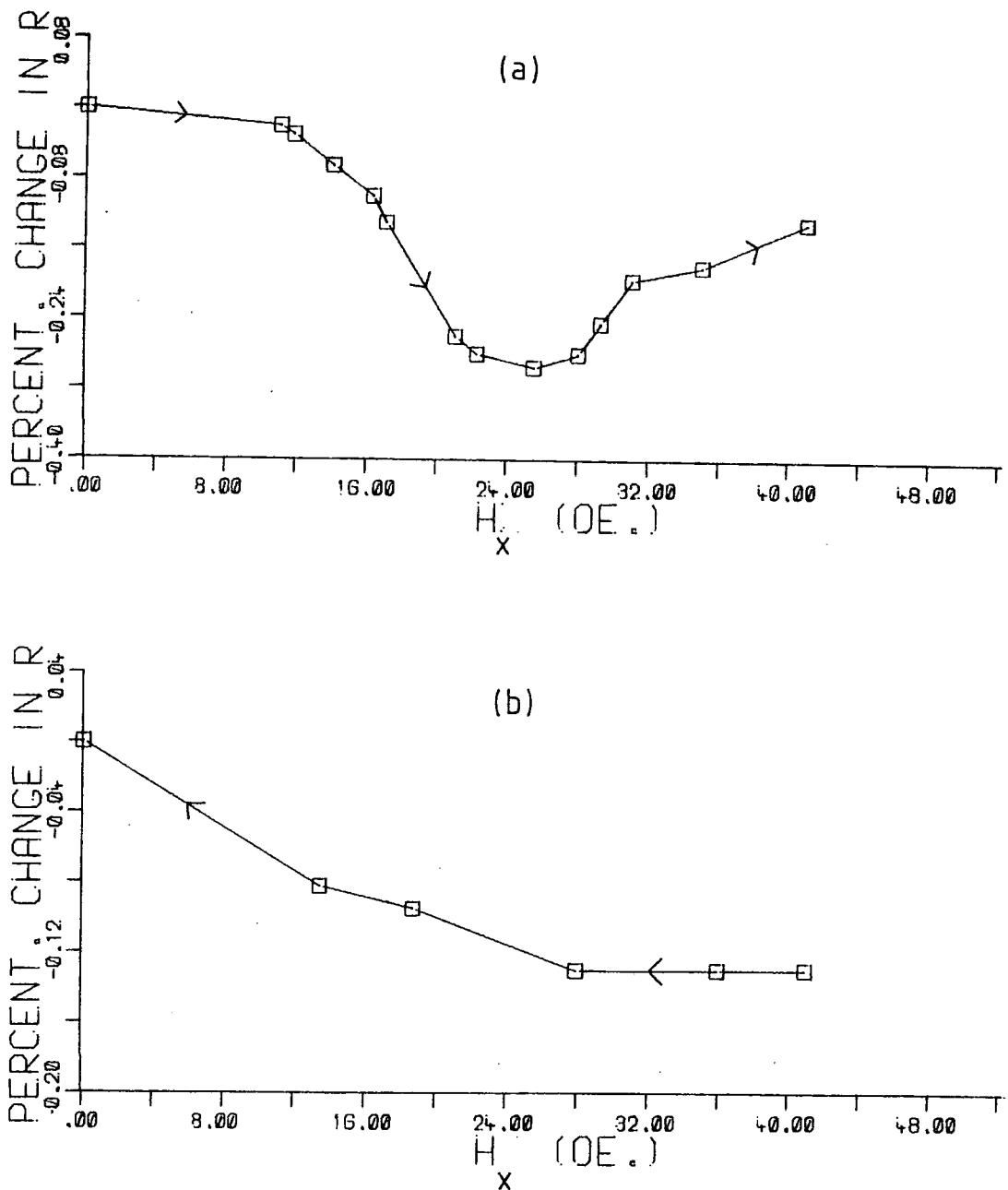


Fig. 7.13. Magnetoresistance in a chevron column with the applied field perpendicular to the column (H_x).
 (a) Field increasing from zero to 41 Oe.
 (b) Field decreasing back to zero.

the 180° walls are swept back to the bar edge, annihilated and the original domain structure is restored.

Fig. 7.14 (a) shows a similar magnetoresistance signal in which the applied field was raised to a maximum of 70 Oe. Again there is a drop in resistance as the field increases but there is also a drop in resistance as the field is reduced to zero. (fig. 7.14(b)) Just as in the case of a 'picture-frame' specimen a sufficiently strong field will saturate the chevron limbs so that reversal of magnetization has to proceed via a second stage of buckling.

7.5 Calculated magnetoresistance of a detector column during buckling.

To a first approximation the magnetoresistance effect in permalloy can be expressed by:

$$\rho = \rho_0 + \Delta\rho \cos^2\theta \quad (7.1)$$

where ρ is the actual resistivity, ρ_0 is the normal D.C. resistivity and $\Delta\rho$ is the magnetoresistance coefficient. θ is the angle between magnetization and current density:

$$\cos \theta = \frac{\vec{M} \cdot \vec{J}}{|\vec{M}| |\vec{J}|}$$

This approximation was used by Collins and Cole (1980) in a calculation of detector signals based on a continuum approach rather than a domain model. For a detector column with a buckled domain structure the resistance change can be estimated by applying equation 7.1 to each domain.

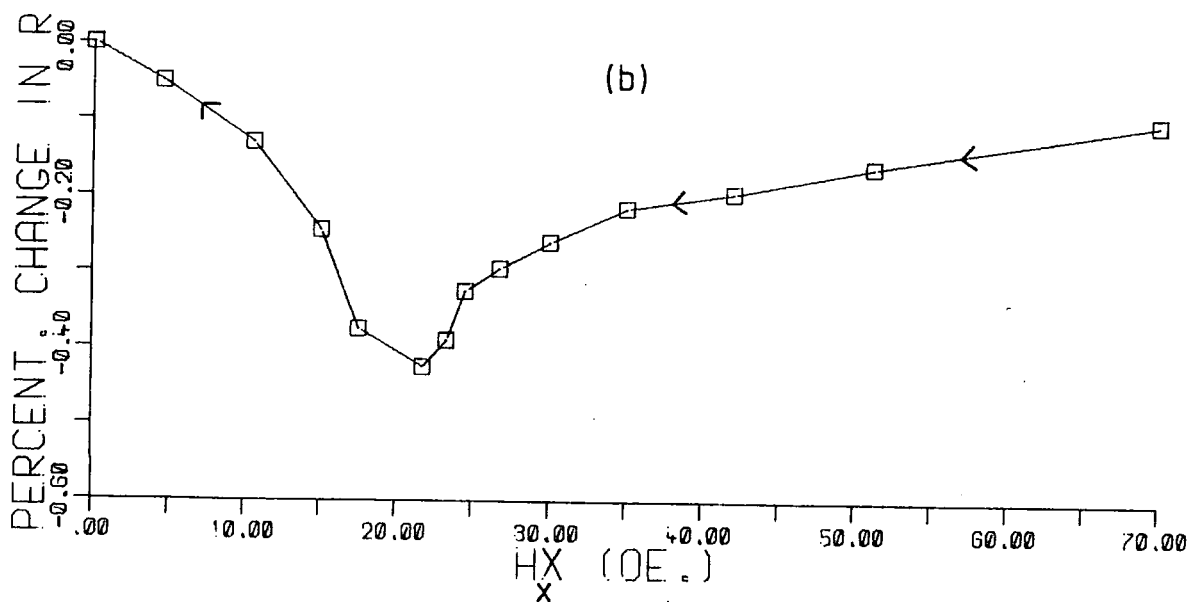
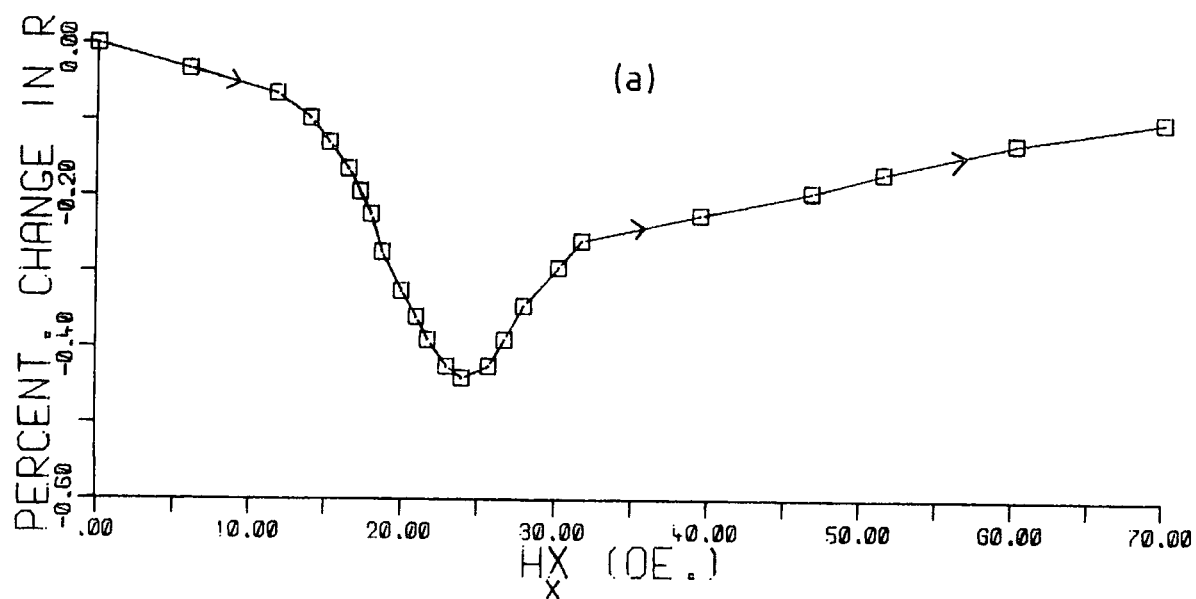


Fig. 7.14 Magnetoresistance in a chevron column with the field applied perpendicular to the column (H_X).

(a) Field increasing from zero to 70 Oe.

(b) Field decreasing back to zero.

Consider the case of a chevron column subjected to a transverse field H_x as in fig 7.6(a). In zero field all domains are magnetized parallel (or antiparallel) to the current so the column resistivity is $\rho_0 + \Delta\rho$. To estimate the percentage drop in resistance caused by a transverse field consider the idealized buckle configuration shown in fig. 7.15(a). This is essentially the interpretation of buckling in $100 \times 12 \times 0.3 \mu\text{m}$ samples given by Huijjer et al. (1979). An 'average resistivity' can be expressed as:

$$\bar{\rho} = \frac{\sum V_i \rho_i}{\sum V_i}$$

where the V_i represent the volumes of individual domains. Considering one wavelength, λ , of the buckle configuration:

$$\begin{aligned} \bar{\rho} &= \frac{1}{\lambda W t} \left[t \lambda (W-l) (\rho_0 + \Delta\rho) + t \lambda l (\rho_0 + \Delta\rho \cos^2 \phi_0) \right] \\ &= \rho_0 + \Delta\rho \left(1 - \frac{l}{W} \sin^2 \phi_0 \right) \end{aligned}$$

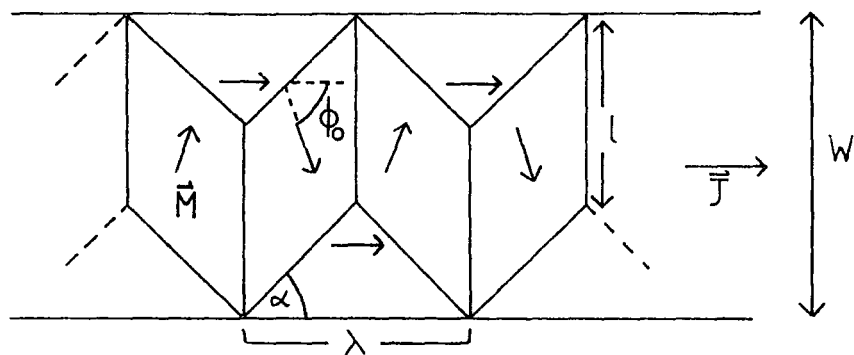
where t is the permalloy thickness and W , l and ϕ_0 are as defined in fig. 7.15. From continuity of the normal component of \vec{M} at domain boundaries:

$$\begin{aligned} \phi_0 &= \pi - 2\alpha \\ \therefore \bar{\rho} &= \rho_0 + \Delta\rho \left(1 - \frac{l}{W} \sin^2 2\alpha \right) \end{aligned} \quad (7.2)$$

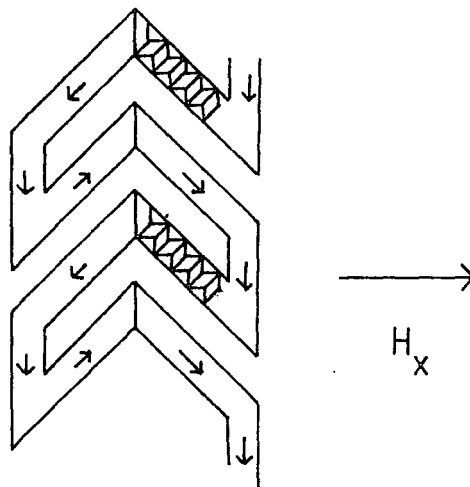
where

$$\alpha = \tan^{-1} 2 \left(\frac{W-l}{\lambda} \right)$$

The contribution from domain walls has been ignored. This can



(a)



(b)

Fig. 7.15 (a) Parameters used to calculate the magnetoresistance for an ideal buckled configuration. The resistance drop can be estimated for a chevron column containing an assumed degree of buckling as in (b)

be justified by comparing the values of λ and W (both of the order of $2\mu\text{m}$) with the wall widths calculated in section 6.1 (of the order of 500\AA). If a fraction p of the column is occupied by buckle and the remainder is assumed to be saturated ($\theta = 0$), the average column resistivity will be:

$$\begin{aligned}\bar{\rho}_{\text{col.}} &= p \left[\rho_0 + \Delta\rho \left(1 - \frac{l}{W} \sin^2 2\alpha\right) \right] + (1-p) \left[\rho_0 + \Delta\rho \right] \\ &= \rho_0 + \Delta\rho \left(1 - p \frac{l}{W} \sin^2 2\alpha\right)\end{aligned}$$

The fractional drop in resistance of the column is therefore:

$$\frac{(\rho_0 + \Delta\rho - \bar{\rho}_{\text{col.}})}{\rho_0 + \Delta\rho} = \frac{\Delta\rho}{\rho_0 + \Delta\rho} \times p \frac{l}{W} \sin^2 2\alpha \quad (7.3)$$

At the Plessey Research Centre the bulk magnetoresistance effect at 25°C was measured and found to be 3.2%, ie. $\frac{\Delta\rho}{\rho_0 + \Delta\rho} \approx 0.032$. The remaining parameters can be estimated by referring back to the ferrofluid pattern in fig. 7.6(a):

$$\begin{aligned}\lambda &\approx W \\ l &\approx \frac{2}{3}W \\ \therefore \alpha &\approx \tan^{-1} \frac{2}{3}\end{aligned}$$

If buckling occurred simultaneously in all bars where the magnetization opposes the applied field p would be approximately 0.36. However fig. 7.6 (which is representative of many ferrofluid observations) suggests that the fraction of the column involved may be only half this value. Substituting $p = 0.18$ and the estimates for λ , l and α given above into equation 7.3 gives 0.33%

as the calculated drop in resistance. This agrees reasonably well with the experimental measurements in transverse fields. For example the curves given in figs 7.13 and 7.14 have minima of -0.29% and -0.44%. respectively.

In fields applied parallel to the column (H_y) the resistance change is generally smaller (eg. 0.2% in fig. 7.12). If the whole column were involved in buckling simultaneously during reversal, equation 7.3 with $p = 1$ would suggest a resistance drop of 1.8%. The fact the actual drop is generally much smaller tends to confirm the view that at a given instant only a fraction of the column is involved in buckling.

7.6 Significance of buckling in a detector column subjected to a rotating field.

Having established the basic behaviour of a chevron column in terms of buckling and magnetization reversal the characteristic magnetoresistive waveform in a uniform rotating drive field can be considered.

Hubbell et al. (1975) made systematic measurements of resistance in a chevron column as a function of the magnitude and orientation of an in-plane field. The geometry of their detector was similar to that studied here (end-connected chevrons as in fig. 7.6) and the scale was also comparable (nominal bar width: $2.5\mu\text{m}$ and column width $20\mu\text{m}$). The permalloy was also sputter deposited to a thickness of 4500Å on glass substrates.

The characteristics of the magnetoresistance waveform vary with the amplitude of rotating field. Fig. 7.16 shows the waveforms in four distinct regions between zero and 90 Oe. A distinctive feature in each region is the frequency of the

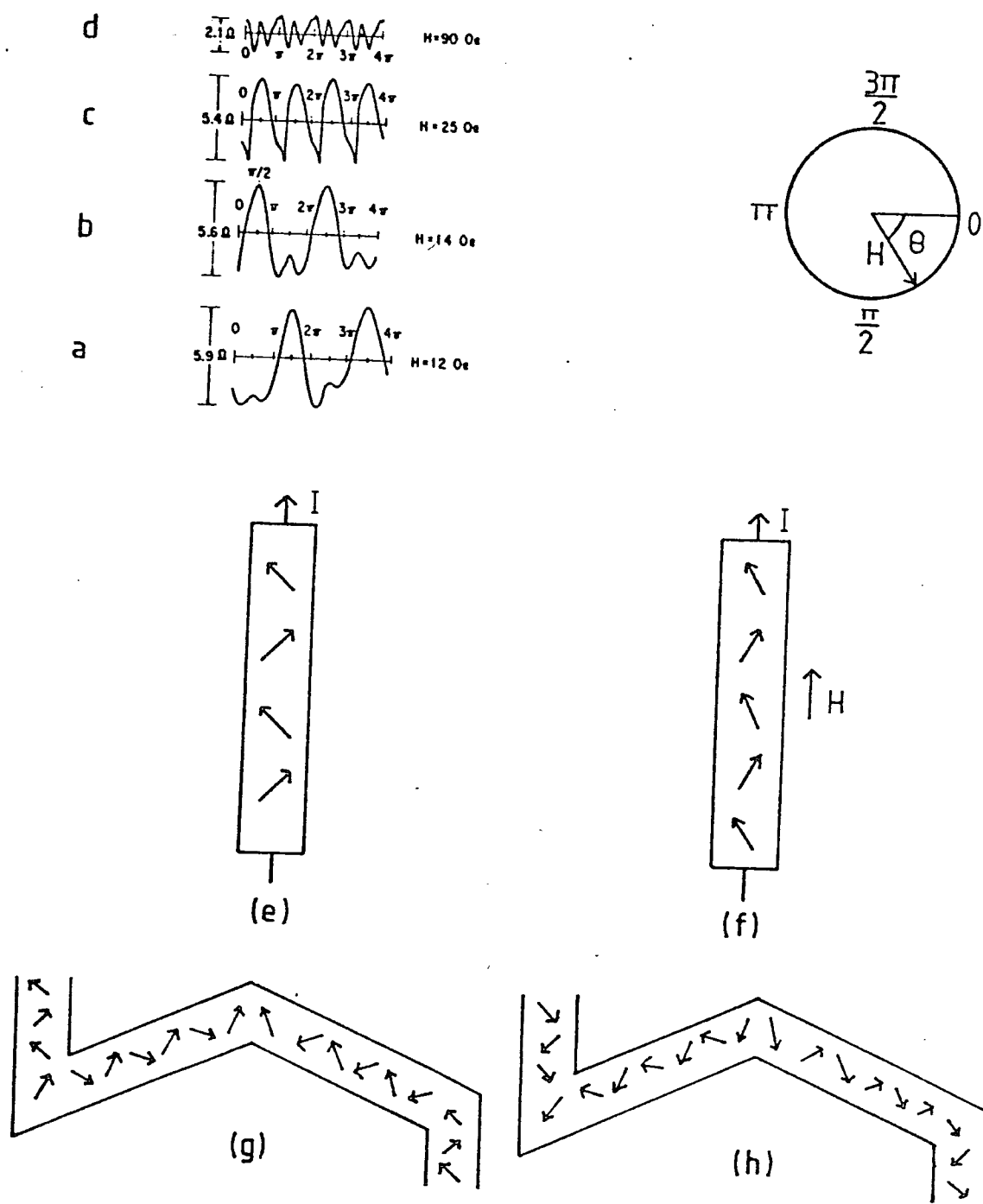


Fig. 7.16 (a),(b),(c),(d) Representative magnetoresistive waveforms for a chevron column (Hubbell et al., 1975). Schematic representations of magnetization fanning in a thin permalloy strip: (e) and (f) and a chevron column: (g) and (h) (West et al., 1975).

response in terms of the frequency of the rotating field (ω). In low fields the wave-form has the same frequency, ω . There is a single peak in resistance each cycle but this peak can occur either at $\theta = \frac{\pi}{2}$ or $\frac{3\pi}{2}$ depending on the magnetic history of the sample. If the sample is subjected to a D.C. field of a few Oe in the direction $\theta = \frac{3\pi}{2}$ or $\theta = \frac{\pi}{2}$ beforehand the subsequent wave-form will peak at $\theta = \frac{3\pi}{2}$ or $\frac{\pi}{2}$ respectively. Above a critical field (for Hubbell's sample, 20 Oe) a 2ω waveform with peaks at $\frac{\pi}{2}$ and $\frac{3\pi}{2}$ is seen (fig. 7.16(c)) and above a second critical field the waveform is found to have four maxima per cycle and a 4ω characteristic (as in fig 7.16 (d) at 90 Oe).

To explain this behaviour, and in particular the ω to 2ω transition, West et al. (1975) postulated that the column possessed a domain structure with magnetization 'fanning'. Fig. 7.16(e) represents a rectangular permalloy bar with a fanned magnetization structure. Applying a field parallel to the average direction of magnetization reduces the degree of fanning and causes the magnetoresistance in that direction to increase (fig. 7.16(f)). Applying a field in the opposite direction causes the fanning to increase and the resistance to fall. According to this model the chevron column can occupy one of two remanent states, each containing an element of fanning as illustrated in fig. 7.16(g) and (h). If the detector occupies the state shown in fig. 7.16 (g) and the applied rotating field has an amplitude which is sufficient to switch the column to its alternative state then the resistance will be highest when the field is applied along $\theta = \frac{3\pi}{2}$ and will be a minimum when $\theta = \frac{\pi}{2}$. The reverse is true if the detector occupies the remanent state shown in fig. 7.16 (h). When the rotating field amplitude exceeds

a critical value the detector can be switched between the two basic states so the resistance peaks twice per cycle, thus explaining the ω to 2ω transition.

The ferrofluid observations and resistance measurements presented earlier can be used to form an alternative model for a detector column in rotating fields. In this model the chevron column is assumed to have two basic remanent states of equal and opposite saturation. The column can in fact be subdivided into sections alternating between these two states (as in the ferrofluid pattern of fig. 7.7 (b)) but it will be assumed that a moderate D.C. field has been applied to establish the whole column in a single state. The saturated state has lower energy than a fanned structure because fanning introduces surface free poles and a positive magnetostatic energy term. The drive field can be resolved into components parallel (H_y) and perpendicular (H_x) to the column. Parallel field components above a critical value H_1 can switch the column between the two basic states. Perpendicular components above a second, broader, level H_2 can switch the direction of magnetization in alternate chevron limbs. H_2 exceeds H_1 (from experiment) and in both cases the switching proceeds via an intermediate stage of magnetization buckling. This causes a drop in resistance.

Consider first the application of a weak rotating field $H < H_1$ to a column with remanent magnetization flow in the direction $\theta = \frac{\pi}{2}$. There will be a peak in magnetoresistance when the field is at $\theta = \frac{\pi}{2}$ because there is no significant change in the domain structure. Fig. 7.12 (b) confirms that there is initially no change in resistance for fields applied parallel to a remanent flow. At $\theta = \frac{3\pi}{2}$ the field is insufficient to reverse

the direction of flow but it will give rise to a certain degree of buckling and a drop in resistance. For intermediate values of θ the resistance will also be less than its peak value since H_x and H_y components may both give rise to a certain degree of buckling depending on the particular magnitude of H . Therefore the actual waveform of fig. 7.16(a), with frequency ω , is consistent with this model. By the same argument an ω frequency characteristic peaking at $\theta = \frac{3\pi}{2}$ will occur if a field $H < H_1$ is applied to a column occupying the alternative remanent state. For drive fields in the region $H_1 \leq H < H_2$, resistance maxima occur at both $\theta = \frac{\pi}{2}$ and $\theta = \frac{3\pi}{2}$ as the column switches between its remanent states. Again the resistance falls for intermediate orientations due to buckling. The H_x component will contribute to buckling but will not be sufficient to completely reverse the direction of magnetization in alternate chevron limbs. The resulting waveform has frequency 2ω as in fig. 7.16(c). Finally when the rotating field exceeds H_2 , switching can occur in alternate chevron limbs to the extent that all limbs are substantially magnetized in the same direction for field orientations $\theta = 0$ and $\theta = \pi$. The resistance should therefore gain two peaks at $\theta = 0$ and π in addition to those at $\frac{\pi}{2}$ and $\frac{3\pi}{2}$. The waveform should have a frequency 4ω in agreement with the experimental curve of fig. 7.16(d) (for which $H = 90$ Oe). That the waveform has a lower amplitude in this region is consistent with fig. 7.12(b) which shows that there is a gradual drop in resistance when the field component parallel to a remanent state is raised significantly above H_1 . Thus a model based on magnetization buckling can account for both the $\omega:2\omega$ transition and the $2\omega:4\omega$ transition in stronger fields. The model agrees with the

observations of Kryder et al. (1980) who detected magnetization buckle in a detector column just below the $\omega : 2\omega$ transition. This transition has the potential to produce a large output signal during bubble detection (George et al., 1976). According to these authors a stripe domain can be considered as temporarily shifting the amplitude of the in-plane field by approximately 8 Oe. Therefore a detector operating in a drive field just below the $\omega : 2\omega$ transition will produce a larger bubble signal since it is temporarily elevated into the 2ω region. However the switching field (H_1) for the $\omega : 2\omega$ transition is generally well below the level of drive field used in a $16\mu\text{m}$ -period bubble device (typically around 40 Oe.) This is confirmed by the measurements made here of switching fields (based on ferrofluid observations and magnetoresistance measurements). H_1 can be modified by the positioning of connecting bars between chevrons, also by the choice of permalloy thickness. (figs. 7.10, 7.11). Even so the best case of a thin ($0.3\mu\text{m}$) detector with end-connected chevrons had a switching field of only 27 Oe. Using thinner permalloy would not be feasible since this would limit the detector current and also enhance the saturation and remanence effects observed in propagation elements. In stronger fields the $2\omega : 4\omega$ transition comes into effect but this transition is much broader. The difference is explained by the basic mechanisms of reversal involved.

8.1 Introduction.

The magnetic field associated with a given distribution of magnetization in a body can be calculated using equation 2.10 given in chapter 2:

$$\vec{H} = \frac{1}{4\pi} \text{grad} \left[\int_S \frac{\vec{M} \cdot \hat{n}}{r} dS + \int_V \frac{\vec{\nabla} \cdot \vec{M}}{r} dV \right]$$

The first integral is taken over the surface of the body where \hat{n} is a unit vector normal to the surface at the point of integration directed into the body. In each case r is the distance between the point of integration and the field point. If for the purpose of calculation the concept of 'magnetic free poles' is introduced, equation 2.10 can be interpreted in terms of surface and volume free pole densities. The element of surface dS produces a field

$$d\vec{H} = \frac{\sigma dS \vec{r}}{4\pi r^3} \quad (8.1)$$

where $\sigma = -\vec{M} \cdot \hat{n}$ is the surface free pole density and \vec{r} is a vector between the surface element and the field point. This form was used for example by Craik (1966) to calculate fields from magnetically subdivided surfaces carrying surface pole density. The equivalent expression for the field component from an element of volume dV is

$$d\vec{H} = \frac{\rho dV \vec{r}}{4\pi r^3} \quad (8.2)$$

where $\rho = -\vec{\nabla} \cdot \vec{M}$ is the volume free pole density. The field associated with a permalloy element can be calculated once the distribution of magnetization is defined, for example in terms of domain structure.

Compared with the number of continuum models which have been developed for permalloy bars there have been few attempts to calculate the magnetostatic fields on the basis of a domain structure. For rectangular bars Della Torre and Kinsner (1973) used a model containing a single domain wall as illustrated in fig. 8.1(a) whilst Khaiyer (1976,b) produced a model which included triangular closure domains (fig. 8.1(b)). In both cases the magnetization in domains was assumed to be uniform and walls were assumed to remain rigid as they moved under the influence of applied fields. Both models seem unrealistic considering the observed behaviour of domain walls in real-size overlay bars. Many bars do not contain closure domains at all (because of the rounded shape of the ends) and the walls which are present are far from rigid. The typical behaviour is illustrated schematically in fig. 8.2. When a longitudinal field is applied the single Bloch wall bows and stretches and at $H = H_g$ part of the wall comes into contact with the edge of the bar. It has been established that the wall displacement versus field is approximately linear up to this point (Lin (1972), Khaiyer and O'Dell (1976)). The problem with modelling this type of behaviour is that colloid patterns reveal only the domain wall. Without additional information on the distribution of magnetization within domains the magnetic field sources are not clearly defined. Fig. 8.2(a) and (b) illustrates two extreme cases. In (a) the magnetization within

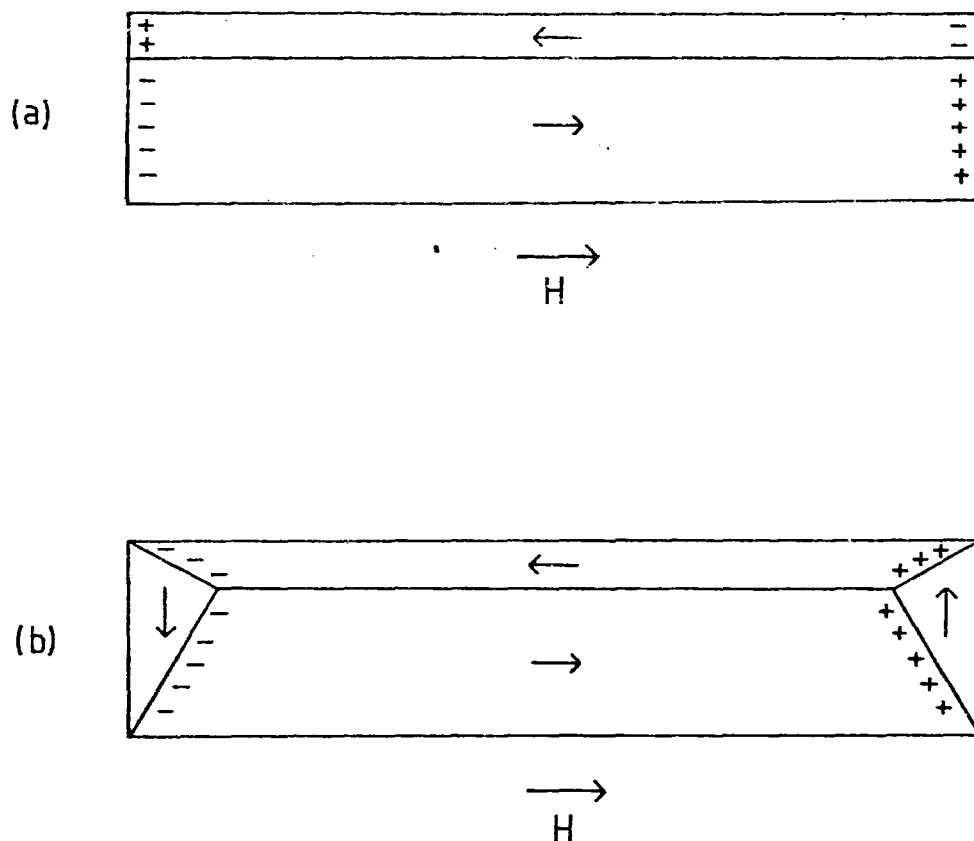


Fig. 8.1 Previous domain models for a rectangular bar
 (a) Della Torre and Kinsner (1973) (b) Khaiyer
 (1976,b).

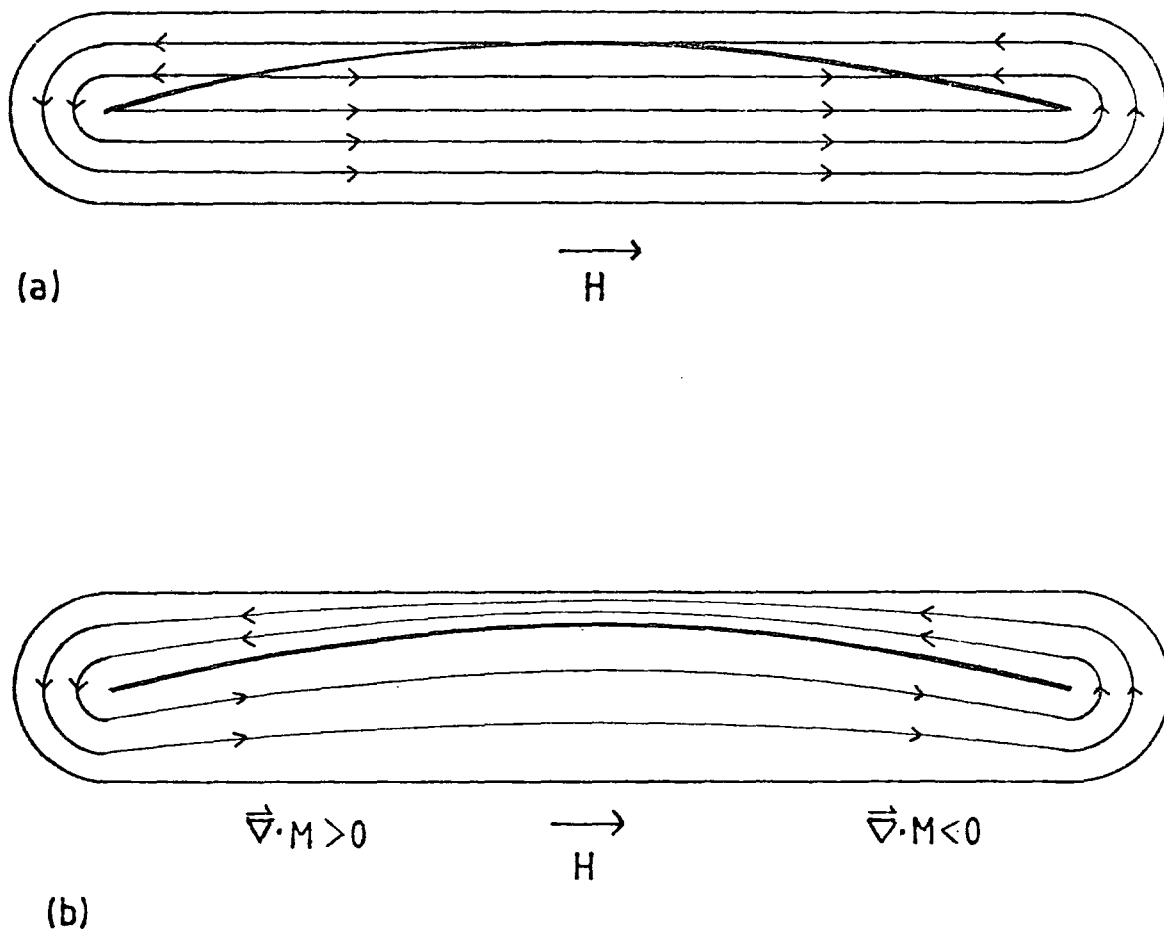


Fig. 8.2 Two possible interpretations for the observed bowing of a Bloch wall. Lines are drawn to represent the flow of magnetization (at each point the local \vec{M} -vector is parallel to these lines).

domains is assumed to remain uniform ($\vec{\nabla} \cdot \vec{M} = 0$) so the pole density is carried entirely by the domain wall. In (b) the domain magnetization is non-uniform, the positive and negative magnetic poles are associated with convergence of \vec{M} in one half of the bar and divergence of \vec{M} in the other in such a way that the Bloch wall has zero surface pole density. Fig. 8.2 (a) and (b) could be viewed as two limiting cases. The situation in a real bar might lie somewhere between. For either case expressions can be obtained for the pole density.

8.2 'Free-pole' density.

Let the domain wall displacement be described by some function $y = f(x)$, where x represents distance along the bar axis. Consider a rectangular element of thickness dx located at x . If the magnetization within domains is uniform, the portion of Bloch wall within this element carries a surface pole density:

$$\sigma(x) = -2M_s \sin\theta$$

where θ is as defined in fig. 8.3 (a). Therefore since

$$\sin\theta = \frac{dy}{dx} \left[1 + \left(\frac{dy}{dx} \right)^2 \right]^{-\frac{1}{2}},$$

$$\sigma(x) = -2M_s \frac{dy}{dx} \left[1 + \left(\frac{dy}{dx} \right)^2 \right]^{-\frac{1}{2}} \quad (8.3)$$

The alternative configuration is shown in fig. 8.3(b). Suppose in this case there is a uniform volume pole density within the element at x :

$$\rho(x) = -(\vec{\nabla} \cdot \vec{M})_x$$

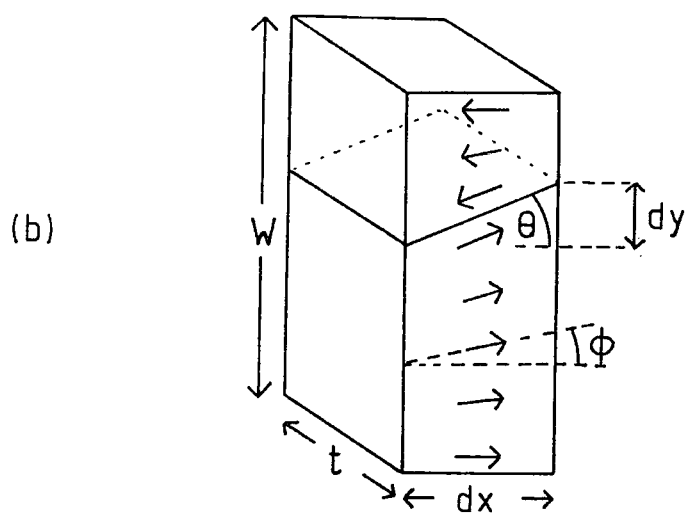
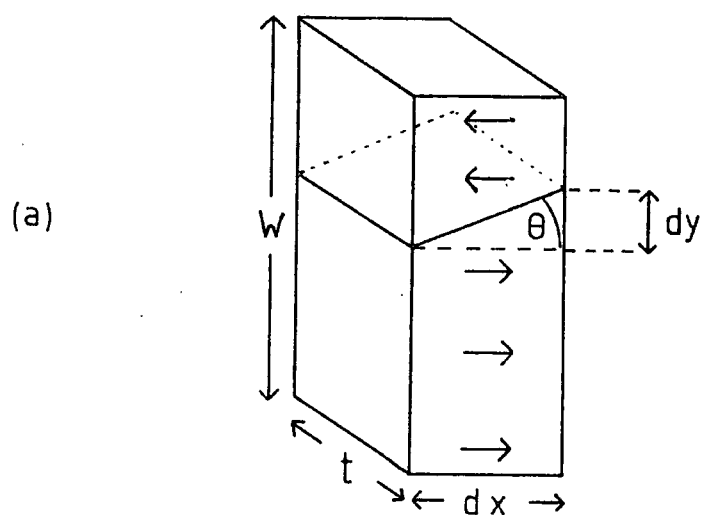


Fig.8.3 Illustrating how (a) the surface pole density or (b) the volume pole density can be related to the wall displacement $y = f(x)$.

(This is effectively a one-dimensional continuum model.)

Applying Gauss' theorem to the element:

$$\int_V \vec{\nabla} \cdot \vec{M} dV = \int_S \vec{M} \cdot \hat{n} dS$$

where the first integral is taken over the volume of the element and the second is taken over its surface (\hat{n} is a unit vector normal to the surface at the point of integration, directed out of the element.) Since $\vec{\nabla} \cdot \vec{M}$ is assumed uniform within the element:

$$-\rho(x)Wtdx = \int_S \vec{M} \cdot \hat{n} dS$$

where W is the bar width and t is the permalloy thickness. The value of $\vec{M} \cdot \hat{n}$ is zero except on the two surfaces normal to the x -axis. Here $\vec{M} \cdot \hat{n} = \pm M_s \cos \phi$ where ϕ defines the direction of the local \vec{M} -vector as illustrated. Contributions to the surface integral from opposite sides of the element cancel except in the section of width dy . On both sides of this section:

$$\vec{M} \cdot \hat{n} = M_s \cos \theta$$

$$\therefore \int_S \vec{M} \cdot \hat{n} dS = 2tdy M_s \cos \theta$$

$$\rho(x) = -2 \frac{M_s}{W} \frac{dy}{dx} \cos \theta$$

Substituting $\cos \theta = \left[1 + \left(\frac{dy}{dx} \right)^2 \right]^{-\frac{1}{2}}$ gives

$$\rho(x) = -2 \frac{M_s}{W} \frac{dy}{dx} \left[1 + \left(\frac{dy}{dx} \right)^2 \right]^{-\frac{1}{2}} \quad (8.4)$$

The volume pole density is inversely proportional to the bar width, W , whilst the 'charged wall' pole density, σ , is independent of W .

In order to proceed further information is required on the wall displacement, y , preferably in an analytical form. According to Ma (1976) the variation of the average magnetization along a permalloy bar (measured with the Kerr effect) resembles the corresponding variation in cross-sectional area for an inscribed ellipsoid. Therefore as a first approximation it would seem reasonable to represent the wall bowing with the equation for an ellipse:

$$\frac{x^2}{a^2} + \frac{y^2}{b^2} = 1 \quad (8.5)$$

where the major axis $2a$ corresponds to the distance between the ends of the domain wall and b defines the amplitude of wall bowing. (Only positive values of y are used.) For a permalloy bar of length L and width W containing a single 180° Bloch wall as in fig. 8.2 :

$$2a \hat{=} L - W$$

In the following calculations it will be assumed that the two ends of the wall remain fixed so a is constant. As the applied field increases from zero to H_s (the field required for partial saturation), b increases from zero to $W/2$. Substituting eqn. 8.5 into eqns. 8.3 and 8.4 gives:

$$\sigma(x) = \frac{2M_s b x}{(a^4 - (a^2 - b^2)x^2)^{\frac{1}{2}}} \quad (8.6)$$

for the charged wall model and :

$$\rho(x) = \frac{2M_s b x}{w(a^4 - (a^2 - b^2)x^2)^{\frac{1}{2}}} \quad (8.7)$$

for the volume free pole model. In each case the magnetic pole density is zero in the middle of the bar and increases to a maximum value at the ends of the domain wall. Magneto-static fields associated with the permalloy bar can now be calculated.

8.3 Demagnetizing Field.

The coordinates used for calculating the demagnetizing field for a curved wall bearing magnetic charge are illustrated in fig. 8.4(a). For convenience cartesian coordinates with origin at the centre of the bar are chosen. The element of wall dS at (x, y, z) creates a magnetic field $d\vec{H}$ at P, a point in the midplane of the bar with coordinates $(0, y', 0)$:

$$d\vec{H} = \frac{\sigma dS \vec{r}}{4\pi r^3}$$

where \vec{r} is the vector between dS and P; $r^2 = x^2 + (y' - y)^2 + z^2$

$$\begin{aligned} dS &= dz(dx^2 + dy^2)^{\frac{1}{2}} \\ &= dz dx \left[1 + \left(\frac{dy}{dx}\right)^2 \right]^{\frac{1}{2}} \end{aligned}$$

and from eqn. 8.3 the charge density on the wall is :

$$\begin{aligned} \sigma &= -2M_s \frac{dy}{dx} \left[1 + \left(\frac{dy}{dx}\right)^2 \right]^{-\frac{1}{2}} \\ \therefore \sigma dS &= -2M_s dy dz \quad (8.8) \end{aligned}$$

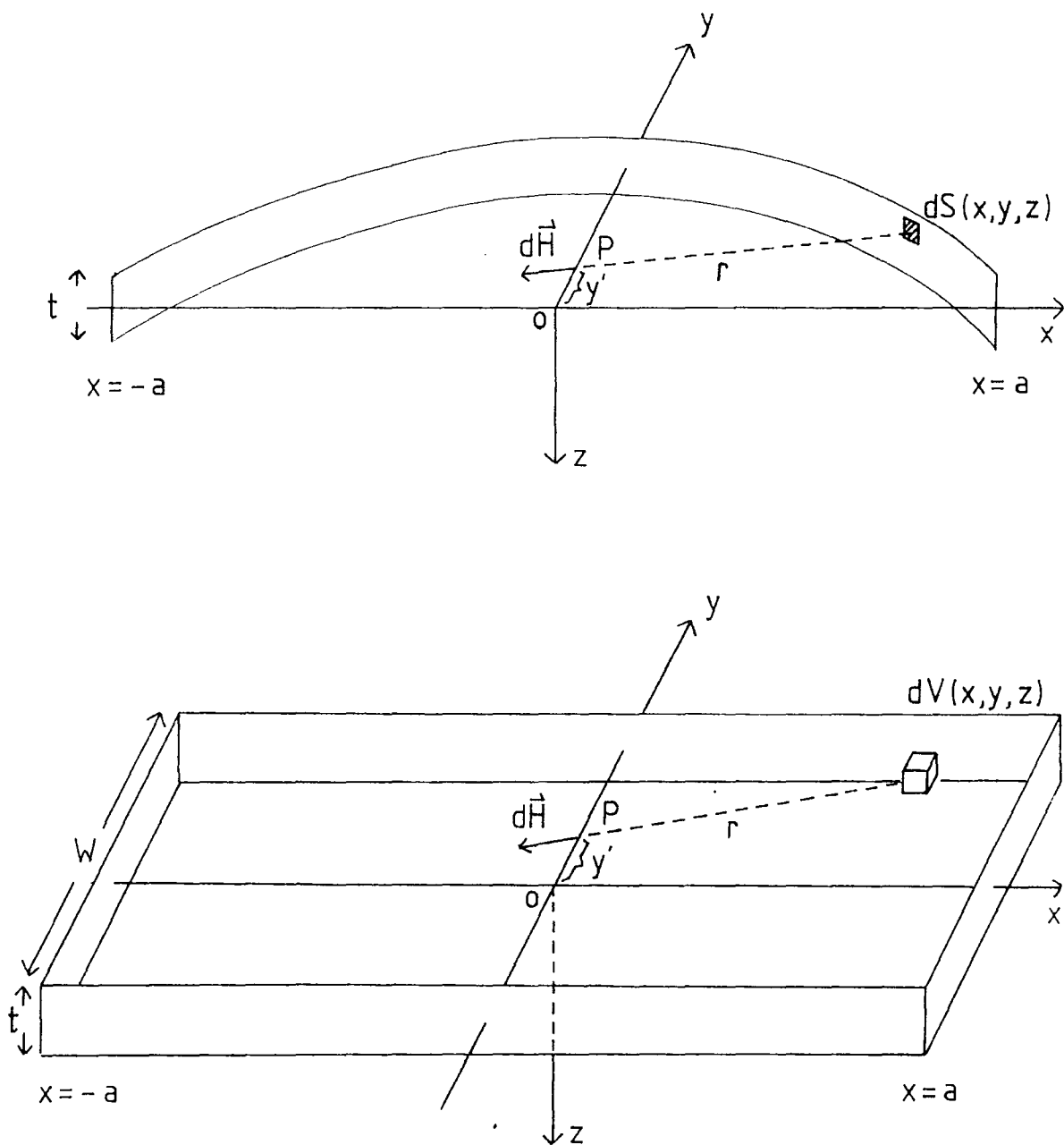


Fig. 8.4 Coordinates used for calculating the internal demagnetizing field at the mid-plane of a bar containing (a) a charged wall or (b) a volume distribution of pole density.

The component of $d\vec{H}$ parallel to the x-axis is:

$$dH_x = \frac{\sigma dS x}{4\pi r^3}$$

$$\therefore dH_x = \frac{M_s x dy dz}{2\pi r^3}$$

Because the wall is symmetrical about the yz-plane in shape (and asymmetrical in charge) the total x-component field at P is twice the integral of dH_x over one half of the wall ($x = 0$ to a or $y = b$ to 0).

$$H_x(0, y', 0) = -\frac{M_s}{\pi} \int_0^b \int_{-\frac{t}{2}}^{\frac{t}{2}} \frac{x dy dz}{[x^2 + (y' - y)^2 + z^2]^{3/2}} \quad (8.9)$$

where $x = a(1 - \frac{y^2}{b^2})^{\frac{1}{2}}$

The coordinates used for calculating H_x in the case where the magnetic pole density is spread through the volume of the bar are illustrated in fig. 8.4(b). In this case the elemental volume dV at (x, y, z) carries a pole density ρ and the corresponding field element at P is:

$$d\vec{H} = \frac{\rho dV \vec{r}}{4\pi r^3}$$

where \vec{r} is as defined previously. The x-component field at P is:

$$dH_x = \frac{\rho dV x}{4\pi r^3}$$

The total x-component field at P is twice the integral of dH_x

from $x = 0$ to a , $y = -\frac{W}{2}$ to $\frac{W}{2}$ and $z = -\frac{t}{2}$ to $\frac{t}{2}$. Therefore substituting the expression for $\rho(x)$ from eqn.8.4;

$$H_x = -\frac{M_s b}{\pi W} \int_0^a \int_{-\frac{W}{2}}^{\frac{W}{2}} \int_{-\frac{t}{2}}^{\frac{t}{2}} \frac{x^2 dx dy dz}{(a^4 - (a^2 - b^2)x^2)^{\frac{1}{2}} (x^2 + (y'-y)^2 + z^2)^{3/2}}$$

$$= -\frac{M_s b t}{\pi W} \int_0^a \int_{-\frac{W}{2}}^{\frac{W}{2}} \frac{x^2 dx dy}{(a^4 - (a^2 - b^2)x^2)^{\frac{1}{2}} (x^2 + (y'-y)^2) (x^2 + (y'-y)^2 + \frac{t^2}{4})^{\frac{1}{2}}}$$
(8.10)

since $\int \frac{du}{(a^2 + u^2)^{3/2}} = \frac{u}{a^2(a^2 + u^2)^{\frac{1}{2}}}$

If magnetostatic energy dominates the behaviour of a permalloy bar the distribution of \vec{M} and the resulting pole density should create a demagnetizing field which is everywhere equal and opposite to the applied field for minimum energy. Therefore if the demagnetizing field H_x can be calculated as a function of wall displacement, the response of a permalloy bar to a uniform in-plane field H_a can be found by setting $H_x = -H_a$.

Unfortunately the demagnetizing fields computed from eqns. 8.9 and 8.10 are non-uniform. Fig. 8.5 shows the variation in H_x across the width of a bar (at $x = 0$). The bar dimensions are $25 \times 2.1 \times 0.3 \mu\text{m}$ and the parameter b has been given the value $1.05 \mu\text{m}$. This corresponds to partial saturation with the curved Bloch wall extended to the edge of the bar. For the charged wall model, fig. 8.5 shows that H_x increases almost linearly across the bar and then becomes infinite on the

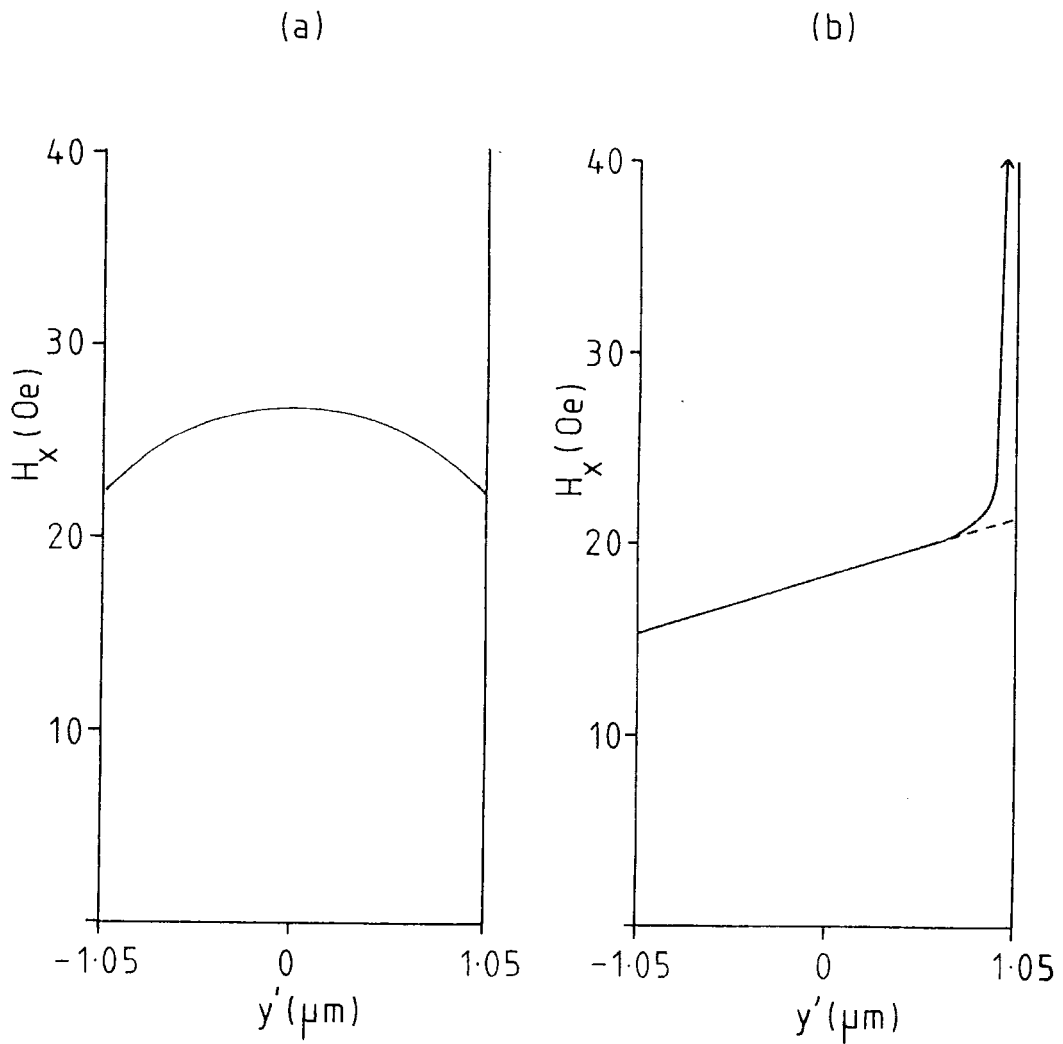


Fig. 8.5 Variation in demagnetizing field (H_x) across the width of a bar (y' -axis) at $x = 0$ for (a) a volume distribution of free pole density and (b) a charged wall. The bar dimensions are $25 \times 2.1 \times 0.3 \mu\text{m}$ and the Bloch wall is located at $y' = 1.05 \mu\text{m}$.

wall itself. For the volume free-pole' model, H_x varies symmetrically about the centre of the bar.

These variations reflect the fact that neither model necessarily represents the exact situation in a real bar. However, useful estimates for the magnitude of H_x can be obtained by averaging across the width of the bar. For the volume free-pole model this is straightforward and for the charged wall model a reasonable value can be extracted by extrapolating the linear region (as suggested by the dashed line in fig. 8.5) thereby avoiding the unrealistic singularity at the domain wall. Values of H_s predicted in this way for I-bars $25 \times 2.1 \mu\text{m}$ and $15 \times 2.1 \mu\text{m}$ are plotted in fig. 8.6 and fig. 8.7 together with the measured saturation fields. The calculated values increase linearly with permalloy thickness t and agree in order of magnitude with the measurements. The agreement is rather better for the charged wall model though even in this case the measured points are a few Oe less than predicted. The calculated ratio between the $15 \mu\text{m}$ and $25 \mu\text{m}$ bars is 2.77 compared with the measured ratio of 2.99. Also plotted in fig. 8.6 and fig. 8.7 are saturation fields predicted by an ellipsoidal approximation and by Copeland's approximation (eqn. 4.3). The former are obtained from the demagnetizing factor of an inscribed ellipsoid with axes corresponding to the dimensions of the bar. Osborn (1945) gave the following expression for the relevant demagnetizing factor in an ellipsoid with semi-major axes $a \gg b \gg c > 0$:

$$\frac{L}{4\pi} = \frac{\cos\phi \cos\theta}{\sin^3\theta \sin^2\alpha} [F(k,\theta) - E(k,\theta)] \quad (\text{c.g.s.})$$

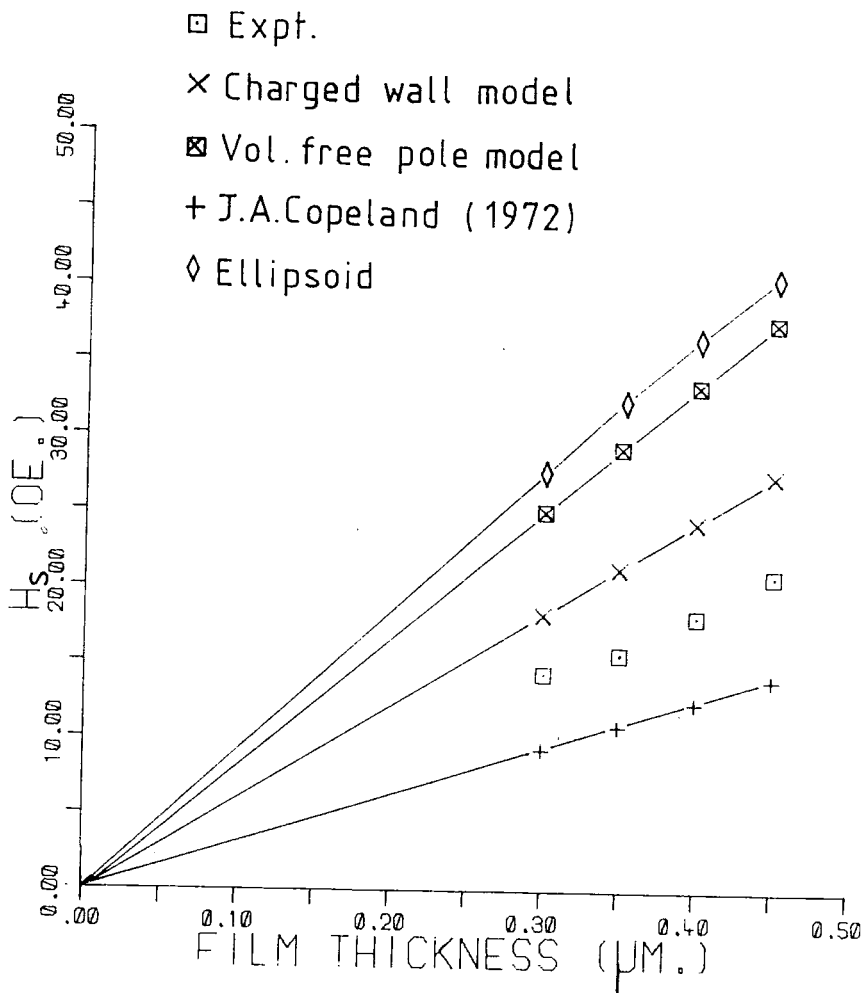


Fig.8-6 Calculated and experimentally measured saturation fields in permalloy bars $25 \times 2.1 \mu\text{m}$

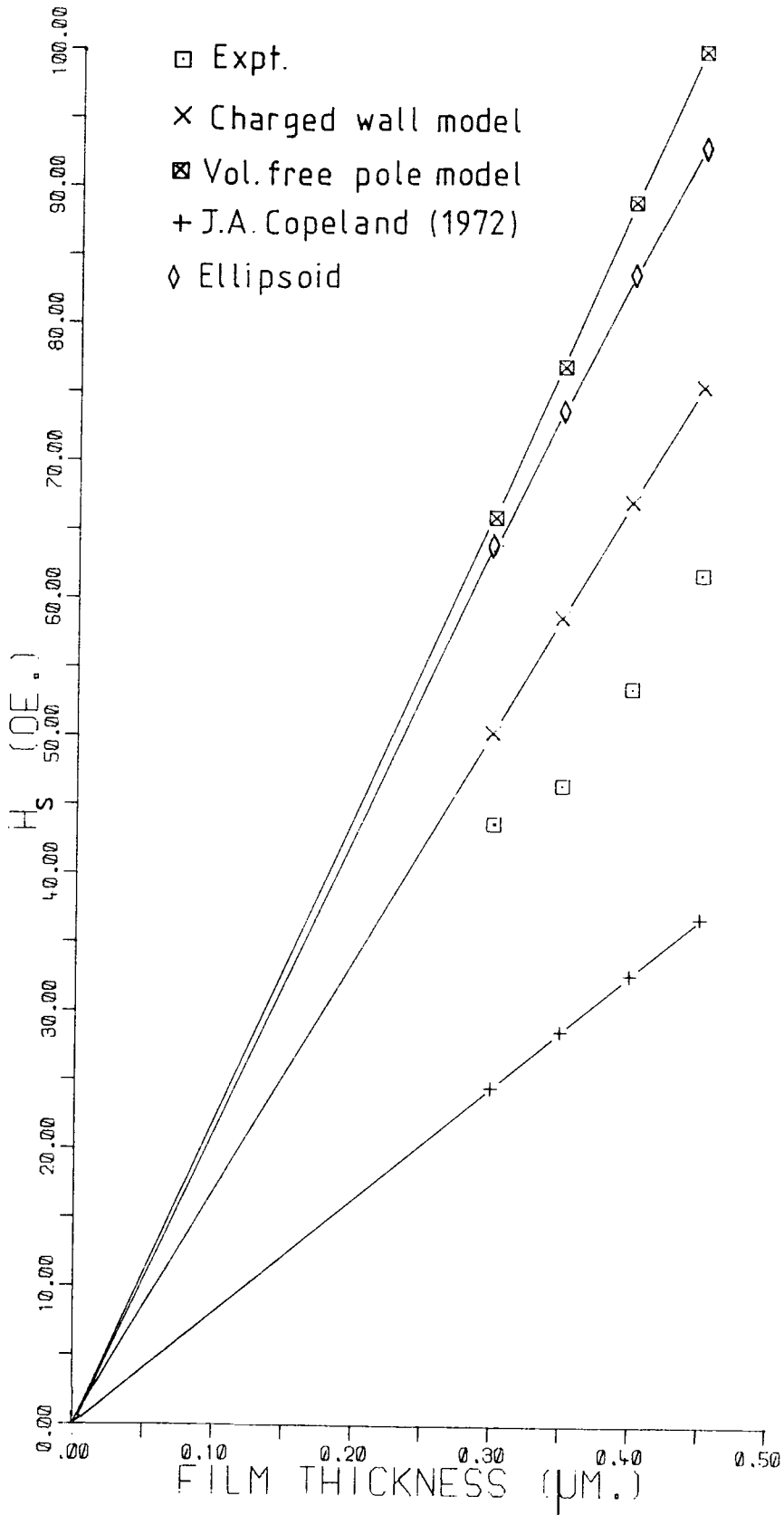


Fig. 8-7 Calculated and experimentally measured saturation fields in permalloy bars 15X2.1 μm.

where $\cos \theta = \frac{c}{a}$, $(0 \leq \theta \leq \frac{\pi}{2})$, $\cos \phi = \frac{b}{a}$ $(0 \leq \phi \leq \frac{\pi}{2})$

$$\sin \alpha = \frac{\sin \phi}{\sin \theta} = k \quad (0 \leq \alpha \leq \frac{\pi}{2})$$

and $F(k, \theta)$ and $E(k, \theta)$ are elliptic integrals of the first and second kinds. For a flat ellipsoid ($a \gg b \gg c$) the following approximation is valid:

$$\frac{L}{4\pi} = \frac{c}{a} \sqrt{(1-e^2)} \frac{K - E}{e^2}$$

where K and E are complete elliptic integrals whose argument is :

$$e = \left(1 - \frac{b^2}{a^2}\right)^{\frac{1}{2}}$$

This explains why the ellipsoidal values in figs. 8.6 and 8.7 increase almost linearly with thickness. In a study of the average magnetization in arrays of I-bars by the Kerr effect, Ma (1976) found that centre saturation could be predicted to within about 5% by this approximation. In the present case the predicted values are roughly 50% larger than the measured points .

For a given bar the demagnetizing field can be calculated as a function of the parameter b between zero and $\frac{W}{2}$. The wall displacement for a given applied field can then be predicted for $0 \leq H \leq H_s$. The result shown in fig. 8.8 for the case of a $25 \times 2.1 \times 0.3 \mu\text{m}$ bar containing a charged wall, is a linear relationship. Although the bars studied here were rather narrow for accurate measurements of wall displacement, the

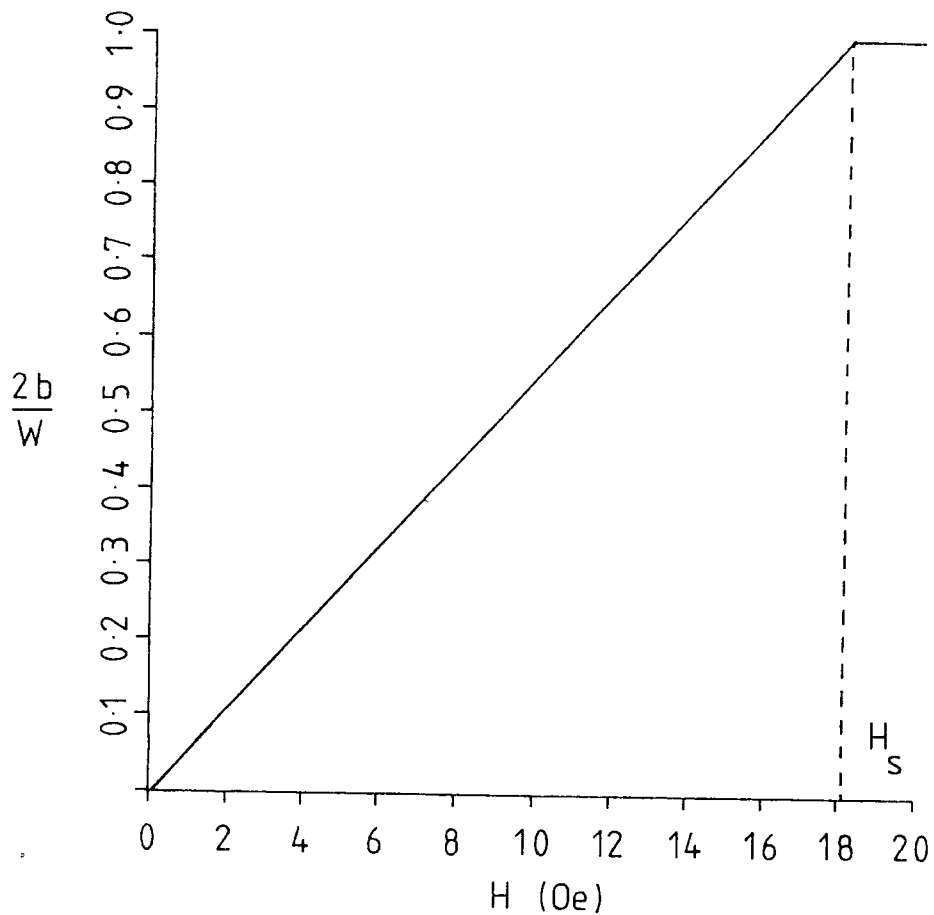
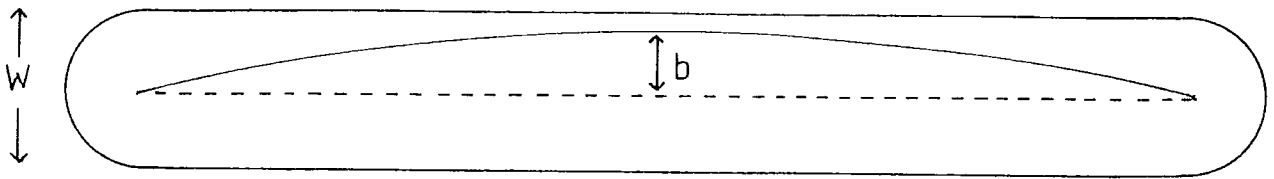


Fig.8.8 The calculated demagnetizing fields increase in proportion to the parameter b , therefore a linear relationship between wall displacement and applied field is predicted up to saturation. (Values plotted for a $25 \times 2.1 \times 0.3$ μm bar using 'charged wall' model.)

results obtained for larger bars by Lin (1972) and Khaiyer and O'Dell (1976) were approximately linear.

Unfortunately only two types of I-bar were available for investigation on the 16- μm period circuits fabricated. As a matter of interest the rectangular bars studied by Huijer et al. (1979) had dimensions 100x12x0.3 μm . and were observed to saturate in the centre at approximately 7.5 Oe. For this size of bar the charged wall model and the volume-free pole model predict $H_s = 6.6$ Oe and $H_s = 8.6$ Oe respectively. However it is worth noting that these rectangular bars possess closure domain walls at the ends of the bar as well as the basic 180° Bloch wall along the centre.

Finally the predicted dependence of H_s on aspect ratio (length to width ratio) is plotted in fig. 8.9. The bar width and thickness are fixed at 2.1 μm and 0.3 μm respectively.

8.4 External Field.

The models described in the previous section can be used to establish whether a curved domain wall will produce the type of external field observed experimentally for permalloy bars. Only the vertical (z-component) field was computed as it is this component which determines the magnetostatic potential well experienced by a bubble domain.

The field well produced by an isolated bar containing a charged wall can be calculated using the coordinate system shown in fig.8.10(a). The element of area dS at (x,y,z) carries a pole density σ and produces a field dH at $P(x',y',z')$

$$d\vec{H} = \frac{\sigma dS \vec{r}}{4\pi r^3}$$

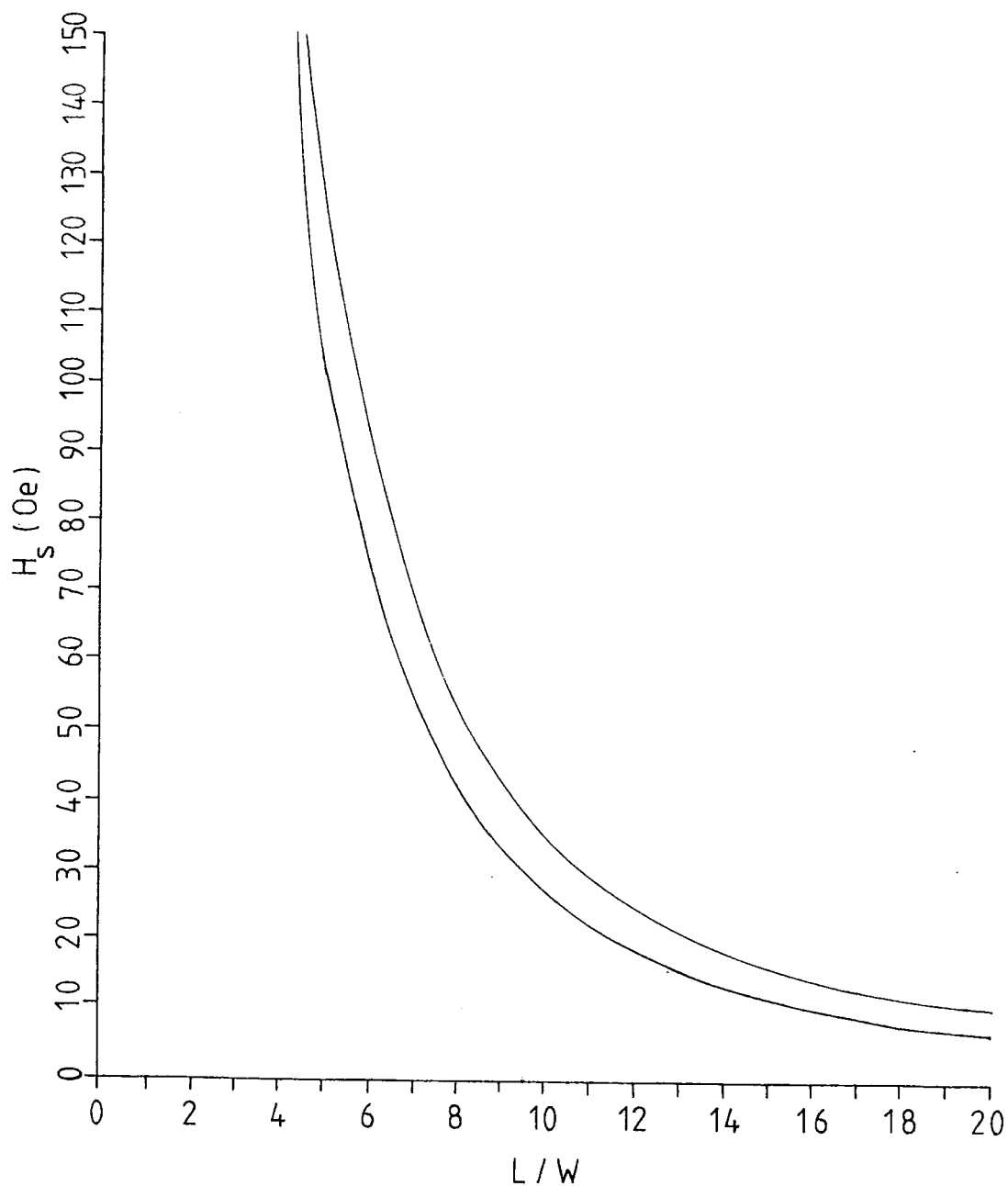


Fig. 8.9 Predicted dependence of saturation field. (H_s) on length/width ratio (upper curve: 'volume free pole' model, lower curve: 'charged wall' model). Bar width and thickness fixed at $2.1\mu\text{m}$ and $0.3\mu\text{m}$ respectively.

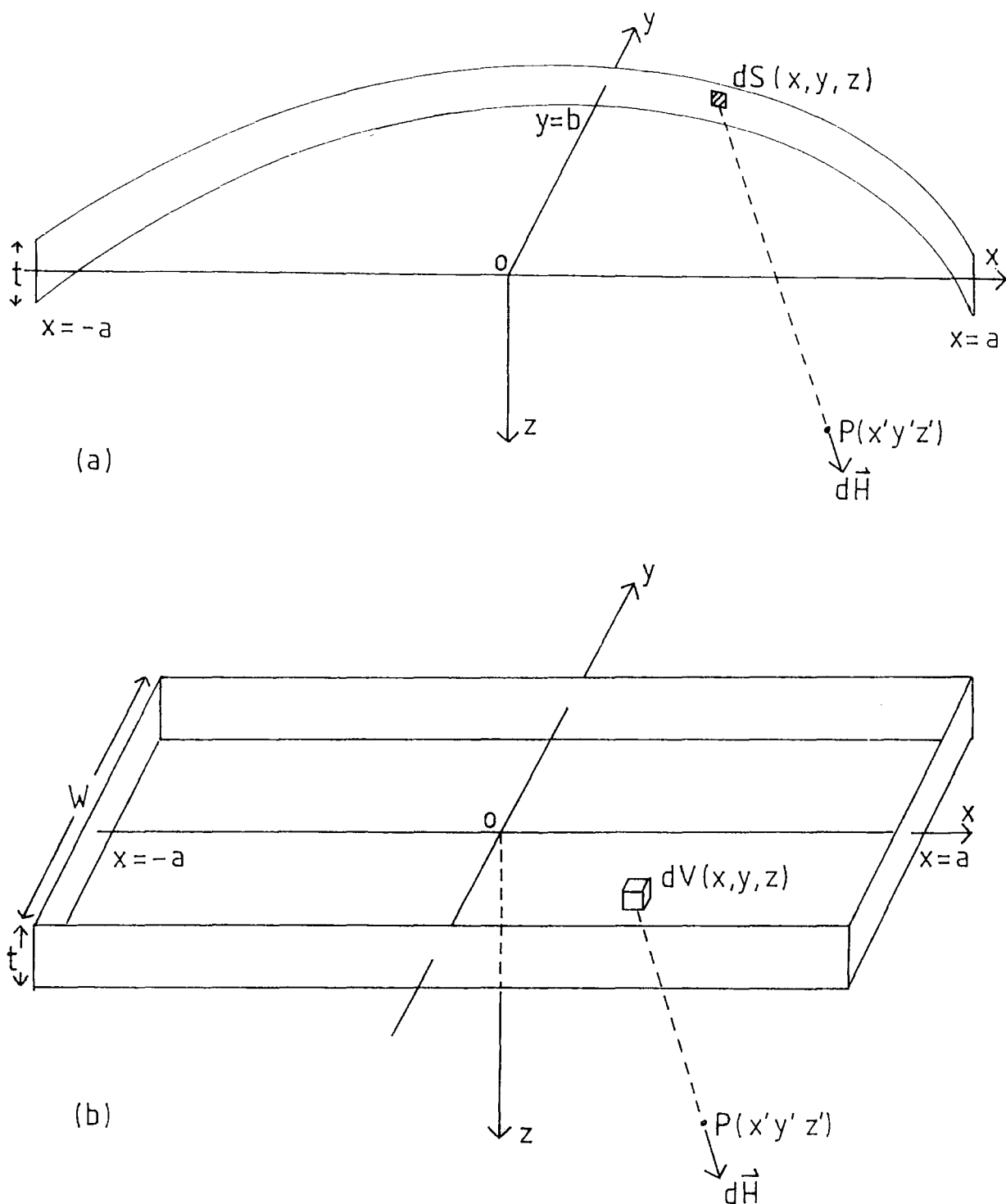


Fig. 8.10 Coordinates used for calculating the z -component external field associated with (a) a charged wall or (b) a volume distribution of pole density.

where $r^2 = (x'-x)^2 + (y'-y)^2 + (z'-z)^2$

As in the calculation of demagnetizing fields ((8.8),

$$\sigma dS = -2M_s dz dy$$

The z-component of the field at P is:

$$\begin{aligned} dH_z &= \frac{\sigma dS (z'-z)}{4\pi r^3} \\ &= \frac{-2M_s dz dy (z'-z)}{4\pi [(x'-x)^2 + (y'-y)^2 + (z'-z)^2]^{3/2}} \end{aligned}$$

The total z-component field at P is obtained by integrating over the entire surface of the wall which extends from $x = -a$ to $x = a$:

$$\begin{aligned} H_z(x', y', z') &= \frac{M_s}{2\pi} \int_{-\frac{t}{2}}^{\frac{t}{2}} \int_{y=0}^b \frac{(z'-z) dy dz}{[(x'-x)^2 + (y'-y)^2 + (z'-z)^2]^{3/2}} \\ &\quad \text{with } x = -\sqrt{a^2(1-\frac{y^2}{b^2})} \\ &+ \frac{M_s}{2\pi} \int_{-\frac{t}{2}}^{\frac{t}{2}} \int_{y=0}^b \frac{(z'-z) dy dz}{[(x'-x)^2 + (y'-y)^2 + (z'-z)^2]^{3/2}} \\ &\quad \text{with } x = +\sqrt{a^2(1-\frac{y^2}{b^2})} \end{aligned} \tag{8.11}$$

If the bar contains a volume distribution of free pole density the coordinates shown in fig. 8.10(b) can be used to calculate the field well. In this case the elemental volume dV at (x, y, z) carries a pole density ρ and produces a field $d\vec{H}$ at

$\rho(x', y', z')$:

$$d\vec{H} = \frac{\rho dV \vec{r}}{4\pi r^3}$$

where $r^2 = (x'-x)^2 + (y'-y)^2 + (z'-z)^2$ and :

$$\rho(x) = \frac{2b}{W} M_s \times (a^4 - (a^2 - b^2)x^2)^{-\frac{1}{2}}$$

The z component of dH is :

$$dH_z = \frac{\rho dV (z' - z)}{4\pi r^3}$$

where $dV = dx dy dz$.

The total z component field at P is obtained by integrating over the volume of the bar :

$$H_z(r) = \frac{M_s \cdot b}{2\pi W} \int_{-a}^a \int_{-\frac{W}{2}}^{\frac{W}{2}} \int_{-\frac{t}{2}}^{\frac{t}{2}} \frac{x(z'-z) dx dy dz}{(a^4 - (a^2 - b^2)x^2)^{\frac{1}{2}} [(x'-x)^2 + (y'-y)^2 + (z'-z)^2]^{3/2}} \quad (8.12)$$

Figure 8.11 shows the field well computed for a bar with dimensions $25 \times 2.1 \times 0.4 \mu\text{m}$ calculated on the basis of a charged domain wall (eqn. 8.11). It has been assumed that the centre of the bar is 50% saturated, i.e. $b = 0.525 \mu\text{m}$. According to the results of the previous section this degree of magnetization would be supported by an in-plane field of $0.5H_s$. The variation in H_z is plotted as a function of x' and y' at $z' = 3.2 \mu\text{m}$. This corresponds to the mid-plane of the bubble medium assuming that the latter is $4 \mu\text{m}$ thick (approximately the bubble diameter for this size of bar) and that there is a spacer layer $1 \mu\text{m}$ thick. The bar produces a 'parabolic' shaped

well with a reasonable degree of cylindrical symmetry about a vertical axis. This is the type of well which has been predicted previously using continuum models (e.g. O'Dell, 1974) and measured experimentally from bubble observations (e.g. George and Chen, 1972). The centre of the well is located some distance in from the end of the bar (approximately $2.3\mu\text{m}$) and this also agrees with experimental observations. The centre of the well is actually displaced a small distance ($0.2\mu\text{m}$) along the positive y' axis in the direction of wall bowing.

In fig. 8.11(c) the variation in well depth is plotted as a function of z' between the imagined upper and lower surfaces of the bubble medium. H_z decays rapidly with z' but the average value is not far from the field magnitude at the mid-plane. (This is why the field well is plotted at $z' = 3.2\mu\text{m}$ in (a)(b)).

In fig. 8.12 the computed field profile is plotted for the same bar with the same degree of magnetization. In this case the pole density associated with the curved domain wall is assumed spread through the volume of the bar and eqn. 8.12 is employed. The field well is similar in shape and magnitude to that plotted for the charged domain wall. The actual values of H_z differ by a few Oe. For the 'volume free pole' model the centre of the well is located at $x' = 10.67\mu\text{m}$ and $y' = 0$. For the 'charged wall' model the well centre is at $x' = 10.23\mu\text{m}$ and $y' = 0.2\mu\text{m}$.

8.5 Permanent Stray Field of the Bloch Wall.

In the preceding calculations the stray fields arising from the intersection of a Bloch wall with the external surface were ignored. An estimate of the fields can be made by

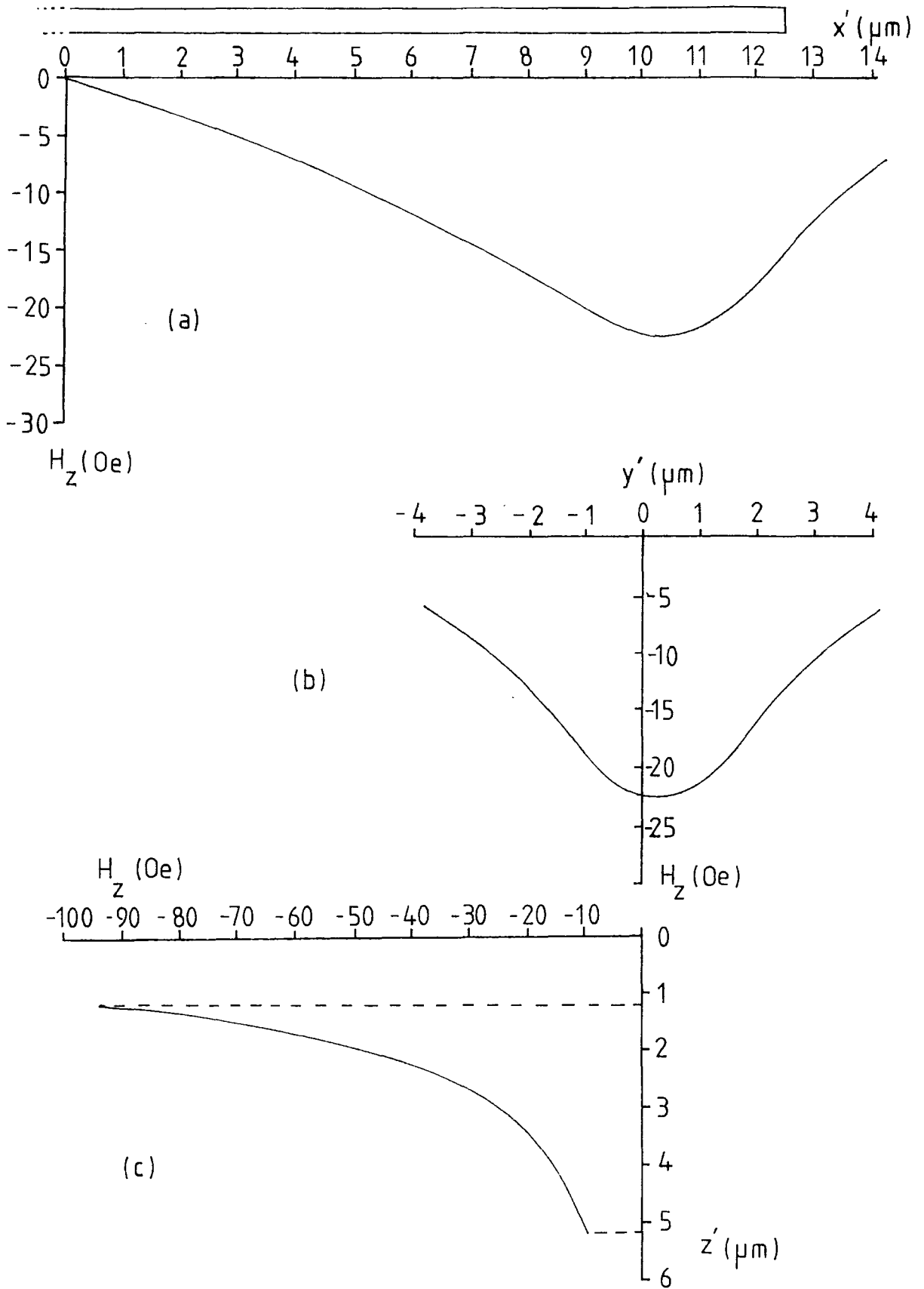


Fig. 8.11 z -component magnetostatic field beneath a bar ($25 \times 2.1 \times 0.4 \mu\text{m}$) containing a single charged domain wall.

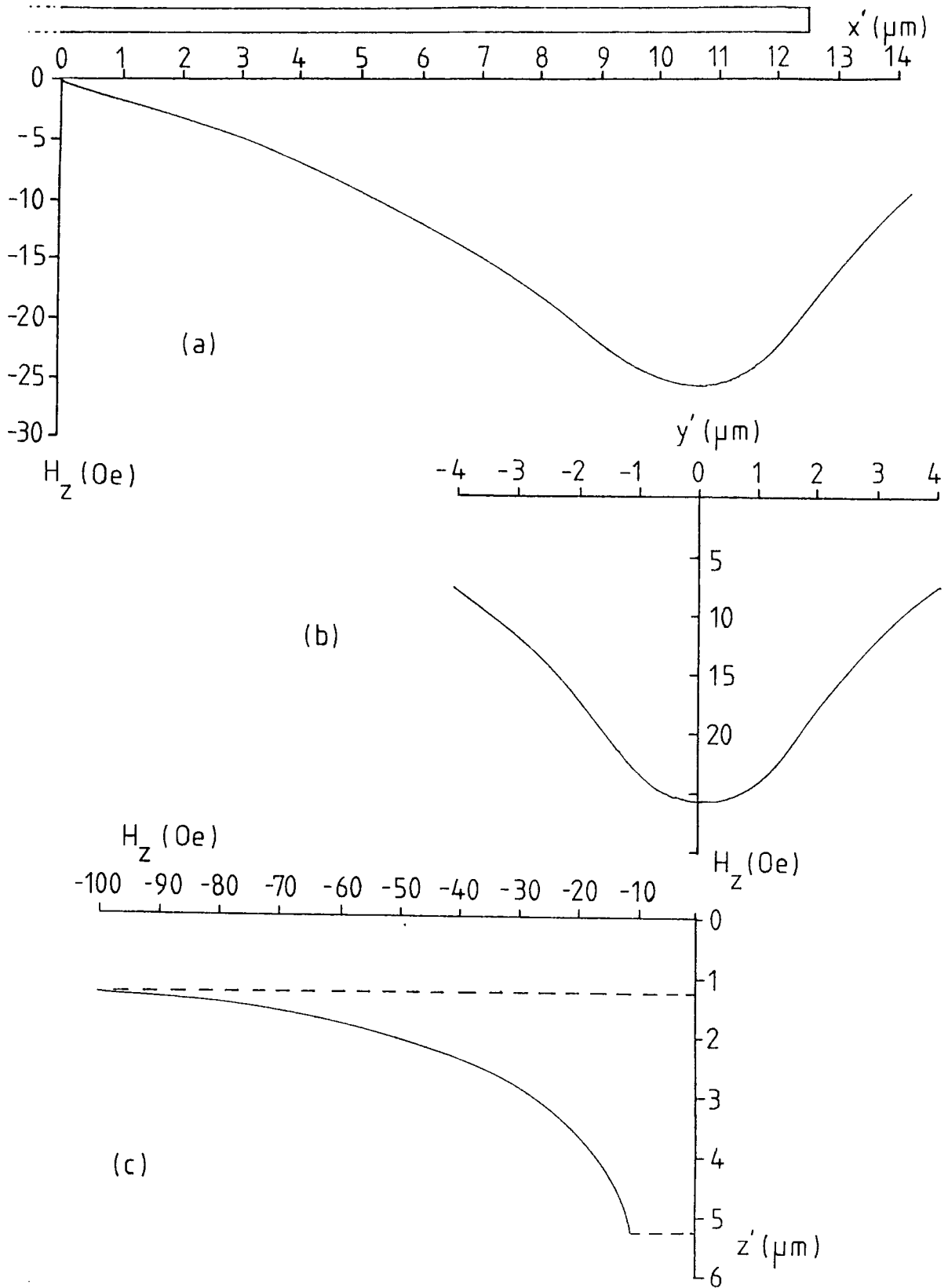


Fig. 8.12 z -component magnetostatic field beneath a bar ($25 \times 2.1 \times 0.4 \mu\text{m}$) containing a volume distribution of magnetic pole density.

representing these intersections with lines of 'free-pole'. Using the Bloch wall model of fig. 6.1, the component of magnetization normal to the external surface varies across the width of the wall having an average value of $\frac{2}{\pi}M_s$. Therefore let the free pole density per unit length be :

$$p = \frac{2}{\pi} M_s \sigma$$

where σ is the wall width.

The field due to a single line of charge (length $2b$) can be obtained using the coordinates shown in fig. 8.15(a). The z component field at S due to the element dx at x is given by:

$$dH_z = \frac{p dx}{4\pi r^2} \cos \theta$$

From symmetry, the total field at S is parallel to the z axis. Therefore by integrating between $x = -b$ and $x = b$:

$$H_z = \frac{pb}{2\pi z(b^2 + z^2)^{\frac{1}{2}}}$$

Therefore the field below a Bloch wall of length $2b$ (as in fig. 8.15(b)) will be :

$$H_z = \frac{pb}{2\pi} \left[\frac{1}{z(b^2 + z^2)^{\frac{1}{2}}} - \frac{1}{(z+t)(b^2 + (z+t)^2)^{\frac{1}{2}}} \right]$$

In fig. 8.16 (a) H_z is plotted as a function of z between the imagined upper and lower surfaces of a bubble film at $z = 1 \mu\text{m}$ and $z = 5 \mu\text{m}$. (Substituting $b = 6.5 \mu\text{m}$, i.e. for a Bloch wall

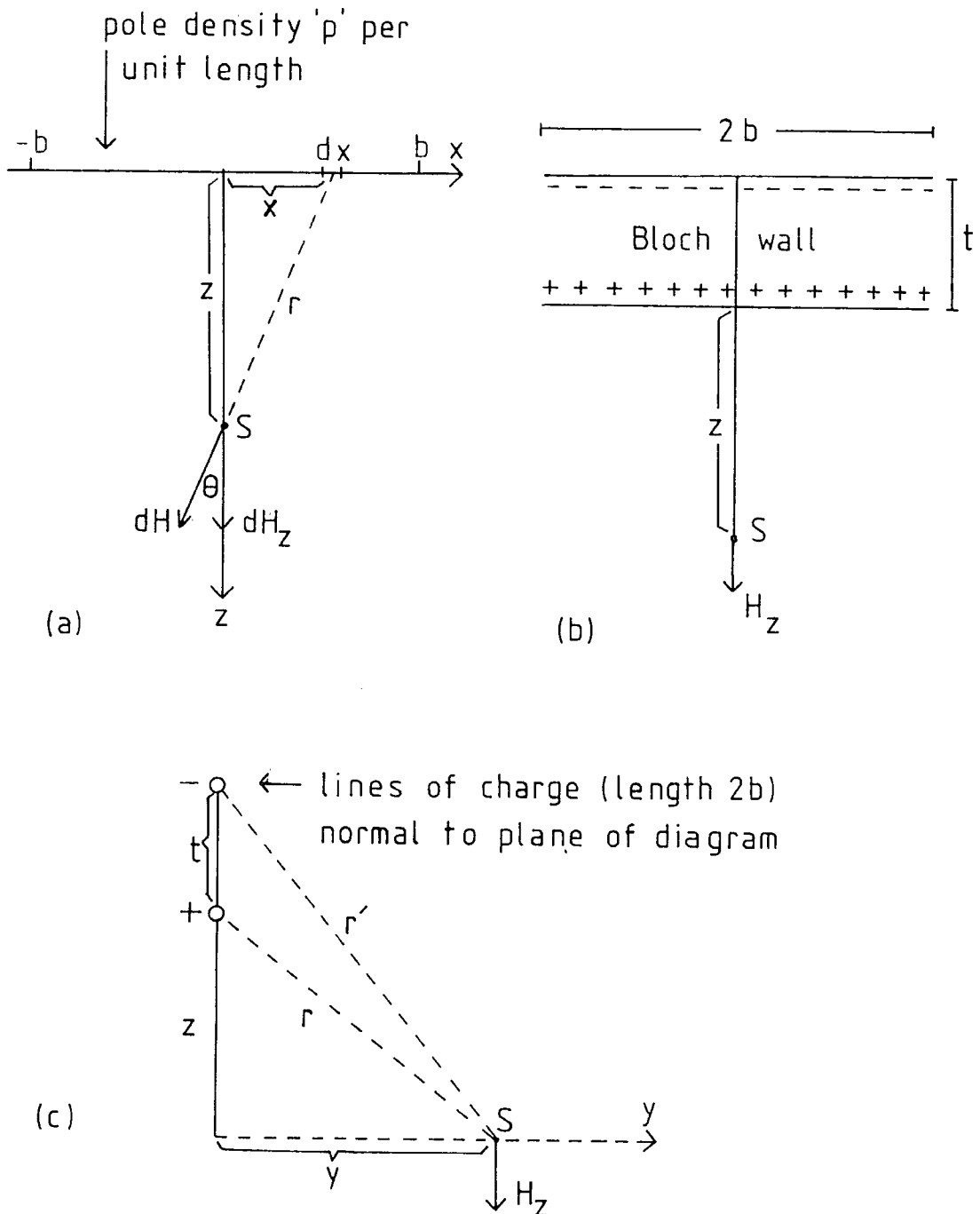


Fig. 8.15 Coordinates used for calculating (a) the field from a line of charge, (b) the field H_z from a Bloch wall and (c) the variation in H_z perpendicular to the wall.

of uniform polarity in a $15 \times 2.1 \mu\text{m}$ bar and $t = 0.4 \mu\text{m}$, $\sigma \approx 500 \text{A}$). H_z is roughly an order of magnitude weaker than the field wells plotted in figs. 8.12, 8.13 and falls off rapidly with z , being approximately 2 Oe in the mid-plane of the bubble medium. Using the coordinates shown in fig. 8.15(c) the variation in H_z along an axis perpendicular to the wall can be estimated. At a distance y along this axis :

$$H_z = \frac{pb}{2\pi} \left[\frac{z}{r^2(b^2 + r^2)^{\frac{3}{2}}} - \frac{z+t}{r'^2(b^2 + r'^2)^{\frac{3}{2}}} \right]$$

$$\text{where } r^2 = z^2 + y^2$$

$$r'^2 = (z+t)^2 + y^2$$

H_z is plotted as a function of y for the mid-plane of the bubble medium ($z = 3 \mu\text{m}$) in fig. 8.16(b). The field gradients are considerably less than those arising from the net magnetization of a bar (see figs. 8.12 and 8.13). The Bloch wall would therefore seem to produce at most a small perturbation on the field experienced by bubble domains ; a perturbation in the form of a shallow magnetostatic field well.

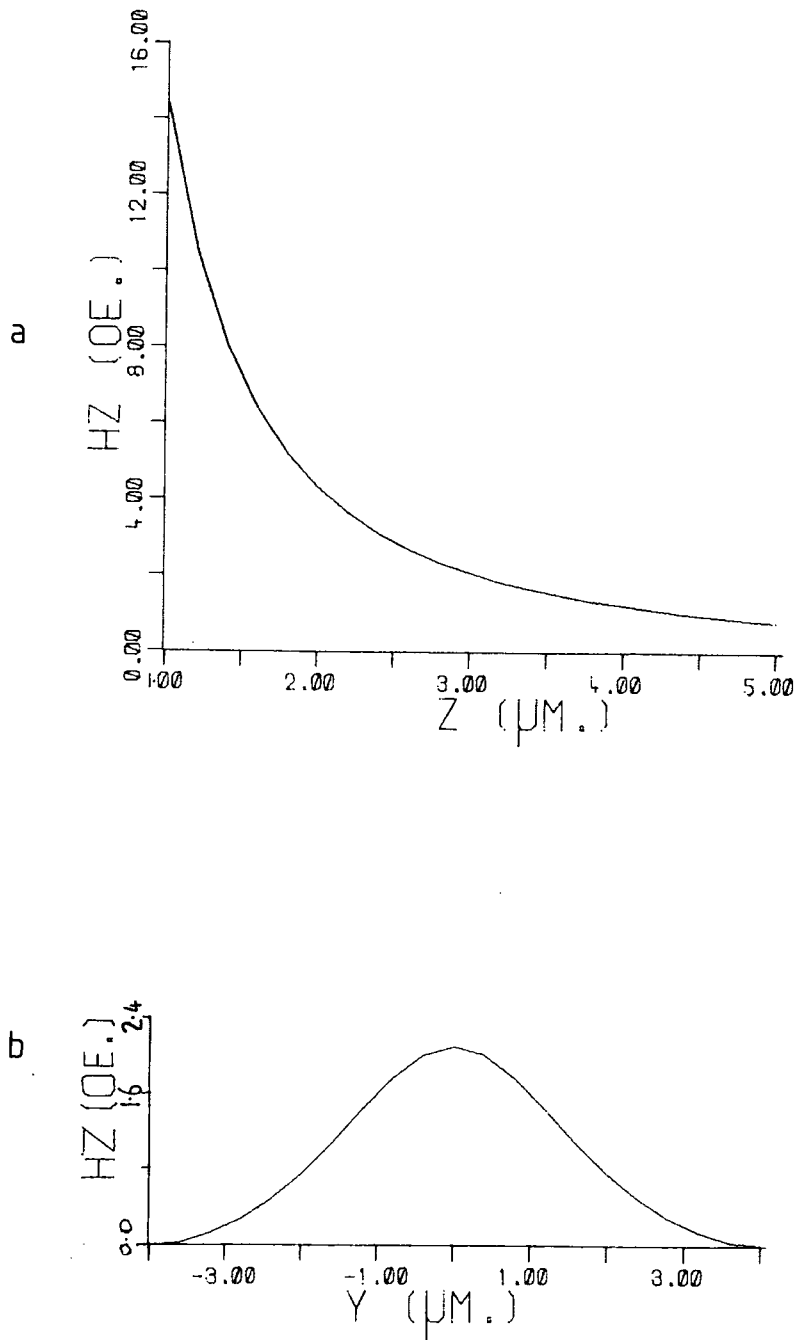


Fig 8.16 (a) z -component magnetic field directly beneath a Bloch wall of length $13.0 \mu\text{m}$ in permalloy of thickness $0.4 \mu\text{m}$. In (b) the field is plotted along an axis perpendicular to the wall in the mid-plane of the bubble medium ($z = 3.0 \mu\text{m}$).

CHAPTER 9 CONCLUSIONS + SUGGESTIONS FOR FURTHER WORK.

The results presented in this thesis confirm that the ferrofluid technique can provide useful information on domains in permalloy overlays. Each method for observing magnetic domains has certain advantages and disadvantages. Ferrofluid can reveal domain wall structures with higher resolution than is generally obtainable with the Kerr effect and can be used on samples which are rather thick for the application of Lorentz microscopy. With the closed module approach, routine observations can be spread over several hours if necessary and the use of oil immersion objectives is facilitated. The resolution is just sufficient for the study of domains in $16\mu\text{m}$ period circuits with approximately $2\mu\text{m}$ bar width. The major disadvantage of the ferrofluid technique is that observations can only be made in at best a quasi-static mode. Neither the Kerr effect nor Lorentz microscopy suffer from this limitation. However useful information can be obtained in slowly changing fields and in zero field especially following saturation and hysteresis.

Of the factors which determine domain structure in overlay bars, magnetostatic energy appears dominant. In general demagnetized bars were found to contain a small number of domains with flux closure in evidence. This applied to all types of geometry and is consistent with previous investigations of T- and I-bars. A simple calculation based on Néel's model for magnetostatic energy in a domain wall suggests that the Bloch walls separating domains in these samples will be quite narrow (a few hundred \AA in width) compared with domain boundaries in bulk permalloy.

For permalloy bars anisotropy generally plays a secondary

role in determining domain structure but it was established that in-plane anisotropy may affect the demagnetized state in some cases. This is manifested in the distribution of internal closure domains. In early examples of overlay circuits bars can be filled with this type of domain and a simple minimum energy calculation suggests that a relatively small anisotropy is required. However the same calculation confirms that more recent circuits with smaller circuit period are less likely to be affected in this way since the required anisotropy field is inversely proportional to bar width. In these patterns internal closure domains seem to occur more sporadically and they can be found both in samples on non magnetic substrate and on bubble garnet. The applicability of the minimum energy principle is demonstrated quite well by measurements on larger areas of permalloy. In particular the relationship between domain spacing and bar width agrees well with theory.

In 'weak' applied fields all $16\mu\text{m}$ period components were observed to respond initially by reversible domain growth. The wall displacement in elements such as the asymmetric chevron is simply proportional to the applied field. This agrees with previous work on T- and I-bars. In this region the coercivity and remanence are particularly small and the basic assumptions of most theoretical models are reasonable. What has not been reported before in real-sized overlay bars is the systematic formation of buckled states with remanent magnetization once the applied field exceeds a critical value H_g . In many respects the hysteretic properties of $16\mu\text{m}$ -period I-bars and more complex elements match those observed by Kerr effect and Bitter colloid in $100 \times 12 \times 0.3\mu\text{m}$ bars.

Apart from the formation of remanence, 'irreversible' changes in the demagnetized state may occur following partial saturation and buckling. In particular it was established that the number of closure domains and Bloch wall segments could change in multiples of two. Following saturation a bar can be found in any one of a number of 'higher order' states through the simpler configurations are usually preferred - in general they will have the lower energy (assuming there is no strong anisotropy present). These changes may not have a marked effect on the propagation of bubble domains but they demonstrate the limitations of applying domain models to overlay bars. On the other hand buckled remanent states may have some effect on the operation of a device especially since they can persist in a rotating field (at least for quasi-static fields). Residual attractive poles associated with remanence would certainly modify the 'magnetostatic potential well' experienced by bubble domains.

The study of H_s as a function of element geometry confirms what might be expected intuitively. Long narrow elements with low demagnetizing fields have small values of H_s compared with more 'compact' elements. The results also show that H_s is approximately proportional to permalloy thickness. If hysteresis is undesirable in overlay components the permalloy used should be thick. However other factors will inevitably be involved such as fabrication problems and detector signal requirements. Eight micron-period bubble circuits with $2\mu\text{m}$ bubbles are now being developed in the laboratory. The graphs presented in figs. 6.25 and 6.26 can easily be used to predict saturation fields for $8\mu\text{m}$ elements. In general permalloy thickness has been maintained as circuit periods have reduced. If t is fixed the saturation

fields should rise in inverse proportion to the circuit period P so H_S for an element with $8\mu\text{m}$ period should be twice that for the same element in a $16\mu\text{m}$ period circuit. However this does not mean that saturation effects will be drastically reduced since the drive field also rises ($H \propto \mu_0 M_S$ where M_S = bubble magnetization, and $\mu_0 M_S$ varies approximately as $d^{-0.8}$ where d is bubble diameter; Eschenfelder (1980, P.118)).

An obvious extension of this work would be to study the influence of bubble domains on the formation of remanent states in an overlay. In theory this could be achieved using ferrofluid though it is difficult to image the permalloy and garnet domain systems simultaneously with good contrast. The preliminary results presented in fig. 6.29 for overlays on random stripe domains in garnet suggest that the bubble medium could have a considerable influence on H_S . Also it would be useful if the details of magnetization buckling in these components could be established by Lorentz microscopy as has already been done for buckling in narrow strips of permalloy (e.g. Herd et al., 1979).

Chapter 7 confirms that magnetization buckling also plays an important role in the response of detector columns to in-plane fields. The behaviour of a closed loop of permalloy is analagous since the natural minimum energy state in both cases is one of saturation with continuous flux flow. In the present study it was established that two types of magnetization reversal by buckling could occur; along the whole column or in alternate chevron limbs. This depends on the direction of the in-plane field (D.C.).

A related magnetoresistance signal was expected since buckling introduces transverse components of magnetization and this was confirmed by measuring column resistance. The percentage

change in resistance is consistent with that calculated on the basis of a simple domain model and the shape of the signals can be related to the different types of reversal involved. On the basis of these observations in D.C. fields an alternative to the 'magnetization fanning model' for a detector column in a rotating field can be developed.

It would clearly be desirable to investigate the influence of stripe domains on a detector column by using ferrofluid. Again this would be a difficult task especially in a rotating field of 40 Oe where colloid contrast is poor. An investigation of the average magnetization using the Kerr effect for chevron columns in rotating fields and with stripe domains has been reported recently by Harrison (1980).

In chapter 8 it was established that the field well produced by a permalloy bar could be modelled on the type of curved domain wall revealed by ferrofluid. Approximate values for the saturation field H_s can also be obtained by computing the average demagnetizing field at the centre of the bar. In a more rigorous analysis it would be better to calculate the average demagnetizing field energy over the whole volume of the bar. (The varying direction of \vec{M} in the volume free pole model would need to be taken into account). This might produce more accurate values for H_s and it would also allow a comparison of the two configurations in terms of total energy. In their review of domain and continuum results, Huijser et al. (1980) made the observation that different configurations of magnetization can produce the same pole distribution and hence identical external fields. The field plots of figs. 8.11 and 8.12 suggest that to some extent the pole distribution itself can be varied without causing a marked

change in the external field profile (at least over distances comparable with the bubble-bar separation).

The calculations presented in chapter 8 are not intended to provide a practical method for modelling overlays but rather as an indication of how the fields might be produced in reality. In a working device the influence of bubble stray fields on the wall displacement would need to be considered and in irregular elements such as the asymmetric chevron or pick-axe the wall movements would be difficult to model. Considering also the irreversible changes in domain structure which take place once the field exceeds H_g it would seem that a continuum approach to modelling is more practical. However, an ideal model for magnetization processes in permalloy overlays would include the residual pole density associated with remanent states.

REFERENCES.

- Almasi, G.S., (1973) Proc. IEEE 61, 438.
- Almasi, G.S., Keefe, G.E., Lin, Y.S. and Thompson, D.A. (1971) J. Appl. Phys. 42, 1268.
- Almasi, G.S. and Lin, Y.S., (1976) IEEE Trans. on Magn. MAG-12, 160.
- Amelio, G.F., (1974) Sci. Am. 230, 23.
- Archer, J.L., Tocci, L., George, P.K. and Chen, T.T., (1972) IEEE Trans. on Magn. MAG-8, 695.
- Banbury, J.R. and Nixon, W.C., (1967) J. Sci. Instrum. 44, 889.
- Bitter, F., (1931) Phys. Rev. 38, 1903.
- Blois, M.S. Jr., (1955) J. Appl. Phys. 26, 975.
- Bobeck, A.H., (1967) Bell Syst. Tech. J. 46, 1901.
- Bobeck, A.H., (1977) Proc. Electro '77, Paper 12-1.
- Bobeck, A.H., Fischer, R.F., Perneski, A.J., Remeika, J.P. and Van Uitert, L.G., (1969) IEEE Trans. on Magn. MAG-5, 544.
- Bobeck, A.H., Spencer, E.G., Van Uitert, L.G., Abrahams, S.C., Barns, R.L., Grodkiewicz, W.H., Sherwood, R.C., Schmidt, P.H., Smith, D.H., and Walters, E.M., (1970) Appl. Phys. Lett. 17, 131.
- Bobeck, A.H., Fischer, R.F., and Smith, J.L., (1971) AIP Conf. Proc. 5, 45.
- Bobeck, A.H., Scovil, H.E.D., (1971) Sci. Am. 224, 78.
- Bobeck, A.H., Blank, S.L., and Levinstein, H.J., (1972) Bell Syst. Tech. J. 51, 1431.
- Bobeck, A.H., Danylchuk, I., Rossol, F.C. and Strauss, W., (1973) IEEE Trans. on Magn. MAG-9, 474.
- Bobeck, A.H., Blank, S.L., Butheris, A.D., Ciak, F.J. and Strauss, W., (1979) IEEE Trans. on Magn. MAG-15, 1519.
- Bonyhard, P.I., Smith, J.L., (1976) IEEE Trans. on Magn. MAG-12, 614.
- Brown, W.F., Jr., (1962) "Magnetostatic Principles in Ferromagnetism." North Holland Pub. Co., Amsterdam.
- Carey, R. and Isaac, E.D., (1966), "Magnetic Domains and Techniques for their Observation."
- Chaudhari, P., Cuomo, J.J., Gambino, R.J., Kirkpatrick, S.

- and Tao, I.J., (1974) AIP Conf. Proc. 24,562.
- Chikazumi, S., (1950) J. Phys. Soc. Japan 5,327.
- Cohen, M.S., Beall, G.W., Kryder, M.H., Mazzeo, N.J. and Collins, T.W., (1979) J. Appl. Phys. 50(3),2201.
- Collins, T.W. and Cole, R.W., (1980) IEEE Trans. on Magn. MAG-16,846.
- Copeland, J.A., (1972) J. Appl. Phys. 43(4),1905.
- Craik, D.J., (1966) Brit. J. of Appl. Phys. 17,873.
- Craik, D.J. and Griffiths, P.M., (1958) Brit. J. of Appl. Phys. 9,279.
- Craik, D.J. and Tebble, R.S., (1965) "Ferromagnetism and Ferromagnetic Domains" North Holland Pub. Co., Amsterdam.
- Danylchuk, I., (1971) J. Appl. Phys. 42,1358.
- DeBlois, R.W. and Graham, C.D., (1958) J. Appl. Phys. 29,931.
- Della Torre, E. and Kinsner, W., (1973) IEEE Trans. on Magn. MAG-9,298.
- Doyle, W.D. and Casey, M., (1973) AIP Conf. Proc. 10,227.
- Dove, D.B., Watson, J.K., Huijjer, E. and Ma, H., (1975) AIP Conf. Proc. 29,44.
- Dove, D.B., Watson, J.K., Ma, H.R. and Huijjer, E., (1976) J. Appl. Phys. 47(5),2237.
- Druyvesteyn, W.F. and Dorleijn, J.W.F., (1971) Philips Res. Rep. 26,11.
- Druyvesteyn, W.F., v d Enden, A.W.M., Kuijpers, F.A., de Niet, E. and Verhulst, A.G.H., (1975) Inst. Phys. Conf. Ser. 25,37.
- Eschenfelder, A.H., (1980) "Magnetic Bubble Technology" Springer Verlag.
- Fairholme, R.J., (1974) Inst. Phys. Conf. Ser. 11,334.
- Fathers, D.J., Joy, D.C. and Jakubovics, J.P., (1974) "Eighth International Conf. on Electron Microscopy." (Canberra) Vol. 1,630.
- Galt, J.K., (1954) Bell Syst. Tech. J. 33,1023.
- George, P.K. and Chen, T.T., (1972) Appl. Phys. Lett. 21,263.
- George, P.K. and Archer, J.L., (1973) J. Appl. Phys. 44,444.

- George, P.K. and Hughes, A.J., (1976) IEEE Trans. on Magn. MAG-12,137.
- George, P.K., Oeffinger, T.R and Chen, T.T., (1976) J. Appl. Phys. 47,3302.
- Gergis, I.S., George, P.K. and Kobayashi, T., (1976) IEEE Trans. on Magn. MAG-12,651
- Giess, E.A., Kuptsis, J.D. and White, E.A.D., (1972) J. Cryst. Growth 16,36.
- Grundy, P.J., Tebble, R.S. and Hothersall, D.C., (1971) J. Phys. D: Appl. Phys. 4,174.
- Grundy, P.J., Jones, G.A. and Tebble, R.S., (1974) AIP Conf. Proc. 24,541.
- Grundy, P.J., (1977) Contemp. Phys. 18(1),47.
- Hagedorn, F.B., (1971) AIP Conf. Proc. 5,72.
- Hale, M.E., Fuller, H.W. and Rubinstein, H., (1959) J. Appl. Phys. 30,789.
- Harrington, J.V., (1958) M.I.T. Lincoln Lab. Tech. Rept. No.166.
- Harrison, C.G., (1980) IEEE Trans. on Magn. MAG-16,861.
- Herd, S.R., Ahn, K.Y. and Kane, S.M., (1979) IEEE Trans. on Magn. MAG-15,1824.
- Hsin, C.H., Matcovich, T.J. and Coren, R.L., (1971) AIP Conf. Proc. 5,245.
- Hu, H.L., Beaulieu, T.J., Chapman, D.W., Franich, D.M., Henry, G.R., Rosier, L.L. and Shew, L.F., (1978) J. Appl. Phys. 49, 1913.
- Hubbell, W.C., Singh, S.K. and West, F.G., (1975) AIP Conf. Proc. 29,26.
- Huber, E.E., Smith, D.O. and Goodenough, J.B., (1958) J. Appl. Phys. 29,294.
- Huijser, E., Dove, D.B., and Watson, J.K., (1978) J. Appl. Phys. 49,1903.
- Huijser, E. and Watson, J.K., (1979) J. Appl. Phys. 50,2149.
- Huijser, E., Watson, J.K. and Dove, D.B., (1980) IEEE Trans. on Magn. MAG-16,120
- Huijser, E., Dove, D.B. and Watson, J.K., (1981) IEEE Trans. on Magn. MAG-17,1124.
- Humphrey, F.B., (1980) J. of Magn. and Mag. Mat. 15-18,1464.

- Ishak, W. and Della Torre, E., (1978) IEEE Trans. on Magn. MAG-14,1035.
- Ishak, W. and Della Torre, E., (1979) IEEE Trans. on Magn. MAG-15,1026.
- Jacobs, I.S., (1979) J.Appl.Phys. 50,7294.
- Jones, G.A., Grundy, P.J. and Brambley, D.R., (1978) J.Phys. D: Appl. Phys. 11,L165.
- Jouve, H. and Puchalska, I.B., (1979) IEEE Trans. on Magn. MAG-15,1016.
- Kestigian, M., Smith, A.B. and Bekebrede, W.R., (1979) J. Appl. Phys. 50,2161.
- Khaiyer, I. and O'Dell, T.H., (1976) AIP Conf. Proc. 29,37.
- Khaiyer, I., (1976) Phys. Stat. Sol. (A) 34,K105.
- Khaiyer, I., (1976b) IEEE Trans. on Magn. MAG-12,114.
- Kittel, C., (1946) Phys. Rev. 70,965.
- Kittel, C., (1949) Phys. Rev. 76,1527.
- Kooy, C. and Enz, U., (1960) Philips Res. Reports 15,7.
- Krinchik, G.S., Chepurova, E.E., Shamatov, U.N., Raev, V.K. and Andreev, A.K., (1975) AIP Conf. Proc. 24,649.
- Krinchik, G.S., Chepurova, E.E., Shamatov, U.N., Egamov, S.V., Raev, V.K. and Andreev, A.K., (1976) IEEE Trans. on Magn. MAG-12,413.
- Krinchik, G.S., Chepurova, E.E. and Shamatov, U.N., (1978) IEEE Trans. on Magn. MAG-14,1129.
- Kryder, M.H., Ahn, K.Y., Almasi, G.S., Keefe, G.E. and Powers, J.V., (1974) IEEE Trans. on Magn. MAG-10,825.
- Kryder, M.H., Ahn, K.Y., Mazzeo, N.J., Schwarzl, S. and Kane, S.M., (1980) IEEE Trans. on Magn. MAG-16,99.
- Lacklison, D.E., Scott, G.B., Giles, A.D., Clarke, J.A., Pearson, R.F. and Page, J.L., (1977) IEEE Trans. on Magn. MAG-13,973.
- Landau, L. and Lifshitz, E., (1955) Physik. Z. Sowjetunion 8, 153.
- Levinstein, H.J., Landorf, R.W. and Licht, S.J., (1971) IEEE Trans. on Magn. MAG-7,470.
- Lilley, B.A., (1950) Phil. Mag. 41,792.
- Lin, Y.S., (1972) IEEE Trans. on Magn. MAG-8,375.

- Lin, Y.S., Almasi, G.S. and Keefe, G.E., (1977) IEEE Trans. on Magn. MAG-13,1744.
- Ma, H.R., (1976) "Magnetostatic Fields in Thin Film Permalloy Bar Arrays." Ph.D. Thesis University of Florida.
- Malozemoff, A.P., (1972) Appl. Phys. Lett. 21,149.
- Matsutera, H. and Hidaka, Y., (1979) J. Appl. Phys. 50,2289.
- Methfessel, S., Middlehoek, S. and Thomas, H. (1960) J. Appl. Phys. 31,302S.
- Methfessel, S., Middlehoek, S. and Thomas, H., (1962) J. Phys. Soc. Japan 17 B1,607.
- Middlehoek, S., (1961) "Ferromagnetic Domains in Thin Nickel-Iron Films." Ph.D. Thesis University of Amsterdam.
- Middlehoek, S., (1963) J. Appl. Phys. 34,1054.
- Morrish, A.H., (1965) "The Physical Principles of Magnetism." Wiley.
- Néel, L., (1955) C.R. Acad. Sci. (Paris) 241,533.
- Nelson, T.J., Wolfe, R., Blank, S.L., Bonyhard, P.I., Johnson, W.A., Roman, B.J. and Vella-Coleiro, G.P., (1980) Bell Syst. Tech. J. 59,229.
- Nielsen, J.W., (1976) IEEE Trans. on Magn. MAG-12,327.
- Nomarski, G. and Weil, A.R., (1955) Revue de Metallurgie L 11, 121.
- O'Dell, T.H., (1974) "Magnetic Bubbles." Macmillan, London.
- Orihara, S., Yanase, T. and Majima, T., (1979) J. Appl. Phys. 50,1692.
- Osborn, J.A., (1945) Phys. Rev. 67,351.
- Perneski, A.J., (1969) IEEE Trans. on Magn. MAG-5,554.
- Popplewell, J. and Charles, S.W., (1979) Phys. Bull. 30,474.
- Prutton, M. (1964) "Thin Ferromagnetic Films." Butterworths, London.
- Rhodes, P. and Rowlands, G., (1954) Proc. Leeds Phil. Lit. Soc. 6,191.
- Roman, B.J., Nelson, T.J., and Smith, J.L., (1980) IEEE Trans. on Magn. MAG-16,489.
- Rosencwaig, A., Tabor, W.J. and Pierce, R.D., (1971) Phys. Rev. Lett. 26,779.
- Rosencwaig, A., (1972) Bell Syst. Tech. J. 51,1440.

- Schultz, L., Giess, E.A., Hogson, R.T. and Sedgwick, T.O., (1979) J.Appl. Phys. 50,5902.
- Scott, G.B. and Lacklison, D.E., (1976) IEEE Trans. on Magn. MAG-12,292.
- Shtrikman, S. and Treves, D., (1960) J. Appl. Phys. 31,1745.
- Slonczewski, J.C., (1973) J. Appl. Phys. 44,1759.
- Slonczewski, J.C., Malozemoff, A.P. and Voegeli, O., (1973) AIP Conf. Proc. 10,458.
- Stoner, E.C., (1945) Phil. Mag. 36,803.
- Strauss, W., (1971) J. Appl. Phys. 42,1251.
- Strauss, W. and Smith, G.E. (1970) J.Appl. Phys. 41,1169.
- Strauss, W., Shumate, P.W. and Ciak, F.J., (1972) AIP Conf. Proc. 5,235.
- Tabor, W.J., Bobeck, A.H., Vella-Coleiro, G.P. and Rosencwaig, A., (1972) Bell Syst. Tech. J. 51,1427.
- Thiele, A.A., (1969) Bell Syst. Tech. J. 48,3287.
- Thiele, A.A., (1970) J. Appl. Phys. 41,1139.
- Van Uitert, L.G., Smith, D.H., Bonner, W.A., Grodkiewicz, W.H., Pictroski, L. and Zydik, G., (1970) Mater. Res. Bull. 5,455.
- Vella-Coleiro, G.P., Hagedorn, F.B., Chen, Y.S. and Blank, S.L., (1973) Appl. Phys. Lett. 22,324.
- Voegeli, O., Calhoun, B.A., Rosier, L.L. and Slonczewski, J.C., (1975) AIP Conf. Proc. 24,617.
- Voermans, A.B., Breed, D.J., van Erk, W. and Carpay, F.M.A., (1979) J. Appl. Phys. 50,7829.
- Vonsovskii, S.W. (1974) "Magnetism," (translated from the Russian by R. Hardin), New York, Wiley.
- Walsh, T.J. and Charap, S.H., (1974) AIP Conf. Proc. 24,550.
- Watson, J.K., Ma, H.R., Dove, D.B. and Huijjer, E., (1976) IEEE Trans. on Magn. MAG-12,660.
- Weiss, P., (1907) J. Phys. 6,667.
- West, F.G., Hubbell, W.C. and Singh, S.K., (1975) AIP Conf. Proc. 29,28.
- Williams, H.J. and Shockley, W., (1949) Phys. Rev. 75,178.
- Williams, H.J. and Goertz, M., (1952) J. Appl. Phys. 23,316.

Wolfe, R. and North, J.C., (1972) Bell Syst. Tech. J. 51, 1436.

Wolfe, R., North, J.C., Johnson, W.A., Spiwak, R.R., Varn-
erin, L.J. and Fischer, R.F., (1973) AIP Conf. Proc. 10,339.

Wolfe, R. and North, J.C., (1974) Appl. Phys. Lett. 25,122.

